

FACILITY FORM 62
 (ACQUISITION NUMBER) N66-13242
 (PAGES) 187 (CODE) 7
 (NASA CR OR TMX OR AD NUMBER) (CATEGORY) 28

NASA CR-54687
 RAD-TR-65-37

GPO PRICE \$ _____

CFSTI PRICE(S) \$ _____

Hard copy (HC) 5.00

Microfiche (MF) 1.25

NASA

853 July 65

ARCJET TECHNOLOGY RESEARCH AND DEVELOPMENT

Prepared for

NATIONAL AERONAUTICS AND SPACE ADMINISTRATION
 LEWIS RESEARCH CENTER
 Cleveland, Ohio

Contract NAS 3-5900

RESEARCH AND ADVANCED DEVELOPMENT DIVISION
 AVCO CORPORATION
 Wilmington, Massachusetts

NASA CR-54687

RAD-TR-65-37

FINAL REPORT

ARCJET TECHNOLOGY RESEARCH AND DEVELOPMENT

3 June 1964 through 11 September 1965

Prepared for

NATIONAL AERONAUTICS AND SPACE ADMINISTRATION

22 December 1965

Contract NAS 3-5900

Technical Management
NASA Lewis Research Center
Cleveland, Ohio
Electric Propulsion Office
Henry Hunczak

RESEARCH AND ADVANCED DEVELOPMENT DIVISION
AVCO CORPORATION
Wilmington, Massachusetts

ABSTRACT

13242

Experimental results are presented on the propulsion performance of an MPD arcjet thruster operated on both gaseous and alkali metal vapor propellants. The overall electric to thrust power efficiency appears to be primarily a function of the specific impulse and propellant type, and is quite insensitive to the absolute value of either the input power or the applied external magnetic field. The propulsion data obtained for engine operation with gaseous propellants at low mass flows is open to question because of the existence of gas entrainment; operation of the MPD arcjet thruster with the condensable alkali metal vapor propellants, and thus reduced test tank back pressures, has reduced but not eliminated the possibility of interaction between the acceleration process and the test tank environment. Although the performance of the MPD arcjet ($> 50\%$ efficiency at 5000 seconds specific impulse) continues to look attractive, work is urgently required to determine the nature and extent of the gas acceleration process.

Author

PRECEDING PAGES BLANK NOT FILMED

CONTENTS

I.	Introduction.....	ii
A.	Program Objective.....	1
B.	Program Organization	1
C.	Program Scheduling ..	1
D.	Technical Summary.....	1
II.	MPD Arcjet Engine	5
A.	Background	5
B.	X-2 High Impulse Engine	7
1.	Engine Configuration.....	7
2.	Auxiliary Magnetic Field	9
3.	Test Systems.....	15
C.	X-2 Engine Operation with Gases	20
1.	Weak External Magnetic Field.....	20
2.	Strong External Magnetic Field	48
D.	Possible Mass Entrainment by the X-2 Engine with Strong External Magnetic Field	75
1.	Qualitative Observations on Zero-Gas Flow Operation.....	75
2.	Quantitative Observations on Zero-Gas Flow Operation.....	77
3.	Observations on Engine Operation in a Closed Tank...	80
4.	Observations on Engine Operation in Different Gaseous Atmospheres	80
5.	Observations on the Behavior of a Thrust Plate in the MPD Arcjet Exhaust.....	80
6.	Ambient Tank Pressures Required to Eliminate Gas Entrainment	81
E.	Alkali Metal Operation -- Water-Cooled.....	83
1.	Engine Configuration.....	83
2.	Feed System	87
3.	Engine Operation	91
4.	Voltage Measurements	91
5.	Propulsion Performance.....	92

CONTENTS (Cont'd)

F.	Alkali Metal Operation -- Radiation Cooled	100
1.	Engine Configuration	100
2.	Propulsion Performance	102
III.	Magnet Subsystem	106
A.	Electromagnet Design	106
1.	Fabry Formula	106
2.	Radiation - Cooled Magnet Subsystem	107
3.	Liquid - Cooled Magnet Subsystem	115
4.	Weight Comparison of Liquid - and Radiation - Cooled Magnet Subsystems	115
B.	Permanent Magnets	122
IV.	Applied Research	124
A.	Introduction	124
B.	Conditions in the MPD Arcjet Exhaust	124
1.	Appearance of the Exhaust	124
2.	Estimates of Density and Mean Free Path	124
3.	Electrical Characteristics	125
4.	Velocity	126
5.	Conclusions	127
C.	Acceleration Mechanism	127
1.	Description	127
2.	Evidence for the Electrothermal Model of MPD Operation	130
3.	Performance Calculations	131
V.	Current Development Status of the MPD Arcjet	138
VI.	Direction for Future Research	140
VII.	References	141

CONTENTS (Concl'd)

Appendixes

A.	High Specific Impulse Engine Performance Data	145
B.	Calculation of Contributions of T_{self}	153
C.	MPD Arcjet Engine Performance Data	159
D.	Propulsion Performance of a Liquid Cooled MPD Thrustor with Cesium Propellant	165
E.	A Theoretical Model for the MPD Arcjet in a Strong Magnetic Field	167
F.	Propulsion Performance of a Radiation Cooled MPD Thrustor with Lithium Propellant	173
G.	Exhaust Velocity Measurements Using a $\underline{u} \times \underline{B}$ Probe	175

BLANK PAGE

ILLUSTRATIONS

Figure	1	Schematic of High Impulse Accelerator	5
	2	X-2A High Specific Impulse Arc Jet Engine; Schematic	8
	2a	Configuration X2-A	10
	2b	Configuration X2-B	10
	3	High Impulse Arcjet	11
	4	X-2C High-Specific Impulse Arcjet Thrustor Disassembled	12
	5	X-2C High-Specific Impulse Arcjet Thrustor Assembled	13
	6	Magnetic Field Map for a Magnet Current of 1200 Amperes	14
	7	Arc Engine Thrust versus Magnetic Field Strength	16
	8	Magnetic Field Map	17
	9	Plasma Generator Chamber Pressure versus Gas Flow Rate	21
	10	Plasma Generator Thrust versus Arc Current (Hydrogen)	23
	11	Plasma Generator Thrust versus Arc Current (Ammonia)	24
	12	Plasma Generator Thrust versus Arc Current (Argon)	25
	13	Plasma Generator MPD Thrust versus Arc Current and Hydrogen Flow Rate	26
	14	Plasma Generator MPD Thrust versus Arc Current and Ammonia Flow Rate	27

ILLUSTRATIONS (Cont'd)

Figure	15	Plasma Generator MPD Thrust versus Arc Current and Argon Flow Rate	28
	16	Plasma Generator MPD Thrust versus Arc Current	30
	17	Cathode Pressure versus Arc Current	32
	18	Plasma Generator Self-Thrust versus Arc Current	34
	19	Arc Voltage versus Arc Current	35
	20	Overall Efficiency versus Arc Engine Specific Impulse (Hydrogen)	37
	21	Overall Efficiency versus Arc Engine Specific Impulse (Ammonia)	38
	22	Overall Efficiency versus Arc Engine Specific Impulse (Argon)	39
	23	Efficiency versus Arc Engine Specific Impulse	41
	24	Gas Enthalpy versus Arc Engine Specific Impulse	43
	25	Gas Temperature versus Arc Engine Specific Impulse	44
	26	Frozen Flow Efficiency versus Arc Engine Specific Impulse (Hydrogen)	45
	27	Frozen Flow Efficiency versus Arc Engine Specific Impulse	47
	28	Arc Voltage versus Arc Current (Hydrogen)	49
	29	Arc Voltage versus Arc Current (Ammonia)	50
	30	Arc Voltage versus Magnetic Field Strength (Hydrogen, Ammonia)	52
	31	Plasma Generator Thrust versus Arc Current (Hydrogen)	54

ILLUSTRATIONS (Cont'd)

Figure	32	Plasma Generator Hall Thrust versus Product of Arc Current and Magnetic Field Strength (Hydrogen)	56
	33	Plasma Generator Thrust versus Arc Current (Ammonia)	57
	34	Plasma Generator Hall Thrust versus Product of Arc Current and Magnetic Field Strength (Ammonia)..	58
	35	Power to Cooling versus Arc Current (Hydrogen)	60
	36	Power to Cooling versus Arc Current (Ammonia)	61
	37	Power to Cooling versus Arc Current (Helium)	63
	38	Power to Cooling versus Arc Current (Nitrogen)	64
	39	Power to Cooling versus Arc Current (Argon)	65
	40	Thermal Efficiency versus Magnetic Field Strength (Hydrogen)	67
	41	Thermal Efficiency versus Magnetic Field Strength (Ammonia)	68
	42	Overall Efficiency versus Arc Engine Specific Impulse (Hydrogen)	70
	43	Overall Efficiency versus Arc Engine Specific Impulse (Ammonia)	71
	44	Overall Efficiency versus Arc Engine Specific Impulse	72
	45	Measured Overall Energy Conversion Efficiency versus Hydrogen Flow Rate	79
	46	Sketch of Liquid Cooled MPD Arcjet Used with Cesium	84
	47	Map of Magnetic Field Used with Cesium MPD Arcjet	85

ILLUSTRATIONS (Cont'd)

Figure	48	Field Strength versus Current for MPD Arcjet Magnet	86
	49	Cesium Vapor Feed System	88
	50	Cesium Vapor Pressure as a Function of Temperature ..	89
	51	Estimated Cesium Mass Flow Rate as a Function of Temperature and Orifice Diameter	90
	52	Photograph of MPD Arcjet Operating with Cesium	94
	53	Arc Voltage versus Magnetic Field Strength for Cesium Operation	95
	54	Anode Heating Power versus Current	97
	55	Efficiency versus Specific Impulse for Cesium	98
	56	Ratio of Overall Efficiency to Arc Efficiency as a Function of Magnetic Field Strength	99
	57	Sketch of Radiation-Cooled MPD Arcjet Used with Cesium	101
	57a	Alkali Feed System	103
	58	Overall Efficiency versus Specific Impulse Radiation-Cooled MPD Arcjet	104
	59	Normalized Magnet Power Input versus Axial Magnetic Field Strength	108
	60	Copper Resistivity versus Temperature	109
	61	Normalized Magnet Power versus Coil Temperature ...	110
	62	Weight of Radiation-Cooled Magnet System versus Axial Magnetic Field Strength: Inner Radius = 1 cm	112
	63	Weight of Radiation-Cooled Magnet System versus Axial Magnetic Field Strength: Inner Radius = 2.5 cm...	113

ILLUSTRATIONS (Concl'd)

Figure	64	Weight of Radiation-Cooled Magnet System versus Axial Magnetic Field Strength: Inner Radius = 5 cm	114
	65	Weight of Liquid-Cooled Magnet System versus Axial Magnetic Field Strength: Inner Radius = 1 cm	116
	66	Weight of Liquid-Cooled Magnet System versus Axial Magnetic Field Strength: Inner Radius = 2.5 cm...	117
	67	Weight of Liquid-Cooled Magnet System versus Axial Magnetic Field Strength: Inner Radius = 5 cm	118
	68	Weight Comparison of Radiation and Liquid-Cooled Magnet System versus Axial Magnetic Field Strength: Inner Radius = 1 cm	119
	69	Weight Comparison of Radiation and Liquid-Cooled Magnet System versus Axial Magnetic Field Strength: Inner Radius = 2.5 cm	120
	70	Weight Comparison of Radiation and Liquid Cooled Magnet System versus Axial Magnetic Field Strength: Inner Radius = 5 cm	121
	71	Magnetic Nozzle Model of MPD Arcjet Operation	129
	72	Shape of the Magnetic Nozzle	132
	73	Enthalpy versus Temperature for Cesium	135
A-1		Configuration X2-A	146
A-2		Configuration X2-B	146
G-1		Comparison of Velocities as Measured by T/\hbar and $\underline{u} \times \underline{B}$ Probe	176

PRECEDING PAGES BLANK NOT FILMED

TABLES

Table I	Overall Efficiency Ratio for Ammonia and Hydrogen	74
II	Comparison of MPD Arc Jet Voltage and Thrust for Propellant Injection Through the Engine and Propellant Injection Outside the Engine	78
III	Maximum Possible Values of Entrained Mass Flow versus Ambient Pressure	82
IV	Magnet Subsystem Specific Weight	123

I. INTRODUCTION

A. PROGRAM OBJECTIVE

The objectives of this program, entitled Arc Jet Technology Research and Development, conducted under Contract NAS 3-5900 with the NASA Lewis Research Center, have been to explore the operation of the magnetoplasma-dynamic (MPD) arcjet thruster and to evaluate the factors contributing to thruster life and overall energy conversion efficiency.

B. PROGRAM ORGANIZATION

This program originated from the Electric Propulsion Office of the NASA Lewis Research Center. Mr. H. Hunczak was Project Manager for the Electric Propulsion Office. Dr. R. R. John was Project Director at Avco RAD and Dr. S. Bennett was Associate Project Director. Principal Avco RAD participants and the areas in which they contributed are: Dr. A. Tuchman, Mr. G. Enos, and Mr. C. Simard, Thruster Development and Performance Testing; Dr. J. Yos, Thruster Analysis; Dr. Tuchman and Mr. W. Powers, Thruster Diagnostics.

C. PROGRAM SCHEDULING

This is the Final Report submitted under Contract NAS 3-5900; it covers the period from 3 June 1964 through 11 September 1965.

D. TECHNICAL SUMMARY

During the initial stages of the program, primary attention, both experimental and analytical, was directed towards the exploration of increases in specific impulse and efficiency which appear to be associated with operation of arcjet thrusters at low propellant mass flow rates and high current levels. It was postulated that these increases resulted from self-induced magnetic field effects. Apparent specific impulse values (thrust/mass flow rate) in excess of 10,000 seconds were obtained in a water-cooled arcjet engine with hydrogen propellant, at overall efficiencies of approximately 50 percent at power levels in the range of 100 to 200 kw. Tests were made with other gaseous propellants as well; in particular, argon, nitrogen and ammonia were used. Engine performance with ammonia was quite similar to that obtained with hydrogen, particularly with respect to the efficiency--specific impulse curve. Simple analyses were made of the engine performance based upon the cathode jet mechanisms proposed by Maecker⁵, and fairly good agreement between the predictions of these analyses and the measured values was obtained.

An external magnetic field coil was added to the engine to compare the increases in specific impulse and efficiency obtained from the self-induced field effects studied during the initial stages of the contract period with those due to externally applied magnetic field effects. Propulsion data were obtained with hydrogen and ammonia as propellants over a wide range of propellant flow rates, arc currents, arc powers, and applied magnetic field strengths. Overall efficiency values (at input power levels of 20 to 160 kw) for hydrogen were found to be 25 percent at 3000 seconds, 30 percent at 4000 seconds, 40 percent at 5000 seconds. For ammonia (at input power levels of 20 to 80 kw) the data indicated efficiencies of 30 percent at 3000 seconds, and 35 percent at 3500 seconds. Some data were also obtained with helium, argon, and nitrogen as propellants. An effort was made to separate the contributions to the measured thrusts from the different thrust producing mechanisms--aerodynamic, self-induced, and external magnetic field effects.

Experimental data were next obtained which suggested that environmental test tank gas entrainment may have been an important factor in the evaluation of magnetoplasmadynamic (MPD) arcjet propulsion performance. Specifically, the MPD arcjet was operated at a condition of zero mass flow (inlet gas off). It was found that electrode erosion was negligible and that at a fixed arc current the measured values of engine thrust and voltage for the gas-off condition were quite similar to the values obtained for the gas on condition. The results thus indicated that under at least some conditions of mass flow rate and tank back pressure, the entrained gas flow was of the same order of magnitude as the metered inlet gas flow. Failure to include the entrained gas flow in the estimates of engine thrust power would lead to overestimated values for the thrust power and thus to overestimated values of the electric to thrust power conversion efficiency.

In order to reduce the gas flow entrained by the MPD arcjet discharge an effort was made to operate the MPD arcjet at as low a back pressure as possible. Experiments with flowing ammonia and hydrogen were carried out at back pressures of the order of 100 microns. By using condensable propellants, e.g., the alkali metals, which can be readily cryopumped, the operating back pressure was reduced by at least three orders of magnitude to about 10^{-1} micron. Experiments were initiated using both cesium and lithium as working fluids in order to obtain lower operating pressures; further, cesium and lithium are both attractive as MPD arcjet propellants because of their potentially high frozen flow efficiencies when compared to hydrogen. Preliminary data were obtained with both cesium and lithium.

During the same period, work was initiated towards a study of magnet subsystems. A critical problem in the application of the MPD arcjet to either a solar-electric or nuclear-electric powered spacecraft is the weight of the required subsystems. The MPD arcjet is inherently a low voltage device, and the power conditioning subsystem requirements are minimal; however, it is likely that the MPD arcjet will require either a permanent magnet or

electromagnet to produce the required external magnetic field. A preliminary study was carried out to determine the weight and power requirements of the external magnetic field subsystem. It became clear from this study that the critical parameter in the determination of the weight and power penalties associated with the external field was, as might be expected, the strength and shape of the required field.

During the second half of the contract period, emphasis was placed upon operation of a low power (5 to 10 kw) MPD arcjet with cesium as the propellant. In a water-cooled thruster design specific impulse values up to nearly 3000 seconds were obtained, with no indication that any limit had been reached. The anode heating losses were substantial under these conditions with between 50 and 70 percent of the input power lost in the anode. The overall propulsive efficiencies were therefore only of the order of 10 percent at 2000 seconds I_{sp} and 14 percent at 3000 seconds I_{sp} . A radiation-cooled thruster was built and operated with cesium as the propellant, and preliminary propulsion data were obtained with it.

With cesium as the propellant, the required pumping speed of the vacuum system was greatly reduced compared to the value for operation in a gas such as hydrogen. Much of the propellant condenses in the test tank and need not be handled by the pumps. Thus a small diffusion pump was inserted into the test system and allowed testing at running pressures of the order of 0.1 micron as measured by an ionization gauge.

During the final quarter thrust data were obtained using cesium and lithium as propellants with a radiation-cooled, low-power (5 to 20 kw) thruster. Operating ambient tank pressures as measured with an ionization gauge were of the order of 0.1 to 0.2 micron, with ambient gas mean free paths of the order of the dimensions of the test tank itself. Operation of the engine with cesium yielded overall propulsive efficiencies of the order of 10 to 15 percent at specific impulse values of 2000-3000 seconds. With lithium as propellant, propulsive efficiencies of the order of 30 to 40 percent were obtained at specific impulse levels of the order of 4000 to 5000 seconds.

A tentative model of MPD arcjet operation with cesium was developed. According to this model the MPD arcjet is principally an electrothermal device with the magnetic field serving in place of the conventional nozzle. Energy is added to the propellant from the electric field in random form. Expansion of the propellant in the magnetic nozzle yields the high observed specific impulse values. The model, though tentative, appears to explain certain qualitative features of MPD arcjet operation which are not easily explained otherwise.

During this period also, measurements were begun to determine the distribution of the magnetic field and current density in the exhaust jet of the thrusters. The measurements were made using Hall effect magnetic field

probes to determine the magnetic field distribution, and the current density distribution was determined from the measured magnetic field with the aid of Maxwell's equations. The preliminary data obtained indicate that a rather sizeable fraction of the total arc current flows outside the physical confines of the engine and lends support to the "magnetic-nozzle" analysis put forth during the fourth quarter.

The following papers were presented during the past year:

1. Experimental Performance of a High Specific Impulse Arc Jet Engine by R. R. John, S. Bennett, and J. F. Connors (AIAA Preprint 64-669), AIAA Fourth Electric Propulsion Conference, Philadelphia, Pennsylvania, 31 August to 1 September 1964.
2. Recent Advances in Electrothermal and Hybrid Electrothermal Electromagnetic Propulsion, by R. R. John, and S. Bennett, Fourth Symposium on Advanced Propulsion Concepts, Palo Alto, California, April 25 to 28, 1965.
3. Cesium Fueled MPD Arc Jet Engine Performance, by S. Bennett G. Enos, R. R. John, and A. Tuchman (AIAA Preprint 65-296), AIAA Second Annual Meeting, San Francisco, California, 26 July to 29 July 1965.

II. MPD ARCJET ENGINE

A. BACKGROUND

While arcjet engines and Hall accelerators have been under development at a number of laboratories^{1,2,3} over the past five years, only within the past two years has the specific impulse level of 2,500 seconds been exceeded. The acceleration mechanisms which produce the greatly increased specific impulse levels now attainable appear to be a combination of aerodynamic, self-magnetic, and applied magnetic field effects. These mechanisms, in different proportions, are now being used in the different laboratories to achieve specific impulse values from 2,500 to 10,000 seconds, with major effort concentrated in the 3,000 to 5,000 second range. A basic geometry, illustrated in figure 1, characterizes virtually all of the improved accelerators. The units are cylindrically symmetrical, consisting of a central cathode surrounded by a coaxial anode. A magnetic coil is mounted coaxially with the thruster, with the thruster exit plane generally slightly downstream of the downstream edge of the coil.

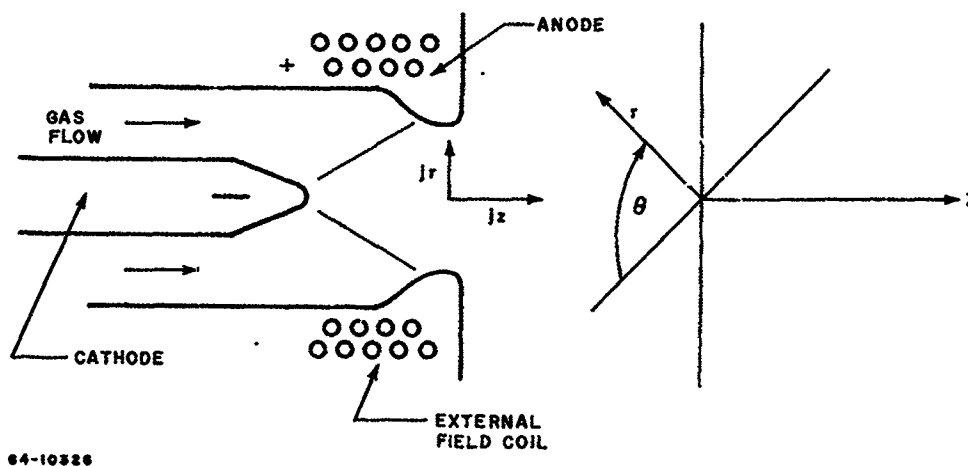


Figure 1 SCHEMATIC OF HIGH IMPULSE ACCELERATOR

Reference 4 discusses in some detail five basic thrust-producing mechanisms which have been identified in the literature as being characteristic of plasma generators of the type illustrated in figure 1. These are (1) aerodynamic pressure forces; (2) magnetic pumping; (3) magnetic blowing; (4) aerodynamic swirl induced by MPD forces; and (5) Hall current acceleration.

With the thrust resulting from mechanism (1) defined as T_{aero} and the thrust from mechanisms (2) and (3) as T_{self} , it is shown in reference 4 that

$$T_{\text{aero}} = P_c A_t \quad (1)$$

and

$$T_{\text{self}} = T_{\text{pump}} + T_{\text{blow}} \quad (2)$$

where

$$T_{\text{pump}} = 5.1 \times 10^{-6} I^2 \quad (3)$$

and

$$T_{\text{blow}} = 1.02 \times 10^{-5} I^2 \left(1/4 + \ln \frac{r_a}{r_c} \right) \quad (4)$$

when the current enters the cathode uniformly after leaving the anode as a ring, or

$$T_{\text{blow}} = 1.02 \times 10^{-5} I^2 \left(\ln \frac{r_a}{r_c} \right) \quad (5)$$

when the current distribution at the cathode is similar to the distribution at the anode.

In equations (1) through (5),

T_{aero} = aerodynamic thrust component, grams

P_c = chamber pressure, grams-force/cm²

A_t = throat area, cm²

T_{self} = self MPD thrust, grams

T_{pump} = magnetic pumping thrust, grams

T_{blow} = magnetic blowing thrust, grams

I = arc current, amp

r_a = outer radius of current distribution at anode, cm

r_c = outer radius of current distribution at cathode, cm.

T_{pump} results from the interaction of the axial discharge current density, j_z , with the self-induced magnetic field, B_θ . T_{blow} results from the interaction of the radial discharge current, i_r , with the self-induced magnetic field, B_θ . Both T_{pump} and T_{blow} were identified by Maecker⁵.

The magnetic swirl mechanism,⁴ is associated with the bulk rotation of the gas and results from the interaction of the radial component of the current, j_r , with an axial component of the applied magnetic field, B_z , and from the interaction of j_z with B_r . In order to produce useful thrust, the rotational energy must be converted into axially directed kinetic energy by means of a nozzle. This basic thrust mechanism has been described by, among others, Hess,⁶ Ellis⁸ and Powers and Patrick⁹.

Finally, the fifth thrust mechanism results from the interaction of an induced azimuthal Hall current, j_θ , with the applied magnetic field. The most likely thrust-producing interaction is the body force given by $j_\theta B_r$, but it is also possible to achieve thrust from the pressure produced by $j_\theta B_z$. These mechanisms have been investigated by Hess⁷, Seikel and Reshotko¹⁰, Cann^{11,12}, Patrick and Powers¹³, and Gourdin¹⁴.

The tests performed during the early part of this contract period were made with engines utilizing only a weak external magnetic field for arc rotation and tested the first 3 of the 5 basic mechanisms (aerodynamic pressure forces and the two mechanisms associated with self-induced magnetic field effects) since their existence is not dependent upon the presence of an external magnetic field. The remaining two mechanisms which result from the interaction of the discharge current with an externally produced magnetic field were explored during the remainder of the contract period.

B. X-2 HIGH IMPULSE ENGINE

1. Engine Configuration

During the course of the third year of the 30-kw arcjet engine program (Contract NAS 3-2593) a 50 to 250-kw liquid-cooled high specific impulse engine was developed and designated as the X-2 design. A sketch of the X-2 engine design is given in figure 2. The cathode consists of a water-cooled copper rod with a tip of thoriated tungsten. The anode is water-cooled copper. Propellant is injected tangentially upstream of the cathode, swirls over the cathode tip and through the throat, and is ejected immediately. There is no constrictor section in the X-2 design, and the arc discharge between cathode tip and anode is not confined or constricted over any appreciable length by a straight section. Moreover, the X-2 design need not include a conical exit nozzle. The nozzle exit plane is very close to the throat (which is relatively large) and is joined to the throat by a rounded contour.

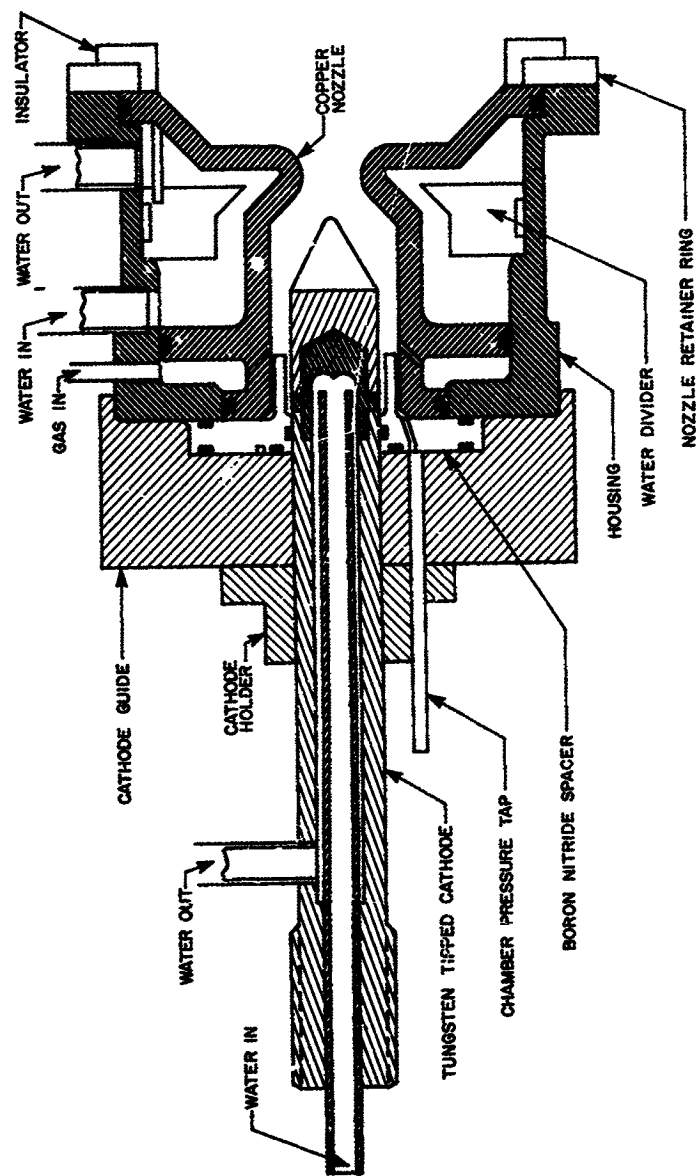


Figure 2 X-2A HIGH SPECIFIC IMPULSE ARC JET ENGINE; SCHEMATIC

64-2979

The elimination of the constrictor section was prompted by a desire to operate an engine with very low mass flow rates. Experience with the 30-kw engines indicated that the anode attachment zone tends to be moved upstream by reduction of the mass flow rate and that reduction below some minimum value tended to move this attachment zone into the constricted region resulting in heavy constrictor damage and eventual engine failure. The desired use of low mass flow rates was also instrumental in the decision to eliminate (or severely truncate) the nozzle since at low mass flow rates and reduced operating pressures, viscous effects are expected to become more important.

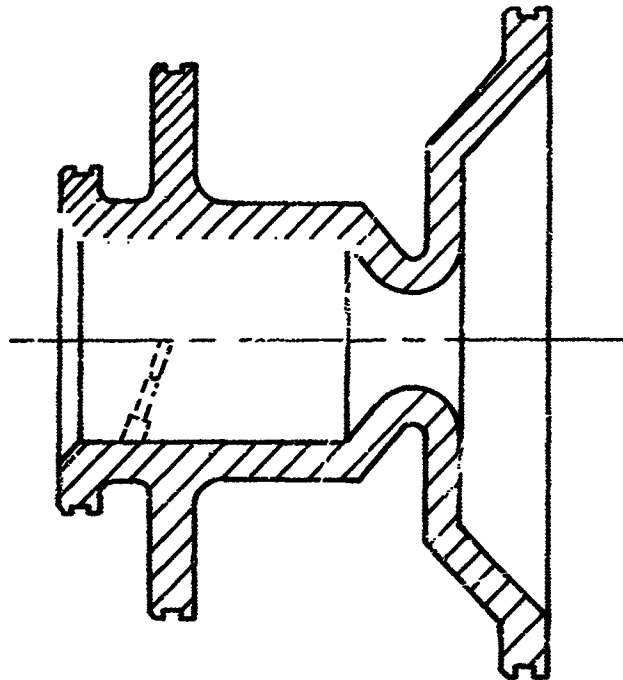
Shown as figures 2a and 2b are two variations of the basic configuration which have been tested. The anode of figure 2b (engine design X-2B) is a straight-through channel; that of figure 3 (engine design X-2C) includes a short supersonic nozzle section. The X-2C engine was used for the majority of the testing performed. For convenience, and comparison, figure 3 shows a schematic of the X-2C high impulse arcjet engine; figures 4 and 5 show photographs of the X-2C engine in assembled and disassembled views.

2. Auxiliary Magnetic Field

a. Weak Field

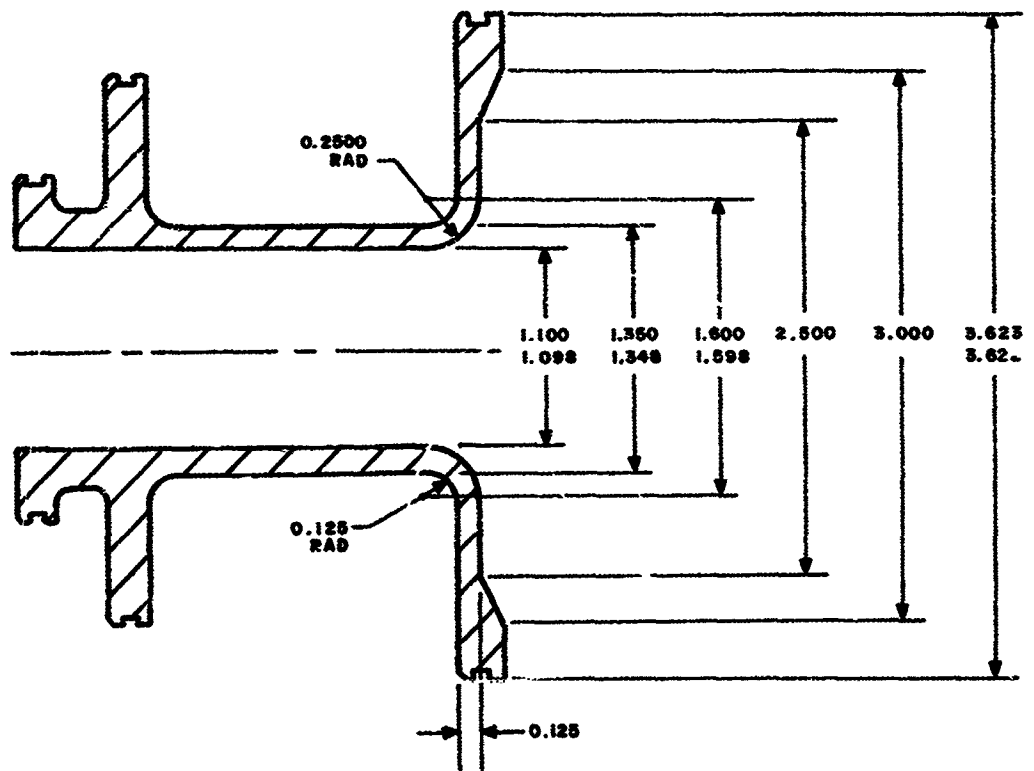
For the exploration of the thrust mechanisms arising from self-induced field effects, an external field coil which produces a maximum axial field strength of 500 gauss was used. The coil consisted of seven 9-inch diameter turns of water-cooled copper tubing, and was separately excited by rectifiers independent of the main discharge power supply. The coil has been mounted both on the test tank, and, in a separate series of experiments, on the thruster. In the first case accelerating forces exerted by the magnet on the propellant should not be sensed by the thrust stand, and in the second case these forces, if they exist, should be sensed.

A map of the magnetic field produced by this coil is shown in figure 6. Each arrow represents a measured value of the magnetic field strength at a coil excitation current of 1200 amp. The length of the arrow is proportional to the magnetic field strength, and its direction is that of the field at the point. The dashed lines of figure 6 have been sketched in using the measured field values as guides. The field strength has also been measured as a function of excitation current, and exhibits linearity over the range of excitation current 300 to 1500 amperes, i. e., $B(r, z) = k I_{\text{field}}$.



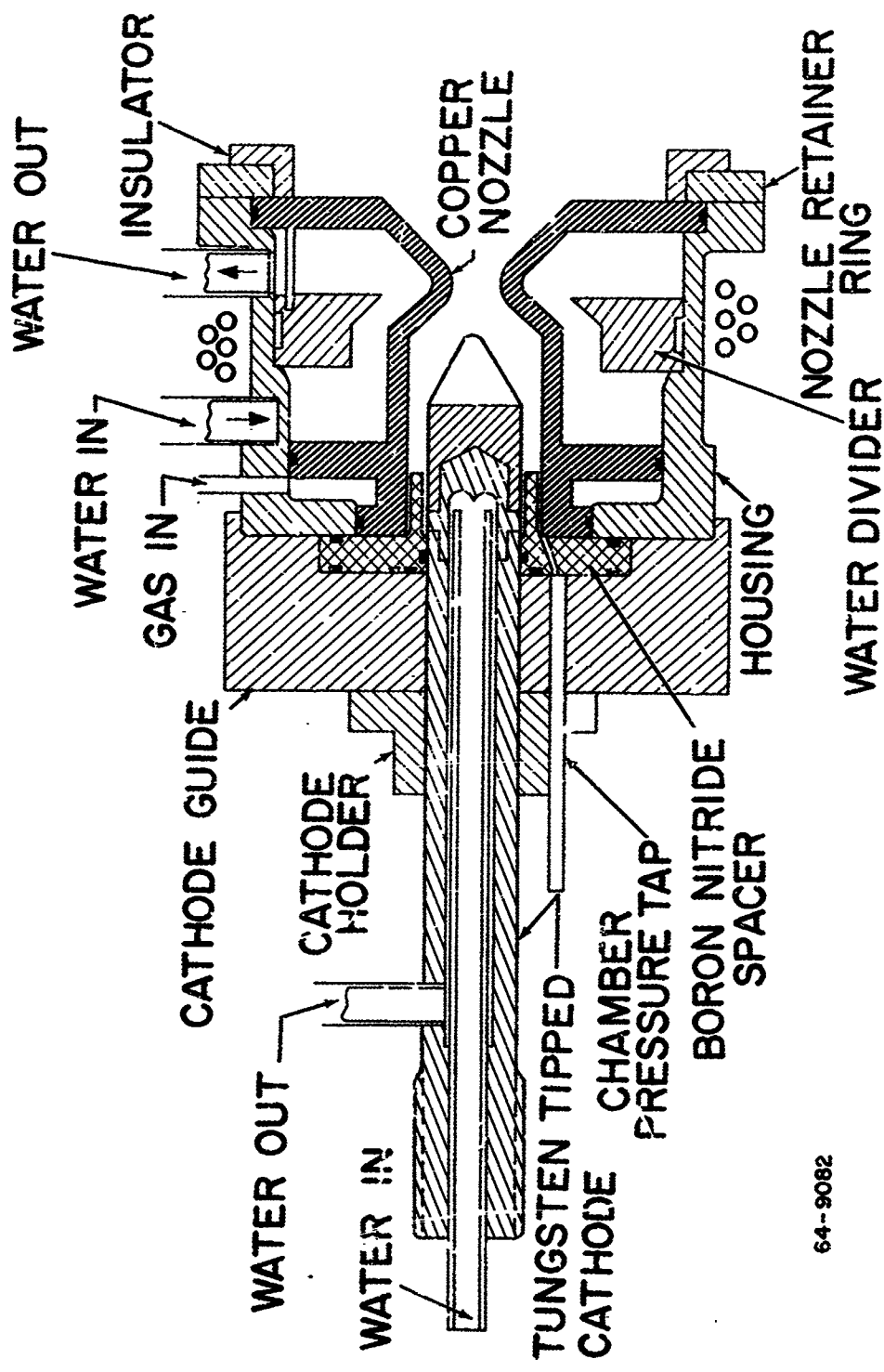
64-10347

Figure 2A CONFIGURATION X2-A



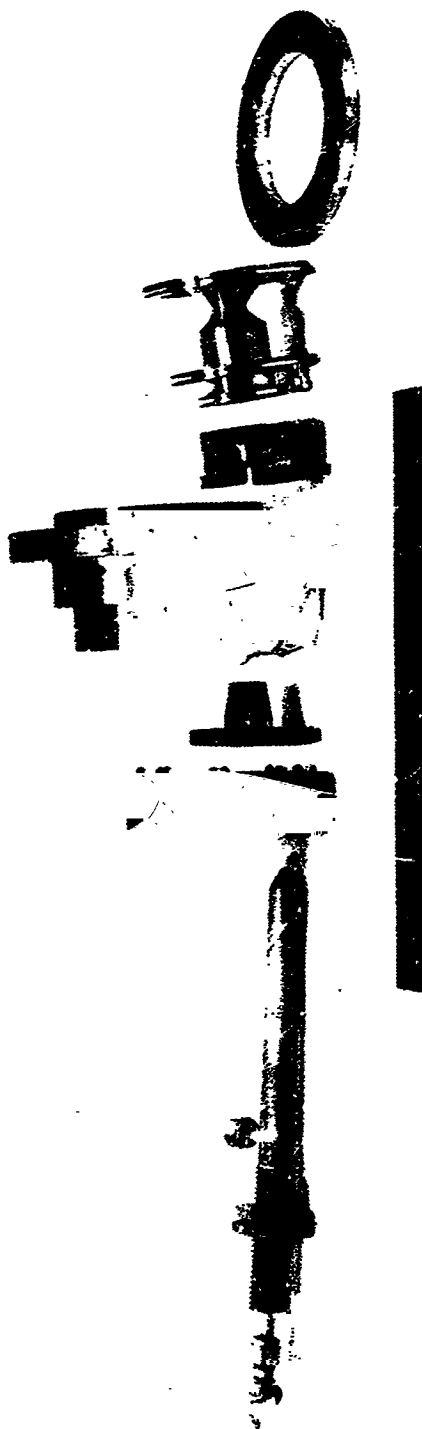
64-10348

Figure 2B CONFIGURATION X2-B



64-9082

Figure 3 HIGH IMPULSE ARCJET



12193-F

Figure 4 X-2C HIGH-SPECIFIC IMPULSE ARCJET THRUSTOR DISASSEMBLED



Figure 5 X-2C HIGH-SPECIFIC IMPULSE ARCJET THRUSTOR ASSEMBLED

12183-D

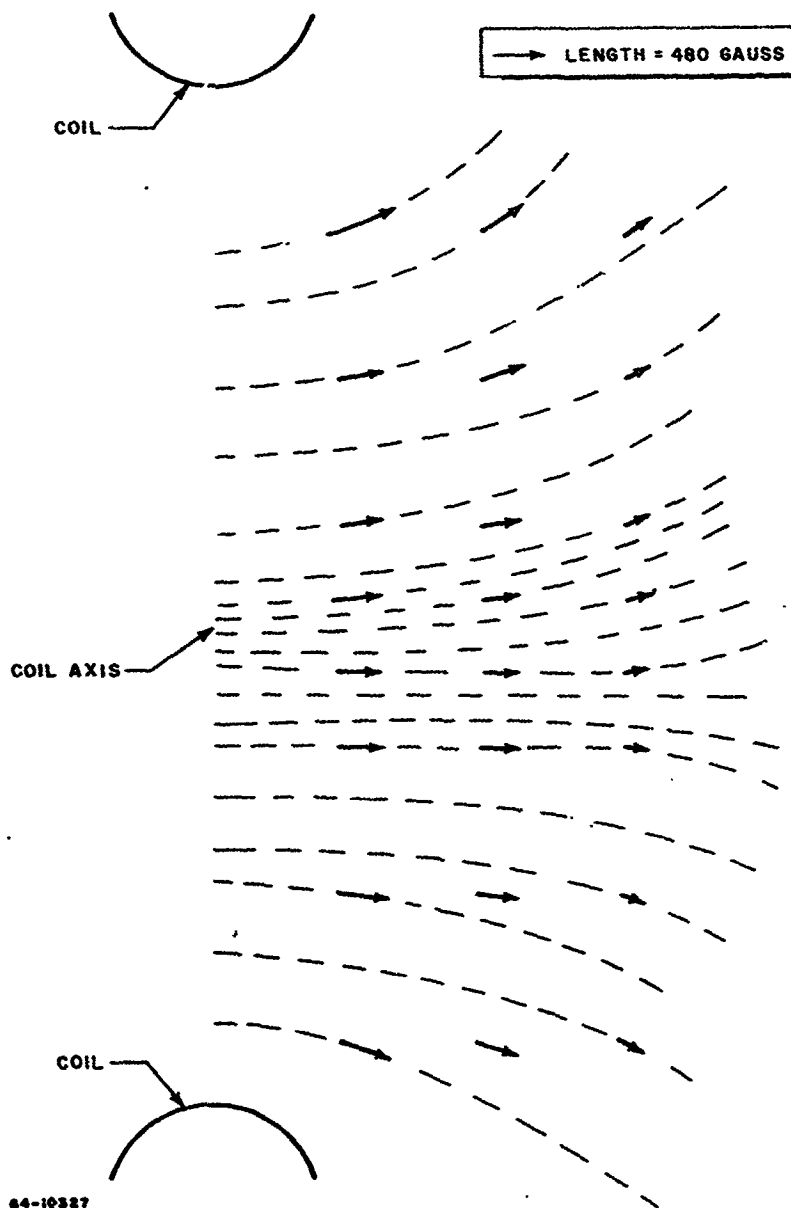


Figure 6 MAGNETIC FIELD MAP FOR A MAGNET CURRENT OF 1200 AMPERES

The value of applied magnetic field strength did have an influence on thruster performance, although this influence was small. Figure 7 shows measured X-2C engine thrust as a function of coil excitation current at an engine current of 2000 amp and a propellant mass flow rate of 0.050 gm/sec of hydrogen. For these measurements the coil was mounted on the test tank, so that the improvement in thrust as coil excitation current is increased is not a result of reaction force on the magnet. It is possible that increased axial field strength improves engine operation by moving the anode attachment region downstream, increasing r_a in equation (3) and thus enhancing T_{blow} . Engine efficiencies were slightly higher with the coil mounted on the engine, indicating that there is some reaction force on the magnet. The difference between magnet-on-thrust-stand and magnet-on-tank efficiency was, however, only of the order of the experimental scatter. The magnetic nozzle model which will be detailed in a later section may well account for both facts and discussion is therefore postponed to a later section.

b. Strong Field

The thrust mechanisms arising from interactions of the current discharge with externally produced magnetic fields were explored using a field coil capable of producing a magnetic field strength of the order of 3 kgauss. The magnetic field coil was wound around the body of the engine with its axis coincident with the axis of the engine. The coil had an inner diameter of 7 inches, an outer diameter of 17 inches, and was 1-3/4 inches long. It consisted of 40 turns of 3/8-inch o.d. copper tubing and was water-cooled. The center of the coil was adjusted to coincide with the cathode tip. The maximum axial magnetic field strength at the center of the coil was limited to about 3 kgauss at a current of 1800 amp by the heat generated in the coil. The magnetic field strength was linearly dependent upon the current.

Figure 8 shows a mapping of the magnetic field. Each arrow represents a measured value of magnetic field strength. Its length is proportional to the field strength, and its direction is along the field at the point. The measured values have been used as guides to sketch in the field lines--shown as dashes in figure 8. The coil has been run at currents from 300 to 1200 amp, corresponding to an axial magnetic field strength in the range 0.5 to 2.0 kgauss.

3. Test Systems

a. Environmental Tank

The X-2C MPD arcjet was tested in a cylindrical aluminum environmental tank with a diameter of four feet and a length of six feet. The

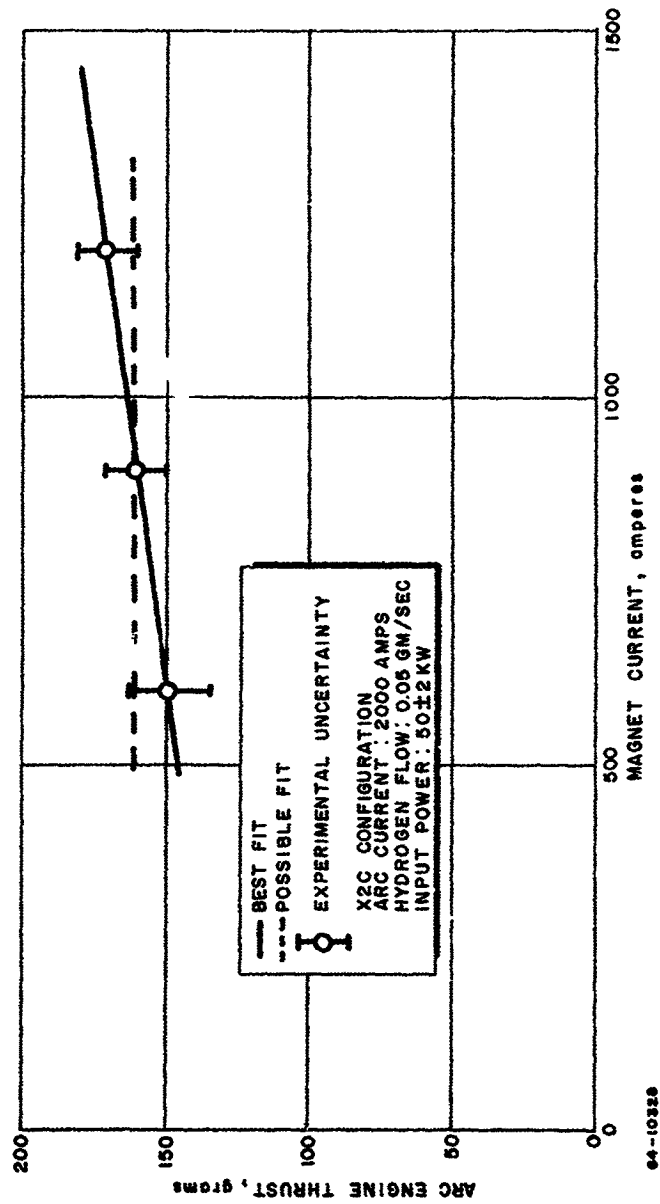


Figure 7 ARC ENGINE THRUST VERSUS AUXILIARY MAGNETIC FIELD STRENGTH

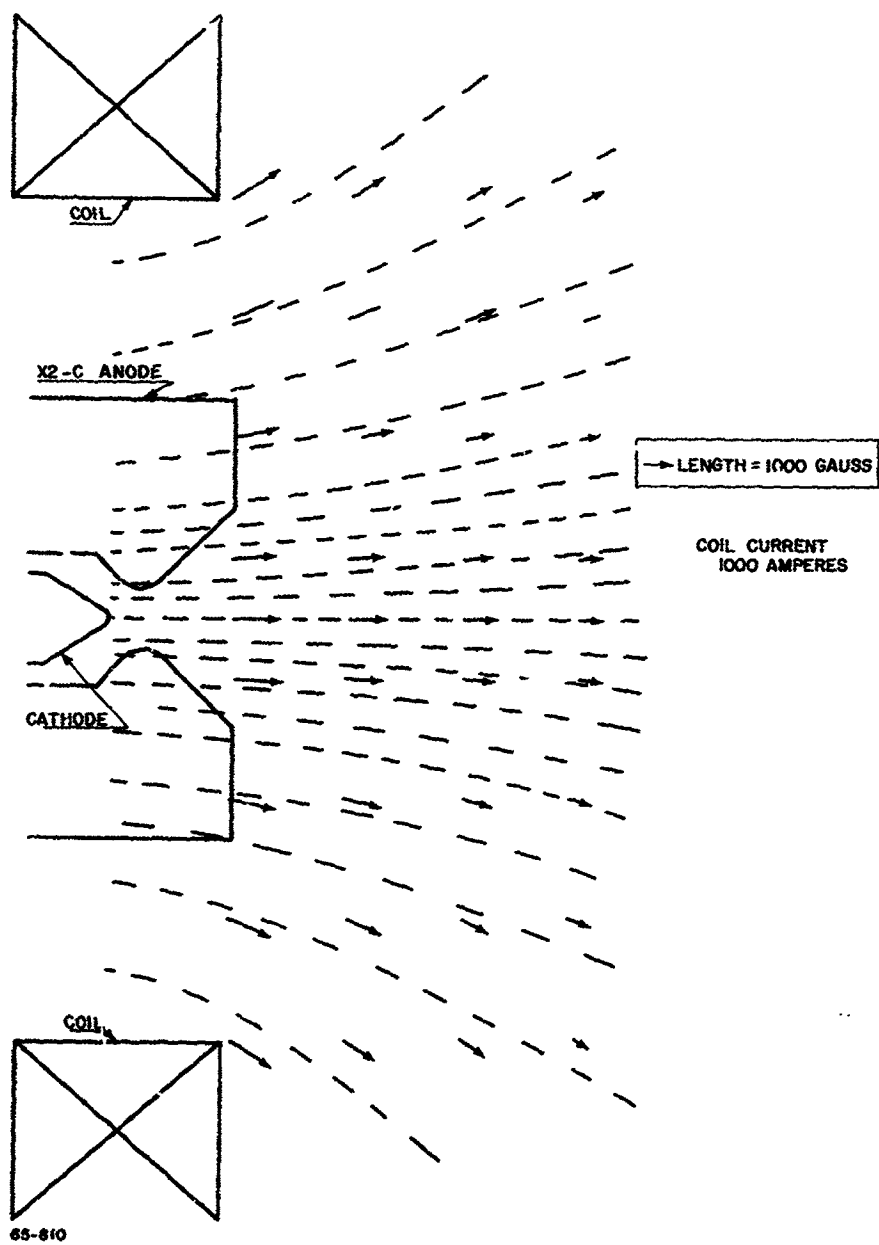


Figure 8 MAGNETIC FIELD MAP

tank walls are water-cooled to permit prolonged engine operation; two water-cooled viewing ports on each side of the tank may be used for visual or photographic inspection of the engine and its exhaust during operation. The amount of magnetic material within and in the immediate vicinity of the tank has been reduced to an absolute minimum. Aluminum, copper, or nonmagnetic stainless steel have been used for the fabrication of the thrust stand and its associated components, as well as for viewing port hinges, gas and liquid fittings, etc. A small tare in the thrust measurement is produced by a portion of the heat exchanger which is located some six feet from the engine and is fabricated from magnetic material. The correction is of the order of a few percent and is included in the reported values.

The primary system used to evacuate the tank is a 6000 ft³/min capacity mechanical pumping system. An auxiliary 34,000 ft³/min capacity pumping system may be used in parallel with this system. The primary system alone is presently capable of maintaining the ambient pressure in the environmental tank below 5 microns at blankoff and at a level of 50-150 microns during engine operation.

The first data obtained with the X-2 engine were taken at pressure levels of the order of 300-500 microns since no effort had been expended in order to reduce this back pressure. With increased understanding of possible effects due to gas entrainment, the pressure levels were reduced to those stated above. However, estimates of the tank pressures required to eliminate gas entrainment showed that pressures of the order of 0.1 to 1 micron were necessary in order to effectively simulate the hard vacuum of space for MPD arcjet operation. This pressure level requirement could be met only by the installation of a large number of immense diffusion pumps and was clearly ruled out.

The most promising technique for reducing the pressure levels in the test chamber during operation and thereby reducing the potential amount of entrained propellant is the use of easily condensable propellants in conjunction with cryogenic pumping. Towards this end, a 6-inch diffusion pump and an 18-inch diameter, liquid nitrogen-cooled baffle plate were installed. Blank-off pressures are maintained at between 10^{-5} and 3×10^{-5} mm Hg by this combined system; operating back pressures are maintained at approximately $1/2 \times 10^{-4}$ to 10^{-4} mm Hg with alkali vapor propellants.

b. Instrumentation

The various test and measurement equipments which are used to determine the performance characteristics of the X-2 engine are: 1) the thrust stand, 2) temperature-measuring thermocouples, 3) current, voltage, and mass-flow meters, and 4) pressure gages. These are more fully described below.

1) Thrust stand

The engine is suspended from a thrust stand which measures thrust force directly. The thrust-stand displacement is sensed by a linear differential transformer whose output is recorded on a Sanborn type 1500 recorder. Calibration of the thrust stand in units of force is accomplished by standard pulley and weight techniques. The calibration is performed statically with the engine off, as well as during engine operation and at all operating values of magnet coil current. The thrust level is generally recorded using a sensitivity of approximately 9 gm./mm on the recorder chart for thrusts in the range from 90-200 gm, and with a correspondingly greater sensitivity for lower thrust levels.

2) Thermocouples

In order to accurately determine the thermal efficiency of the X-2 engines, the power dissipated in heating of the anode and cathode is measured by a standard calorimetric method. The temperature rise of cooling water in the anode and cathode is measured by differential iron-constantan thermocouples and recorded individually on a Sanborn recorder. The temperature difference between water inlet and outlet is converted to heat power from a knowledge of the rate-of-water flow through the electrodes.

3) Current, voltage, and mass flow

Both arc current and coil current are measured using precision 50-mv shunt resistors and precision dc millivoltmeters. The arc voltage is measured with a precision dc voltmeter. The arc current and arc voltage are also measured and recorded on the Sanborn recorder to allow direct comparison with thrust and anode-cathode power at any time. As an extra precaution, the meter readings are hand-recorded as well.

The propellant mass flow is measured with Fisher-Porter rotameter-type flowmeters. Coolant flow rates are measured using standard liquid flowmeters.

4) Pressure gages

Both engine chamber pressure and ambient tank pressure are measured with precision Wallace and Tiernan vacuum gages. The chamber pressure is measured with a 0-50 mm Hg gage in parallel with a 0-800 mm Hg gage for use at high mass flows.

The vent pressure gage has a range from 0-20 mm Hg. Tank pressures below about 1 mm Hg are measured with a Stokes McLeod gage, and NRC alphanatron, thermocouple, and/or ionization gages.

c. Power

Electrical power to the X-2C engine is supplied from either one or both of a pair of 300-kw silicon diode rectifiers, or from a set of 4-40-kw selenium rectifiers for low power operation. The power for the magnetic field coil is supplied from a pair of 40-kw selenium rectifiers. Both the arc current and the magnetic field coil excitation current are brought to the thrust-stand mounted engine through mercury pots in the base of the test tank. The engine is electrically isolated from the thrust stand and the anode, cathode and magnetic field coil are electrically isolated from each other as well as from the environmental tank. The mercury in the mercury pots is covered by about an inch of diffusion pump oil in order to permit low-pressure operation.

C. X-2 ENGINE OPERATION WITH GASES

1. Weak External Magnetic Field

a. Thrustor Performance

The X-2C thrustor has been tested with varying input power levels and propellant mass flow rates in the gases hydrogen, ammonia, and argon. The thrustor chamber pressure is found to be a function of mass flow rate in each of the three gases, and to depend weakly upon the thrustor current. As the current is increased at fixed mass flow rate the chamber pressure at first rises slightly, and then falls off after reaching a maximum value. The current level at which the maximum is reached is dependent upon the mass flow rate and the propellant type. The variation with current is slight compared to the variation with mass flow rate. Figure 9 shows the measured chamber pressure as a function of mass flow rate for each of the three gases tested. Measured pressure values for different thrustor currents are combined on the same figure. For hydrogen in the mass flow range 0.01 to 0.05 gram/sec the chamber pressure varies approximately in the range 5 to 25 mm Hg, for ammonia from 4 to 17 mm Hg, and for argon from 2 to 13 mm Hg. The pressure is approximately linear with mass flow rate for all three gases. An analytical comparison of chamber pressure values among the three gases for a given mass flow rate depends upon information on the gas velocities and temperatures within the accelerator which is not yet available.

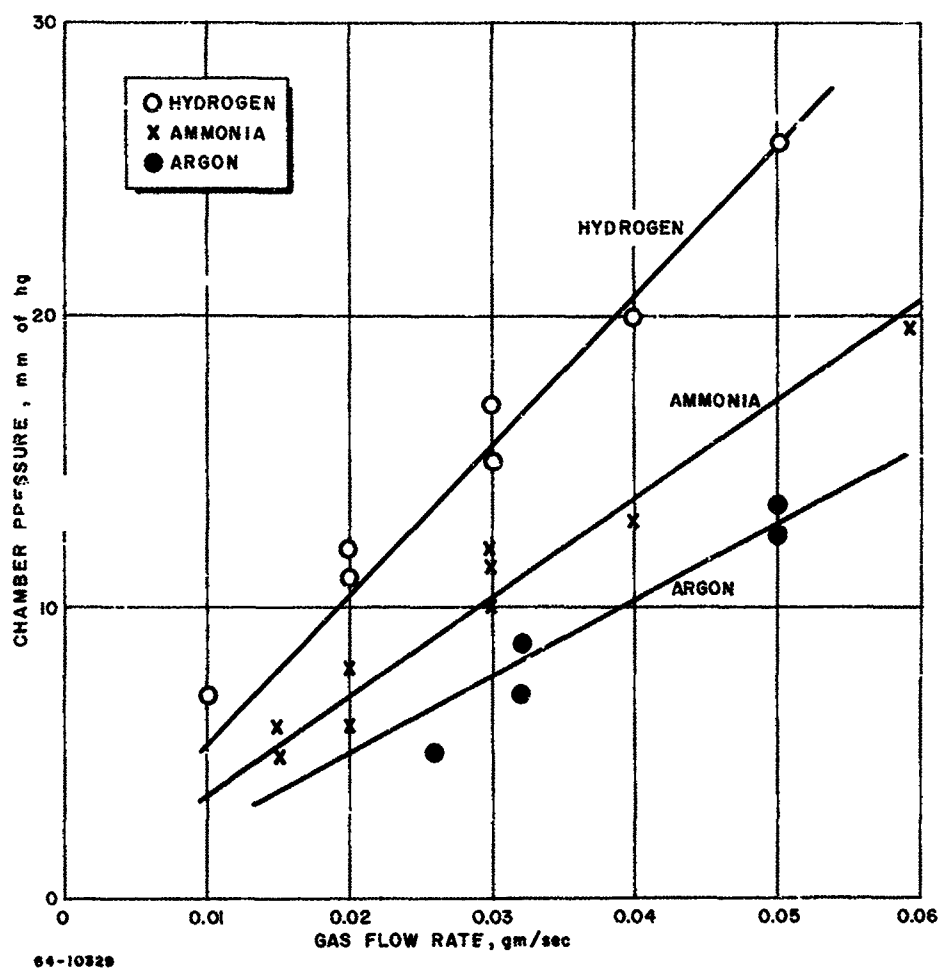


Figure 9 PLASMA GENERATOR CHAMBER PRESSURE VERSUS GAS FLOW RATE

With the measured chamber pressures used as indicated in figure 9 along with the measured throat area, aerodynamic thrust can be evaluated from equation (1) with the thrust coefficient set equal to unity. Figures 10, 11, and 12 display, for hydrogen, ammonia, and argon, respectively, total measured thrust and aerodynamic thrust as a function of arc current. For hydrogen (figure 10) the propellant flow rate is 0.05 gram/sec. The total thrust rises sharply with increasing current, going from a value of approximately 70 grams at an arc current of 1000 amp to a value of approximately 220 grams at an arc current of 2500 amp. Over the same current range the aerodynamic thrust, calculated from equation (1) using measured values of chamber pressure, increases only from about 25 to 50 grams.

The same trends are apparent in figure 11 for an ammonia flow rate of 0.03 gram/sec. The total thrust again rises sharply with current, from slightly less than 50 grams at 1000 amp to more than 150 grams at 2500 amp, while the aerodynamic thrust is nearly constant at approximately 25 grams over the entire current range.

For argon (figure 12) the picture is not so clear. The total thrust exceeds the aerodynamic thrust by a factor of approximately 2, but the total thrust does not rise significantly as the current is raised from 1500 amp to 2000 amp. More data are required to determine if this behavior is standard for argon, or if one or more of the data points plotted in figure 12 is in error.

It is of interest to plot the portion of the total thrust which does not come from aerodynamic pressure forces, T_{self} , where

$$T_{self} = T_{total} - T_{aero} \quad (6)$$

as a function of current. This has been done for hydrogen, ammonia, and argon, respectively, in figures 13, 14, and 15. The plots are logarithmic, so that apparent linearity corresponds to the relation

$$T_{self} \propto I^n \quad (7)$$

where I is the current in amp and the exponent n is given by the slope of the line. Both the pumping and blowing mechanisms described previously depend on the square of the current, so that if no other effects are present one should expect to find $n = 2$.

Figure 13 displays T_{self} obtained from equation (6) as a function of current in the current range 1000 to 2500 amp. Data for different hydrogen mass flows ranging from 0.013 to 0.050 gram/sec have been used. There is apparently no effect of mass flow rate upon the

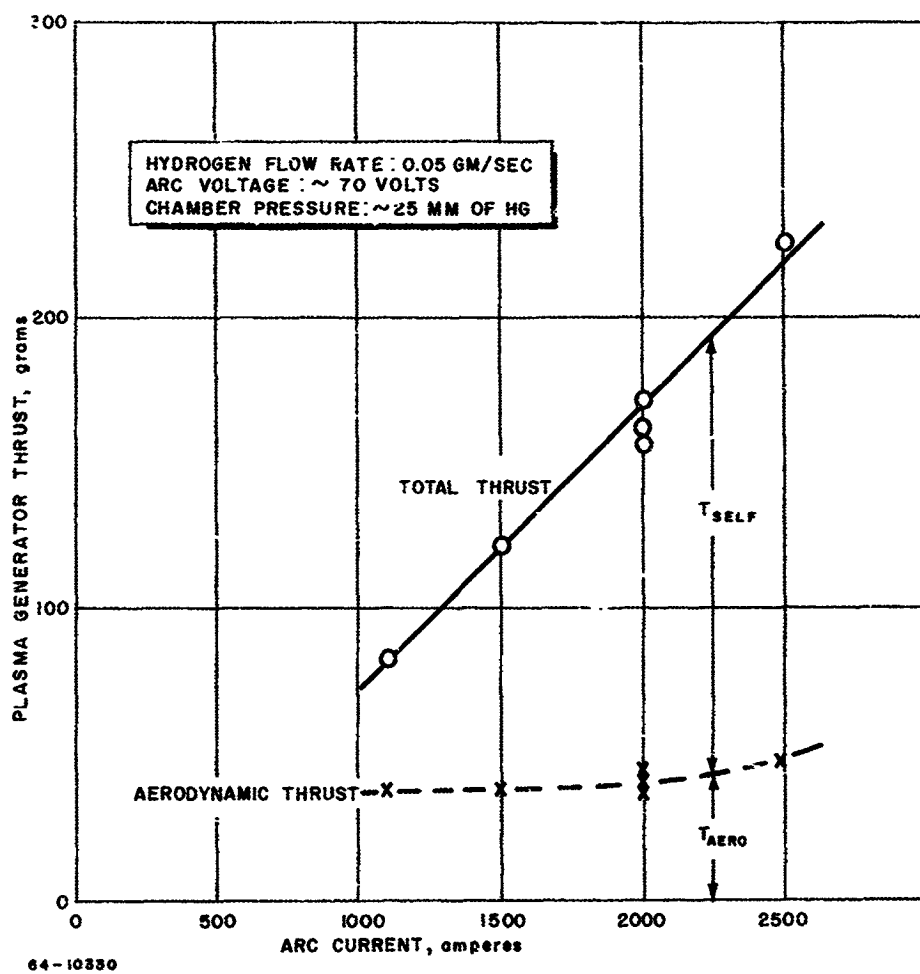


Figure 10 PLASMA GENERATOR THRUST VERSUS ARC CURRENT (HYDROGEN)

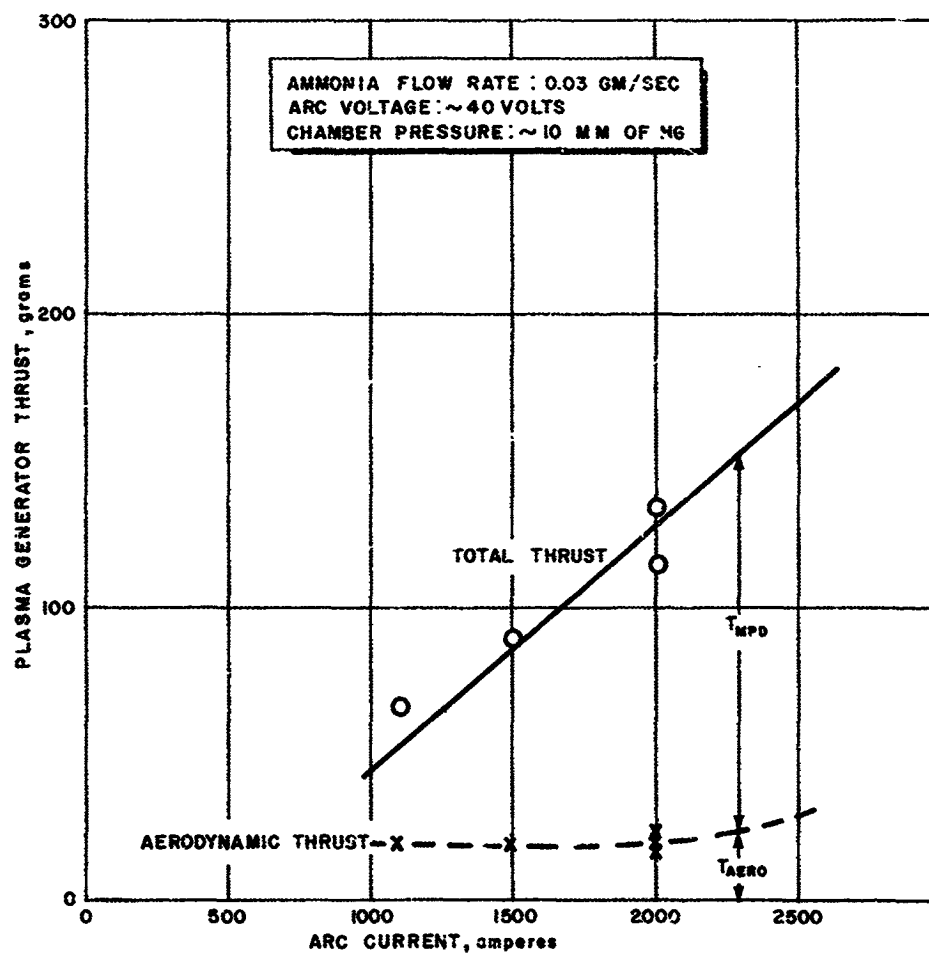


Figure 11 PLASMA GENERATOR THRUST VERSUS ARC CURRENT (AMMONIA)

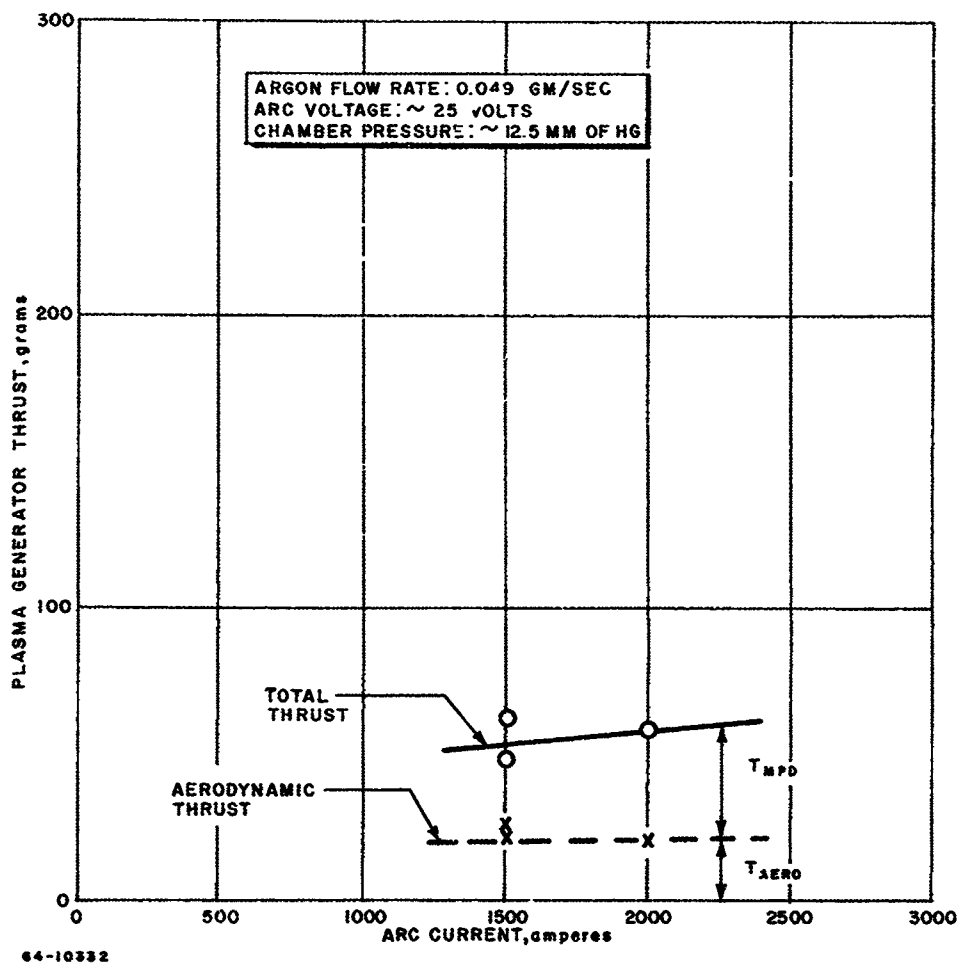


Figure 12 PLASMA GENERATOR THRUST VERSUS ARC CURRENT (ARGON)

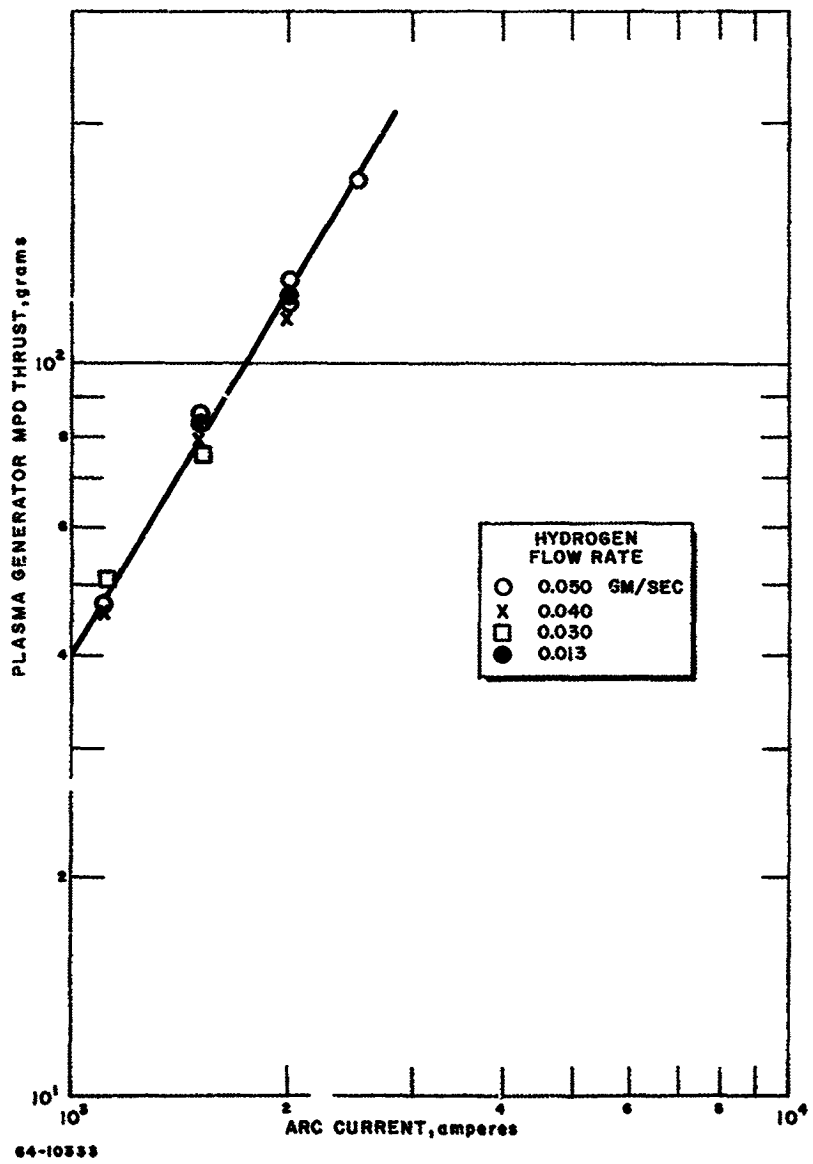


Figure 13 PLASMA GENERATOR MPD THRUST VERSUS ARC CURRENT AND HYDROGEN FLOW RATE

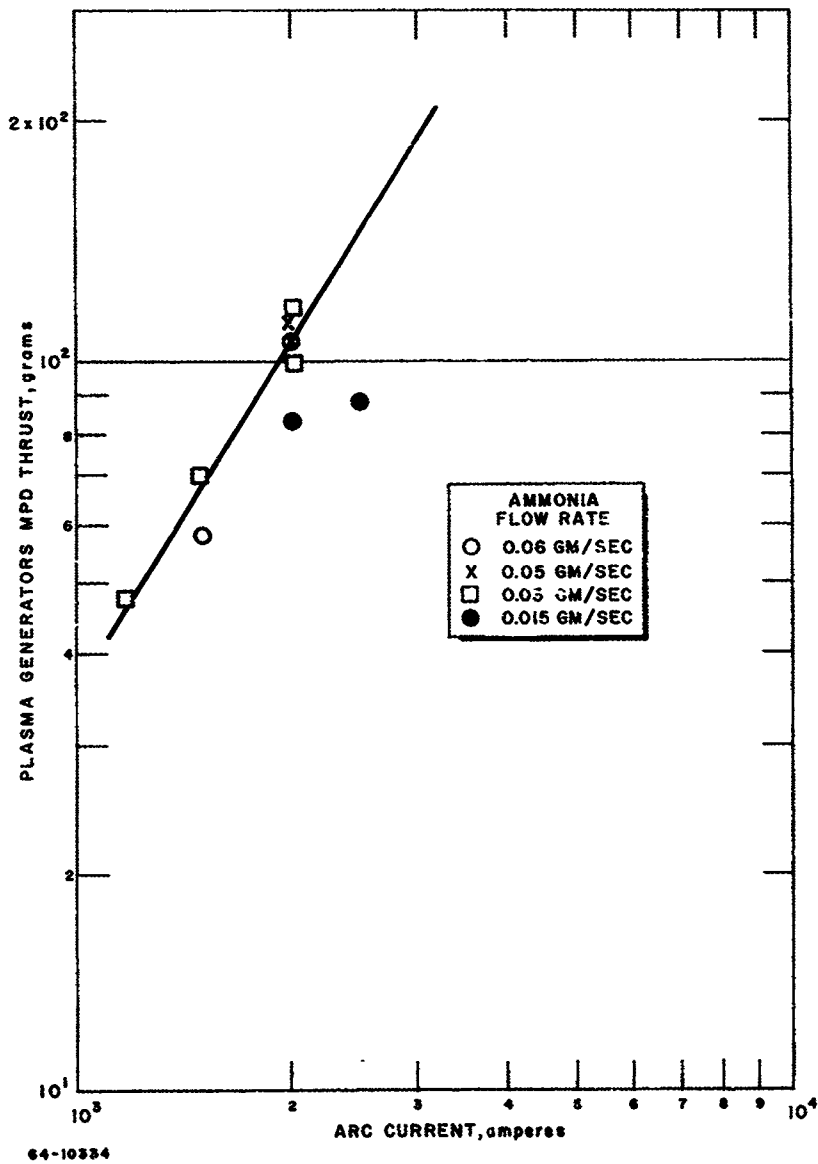


Figure 14 PLASMA GENERATOR MPD THRUST VERSUS ARC CURRENT AND AMMONIA FLOW RATE

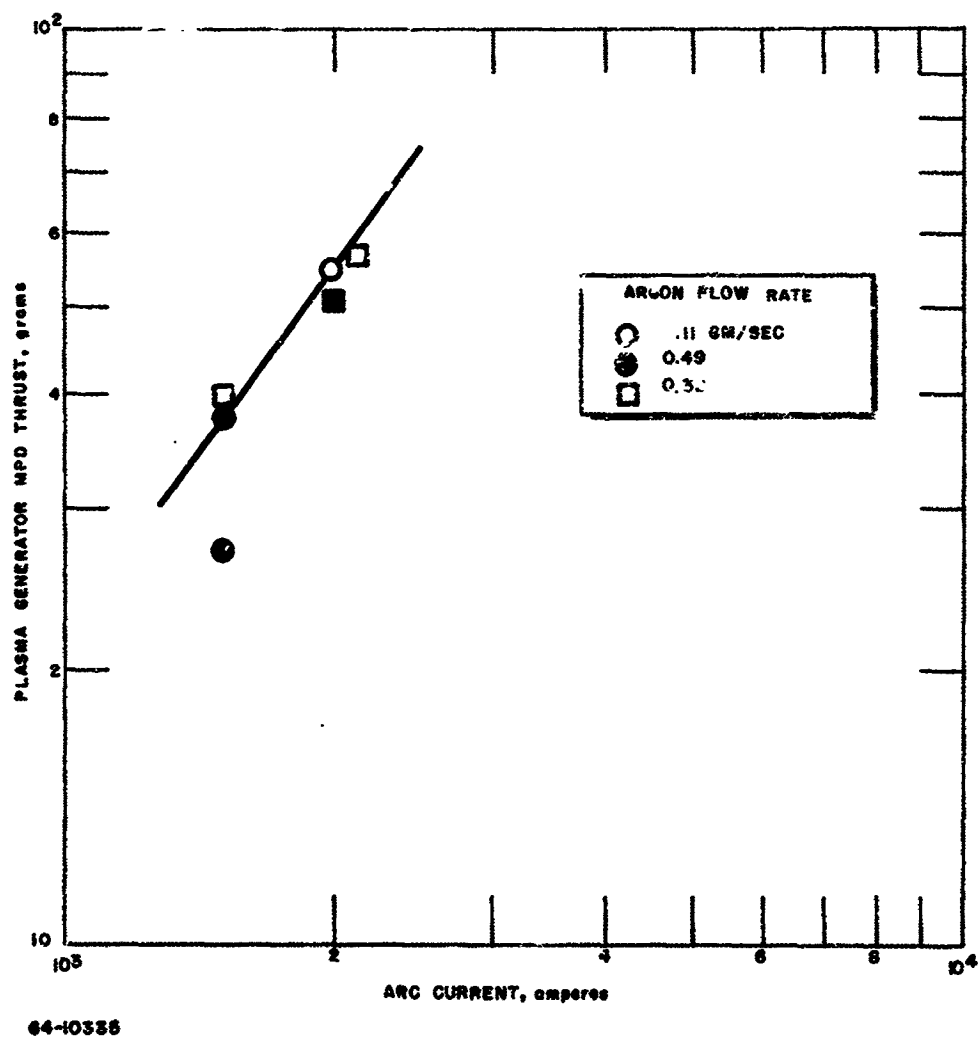


Figure 15 PLASMA GENERATOR MPD THRUST VERSUS ARC CURRENT AND ARGON FLOW RATE

magnetoplasmadynamic thrust in the mass flow range investigated. This appears to be true within experimental uncertainties for ammonia and for argon as well (from inspection of figures 14 and 15) although not enough data points have been obtained with these gases to reduce the experimental scatter. Returning to figure 13, the apparent slope of the experimental points is 1.63, not far from the value of 2 given by the simple theory.

The ammonia data of figure 14, for flow rates of 0.015 to 0.06 gram/sec give similar results, although the scatter is more severe. Again T_{self} is insensitive to mass flow rate, and increases with a power of the current equal to about 1.60.

For argon (figure 15) there is again the indication that T_{self} is insensitive to mass flow rate over the range 0.032 to 0.11 gram/sec. The apparent slope of figure 15 is 1.35, different from the slopes obtained for hydrogen and ammonia, and departing more strongly from the simple theoretical value of 2. Again, more data are required to substantiate these preliminary results with argon, or to change them.

Figure 16 is a summary plot of the information contained in figures 13, 14 and 15 for hydrogen, ammonia, and argon. T_{self} is plotted versus current. The similarity of the results for hydrogen and ammonia is marked, as is the difference between these gases and argon. For reference, the magnetic pumping thrust ($1/2 I^2$) is plotted on the same curve, to indicate the relative importance of this term and the blowing term in making up the total MPD thrust, and to indicate the theoretical slope of 2.

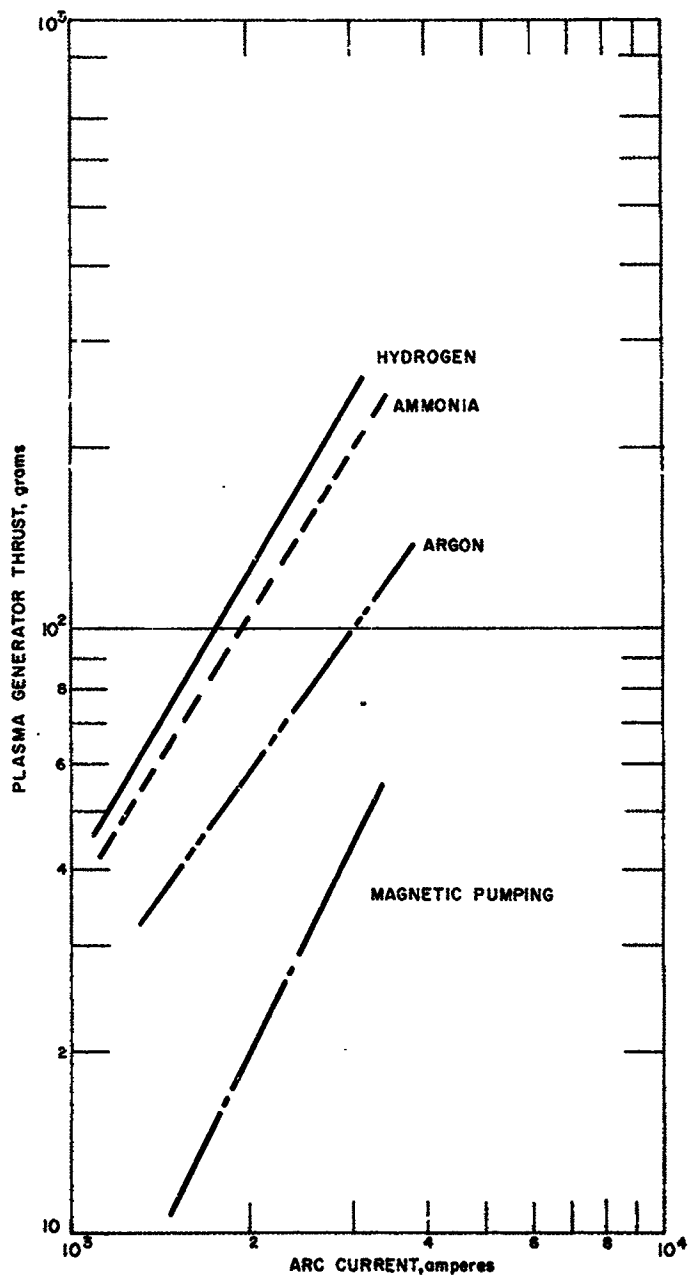
b. Thrustor Diagnostics

The principal diagnostic activity carried out at low applied magnetic field strengths has been to attempt to separate the pumping and blowing contributions to the MPD thrust, and thereby to verify the model of arc operation which includes the first three of the thrust mechanisms proposed in section II. A. The method which was employed is based upon measurement of the static pressure at the cathode tip.

The thrust which is produced by the pumping mechanism is given for a uniform current distribution or for a cylindrical current sheet by the relation

$$T_{\text{pump}} = 1/2 I^2$$

in electromagnetic units. This thrust is delivered to the engine in the form of pressure forces exerted upon the surface of the cathode tip, such that



64-10336

Figure 16 PLASMA GENERATOR MPD THRUST VERSUS ARC CURRENT

$$T_{\text{pump}} = \int \Delta P_{\text{cathode}} dA_{\text{cathode}} \quad (8)$$

where $\Delta P_{\text{cathode}}$ is the excess pressure on the cathode owing to the magnetic pinch on the current. If the approximation is made that $\Delta P_{\text{cathode}}$ is constant over the effective area of the cathode within the limits of the current distribution (equivalent to assuming that the current leaves the cathode tip in a cylindrical sheet), then the integral of equation (8) can be replaced simply by

$$T_{\text{pump}} = (\Delta P_{\text{cathode}}) (A_{\text{cathode}}) \quad (9)$$

Substituting for T_{pump} from equation (3), and solving for A_{cathode} gives:

$$A_{\text{cathode}} = 1/2 I^2 / \Delta P_{\text{cathode}} \quad (10)$$

Therefore, a measurement of the current and the overpressure at the cathode tip gives an estimate of A_{cathode} and hence of r_c in equation (5). Now, with the assumption that r_a is equal to the throat radius of the engine, T_{blow} can be evaluated from equation (5), and the sum $T_{\text{aero}} + T_{\text{pump}} + T_{\text{blow}}$ can be formed and compared with the experimentally measured thrust.

To make the required measurements of cathode overpressure a cathode was made with a 2.3-mm-diameter hole bored on its axis and inserted in the X-2C engine. In experiments performed with this modified cathode, measurements were made of arc voltage, arc current, propellant mass flow rate, thrust, chamber pressure, and cathode tip pressure. The ambient tank pressure was maintained below 1 mm Hg. It was observed that engine performance was not so good with the modified cathode as with a regular cathode, but sufficiently large MPD thrusts were obtained to make this diagnostic experiment useful. (See table A-4 of appendix A.)

Figure 17 shows measured cathode tip overpressure (i. e., the excess of cathode tip pressure over chamber pressure) as a function of current and hydrogen mass flow rate. Also shown on the figure are the results reported by Ducati¹, et al, as well as much earlier work by Maecker⁵ in a high current carbon arc at atmospheric ambient pressure. The dependence of cathode tip overpressure on current is seen in figure 17 to be about the same for all the data; the agreement in absolute value is somewhat fortuitous, and apparently indicates that cathode spot sizes are nearly the same in all three experiments.

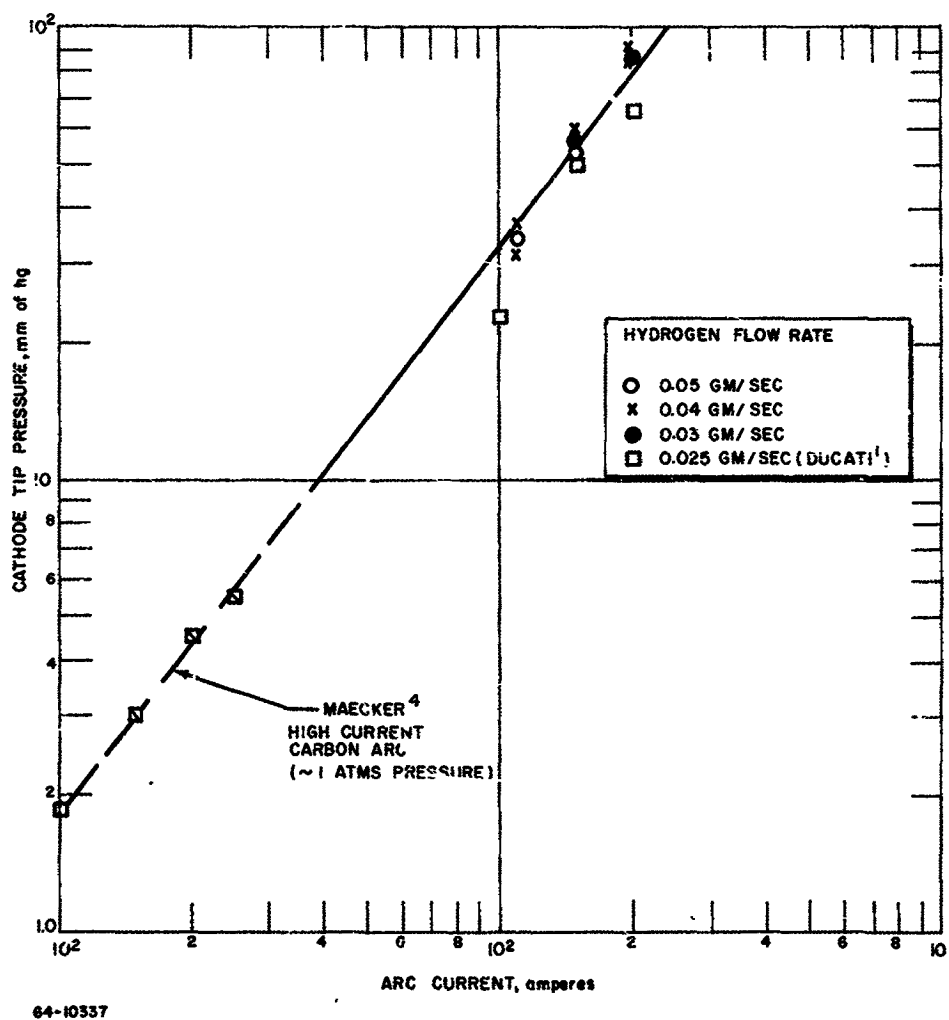


Figure 17 CATHODE PRESSURE VERSUS ARC CURRENT

The area over which this cathode overpressure must act is now determined from equation (10), which, as has been pointed out earlier, is equivalent to assuming that the current leaves the cathode tip in a cylindrical sheet. Now, setting

$$A_{\text{cathode}} = \pi r_c^2$$

an estimate for r_c can be obtained. Equation (5) can now be used to evaluate the contribution of the magnetic blowing term to the total thrust. Figure 18 shows the results of calculations made for currents of 1000, 1500, 2000, and 2500 amp. For each current the appropriate cathode overpressure is determined from figure 17 and the effective cathode area from equation (10). The radius ratio is then determined using the throat radius as r_a , and the blowing and pinch terms are evaluated to give T_{self} obtained by subtracting T_{aero} from the total measured thrust. Also shown on figure 18 is a theoretical line obtained from an analysis with a different assumption about the current distribution at the cathode, namely, that the current is uniformly distributed in an annulus at the cathode, the inner radius of the annulus being the radius of the pressure tap orifice. This analysis is mathematically more complicated, and is given in detail in appendix B. The values of T_{self} obtained with this current distribution are somewhat smaller than those obtained from the cylindrical current sheet assumption, but the total change is only of the order of 5 grams thrust.

The agreement between experiment and theory indicated in figure 18 is reasonably good, although far from perfect. With consideration for the fact that the analyses are affected in some degree by the assumptions which have been made (that the thrust coefficient is precisely 1, that the current all enters the anode at the throat, that the device is characterized by complete azimuthal symmetry, etc.), the degree of correlation between the theory and experiment is encouraging.

c. Thrustor Electrical Characteristics

Figure 19 shows the measured thruster voltage as a function of current for a mass flow rate of approximately 0.03 gram/sec in the three gases hydrogen, ammonia, and argon. Over the range of current for which measurements have been made the applied voltage is relatively insensitive to current, rising slightly for each propellant as the current is increased from 1000 to 2000 amp. The voltage in hydrogen (approximately 65 volts) is significantly larger than in the other two gases, while ammonia and argon are fairly close to one another, at 35 to 25 volts, respectively. At a given current level the

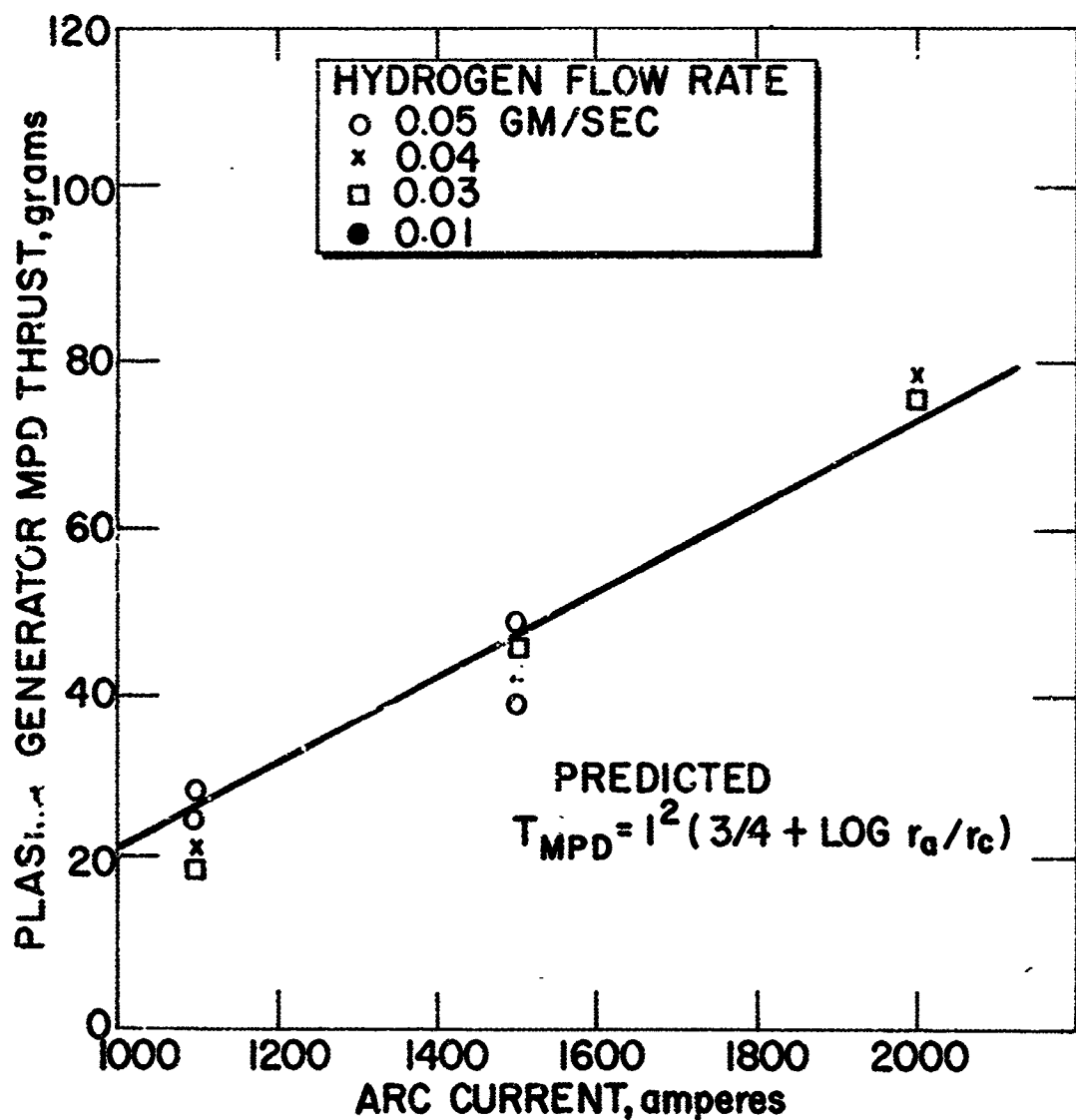


Figure 18 PLASMA GENERATOR SELF-THRUST VERSUS ARC CURRENT

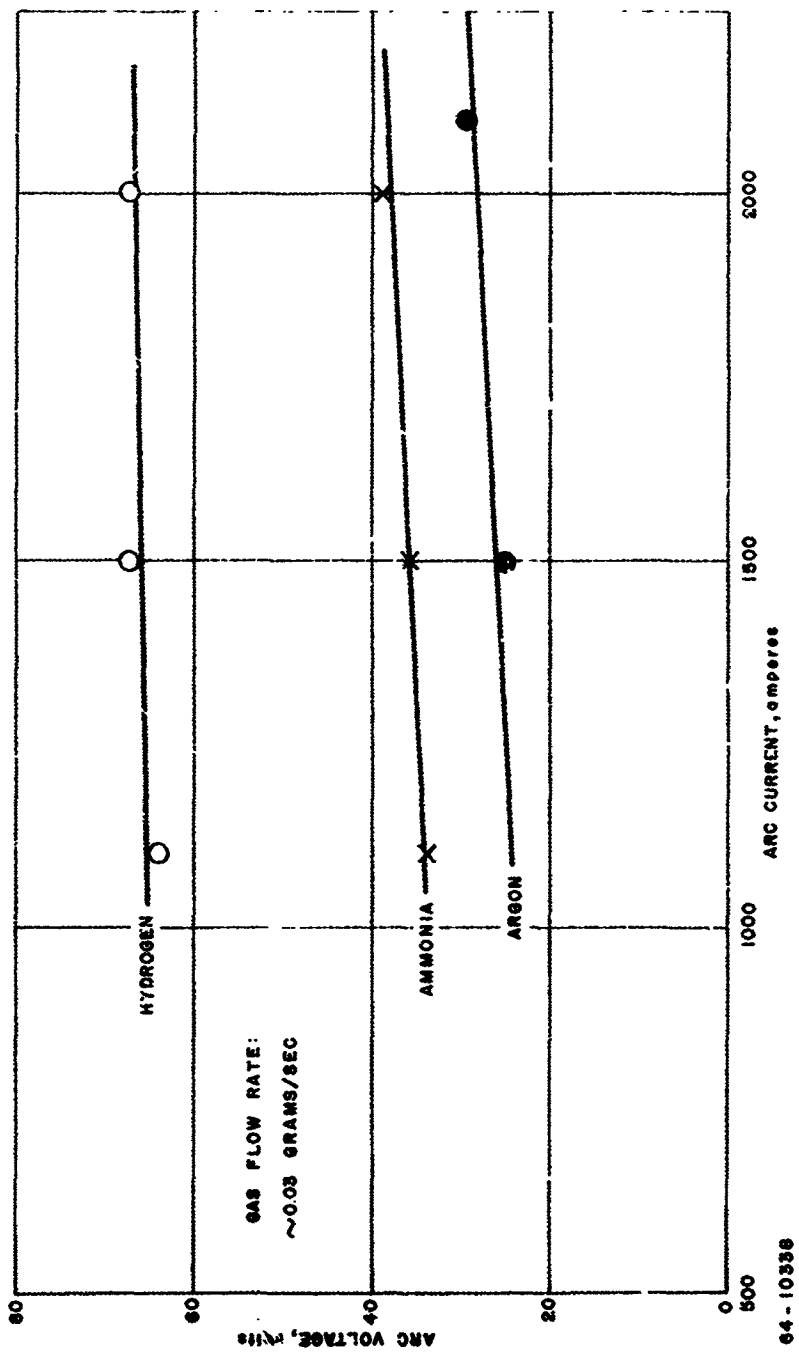


Figure 19 ARC VOLTAGE VERSUS ARC CURRENT

voltage determines the input power, which is divided into power lost to engine cooling, power invested in propellant static enthalpy, and power invested in propellant acceleration. The higher voltage in hydrogen at this mass flow rate may be due to a higher investment in propellant static enthalpy, particularly in ionization. At higher mass flow rates the investment in propellant enthalpy rises, while the thrust power falls; at lower mass flow rates the reverse holds. As a result, the voltage tends to be insensitive to mass flow rate for a given propellant, within the ranges of current and mass flow rate which have been investigated.

d. Thrustor Propulsion Characteristics

The overall efficiency of the X-2C high impulse thruster is shown for hydrogen, ammonia, and argon in figures 20, 21, and 22, respectively, as a function of propellant specific impulse.

The propellant specific impulse and overall efficiency are defined by the relations

$$I_{sp} = T/\dot{m} \quad (11)$$

$$P_{thrust} = 4.8 \times 10^{-5} T^2/\dot{m} = 4.8 \times 10^{-5} T I_{sp} \quad (12)$$

$$Eff = P_{thrust}/P_{in} \quad (13)$$

where I_{sp} is the propellant specific impulse in seconds, T the thrust in grams force, \dot{m} the propellant mass flow rate in gram/sec, and Eff the overall electric to propulsive efficiency expressed as a fraction of unity, P_{thrust} the thrust power in kilowatts, and P_{in} the input power in kilowatts. Strictly, P_{in} should contain a quantity to account for the incoming propellant enthalpy (the propellant is injected at approximately room temperature) but this correction is small for the final enthalpies associated with the X-2C thruster, and has been neglected. Hence P_{in} is given by $10^{-3} V I$, where V and I are the arc voltage and current in volts and amperes.

With reference to figure 20, over the input power range of 75 to 250 kw, and for mass flows between 0.01 and 0.05 gram/sec of hydrogen, the efficiency is approximately linearly related to specific impulse, increasing from about 10 percent at 2000 seconds to about 60 percent at 13,000 seconds. Also shown in figure 20 are data reported by Ducati¹, which exhibit similar behavior. It should be noted that the data exhibit considerable scatter: it is not known at this time if the scatter reflects slightly different operating modes from one engine test to the next, or if it is simply an indication that the random

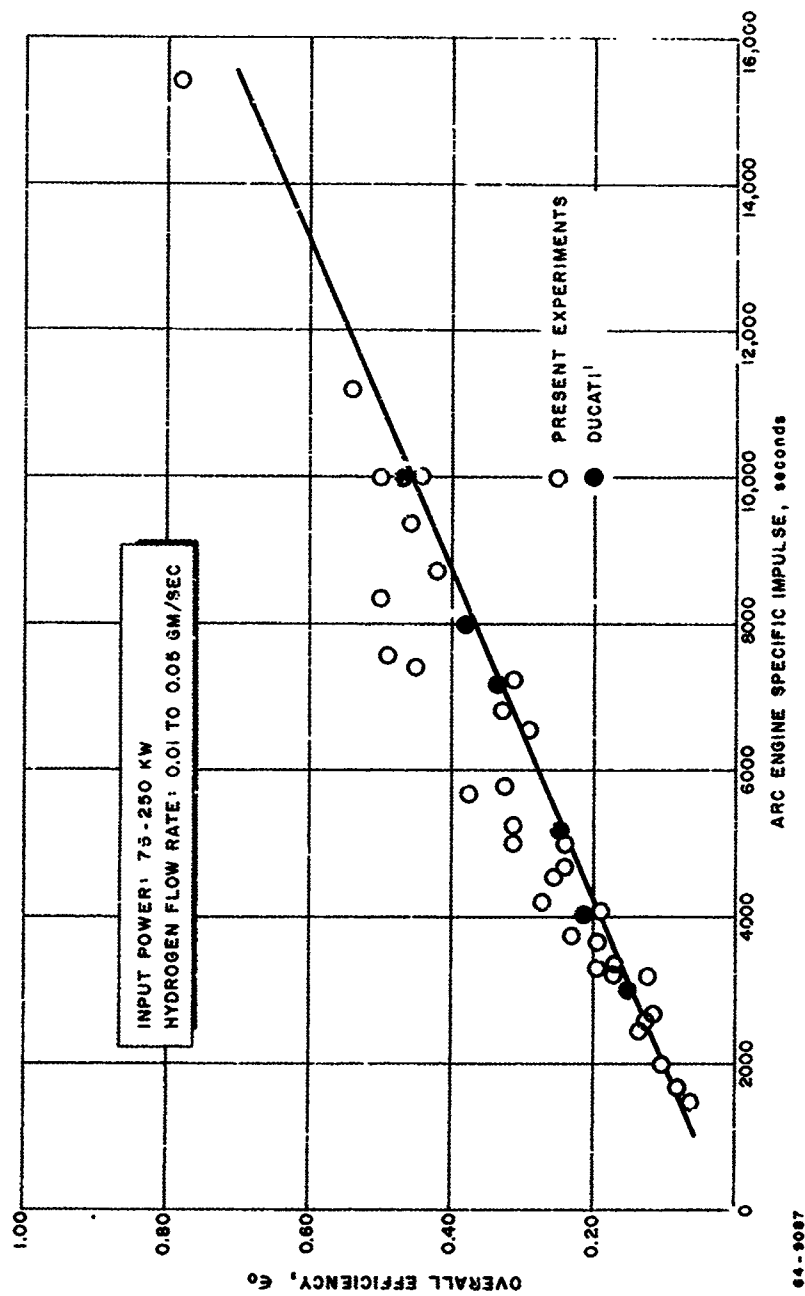


Figure 20 OVERALL EFFICIENCY VERSUS ARC ENGINE SPECIFIC IMPULSE (HYDROGEN)

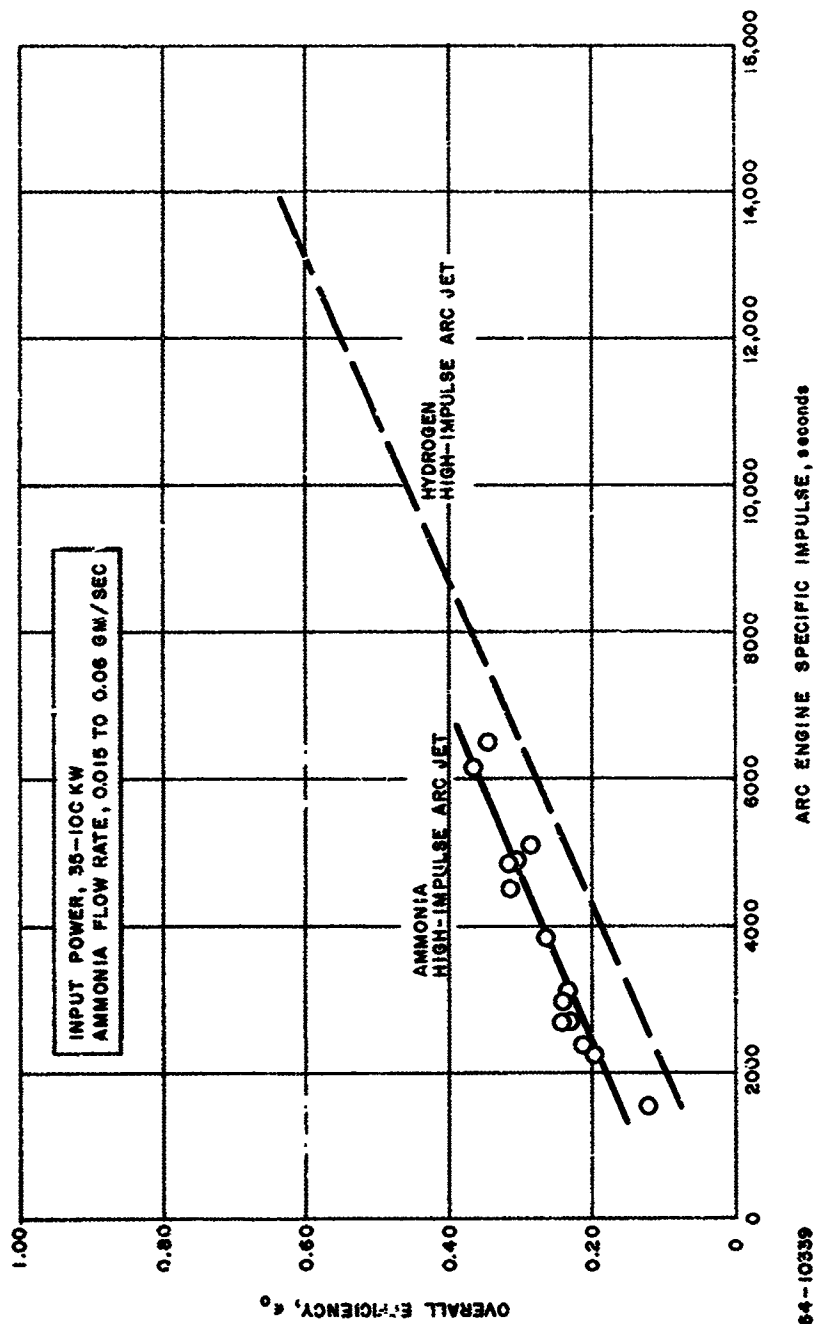


Figure 21 OVERALL EFFICIENCY VERSUS ARC ENGINE SPECIFIC IMPULSE (AMMONIA)

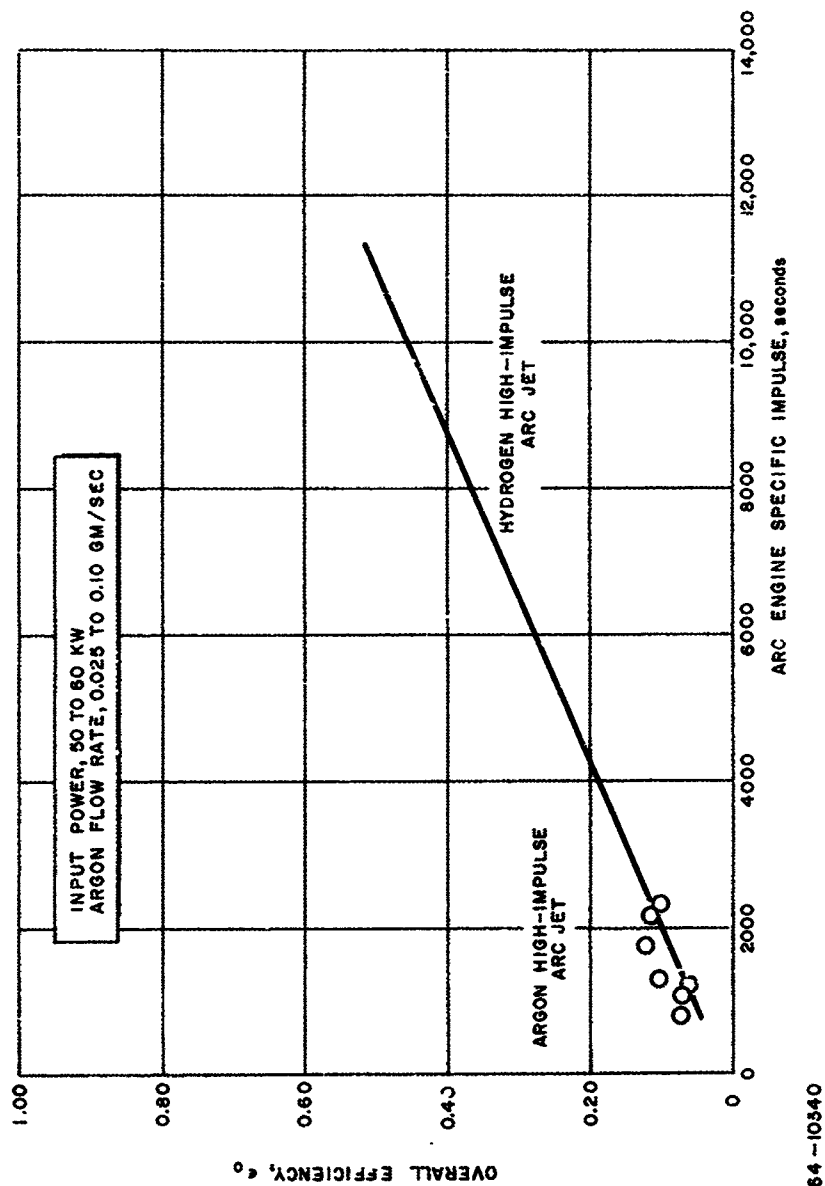


Figure 22 OVERALL EFFICIENCY VERSUS ARC ENGINE SPECIFIC IMPULSE (ARGON)

Experimental errors are of this order. More effort at duplication of these measurements should resolve this question.

For ammonia in the mass flow range 0.015 to 0.06 gram/sec, and the power range 35-100 kw, the overall efficiency is slightly higher than for hydrogen. This is indicated in figure 21 where the ammonia data and a line representing the hydrogen data of figure 20 are both plotted. It should be expected that the efficiency would be higher with ammonia in the specific impulse range from 2000 to 6000 seconds, owing to frozen flow considerations to be discussed later in this report, but the argon data of figure 22 are in contradiction of this effect. In figure 22 the data for argon obtained at mass flow rates of 0.025 to 0.10 gram/sec, and in the power range of 50 to 60 kw are plotted along with the line representing the hydrogen results. The argon data fall on the hydrogen line, while the frozen flow efficiency of argon should be much superior to that of hydrogen around 2000 seconds. Again it is pointed out that the argon data are preliminary and consist of only a few points. More measurements are required to firmly establish the efficiency-specific impulse curves for all three gases, but particularly for ammonia and argon.

When the hydrogen data of figure 20 are used it is possible to develop estimates of the important power loss mechanisms. These are indicated in figure 23 which again displays efficiency as a function of specific impulse. Partial efficiencies are defined as

$$\epsilon_{arc} = \text{Power to propellant/input power} \quad (14)$$

$$\epsilon_{frozen} = \text{Power not in dissociation and ionization/power to propellant} \quad (15)$$

$$\epsilon_{expansion} = \text{Thrust power/power not in dissociation and ionization} \quad (16)$$

$$\epsilon_{overall} = \epsilon_{arc} \epsilon_{frozen} \epsilon_{expansion} \quad (17)$$

The arc efficiency can be evaluated as the ratio of the difference of input power and power in the coolant to input power. These are all measured quantities, and these values are plotted on figure 23, along with the measured overall efficiency. The frozen flow efficiency can now be estimated based upon the gas stagnation enthalpy, if thermal equilibrium is assumed. Actually, a portion of the input power is translated directly into thrust power without passing through a thermal stage, and it is therefore likely that this estimate of the frozen flow loss is pessimistic, although it is thought to be not grossly so.

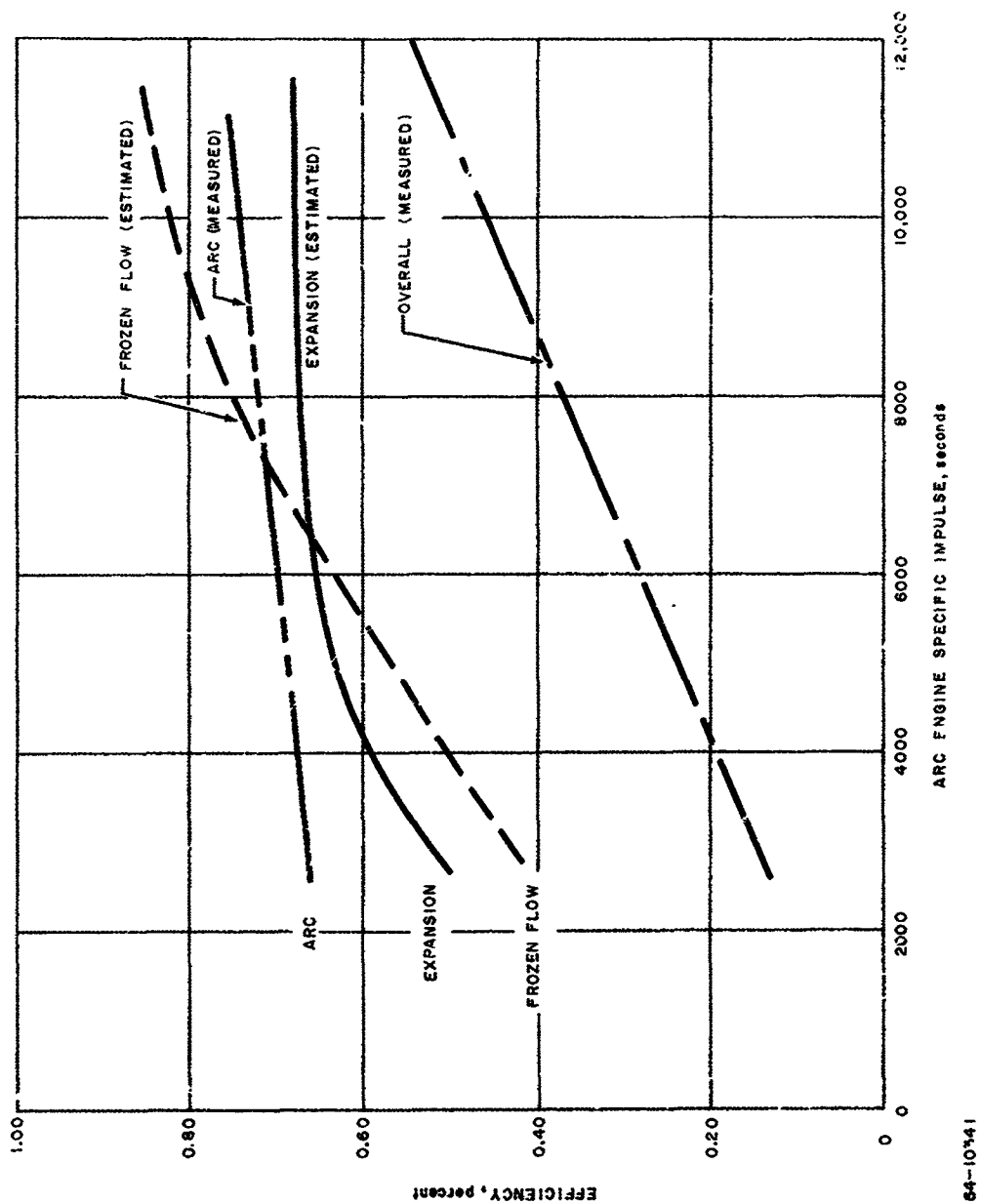


Figure 23 EFFICIENCY VERSUS ARC ENGINE SPECIFIC IMPULSE

Finally, by using equation (17), the expansion efficiency can be calculated. The interesting feature of the result of this calculation is that the expansion efficiency appears to level off at a value of about 64 percent for the specific impulse range beyond 5000 seconds. It appears from this preliminary analysis of the propulsive efficiency that the best immediate hope of increasing the efficiency may lie, therefore, in reducing the frozen flow losses and in increasing the arc heater efficiency (by use of radiation cooling, for example) rather than by concentrating efforts on increasing the expansion efficiency.

Figures 24 and 25 display the calculated hydrogen enthalpy and temperature, respectively, as a function of specific impulse. The total enthalpy in figure 24 is obtained from

$$h_t = \epsilon_{\text{arc}} P_{\text{in}} / \dot{m} \quad (18)$$

where h_t is the total enthalpy in erg/gram, and where 1 kw is equivalent to 10^{10} erg/sec. The total enthalpy, h_t , in turn is related to the static enthalpy, h_s , by

$$h_s = h_t - 1/2 u^2 \quad (19)$$

where u is the propellant exit velocity in cm/sec ($= 980 I_{sp}$). The static enthalpy as a function of specific impulse has been calculated from equation (19), and is plotted as the dashed line in figure 24. The static enthalpy is seen to level off at about 6000 seconds, while the increase in total enthalpy comes almost entirely from the $1/2 u^2$ term. Figure 25 has been obtained from the data of figure 24 by employing the assumption of thermal equilibrium to convert the enthalpies to temperatures. Total temperatures of a very high order are obtained, exceeding 10^5 °K at a specific impulse value of only 8000 seconds. However, the static temperature levels off at about 40,000 °K, and further increases in the total temperature come from increased directed velocity rather than increased random velocity.

The frozen flow efficiency can be computed once the enthalpy is specified, but there is an ambiguity as to whether the stagnation or static enthalpies should be used in making the calculation. This will actually depend somewhat upon the detailed mechanisms of energy addition to the gas, which are not yet well understood. Therefore, figure 26 shows the frozen flow efficiency calculated in each way, as a function of specific impulse, and based upon the division between static and kinetic enthalpy of figure 24. The definitions of the frozen flow efficiencies plotted in figure 26 are as follows:

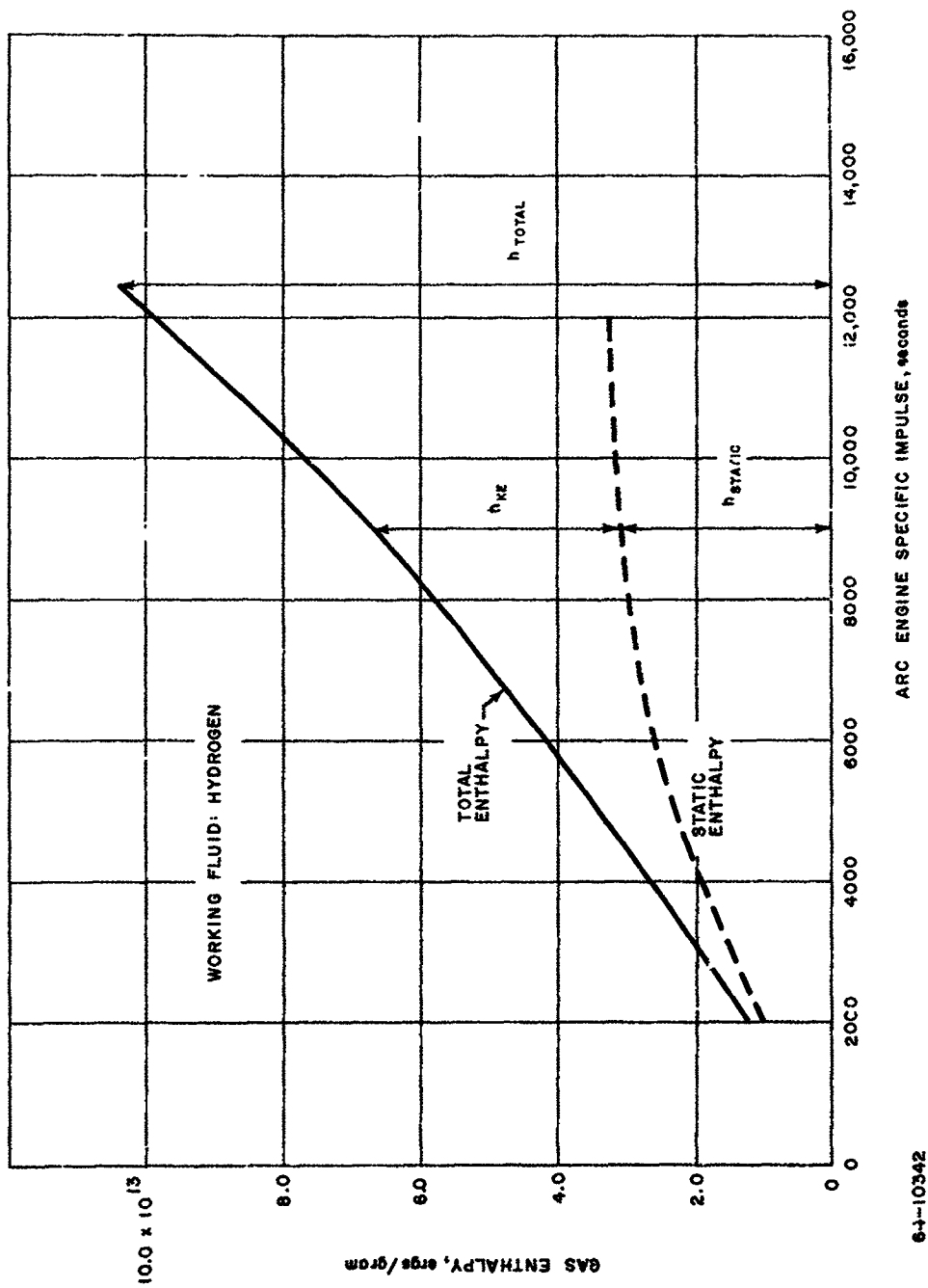


Figure 24 GAS ENTHALPY VERSUS ARC ENGINE SPECIFIC IMPULSE

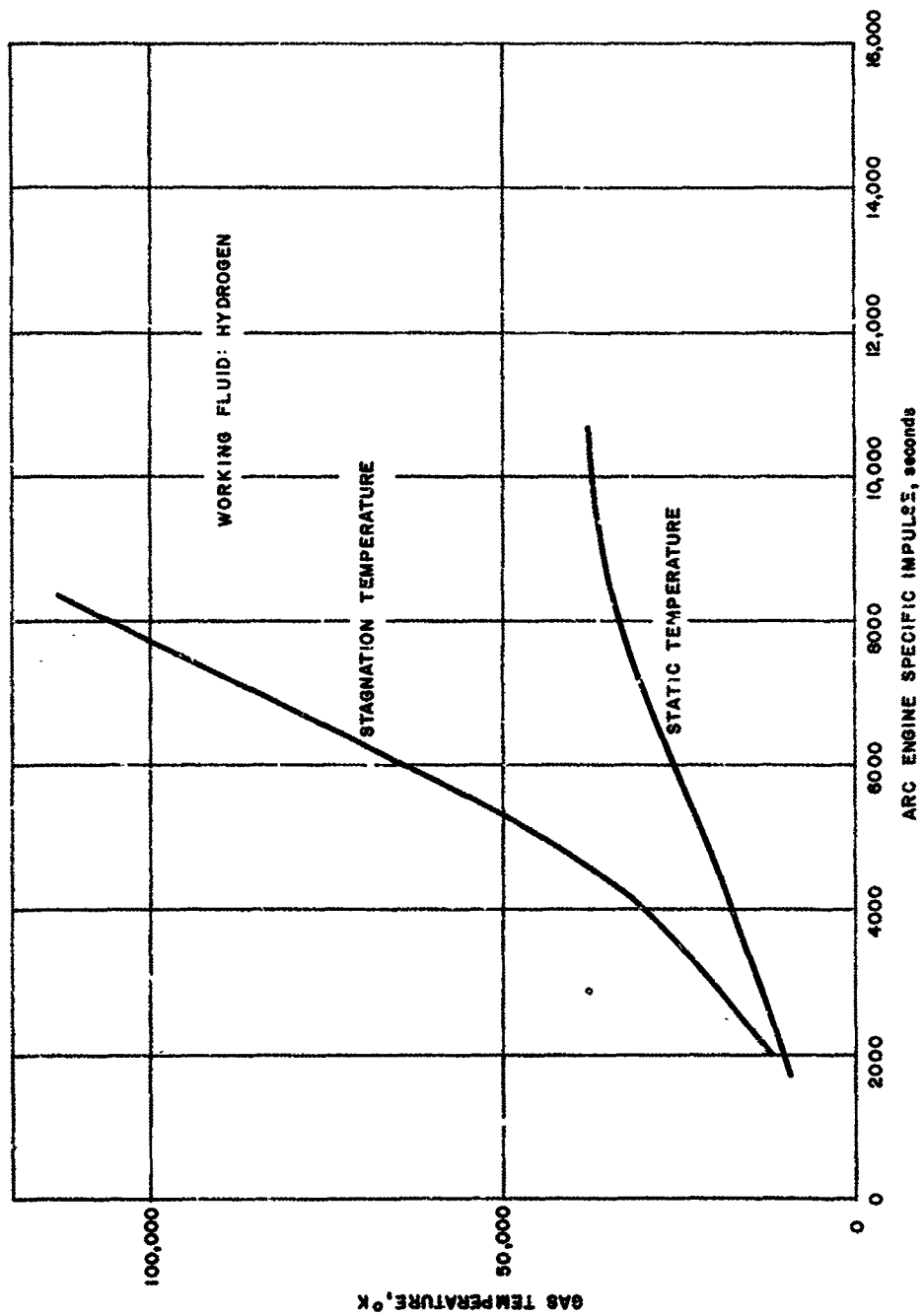


Figure 25 GAS TEMPERATURE VERSUS ARC ENGINE SPECIFIC IMPULSE

64-10343

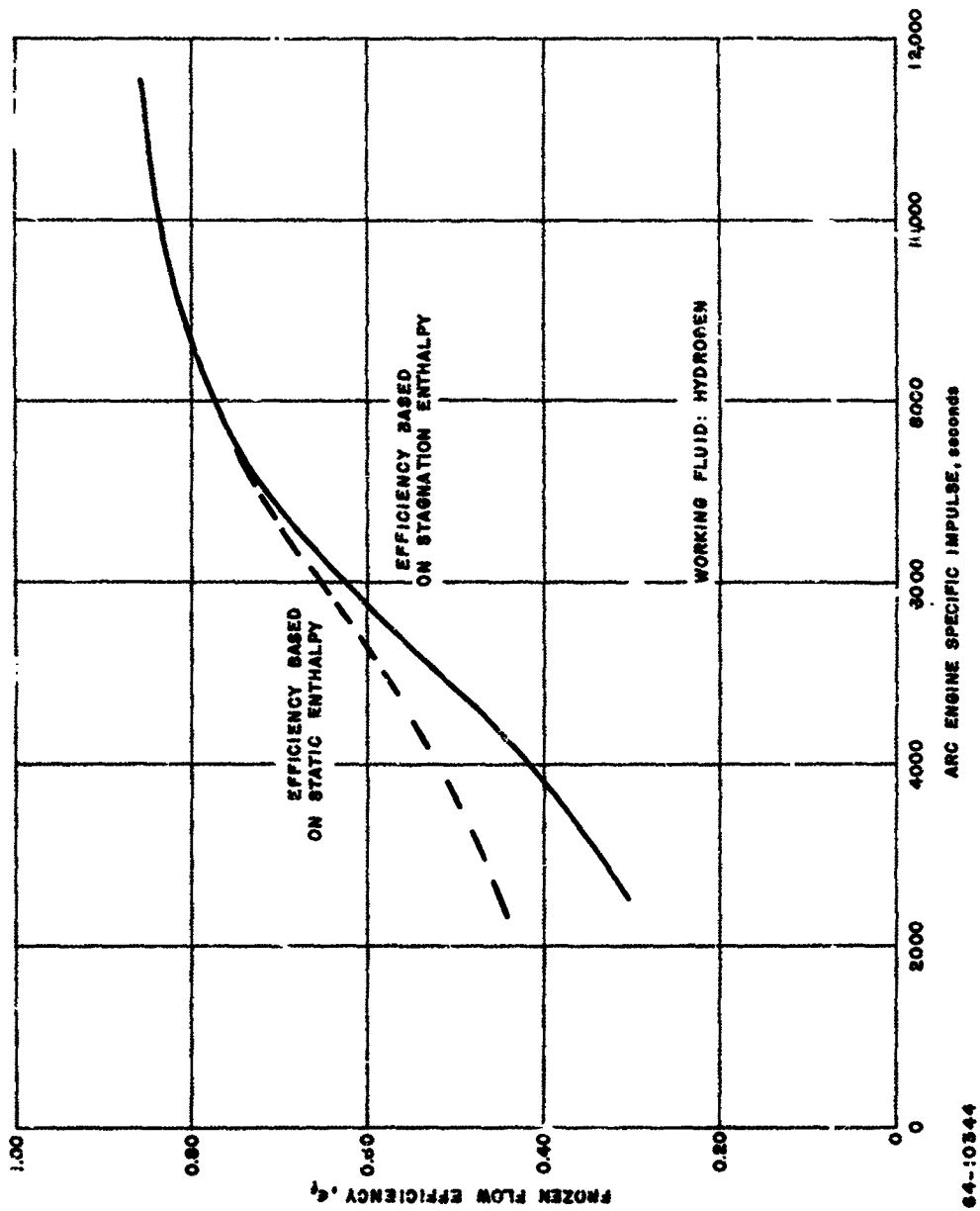


Figure 26 FROZEN FLOW EFFICIENCY VERSUS ARC ENGINE SPECIFIC IMPULSE (HYDROGEN)

$$\epsilon_{\text{frozen}, h_t} = \frac{h_t - (E_{\text{diss}}(h_t) + E_{\text{ion}}(h_t))/\dot{m}}{h_t}$$

$$\epsilon_{\text{frozen}, h_s} = \frac{h_t - (E_{\text{diss}}(h_s) + E_{\text{ion}}(h_s))/\dot{m}}{h_t}$$

where $\epsilon_{\text{frozen}, h_t}$ is the frozen flow efficiency based on the total enthalpy, h_t , and $E_{\text{diss}}(h_t)$ and $E_{\text{ion}}(h_t)$ are the powers associated with dissociation and ionization, respectively, at the enthalpy level given by h_t ; alternatively, $\epsilon_{\text{frozen}, h_s}$ is the frozen flow efficiency based on the static enthalpy, h_s , and $E_{\text{diss}}(h_s)$ and $E_{\text{ion}}(h_s)$ are the powers associated with dissociation and ionization, respectively, at the enthalpy level given by h_s .

The frozen flow efficiency based upon static enthalpy is always higher than that based on stagnation enthalpy at a given specific impulse, but the difference is small for values of specific impulse in excess of 6000 seconds where both frozen flow efficiencies are in excess of 0.6. However, at 2500 seconds the difference is appreciable, the frozen flow efficiency being 0.45 based on static enthalpy and 0.30 based on total enthalpy.

The desire for a higher frozen flow efficiency motivates an examination of heavier molecular weight gases than hydrogen. Figure 27 shows an approximation of the frozen flow efficiency for argon, lithium, ammonia, and hydrogen as a function of specific impulse. These have been calculated with the assumption that dissociation of molecules into atoms is complete, and that each atom is singly ionized, independent of the specific impulse level. These assumptions allow the calculations to be made most simply, but they are probably unrealistic at low values of specific impulse (order of 2000 seconds) and again at higher specific impulse for the heavier propellants. At the low specific impulse levels the ionization is quite probably not complete, while at the very high levels it is likely that multiple ionization of some of the propellants becomes important. The degree of multiple ionization will depend first on whether thermal equilibrium is established, and if not then on whether the ionization level is established at a value appropriate to the static enthalpy or to the stagnation enthalpy, or to some intermediate value.

If the curves of figure 27 are accepted in general as guidelines, with the realization that the absolute accuracies are doubtful, then it is still clear that the frozen flow situation improves in general as the

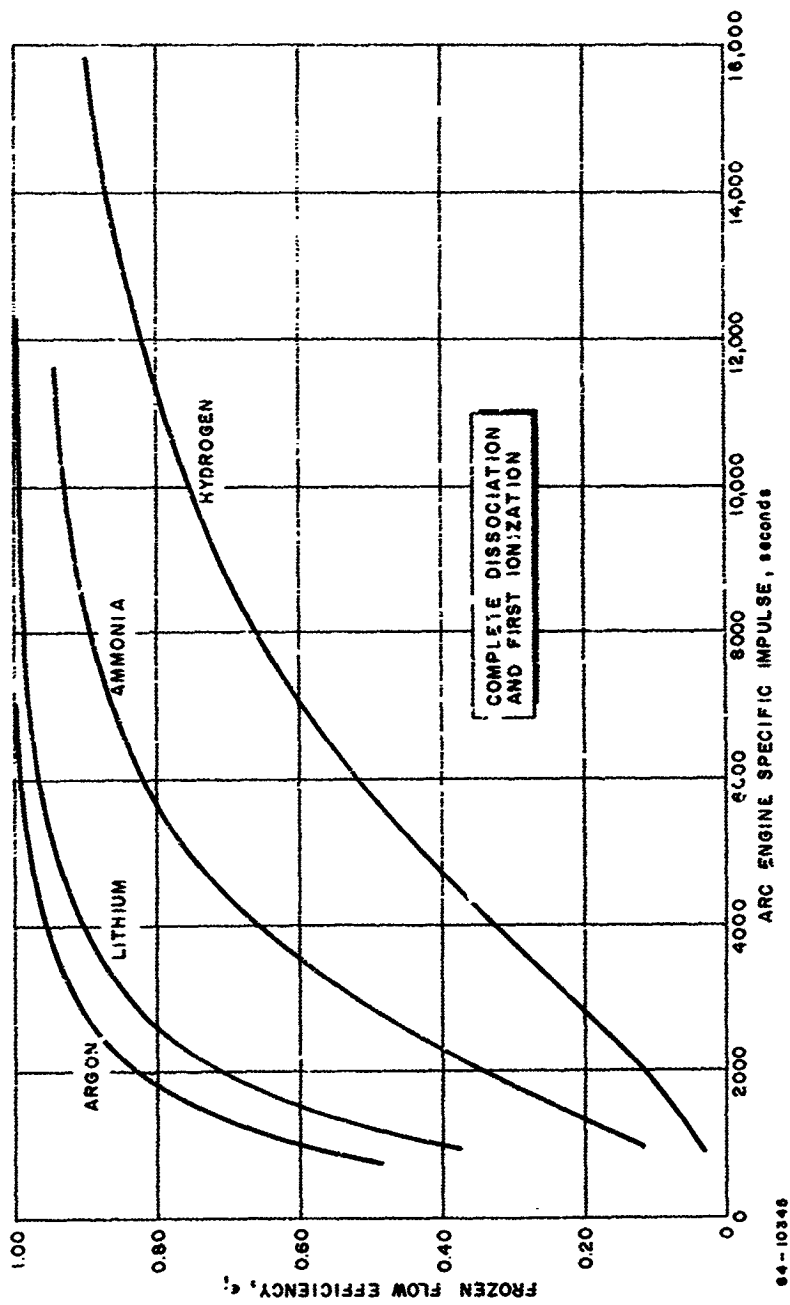


Figure 27 FROZEN FLOW EFFICIENCY VERSUS ARC ENGINE SPECIFIC IMPULSE

molecular weight is increased. In fact, with lithium, the frozen flow efficiencies are quite high although the molecular weight is only 7, owing to the very low first ionization potential. However, it must be pointed out that the indications of figure 27 are that argon should be greatly superior to ammonia, while in fact this has not proved to be the case in the laboratory.

An investigation was made of the possibility that the relatively poor propulsion performance with argon was due to the fact that much higher levels of ionization than the first may be present.

Ionization up to four times was considered. Even with this level of ionization the frozen flow efficiency of argon is superior to that of hydrogen, and it is also superior to ammonia if the latter is dissociated into nitrogen and hydrogen atoms, followed by ionization of the hydrogen and single ionization of the nitrogen atoms. It seems unlikely that argon atoms would be four times ionized without at least single ionization of hydrogen and nitrogen. Therefore, it has been tentatively concluded that the failure of argon to yield improved propulsion efficiency over hydrogen or ammonia is probably due to causes other than multiple ionization.

2. Strong External Magnetic Field

a. Thrustor Electrical Characteristics

An investigation has been made of the voltage-current characteristics of the X-2C MPD arcjet oriented in hydrogen and in ammonia. The variables were arc current, applied magnetic field strength, and propellant flow rate. For all of these tests the ambient tank pressure was in the range 200 to 500 microns. Power was supplied to the engine from a silicon diode rectifier with a 300-kw capability.

Figure 28 shows, for hydrogen mass flow rates of 0.02 and 0.05 gm/sec, the measured X-2C voltage as a function of arc current. The magnetic field strength is 1000 or 2000 gauss. (The magnetic field is characterized for discussion by the maximum value of the axial component, which is found at the cathode tip.) In the current range shown, the voltage-current slopes are near zero. There is some experimental evidence that at lower current values the slopes are negative. At a given current in the range 500-1600 amp the voltage level increases with magnetic field strength and mass flow rate.

Figure 29 is a plot of the voltage-current characteristics for ammonia at mass flow rates of 0.029 and 0.058 gm/sec, again for magnetic field strengths of 1000 and 2000 gauss. Compared with the data for

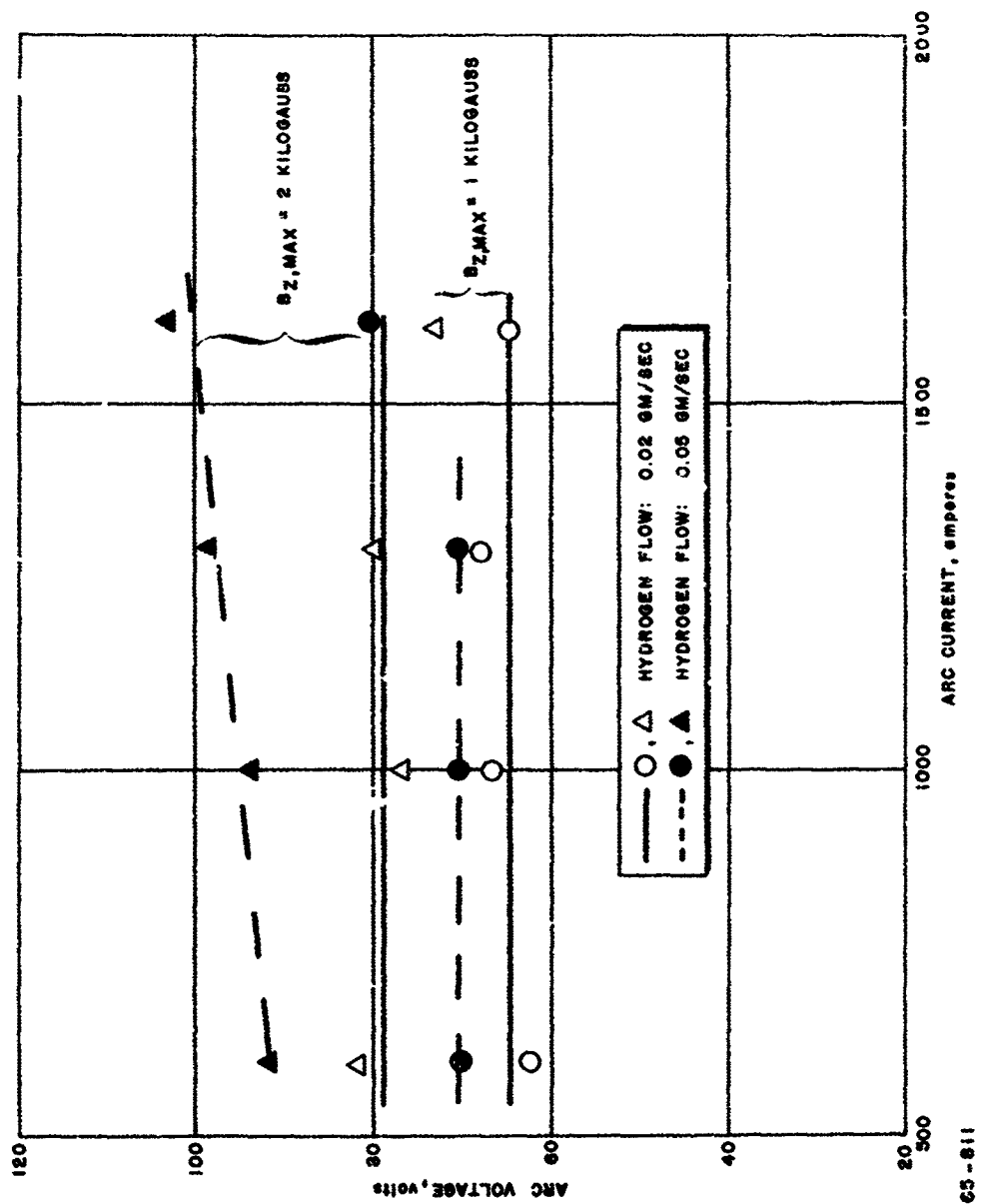


Figure 28 ARC VOLTAGE VERSUS ARC CURRENT (HYDROGEN)

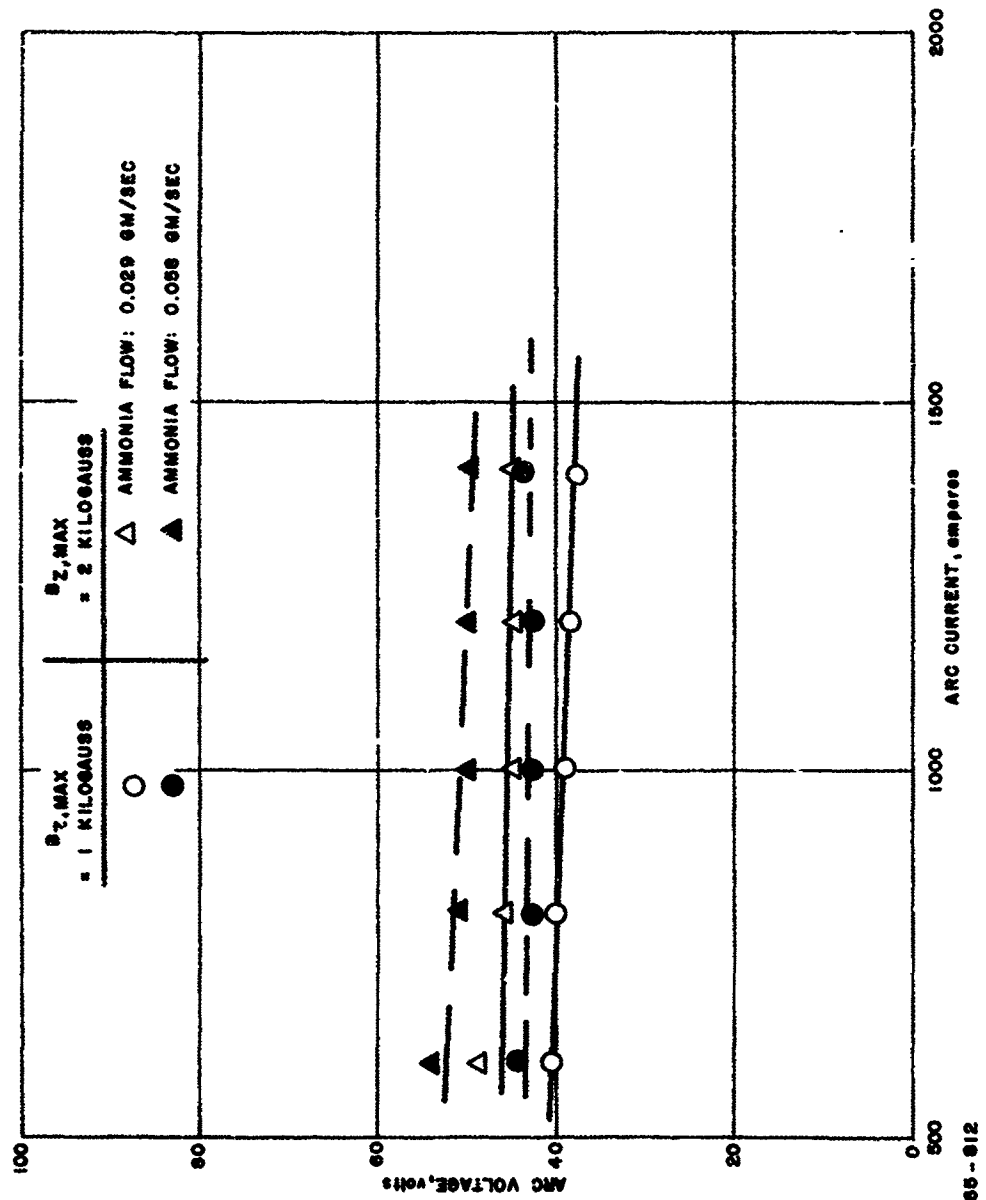


Figure 29 ARC VOLTAGE VERSUS ARC CURRENT (AMMONIA)

hydrogen, the ammonia voltages are significantly lower; however, they show the same general lack of sensitivity of the voltage to current level, and the same tendency for voltage to increase with magnetic field and mass flow rate at a given current.

For all of the hydrogen data summarized in figure 28, the voltage spread is approximately 80 ± 20 volts. For the ammonia data of figure 29 the spread is in the range 46 ± 8 volts, so that not only is the voltage generally lower in ammonia, but the sensitivity of the voltage to variation of mass flow rate and magnetic field is also lower.

In figure 30 voltage is plotted against magnetic field strength for both hydrogen and ammonia. Data are combined for different mass flow rates and currents, thus contributing to the scatter in the figure. There appears, however, to be a tendency with both propellants for the voltage to rise with magnetic field strength at a rate sufficient to be apparent even with the experimental scatter.

The data of figure 30 can be fit by relations of the form

$$V = V_0 + kB \quad (20)$$

where V_0 and k are unknown constants. V is the measured voltage and B the applied magnetic field strength.

Patrick and Schneiderman¹⁵ have proposed a theoretical justification for a relation of this form. A paraphrase of the discussion of reference 15 suggests that the voltage for the device is established in that geometrical region where the initial ionization occurs. By equating the ratio E/B in this region to the critical velocity for the propellant, u_c , the relation

$$V = V_0 + u_c Bl \quad (21)$$

is obtained, where u_c is the critical velocity (that velocity for a molecule at which the kinetic energy, $1/2 mv^2$, is equal to the energy required to dissociate the molecule and ionize the constituent atoms to the first level) and l is an unknown length related to some geometrical feature of the plasma generator. Data obtained with hydrogen, argon, and nitrogen were correlated with this formula in reference 15, and V_0 selected for each propellant, but with a constant value of l , the length. In the plasma generator of Patrick and Schneiderman, this length was taken as one centimeter, which is characteristic of the radial separation of the discharge region of attachment at the anode from the cathode tip.

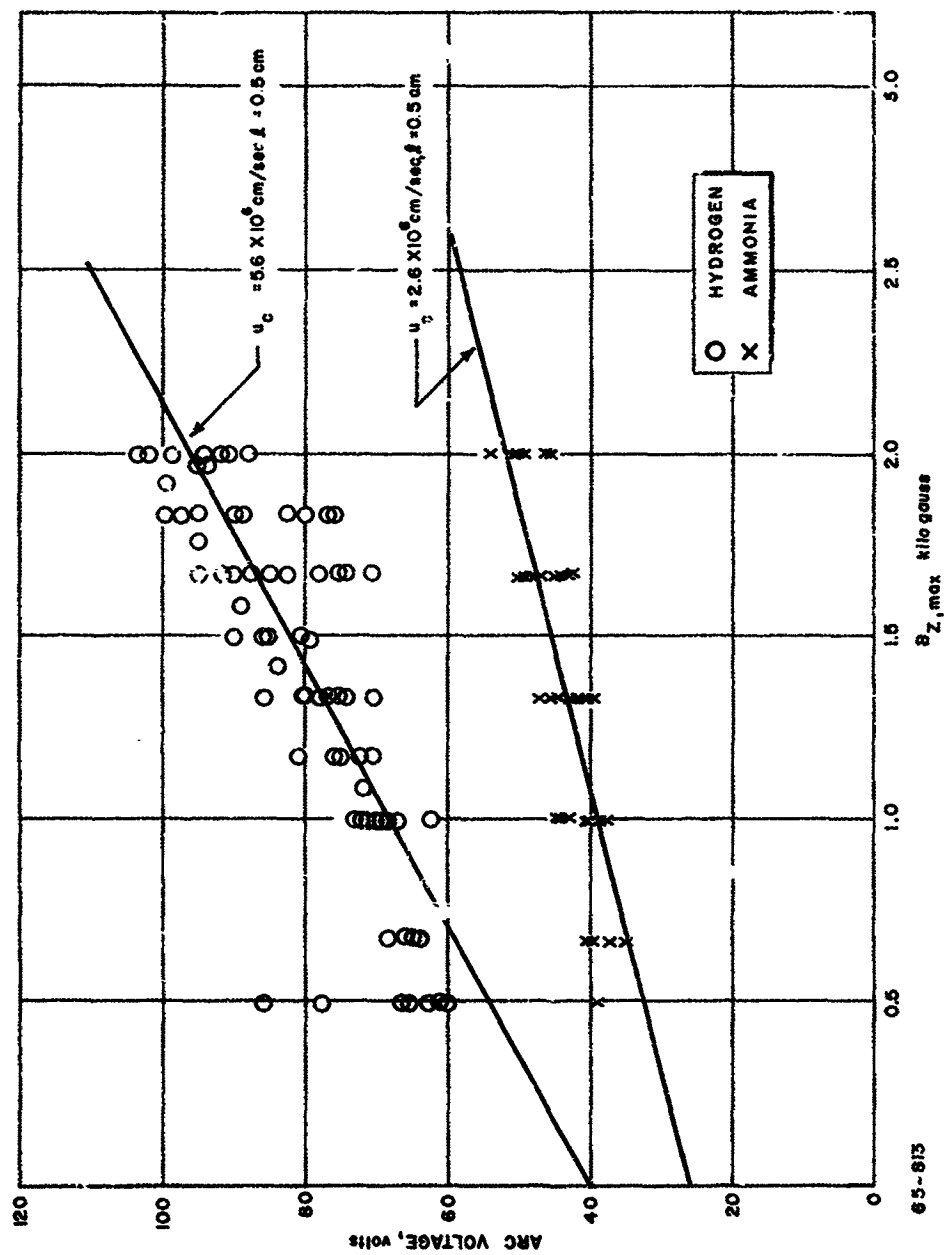


Figure 30 ARC VOLTAGE VERSUS MAGNETIC FIELD STRENGTH (HYDROGEN, AMMONIA)

The critical velocity, u_c , is 5.6×10^4 m/sec for hydrogen and 2.6×10^4 m/sec for ammonia. Selection of $V_0 = 40$ volts for hydrogen, to agree with reference 15, led to a choice of $l = 5$ mm to fit the hydrogen data; the line drawn through the hydrogen data in figure 30 corresponds to this choice for l . With l fixed at 5 mm, the slope for the ammonia data is fixed, and the best-fit line of this slope is drawn on figure 30.

Inspection of the fit obtainable in this way, especially for the ammonia data, indicates that agreement with the first order theory is less satisfactory for these data than for those of reference 15; however, the theory does predict a lower slope for ammonia, which is observed, and further, it is plausible that the value of l applicable to the X-2C MPD arcjet should be smaller than that reported in reference 15, since the geometry employed there is more open, while the X-2C MPD arcjet geometry employs a throat downstream of the cathode. Hence, it is quite possible that the theory is an acceptable first-order characterization of variation of voltage with magnetic field in axisymmetric MPD arcjet devices.

Figure 31 is a plot of measured X-2C thrust as a function of arc current for a fixed strong field (the applied magnetic field is approximately 2000 gauss, axial, maximum), and hydrogen mass flow rate (0.05 gm/sec). As the arc current is varied from 600 to 1600 amp, the thrust rises from 80 to 260 grams. Over this same current range, T_{aero} varies from 32 to 40 grams. If one uses equations (2), (3), and (4) for T_{self} , and the values reported earlier for r_c , a curve to represent T_{self} can be calculated and drawn. This is indicated in figure 31. However, the sum of T_{aero} and T_{self} varies only between 40 and 95 grams over the current range 600 to 1600 amp, leaving the larger portion of the thrust unaccounted for. This excess of the thrust, the difference between the total measured thrust and the thrust which can be accounted for by the sum of T_{aero} and T_{self} , is thought to be associated with the interaction with the strong applied magnetic field. We denote this extra thrust, for convenience, as T_{Hall} , although it is by no means certain that a Hall effect is actually the thrust producing mechanism.

It is not clear on a priori grounds what the dependence of Hall thrust should be on an applied current and magnetic field, although it is anticipated that both parameters should be important in determining the magnitude of thrust. If the Hall current magnitude were proportional to $(\omega r)_c$ and hence to B , it would be expected that the thrust would vary roughly as $I B^2$; and one power of B establish the Hall current magnitude, while another power of B is involved in determining the $j \times B$ force resulting. However, this assumes that the volume of interaction is independent of B (the thrust is a volume integral of $j \times B$) and this need not be so.

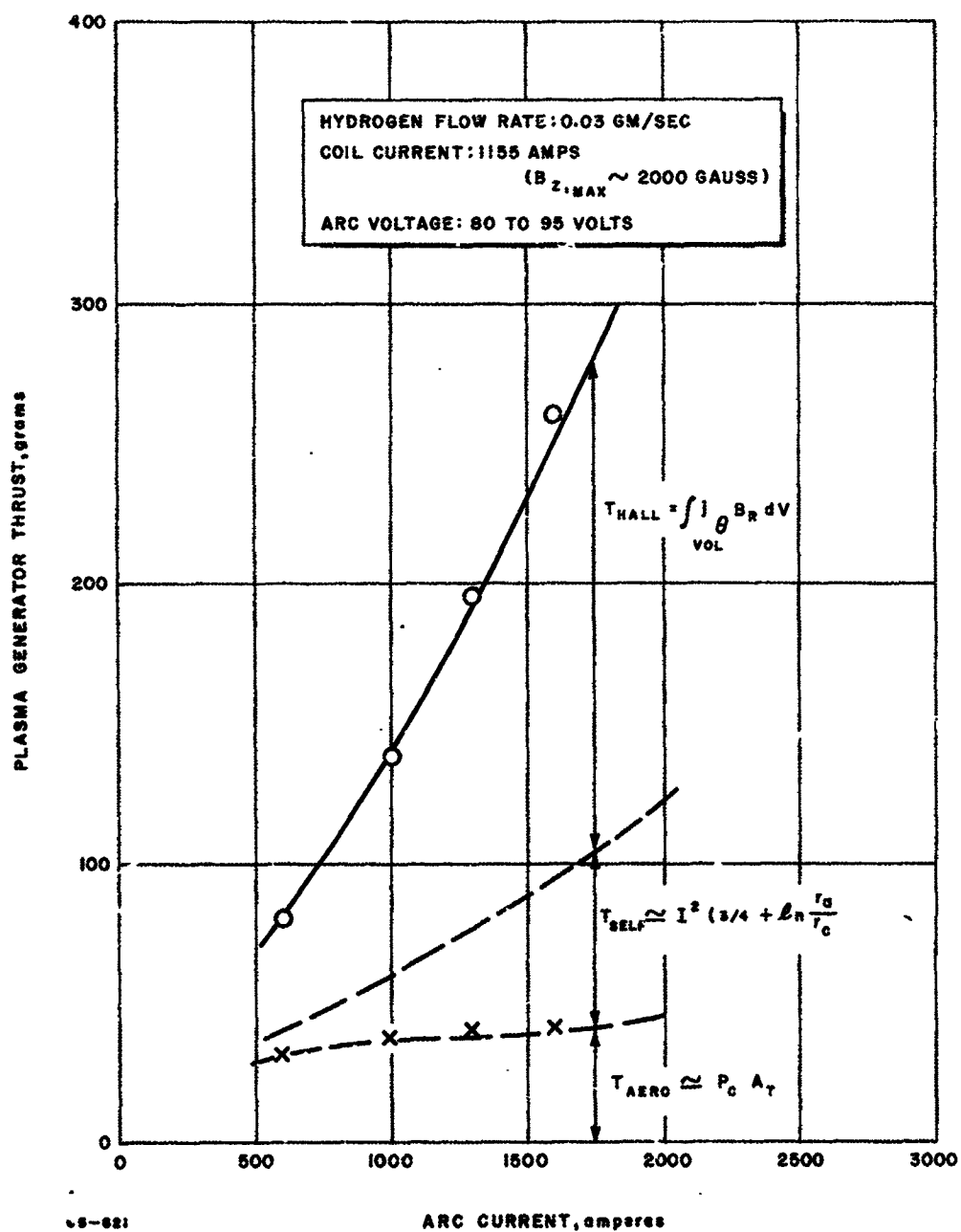


Figure 31 PLASMA GENERATOR THRUST VERSUS ARC CURRENT (HYDROGEN)

Hess¹⁸ offers experimental evidence that in the range of currents, mass flow rates, and magnetic fields applicable to these experiments, the Hall current magnitude is relatively insensitive to B. If this were the case for the X-2C engine operation, the Hall thrust would become a linear function of $I \times B$, assuming again that the volume over which the interaction takes place is not B-dependent.

In figure 32 the Hall thrust, defined as

$$T_{\text{Hall}} = T_{\text{Total}} - T_{\text{aero}} - T_{\text{self}} \quad (22)$$

is plotted versus the product IB , where I is the total arc current and B is the axial field strength at the cathode tip. I varies from 600 to 1600 amperes and B from 1 to 2 kgauss. Data for hydrogen mass flow rates of 0.02 and 0.03 gm/sec are included on the same figure. Although there is experimental scatter, the correlation is fairly good.

T_{Hall} goes to zero for null values of the product IB and reaches approximately 160 grams at the peak IB value.

Figures 33 and 34 are drawn for X-2C operation with ammonia. In figure 33 overall thrust is plotted against arc current for applied magnetic field strength of approximately 2000 gauss, axial, at the cathode tip. The ammonia mass flow rate is 0.029 gm/sec, and the arc current varies from 600 to 1600 amperes. As in the case of figure 31 for the hydrogen data, the aerodynamic and self thrusts have been estimated and plotted on figure 33. The difference between the total measured thrust and that which can be accounted for by aerodynamic and self magnetic mechanisms alone is assigned, tentatively, to the Hall effect.

In figure 34 the Hall thrust deduced in this way, T_{Hall} , is plotted against the product of arc current and peak applied axial magnetic field strength. The correlation of T_{Hall} with IB is less satisfactory for ammonia (figure 34) than for hydrogen (figure 32). Perhaps more important, the magnitude of T_{Hall} is smaller in ammonia than in hydrogen at each value of IB ; at the higher values of IB by a factor of 3 to 4. Hence, it appears that the applied magnetic field plays a smaller role in acceleration of ammonia than in acceleration of hydrogen. It has indeed already been noted that the arc voltage in ammonia is less sensitive to magnetic field than the arc voltage in hydrogen.

c. Thrustor Thermal Efficiency

In this section, data are presented which determine the "thermal" efficiency of the X-2C MPD arcjet. By thermal or arc efficiency is meant the quantity

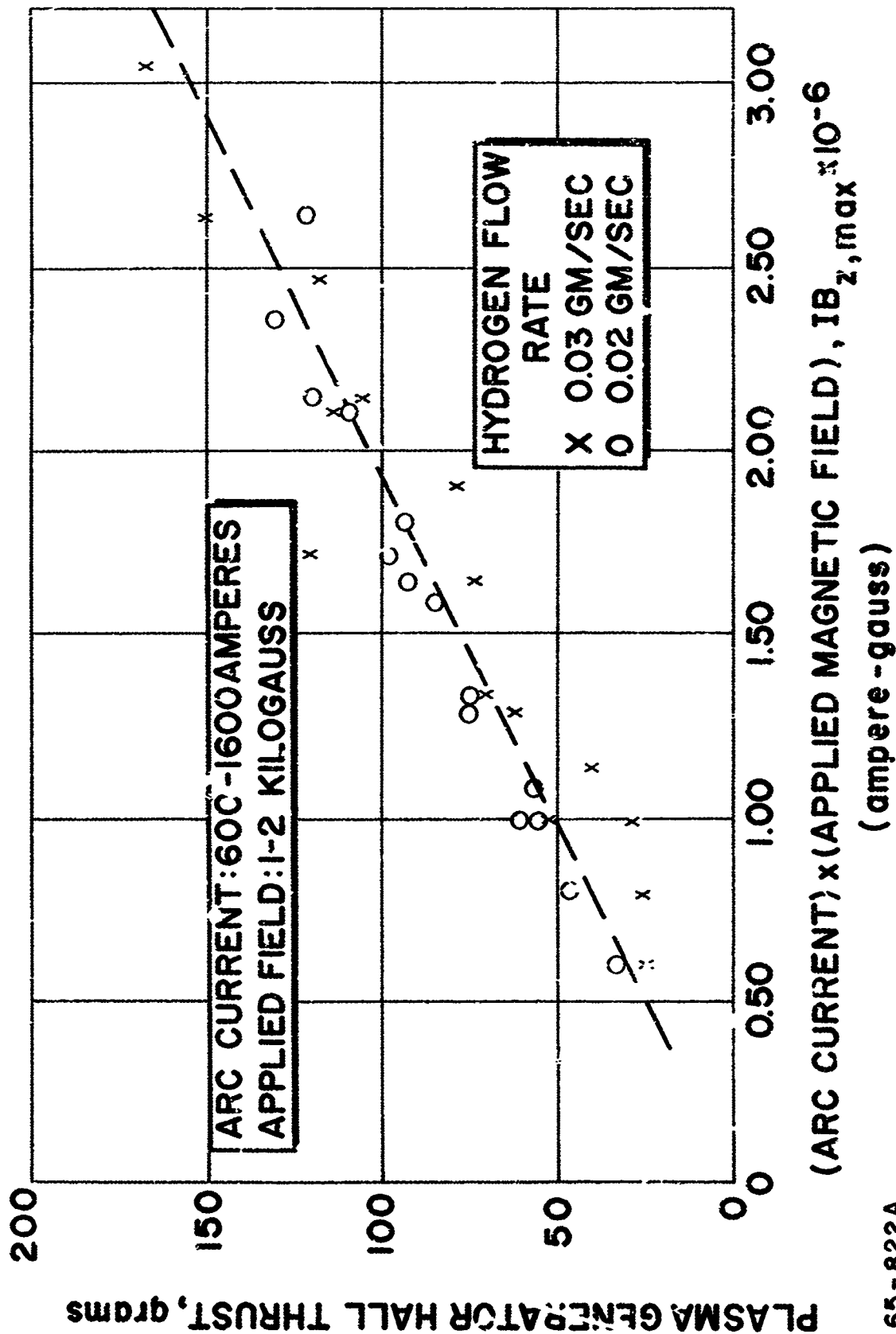


Figure 32 PLASMA GENERATOR HALL THRUST VERSUS PRODUCT OF ARC CURRENT AND MAGNETIC FIELD STRENGTH (HYDROGEN)

65-822A

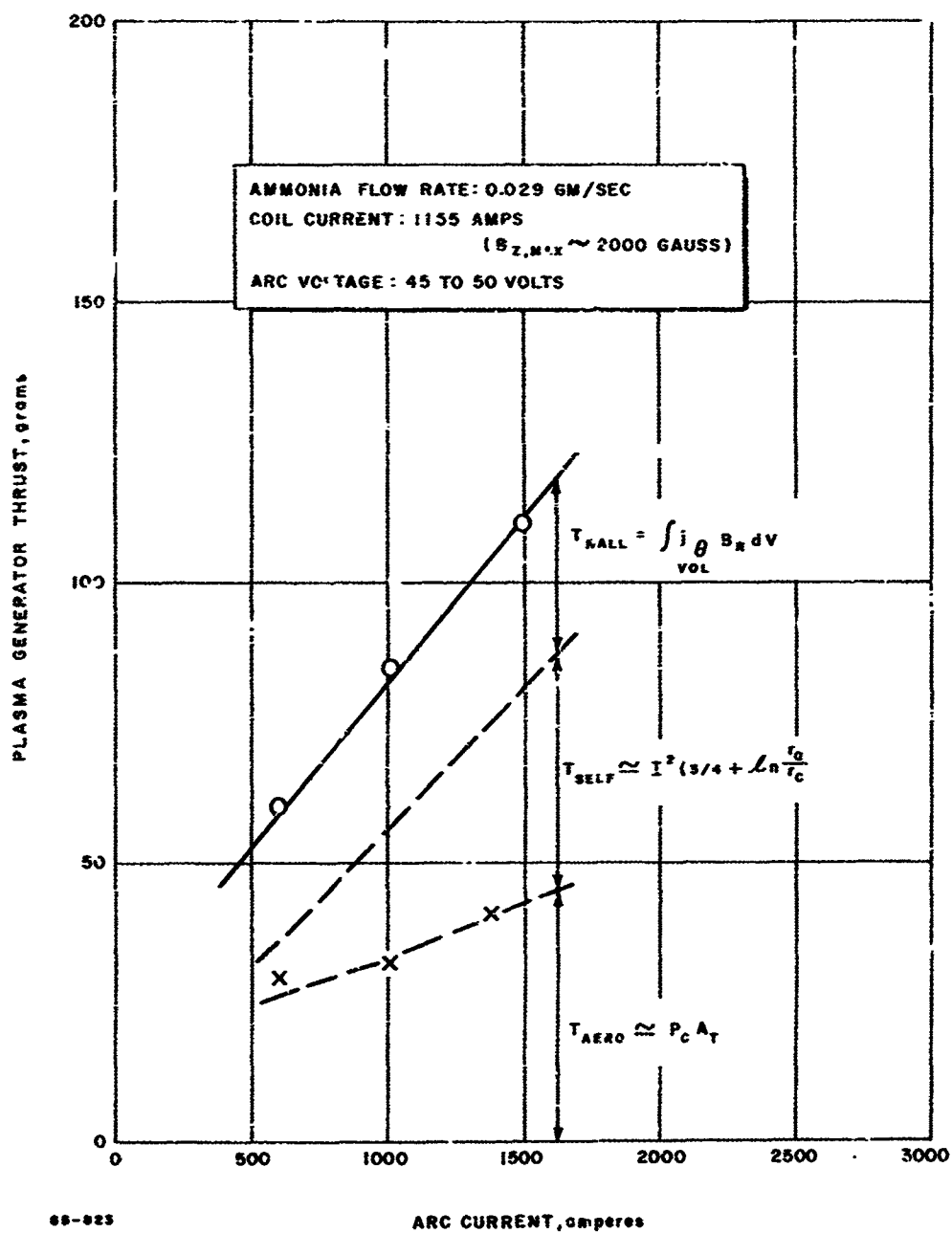


Figure 33 PLASMA GENERATOR THRUST VERSUS ARC CURRENT (AMMONIA)

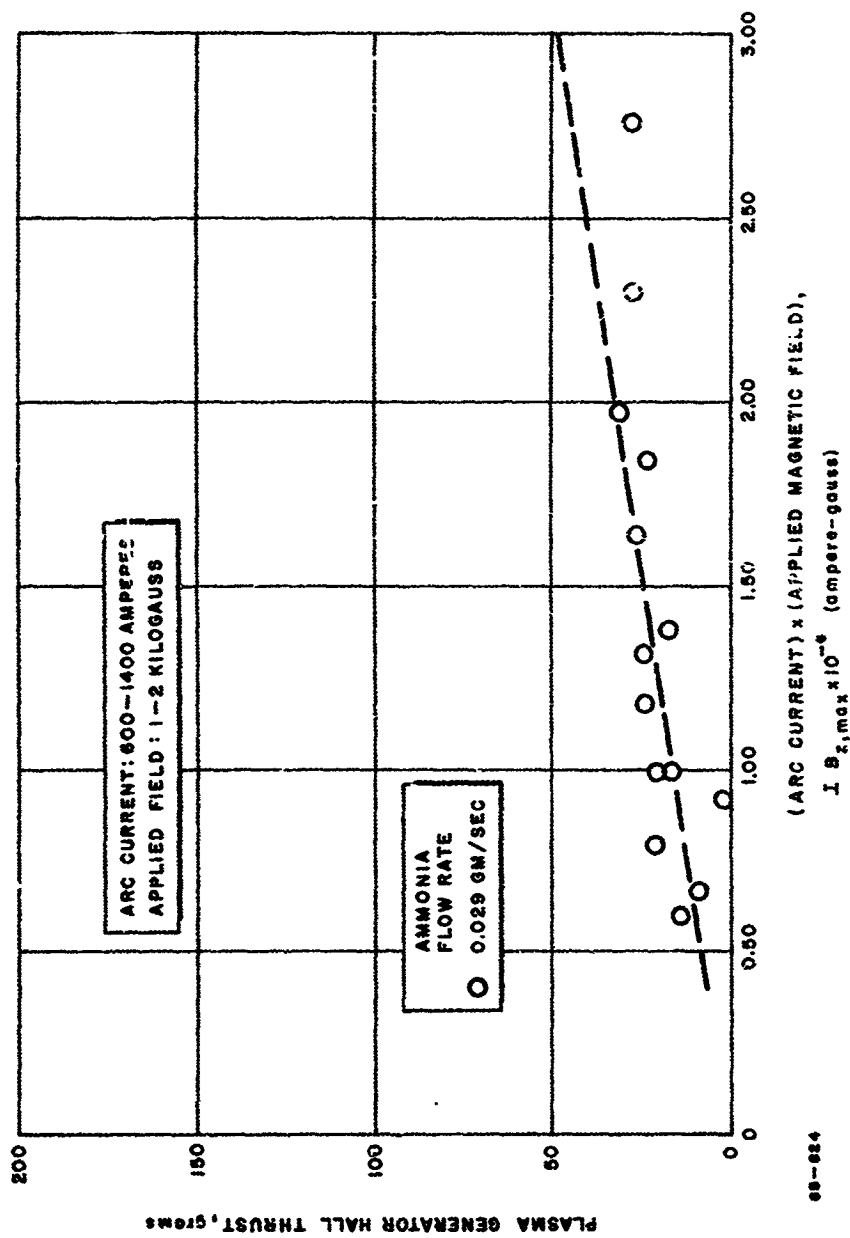


Figure 34 PLASMA GENERATOR HALL THRUST VERSUS PRODUCT OF ARC CURRENT AND MAGNETIC FIELD STRENGTH (AMMONIA)

$$\epsilon_{\text{arc}} = \frac{\text{Power to gas}}{\text{Power to arc}}$$

where the power input is taken as the product of applied voltage and arc current without correction for the incoming gas enthalpy. For the enthalpy levels associated with the X-2C MPD arcjet this correction is negligible. (Actually, much of the power input to the engine is in the form of directed kinetic energy without passing through a thermal stage, but the term "thermal efficiency" is taken over from the usual arc heater terminology.) The heater efficiency is determined by measuring the power lost to the anode and cathode water cooling circuits, according to equation 23a.

$$\epsilon_{\text{arc}} = 1 - \frac{P_{\text{cool}}}{P_{\text{in}}} = 1 - \frac{\dot{m}_w C_{p,w} \Delta T_w}{VI} \quad (23a)$$

where \dot{m}_w , $C_{p,w}$ and ΔT_w are the mass flow rate, specific heat, and temperature rise, respectively, of the coolant water.

In practice, the cathode heat loss is small under all conditions of X-2C MPD arcjet operation, varying between approximately 0.5 and 2 kw as a function of current and mass flow rate. The anode heat loss, on the other hand, is in general substantial.

In figure 35 P_{cool} in kilowatts is plotted as a function of current for a number of test runs of the X-2C MPD arcjet. The tests were made in hydrogen at mass flow rates of 0.02 and 0.05 gm/sec, and with applied magnetic field strengths varying from 500 to 2000 gauss. Data points corresponding to the mass flow rate of 0.02 gm/sec are indicated by open circles, while those for the 0.05 gm/sec flow rate are represented by crosses. In addition to these points are plotted several reported by Cann¹⁶ and by Ducati¹⁷; the data of reference 16 were obtained at a hydrogen flow rate of 0.02 gm/sec, while those of reference 17 correspond to a hydrogen flow rate of 0.025 gm/sec.

Several features are clear from inspection of figure 35. First, the correlation of P_{cool} with current is fairly good; the data points corresponding to different mass flow rates and to different magnetic field strengths exhibit relatively little scatter. Second, the data reported by Cann¹⁶ and by Ducati¹⁷ also correlate reasonably well with those measured at this laboratory, although there are differences in the MPD arcjet geometry and magnetic field configuration among the devices employed at the three laboratories. Finally, these data can be represented reasonably well over most of the current range by a straight line of slope equal to unity, which is consistent with a

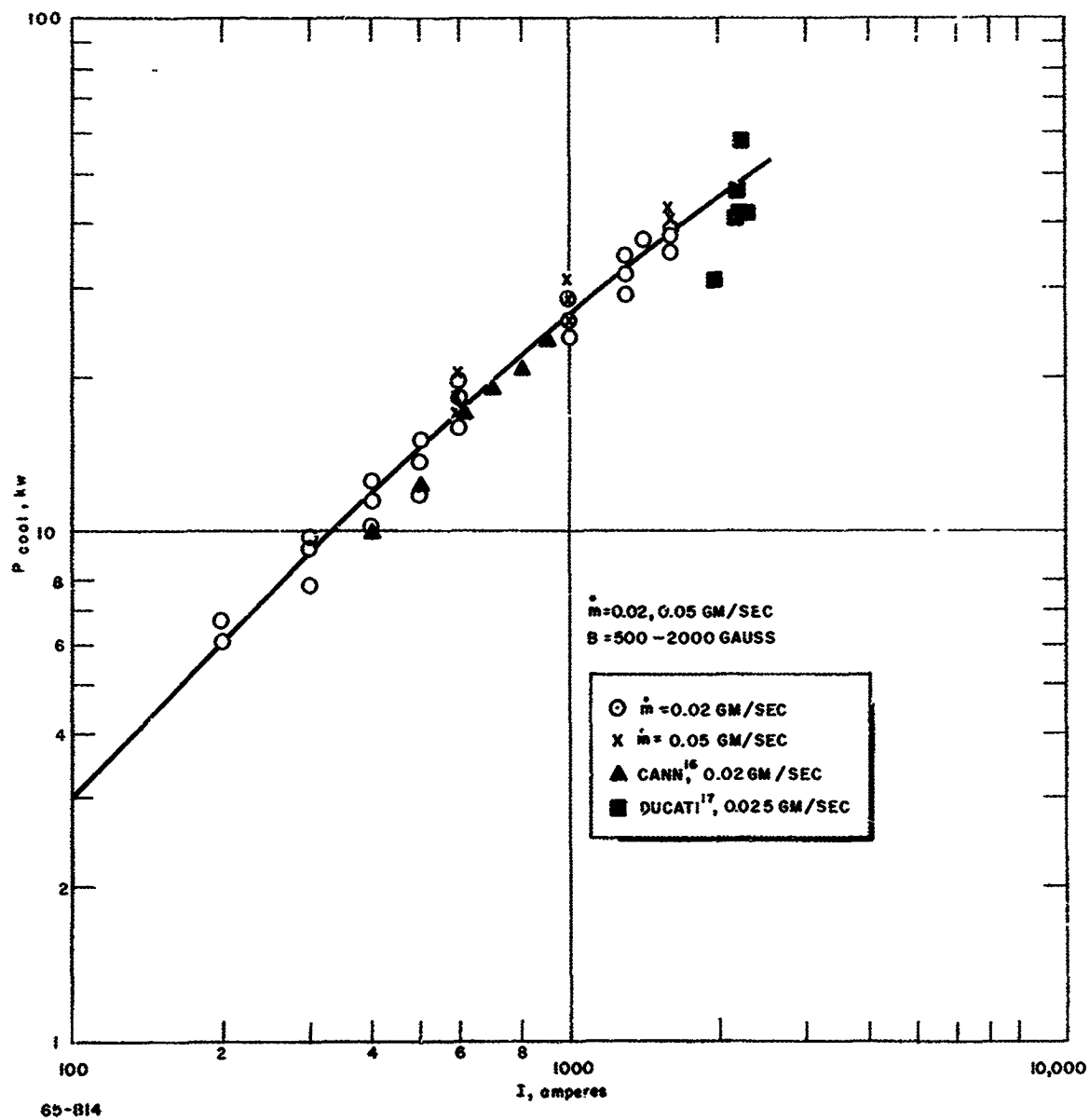


Figure 35 POWER TO COOLING VERSUS ARC CURRENT (HYDROGEN)

constant voltage drop at the electrodes representing most of the heating. At the highest currents P_{cool} tends to fall away from this line, but within about 30 percent the data for currents ranging from 100 to 3000 amp can be accounted for by a constant voltage drop of about 26 volts. In contrast, the sensitivity of the anode and cathode heat transfer to mass flow rate seems very slight.

The line drawn on figure 35 is simply a smooth curve fitted by inspection to the data. This same smooth curve is repeated on figure 36, where P_{cool} is plotted as a function of current for X-2C operation with ammonia as the propellant. The ammonia mass flow rates represented in figure 36 are 0.029 and 0.058 gm/sec compared with the hydrogen flow rate of 0.02 and 0.05 gm/sec of figure 35. The magnetic field variation for the data of figure 36 is again 500 to 2000 gauss. Inspection of figure 36 reveals that the data are fitted remarkably well by the line drawn to represent the hydrogen data of figure 35; therefore, the major features of the electrode heating in hydrogen operation are applicable also to operation in ammonia. Again, sensitivity to mass flow rate of propellant is slight for the two mass flow rates plotted in figure 36.

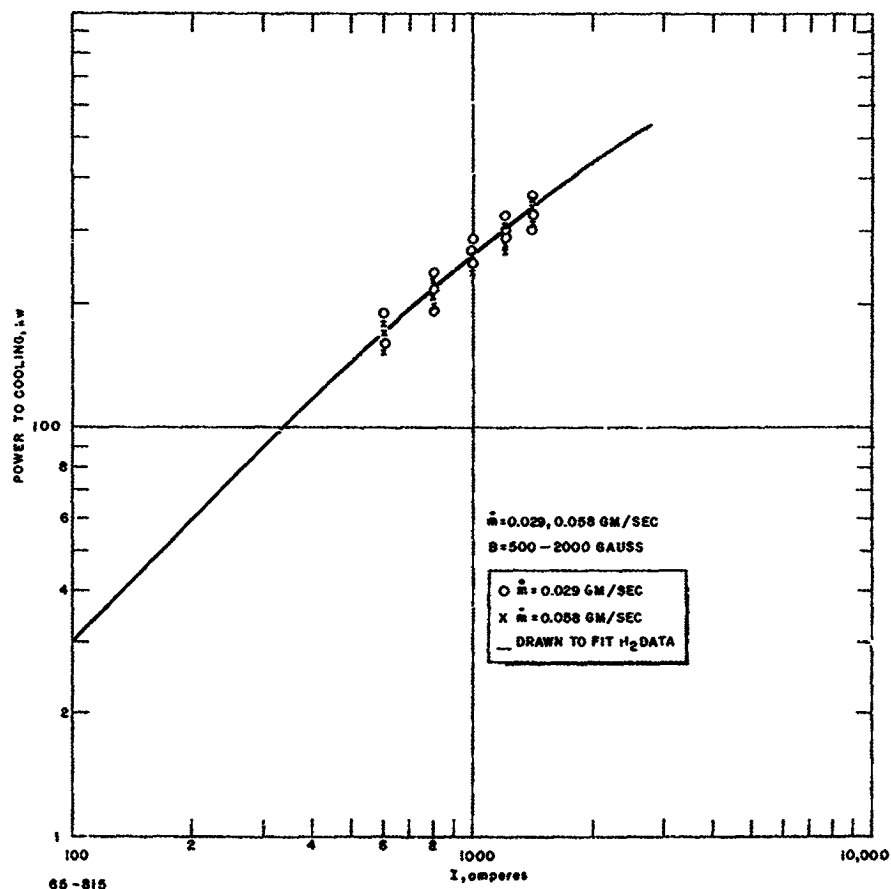


Figure 36 POWER TO COOLING VERSUS ARC CURRENT (AMMONIA)

The success in fitting heat transfer data for both hydrogen and ammonia with a single curve motivates examination of data which have been obtained in other gases as well. Figures 37, 38, and 39 are curves analogous to figures 35 and 36, and are drawn for helium, nitrogen, and argon. In each case the smooth curve is the one which was fitted to the hydrogen data of figure 35.

In figure 37, data are presented for helium mass flows of 0.014 and 0.058 gm/sec; only a single magnetic field strength of 500 gauss was employed. The scatter of these few data points is more severe, and it is not at all certain that the quantitative trend of P_{cool} with current is precisely the same as for hydrogen. Further, there appears to be a systematic but small dependence upon mass flow rate. Still, the hydrogen curve fits the data tolerably within the accuracy with which the helium trend can be estimated.

Figure 38, for nitrogen, can be commented upon in much the same way. There is some apparent dependence upon mass flow rate between flow rates of 0.018 and 0.055 gm/sec, but very little difference between 0.055 and 0.09 gm/sec. For the few data points which are available, the hydrogen curve provides a tolerable fit.

Finally, argon also seems to fit this general heat transfer characteristic, as indicated by figure 39. For argon there is little systematic dependence of heat transfer on mass flow rate between 0.044 and 0.088 gm/sec. The hydrogen curve is again a tolerable fit.

Several conclusions may be tentatively reached on the basis of the data of figures 35 through 39. These are:

- 1) Electrode heat transfer rates are most sensitive to current among the parameters which have been varied.
- 2) Electrode heat transfer is much less sensitive to accelerator configuration (e. g., the agreement between values obtained at this laboratory and those of references 16 and 17), magnetic field strength, propellant mass flow rate and propellant type. Further, since different propellants have widely varying characteristic voltages (see, for example, figure 30), operation at a given current in two different propellants implies operation at different input power levels; therefore, electrode heat transfer is sensitive neither to mass flow rate nor to input power, and so it is insensitive, over the ranges plotted, to enthalpy.
- 3) The electrode heat transfer can be represented fairly well by a constant electrode voltage drop of approximately 26 volts.

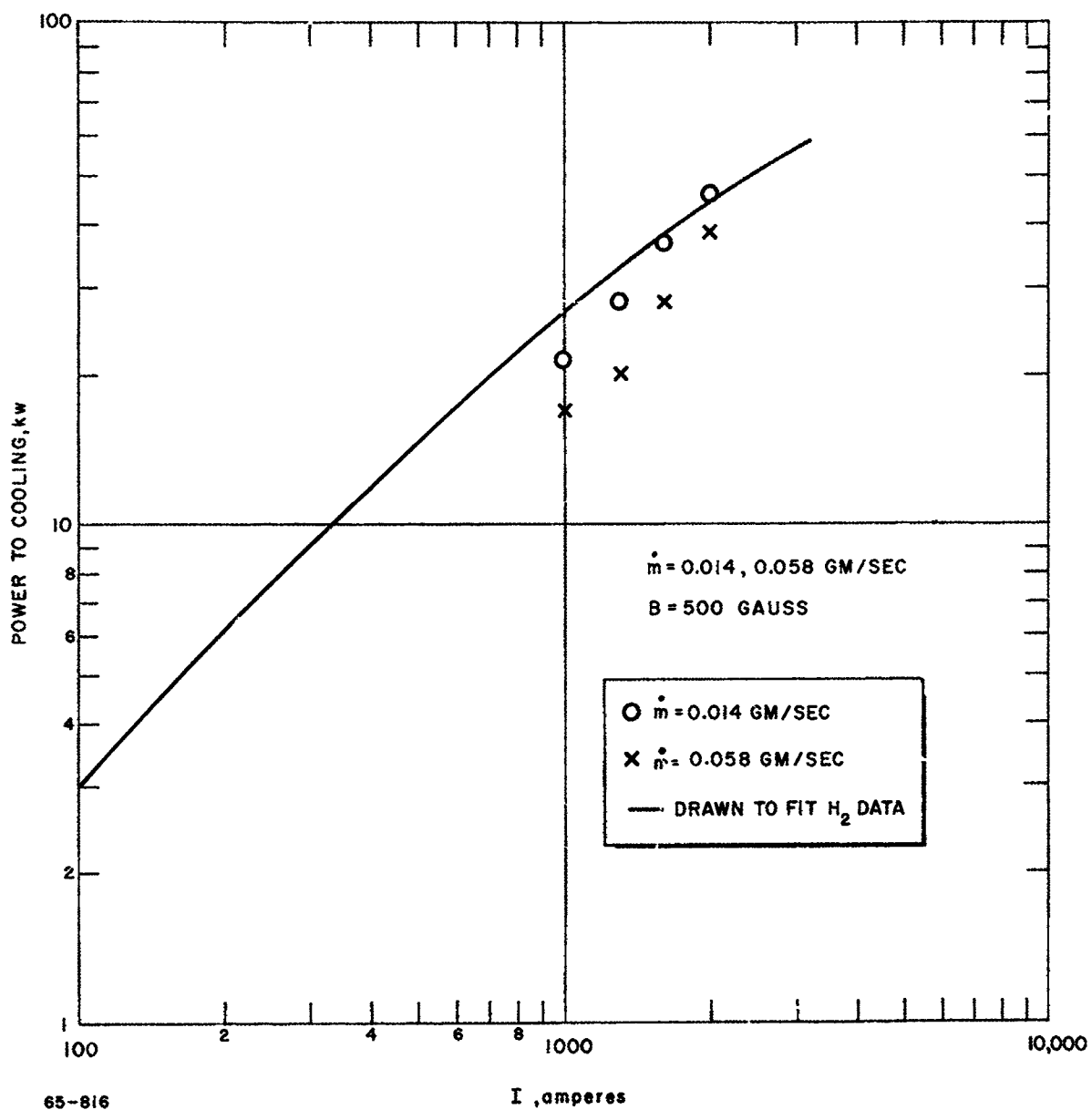


Figure 37 POWER TO COOLING VERSUS ARC CURRENT (HELIUM)

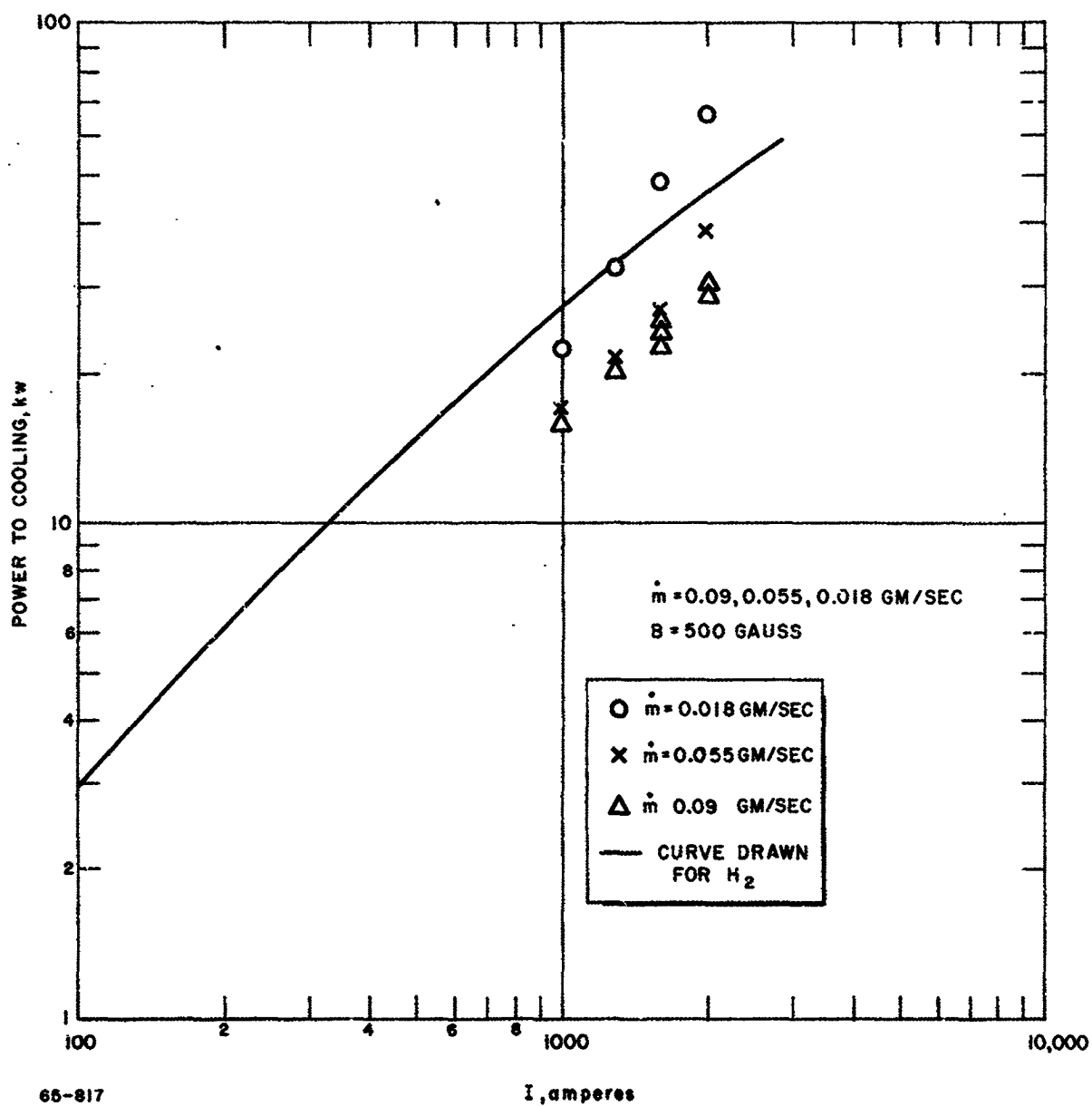


Figure 38 POWER TO COOLING VERSUS ARC CURRENT (NITROGEN)

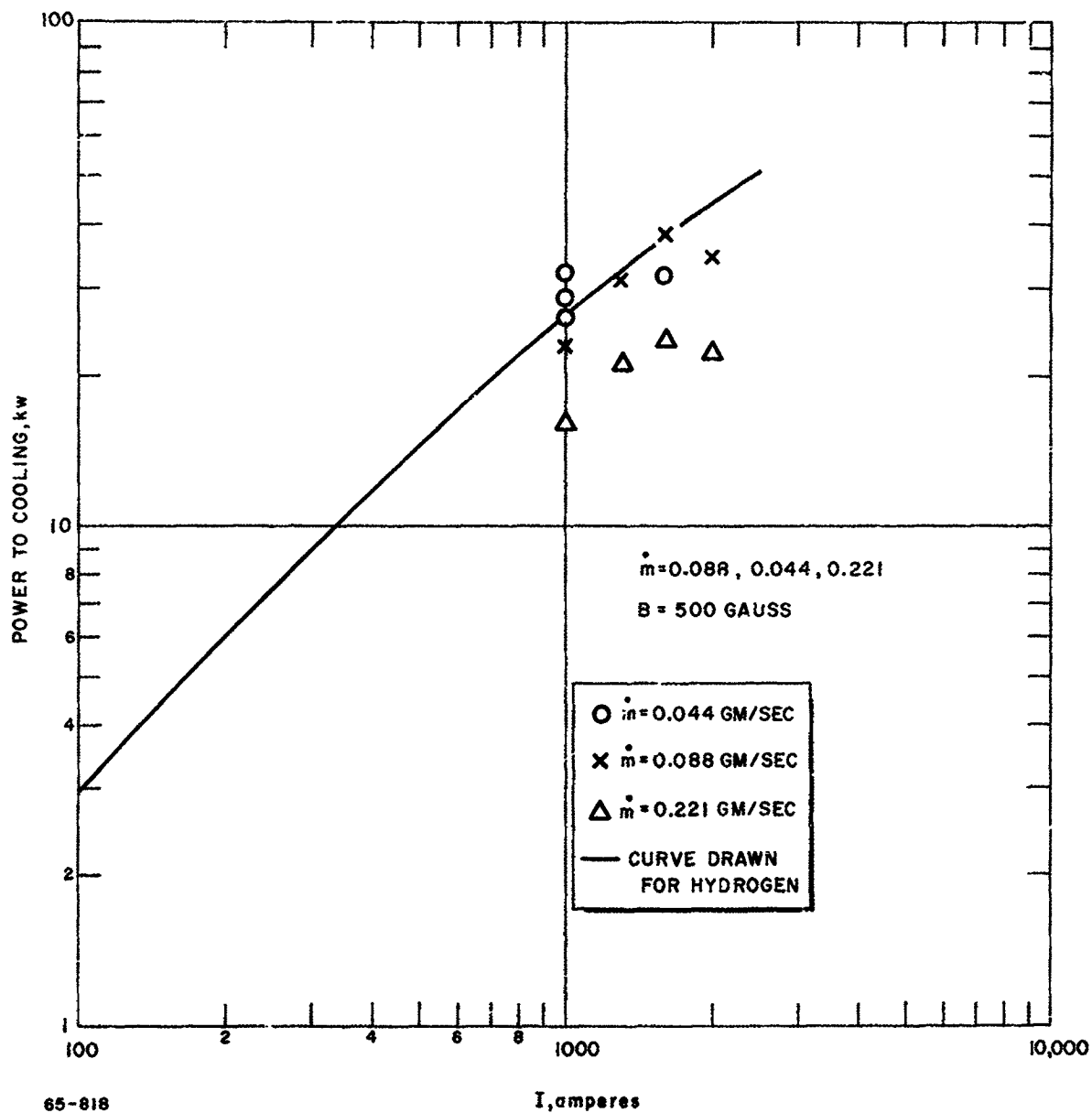


Figure 39 POWER TO COOLING VERSUS ARC CURRENT (ARGON)

4) On the basis of conclusions 1) through 3) it would appear that convection is not a dominant process in transferring heat to the electrodes. Rather, some effect involving plasma sheaths and the electrode fall zones seems to be much more important.

With this understanding of the absolute magnitude of the electrode power losses in the X-2C MPD arcjet, the thermal efficiency data are readily explained. Figure 40 shows, for hydrogen, thermal efficiency as a function of applied magnetic field strength. Mass flows of 0.02 and 0.05 gm/sec were used, with arc currents of 500, 600, 1000, and 1600 amp. The solid symbols represent data obtained for the higher mass flow, and the dashed curves are drawn through these symbols. In general, based on figure 40, the thermal efficiency increases with current and magnetic field strength for the higher mass flow rate, and shows very little systematic variation with either current or magnetic field strength at the lower mass flow rate. In the range of parameters where the best propulsion performance has been obtained (high current, high magnetic field strength) the thermal efficiency varies between 65 and 75 percent. Referring to figure 28, it can be seen that the arc voltage shows only a slight dependence on current and on magnetic field strength at the 0.02 gm/sec mass flow rate, while it increases with magnetic field strength at the 0.05 gm/sec mass flow rate. Since the cooling power losses are essentially fixed by the arc current according to figure 35, thermal efficiency is determined essentially by the arc voltage.

Figure 41 is drawn for ammonia and again plots thermal efficiency versus applied magnetic field strength for mass flow rates of 0.02 and 0.058 gm/sec and arc currents of 500, 1000, and 1400 amp. There is some apparent tendency for the thermal efficiency to rise with current and magnetic field strength, and, at the higher currents, with mass flow rate. At the higher values of current and magnetic field strength, thermal efficiencies in the range 35 to 50 percent characterize the data.

Thus, the thermal efficiencies for ammonia are, under similar conditions, on the order of two-thirds of the thermal efficiencies in hydrogen. Referring again to figure 30, the same statement can be used to describe the operating voltage. The implications for overall propulsive efficiency are examined in the following section.

d. Overall Efficiency

The overall propulsive efficiency is defined as the ratio of thrust power to input power:

$$\epsilon_o = \frac{4.8 \times 10^{-3} T^2}{\dot{m} P_{in}} = \frac{4.8 \times 10^{-3} T I_{sp}}{P_{in}} \quad (23)$$

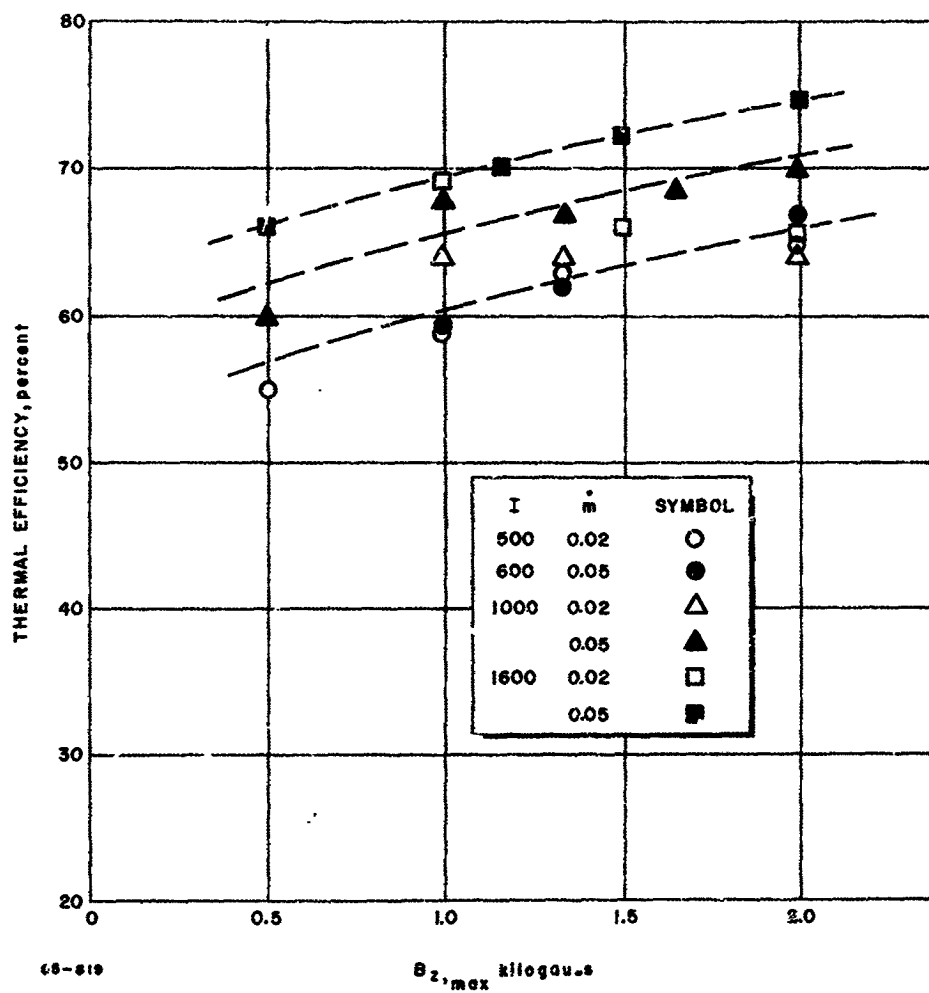


Figure 40 THERMAL EFFICIENCY VERSUS MAGNETIC FIELD STRENGTH (HYDROGEN)

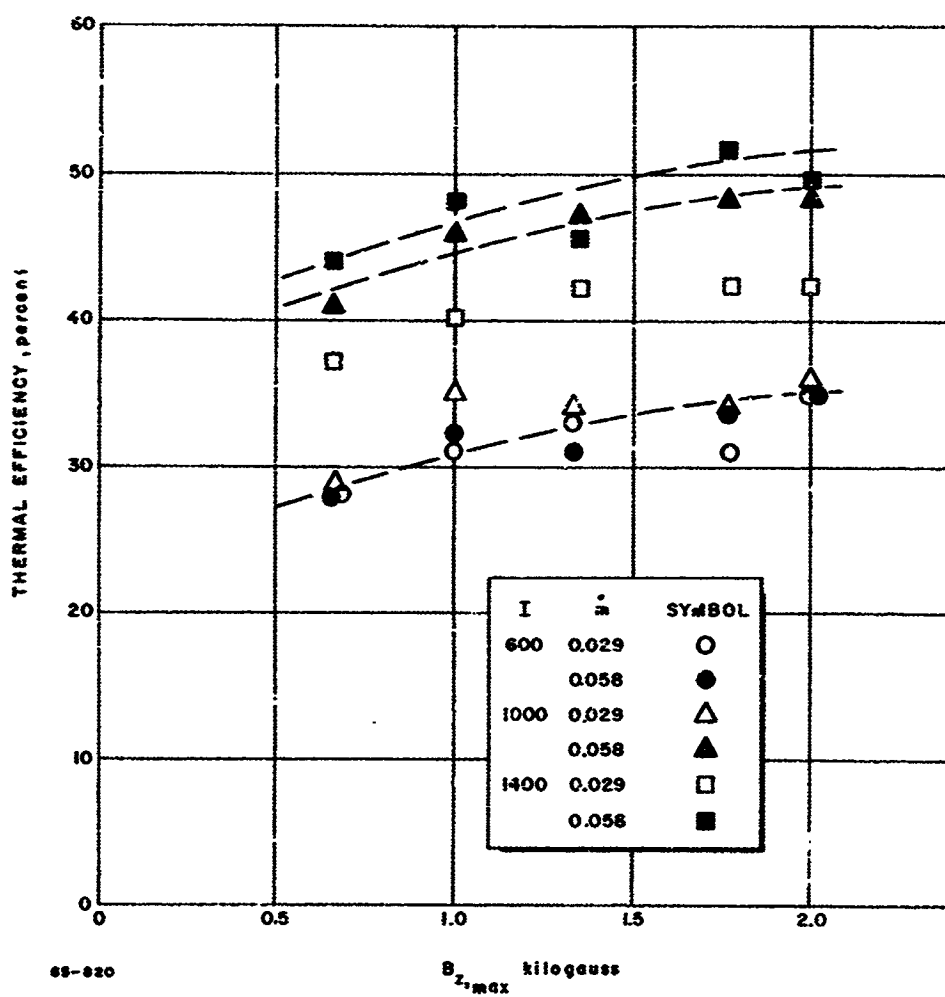


Figure 41 THERMAL EFFICIENCY VERSUS MAGNETIC FIELD STRENGTH (AMMONIA)

where η_o is the overall propulsive efficiency expressed in percent, T is the total thrust in grams, \dot{m} the propellant mass flow rate in gm/sec, and I_{sp} the specific impulse in seconds. P_{in} , the input power, is taken as $10^{-3} I V$ in kilowatts.

Figures 42 and 43 show, for hydrogen and for ammonia, the overall efficiency as a function of specific impulse.

Each figure includes data taken over a wide range of conditions; in figure 42, for hydrogen, the arc current varies approximately by a factor of 5 between 300 and 1600 amperes, the applied magnetic field by a factor of nearly 3 between 0.75 and 2 kgauss, the propellant mass flow rate by a factor of 2.5 between 0.02 and 0.05 gm/sec, and the arc voltage by a factor of 2 between 55 and 105 volts. In figure 43 for ammonia, the variation is between 600 and 1400 amp in arc current, 0.75 and 2 kgauss in applied magnetic field, 0.029 and 0.058 gm/sec in ammonia flow rate, and 35 and 55 volts in arc voltage.

Still, for each propellant, all the data on overall efficiency versus specific impulse fit very closely to a single curve. Within the range of parameters tested, the overall efficiency is then essentially a function only of I_{sp} , and not independently of field strength, power input, current, or propellant flow rate. To emphasize the independence of efficiency, at a given impulse, to input power level, the data of figures 42 and 43 have been coded so that different symbols apply to the different power ranges 20 to 40 kw, 40 to 80 kw, and 80 to 160 kw. Inspection of the figures indicates that the curves drawn to represent each power level are, within the experimental scatter, the same curves. It could be concluded, tentatively, that it should therefore be possible to achieve comparable efficiency-specific impulse curves at lower levels than those which have been employed.

Figure 44 is drawn for comparison of hydrogen and ammonia in terms of overall propulsive efficiency. In each case the smooth curve is drawn to fit the data of figures 42 or 43, and the experimental scatter is indicated by the bars drawn on the ammonia curve. The indications of figure 44 are that the overall propulsive efficiency of the X-2C engine is somewhat higher in ammonia than in hydrogen by approximately 5 to 10 absolute points. That is, at a specific impulse of 4000 seconds the efficiency with hydrogen is almost exactly 30 percent, while for ammonia the range 35 to 40 percent is indicated. Estimation of the frozen flow efficiency is difficult, since the enthalpy level at which freezing occurs is unknown. A considerable portion of the input energy is inserted directly in the kinetic form, so that the static enthalpy need not be excessively high. Estimation of the expansion

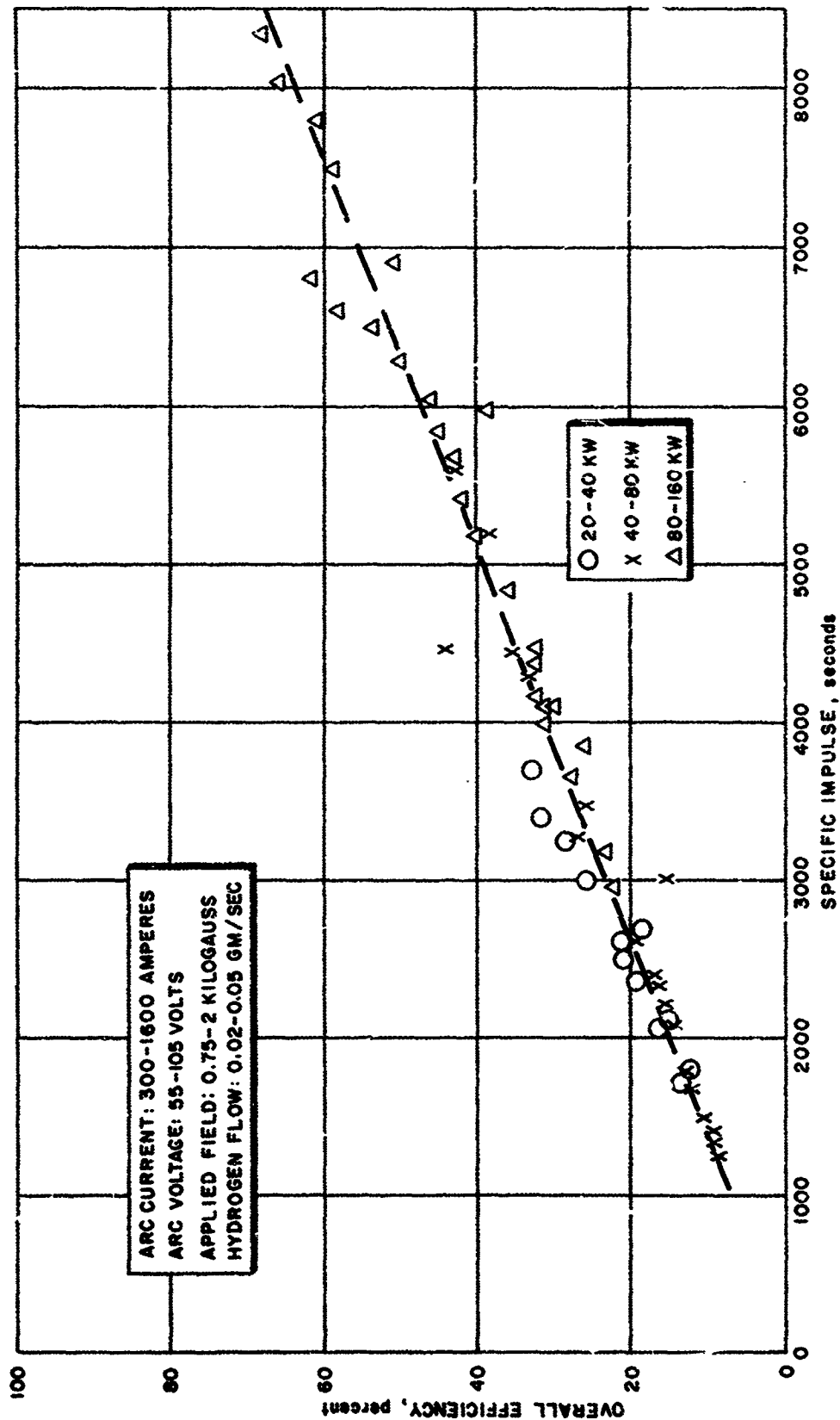


Figure 42 OVERALL EFFICIENCY VERSUS ARC ENGINE SPECIFIC IMPULSE (HYDROGEN)

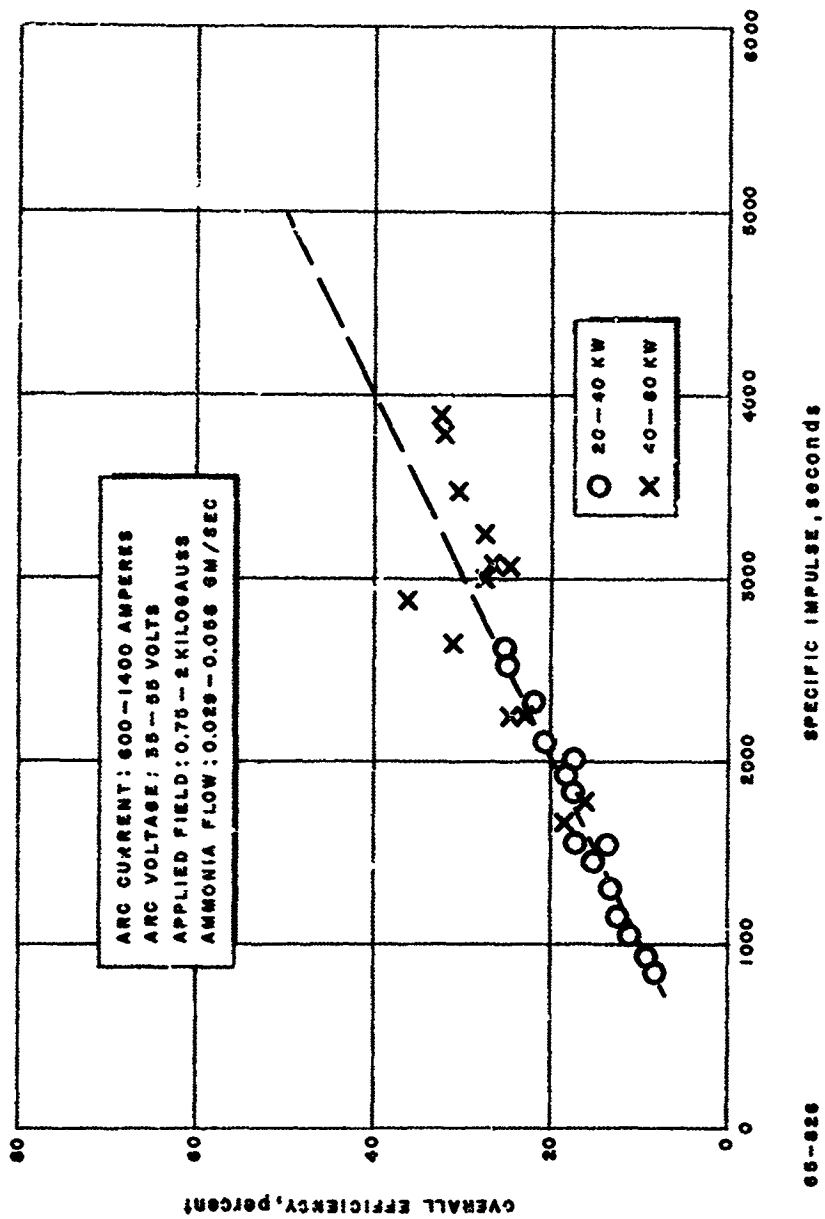


Figure 43 OVERALL EFFICIENCY VERSUS ARC ENGINE SPECIFIC IMPULSE (AMMONIA)

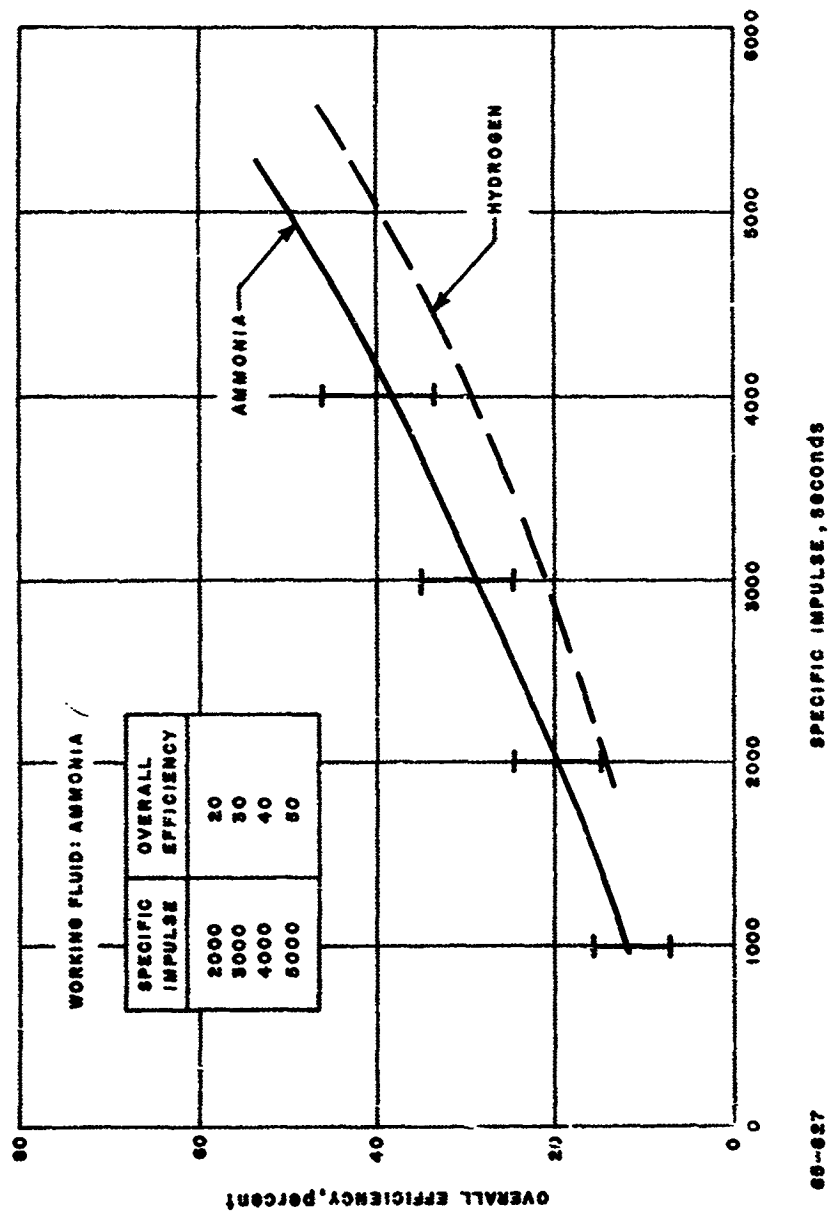


Figure 44 OVERALL EFFICIENCY VERSUS ARC ENGINE SPECIFIC IMPULSE

efficiency is equally difficult, since the factors which contribute to this efficiency (velocity profile loss, angular spread, failure to convert random to directed motion, etc.) are closely tied to the acceleration mechanisms, which are themselves not understood in detail. However, two simplifying assumptions may be made which permit comparison of the hydrogen and ammonia efficiency data. These assumptions are crude, but satisfactory for the present stage of understanding of MPD arcjet behavior. The first assumption is

$$\epsilon_{\text{exp}, \text{H}_2} = \epsilon_{\text{exp}, \text{NH}_3} \quad \text{for } 1000 \text{ sec} < I_{\text{sp}} < 5000 \text{ sec}$$

that is, the fraction of input power which is lost in velocity profiles, etc., is the same for hydrogen and ammonia at any given specific impulse in the range 1000 to 5000 seconds. This range of specific impulse is the range where overlapping data in hydrogen and ammonia are available.

The second assumption involves the frozen flow efficiency. Here it is assumed that the percentage of dissociation and ionization for hydrogen and ammonia are the same at a given specific impulse; e.g., if hydrogen is 10 percent ionized at 2000 seconds, then ammonia is also 10 percent ionized at this specific impulse. Then, approximately, the ratio $\epsilon_f, \text{H}_2 / \epsilon_f, \text{NH}_3$ at a given I_{sp} is the same as the ratio which would hold for full ionization even though it is not at all necessary that ϵ_f, H_2 or ϵ_f, NH_3 represent full ionization.

With these assumptions, the overall efficiency ratio for ammonia and hydrogen can be written

$$\frac{\epsilon_o, \text{NH}_3}{\epsilon_o, \text{H}_2} = \frac{\epsilon_{\text{arc}}, \text{NH}_3}{\epsilon_{\text{arc}}, \text{H}_2} \times \frac{\epsilon_f, \text{NH}_3}{\epsilon_f, \text{H}_2}$$

Table I evaluates this ratio and compares it with that experimentally obtained. Data on ϵ_f are taken from figure 27, which assumes full dissociation and 1st ionization of all atoms.

Agreement between the overall efficiency ratios calculated in this fashion and those measured is fairly good, except at the lowest specific impulse value, 2000 seconds. At the lower values of I_{sp} the calculation of ϵ_f is expected to be particularly crude, so that this result is not surprising.

TABLE I

OVERALL EFFICIENCY RATIO FOR AMMONIA AND HYDROGEN

I_{sp} (seconds)	ϵ_{arc, NH_3} (percent)	ϵ_{arc, H_2} (percent)	$\frac{\epsilon_{f, NH_3}}{\epsilon_{f, H_2}}$	$\frac{\epsilon_{o, NH_3}}{\epsilon_{o, H_2}}$ (calculated)	$\frac{\epsilon_{o, NH_3}}{\epsilon_{o, H_2}}$ (measured)
2000	42	65	3.04	1.9	1.4
3000	42	65	2.42	1.5	1.4
4000	42	65	1.97	1.3	1.3
5000	42	65	1.72	1.1	1.2

The results of table I indicate that, at least to first order, the overall efficiency data for hydrogen and ammonia can be compared on the basis that the expansion efficiency is essentially the same for the two propellants, and that the differences in overall efficiency can be attributed to the arc and frozen flow efficiencies.

Nonetheless, the apparent close fit of the overall efficiency versus specific impulse data to a single curve which closely approximates a straight line presents a problem of much greater import. Besides the fact that the electric-to-thrust power efficiency apparently is basically fixed by the selection of a propellant and specific impulse level, and is relatively insensitive to the particular combination of mass flow rate, input power, arc current and magnetic field strength by which the specific impulse level is achieved, the most striking feature of the efficiency-impulse curve is its seemingly constant slope. An extrapolation of the curve to higher values of specific impulse would yield overall efficiency values greater than 100 percent; this is clearly a violation of the principle of energy conservation. A series of high input power, very low mass flow rate tests was made in order to determine whether the extrapolated values were experimentally obtained. Efficiencies of more than 100 percent were indeed measured, and an exhaustive study of the measuring system was undertaken in an attempt to explain the unrealistic results. It was determined that all measurements were properly made, and that the data as recorded

were correct. The method of calculating the overall efficiency and specific impulse in terms of the measured quantities was then considered. Both the overall efficiency and the specific impulse are calculated using expressions which contain the mass flow rate as a term in the denominator. (See, for example, equations (11), (12), and (13).) If the measured mass flow rate--the mass flow introduced through the engine inlet ports--were different from the true mass flow which the engine is accelerating, erroneous values would be obtained for both the efficiency and the specific impulse. This phenomenon is denoted by entrainment.

If the true mass flow rate (metered mass flow plus entrained mass flow) were always 0.03 gm/sec while the mass flow rate introduced through the engine and measured at the inlet ports ranged from, say 0.03 to 0.01 gm/sec, the overall efficiency and specific impulse expressions would yield values up to three times as large as those actually achieved. This would also imply that the efficiency--impulse curve may truly be a straight line, but only up to some value of specific impulse (and overall efficiency) corresponding to a mass flow rate of 0.03 gm/sec, thereafter increasing perhaps to an asymptotic value of somewhat less than 100 percent at specific impulses obtainable with and MPD arcjet.

The following section discusses some experiments performed to test for the existence of gas entrainment, and outlines the reasons for the conclusion that gas entrainment is a major factor in the observed operation of the MPD arcjet in "high" back pressure environmental tanks. The next section then considers the operation of the MPD arcjet with alkali metal propellants and the ensuing benefits including the advantage of reduced tank back pressure operation.

D. POSSIBLE MASS ENTRAINMENT BY THE X-2 ENGINE WITH STRONG EXTERNAL MAGNETIC FIELD

1. Qualitative Observations on Zero-Gas Flow Operation

A series of experiments was carried out to examine the role of possible gas entrainment in the performance of the MPD arcjet engine. With reference to equation (24), the beam or thrust power of any propulsion device is given by

$$P_{\text{thrust}} = 4.8 \times 10^{-5} T^2 / m_{\text{total}}$$

(24)

where P_{thrust} (kw) is the thrust power, $T_{\text{(grams)}}$ is the measured thrusts, \dot{m}_{total} (gm/sec) is the total accelerated propellant flow rate. If there is significant gas entrainment during the gas acceleration process, the actual value of thrust power will be less than the estimated value of thrust power based only on the measured propellant flow rate.

The overall propulsion efficiency is given by an expression of the form

$$\epsilon = 4.8 \times 10^{-2} T^2 / \dot{m}_{\text{total}} IV \quad (25)$$

or

$$\epsilon = 4.8 \times 10^{-2} T^2 / \dot{m}_{\text{meas}} (1 + \dot{m}_{\text{entrain}} / \dot{m}_{\text{meas}}) IV \quad (26)$$

where, \dot{m}_{meas} (gram/sec) is the measured input flow rate to the engine and \dot{m}_{entrain} is the flow rate entrained from the ambient environment during the acceleration process; I (amperes) is the arc current and V (volts) is the arc voltage. Thus, for a given power input, gas entrainment in the acceleration region will reduce the estimated value of the overall electric to thrust power conversion efficiency.

The most striking qualitative evidence for the existence of gas entrainment is the observation of Ducati¹⁹, Hess and Brockman²⁰, and this laboratory, that the MPD arcjet will run without any gas flow passing through the engine. If there were no gas entrainment then this situation would, of course, correspond to an infinite thrust power, and since the input power remained finite for this condition, an infinite value of the overall energy conversion efficiency. Thus, the engine must either be running on electrode material, or on entrained tank gases. Measurements of the weight loss of electrode material have clearly indicated that in the no-gas flow tests run at this laboratory the engine was running on the ambient gas (100 microns) in the test tank and not on electrode material.

On the basis of this simple observation, it is clear that the propulsion performance results reported to date^{4, 15, 21, 22} on MPD arcjet-like devices are open to some question and will remain open to question until quantitative answers are obtained to the problem of gas entrainment.

2. Quantitative Observations on Zero-Gas Flow Operation

A detailed series of experiments has been carried out to examine the possibility of gas entrainment.

First, a two-way gas valve was placed in the incoming propellant line so that a given mass flow rate of propellant could be passed either through the thruster as in normal operation, or through the tank wall thus bypassing the thruster. In either case, the ambient pressure was unchanged since the total mass flow throughput seen by the vacuum pump was a constant. Qualitatively, it was observed that the thruster operation, e.g., visual appearance of the jet, was relatively insensitive to whether the gas was admitted through the thruster or the vacuum tank wall. As indicated below, at a given current both the thruster voltage and measured thrust changed only a few percent as the flow was diverted from the engine through the tank wall. This observation is taken as clear evidence that the thruster can act as a pump acting on the ambient gases.

Table II presents measured values of the engine voltage (V) and engine thrust (T) for gas passing through the engine (V_{in} and T_{in}) and for gas passing through the tank wall (V_{out} and T_{out}) as a function of arc current and hydrogen flow rate. The magnet coil current was held constant. The ambient pressure ($P_{ambient}$) is a function of only the mass flow entering the vacuum pump, and increases with increase in mass flow rate rising from 100 microns at 10 mg/sec to 300 microns at 50 mg/sec. The tank pressure is, of course, independent of whether the gas flow passes through the engine or through the tank wall.

With reference to table II, there appears to be little significant variation in either voltage or thrust as the gas flow is switched from the engine to the tank wall. At a current of 500 amps, the measured thrust (T_{in}) for gas flow through the engine increases from 42 grams to 55 grams as the hydrogen flow rate increases from 10 to 50×10^{-3} gm/sec; under the same current conditions and over the same mass flow range, the measured thrust (T_{out}) for vacuum tank injection remains constant at about 42 grams. The difference in behavior might be accounted for simply on the basis of the aerodynamic thrust mechanism. However, as indicated previously, overall there is little significant difference in either engine thrust or voltage behavior as the gas flow is switched-off from the engine and introduced through the tank wall.

TABLE II
COMPARISON OF MPD ARC JET VOLTAGE AND
THRUST FOR PROPELLANT INJECTION THROUGH THE ENGINE
AND PROPELLANT INJECTION OUTSIDE THE ENGINE

Hydrogen Flow Rate	Arc Current	Tank Pressure	Arc* Voltage		Arc** Thrust	
\dot{m} (mg/sec)	I (amperes)	P_{tank} (microns)	V_{in} (volts)	V_{out} (volts)	T_{in} (grams)	T_{out} (grams)
20	500	100	62	58	42	42
30		200	72	55.5	45	36
50		300	78.5	61.5	55	42
10	800	100	60	66	70	78
30		200	70	63	75	73
30	1100	200	69.5	74	106	96

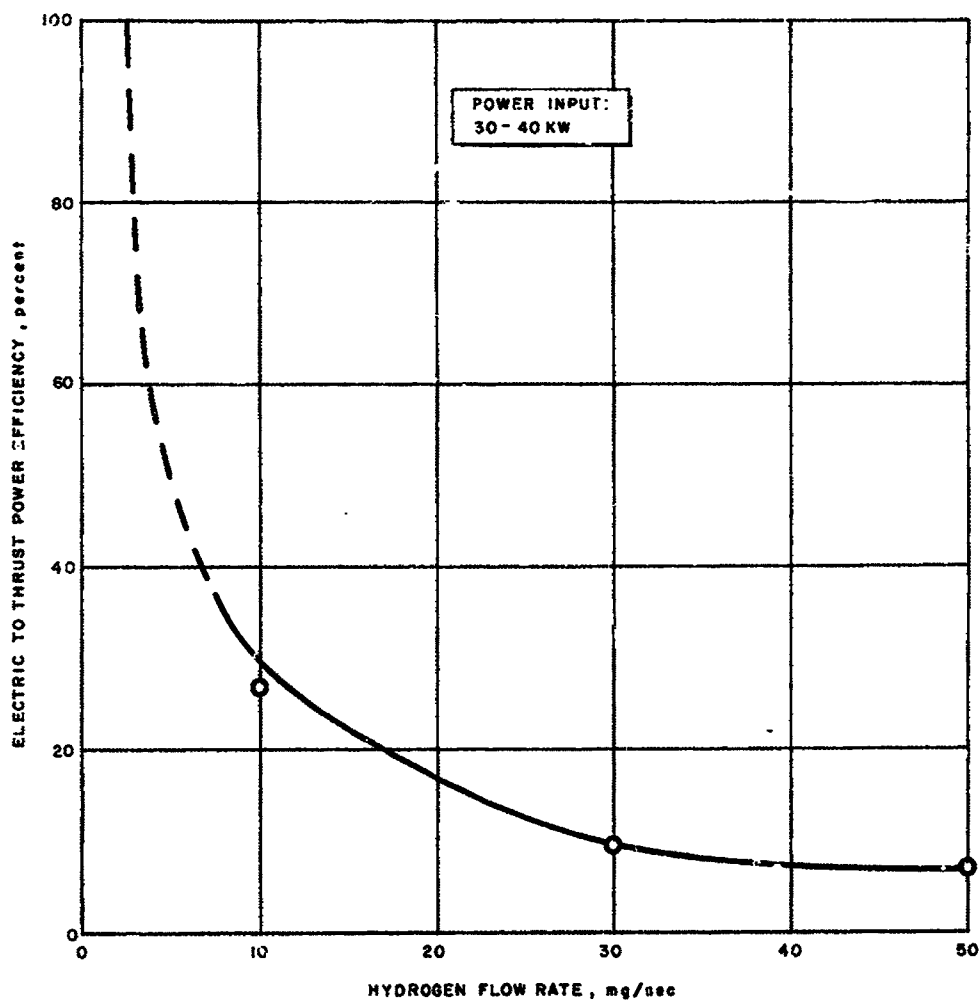
* V_{in} - Voltage with flow through engine

V_{out} - Voltage with flow through tank wall

** T_{in} - Thrust with flow through engine

T_{out} - Thrust with flow through tank wall

Figure 45 presents a curve of measured overall energy conversion efficiency as a function of hydrogen flow. The overall efficiency is based on the measured flow rates, engine thrust levels, and input current and voltages shown in table II. Based on the measured flow rate the overall efficiency exceeds 100 percent at a mass flow equal to about 3×10^{-3} gm/sec. Thus, at a current of 500 amps and a nominal value of back pressure equal to 100 microns, at least 3×10^{-3} gm/sec must be entrained into the MPD arcjet acceleration region for the condition of no gas flow through the engine. If this were not the case, there would no longer be conservation of energy.



65-4875

Figure 45 MEASURED OVERALL ENERGY CONVERSION EFFICIENCY VERSUS HYDROGEN FLOW RATE

3. Observations on Engine Operation in a Closed Tank

In the next experiment the input mass flow was reduced to zero and the vacuum pump was cut out of the system by means of a shut-off valve. No gas entered or left the system except through minor leaks in the vacuum tank and associated piping. The engine continued to operate stably at ambient pressures as low as 20 microns, and for periods of time of the order of 1 hour. Similar observations on stable MPD arcjet operation in a closed test chamber, with no gas flow passing through the engine, have been reported by Hess and Brockman²⁰ at NASA, Langley. In these experiments stable engine operation was obtained in an argon atmosphere at pressures as low as 0.10 micron back pressure.

4. Observations on Engine Operation in Different Gaseous Atmospheres

The engine was operated with nitrogen flow passing through it while hydrogen was admitted through the vacuum tank wall; the vacuum pump was operative so that the ambient pressure was held constant. The exhaust jet showed characteristic nitrogen radiation until hydrogen was introduced into the tank; the visible jet then gradually began to show hydrogen radiation starting at its downstream end; as the hydrogen concentration in the tank increased, the characteristic hydrogen radiation moved upstream to within about one inch of the nozzle exit plane. The test was performed again, in this case with hydrogen flow through the engine and nitrogen through the side of the tank; the results were equivalent; that is, the jet was initially pure hydrogen. However, as the nitrogen concentration in the tank increased the nitrogen concentration in the jet appeared to increase.

5. Observations on the Behavior of a Thrust Plate in the MPD Arcjet Exhaust

Finally, a small, thin tungsten wafer was lowered on a fine tungsten wire into the exhaust jet immediately downstream of the nozzle exhaust plane. With no mass flow through the engine, a definite eddy pattern was observed, i. e., from the observed deflection of the tungsten wafer, in the flow. At large radial distances from the engine axis the wafer hung motionless; as it was lowered towards the axis, from its initial position above the axis, it reached a region where it was violently pushed upstream towards the nozzle exit plane. As it was lowered further, it was violently pushed downstream away from the nozzle exit plane. Thus, for the zero mass flow condition there was clear evidence of a strong eddy ingesting gas into the engine and sending it out along the axis.

As the mass flow through the engine was increased, the eddy began to weaken until at mass flows greater than 5×10^{-3} gm/sec evidence for the eddy disappeared. It is important to note, however, that even at mass flow rates greater than 5×10^{-3} gm/sec there is evidence of gas entrainment in the main jet downstream of the engine.

These experiments indicate clearly that at the lowest mass flow rates, in the test facility now being used, the engine drew gas from the ambient environment and recirculated it. At mass flow rates greater than 5×10^{-3} gm/sec there is as yet no evidence that this occurs, but the gas mixture experiments do suggest that the ambient tank gas enters the exhaust jet in appreciable quantity as close as one inch downstream of the exit plane. If there is acceleration downstream of this point, the ambient gas can participate. The measured mass flow rates and overall values of energy conversion efficiency reported so far for the MPD arcjet are thus of questionable status until the question of entrainment is resolved.

6. Ambient Tank Pressures Required to Eliminate Gas Entrainment

An estimate can be made of the possible mass entrainment by considering the flux of particles from the surrounding environment which strike the surface of the jet. If the jet surface area is A (cm^2) the ambient pressure P (mm of Hg), and the sound velocity is c (cm/sec), then the mass striking the jet surface in unit time by random diffusion is

$$\dot{m}_e \approx nmcA/4. \quad (27)$$

Since, for fixed pressure, $c \sim \sqrt{T}$ and $m \sim T^{-1}$, \dot{m}_e varies as $T^{-1/2}$.

Assuming that the gas near the jet has a temperature $T \sim 300^\circ \text{K}$, then for hydrogen $c = 1.2 \times 10^5$ cm/sec, and nm , where n is the particle density and m the particle mass, is given by 9.25×10^{-5} gm/cm³ at atmospheric pressure. Thus, with P millimeters of mercury,

$$\dot{m}_e \approx 3.7 \times 10^{-3} P A \text{ gm/sec}. \quad (28)$$

It is not clear what value to use for A but it probably lies between 100 and 1000 cm^2 , based on the jet appearance. Hence

$$3.7 \times 10^{-1} P < \dot{m}_e < 3.7 P. \quad (29)$$

Values of the potential entrained mass flow are presented in table III.

TABLE III
MAXIMUM POSSIBLE VALUES OF ENTRAINED MASS
FLOW VERSUS AMBIENT PRESSURE

Ambient Pressure P microns	Max. Entrained Mass Flow ($A_e = 100 \text{ cm}^2$) milligrams/sec	Max. Entrained Mass Flow ($A_e = 1000 \text{ cm}^2$) milligrams/sec
1000 (1 mm of Hg)	370	3700
100 (10^{-1} mm of Hg)	37	370
10 (10^{-2} mm of Hg)	3.7	37
1 (10^{-3} mm of Hg)	0.37	3.7
0.1 (10^{-4} mm of Hg)	0.037	0.37

To eliminate potential gas entrainment effects in the power range from 1 to 50 kw, the ambient pressure must have a value such that the maximum potential entrained mass flow, i. e., $\dot{m} = c_m A$ is less than 1 mg/sec. The ambient pressure must, therefore, be less than 10^{-4} mm Hg (0.10 microns).

Several speculative comments may be made at this point:

- a. Reduction of the mass flow does not help to reduce the entrainment fraction unless the jet area is reduced.
- b. At pressures greater than 10 microns the potential magnitude of the entrained gas flow is comparable to the engine mass flow for engines operated in the range from 1 to 50 kw.
- c. In the situation of no-gas flow through the engine, it can be speculated that the thrust level will remain approximately constant and the entrained gas flow will decrease as the ambient pressure is reduced. Thus, since, with decrease in pressure level, the quantity of accelerated gas flow decreases, the thrust power, i. e., T^2/\dot{m} will increase, and there will be a corresponding increase in arc voltage.

d. The crucial question pertains, of course, to the extent to which gas entrainment invalidates the existing overall efficiency versus specific impulse data on the MPD arcjet. It is likely that at the higher values of specific impulse (i. e., 10,000 seconds for H_2) and correspondingly the lower values of mass flow, considerably more flow was being accelerated by the engine than passed through the engine flow-meter. The existence of extra entrained mass flow would probably tend to leave the thrust level unchanged, but would reduce the operating voltage below the no-gas entrainment value. Thus, the presence of gas entrainment can lead to higher estimated values of the energy conversion efficiency than would be obtained if the engine were operating in the hard vacuum of space. The extent of this performance deterioration can only be determined empirically.

E. ALKALI METAL OPERATION--WATER-COOLED

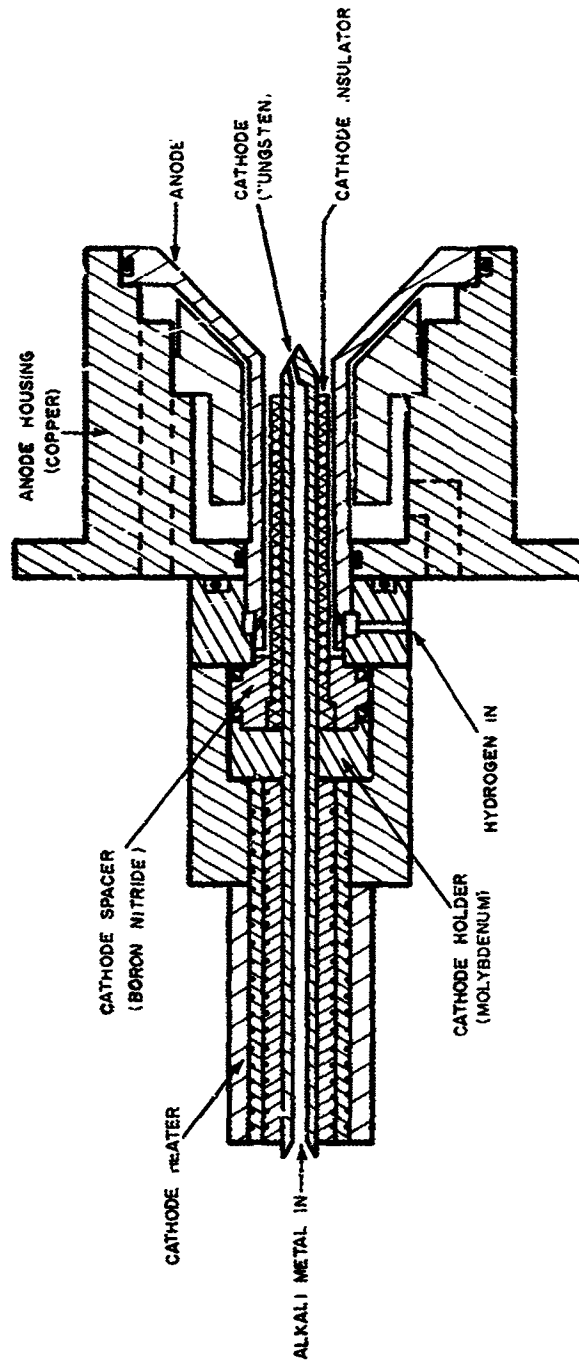
The most promising technique for reducing the pressure in the test chamber and thereby reducing the potential amount of entrained propellant is the use of easily condensable propellants such as the alkali metals, e.g., cesium and lithium, in conjunction with a cryogenic pumping system. The alkali metals, moreover, are attractive in their own right as MPD arcjet propellants because of their relatively high frozen flow efficiencies.

1. Engine Configuration

The basic plasma accelerator designed for water-cooled alkali metal operation is shown in figure 46. As in the X-2C engine, the unit is cylindrically symmetric. It consists of a central tungsten cathode surrounded by a coaxial, water-cooled, copper anode. A magnetic field coil is mounted coaxially with the thruster and produces an external magnetic field with axial, B_z , and radial, B_r , magnetic field components.

For operation with the alkali metals, the cathode is fabricated from 1/4-inch diameter tungsten rod, drilled out to a 1/8-inch diameter almost to its tip, and insulated from the anode by a boron nitride tube. Near the tip, three symmetrically placed, 0.075-inch diameter holes are drilled, each making a 25-degree angle with the cathode axis, and meeting at its center (see figure 46). The cathode is then an integral part of the propellant feed system.

The anode is water-cooled copper. Propellants other than the alkali metals are injected tangentially through four ports in the anode, which are aligned normal to the engine axis (see figure 46) and which are presently used for starting. A boron nitride tube is press-fitted into the anode, and insulates it electrically from the cathode, preventing attach-



65-10587

Figure 46 SKETCH OF LIQUID COOLED MPD ARCJET USED WITH CESIUM

ment of the discharge to the inside surface. A water flow rate of the order of 6 GPM is maintained through the anode to cool the copper.

The external magnetic field coil consists of 40 turns of 5/16 o.d. copper tubing, and is water cooled. It has an inner diameter of 3-1/8 inches, an outer diameter of 8 inches, and is 2 inches long. Figure 47 shows a mapping of the magnetic field distribution for a coil current of 400 amps. Each arrow represents a measured value of the magnetic field strength at that excitation current. The arrow length is proportional to the magnetic field strength, and its direction is that of the field at the point. The dashed lines of figure 47 have been sketched in using the measured values as guides. The field strength exhibits the expected linearity with excitation current, as shown in figure 48. The peak axial field strength at the cathode tip is of the order of 3 kgauss.

As in previous MPD arcjet tests, the thruster and its auxiliary magnetic field coil are mounted on a liquid-cooled thrust stand. Measurements are made of the engine thrust, arc current, power removed by the anode cooling water, vaporizer pot temperature, and ambient tank pressure.

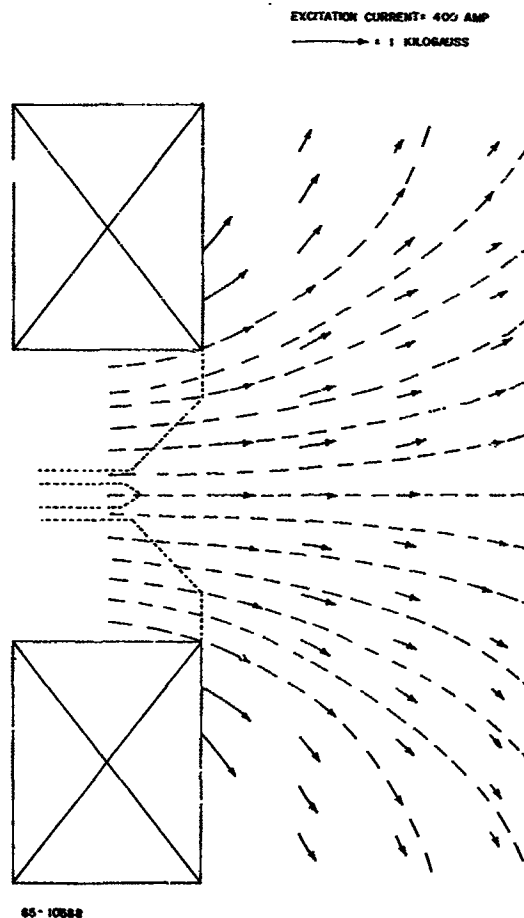
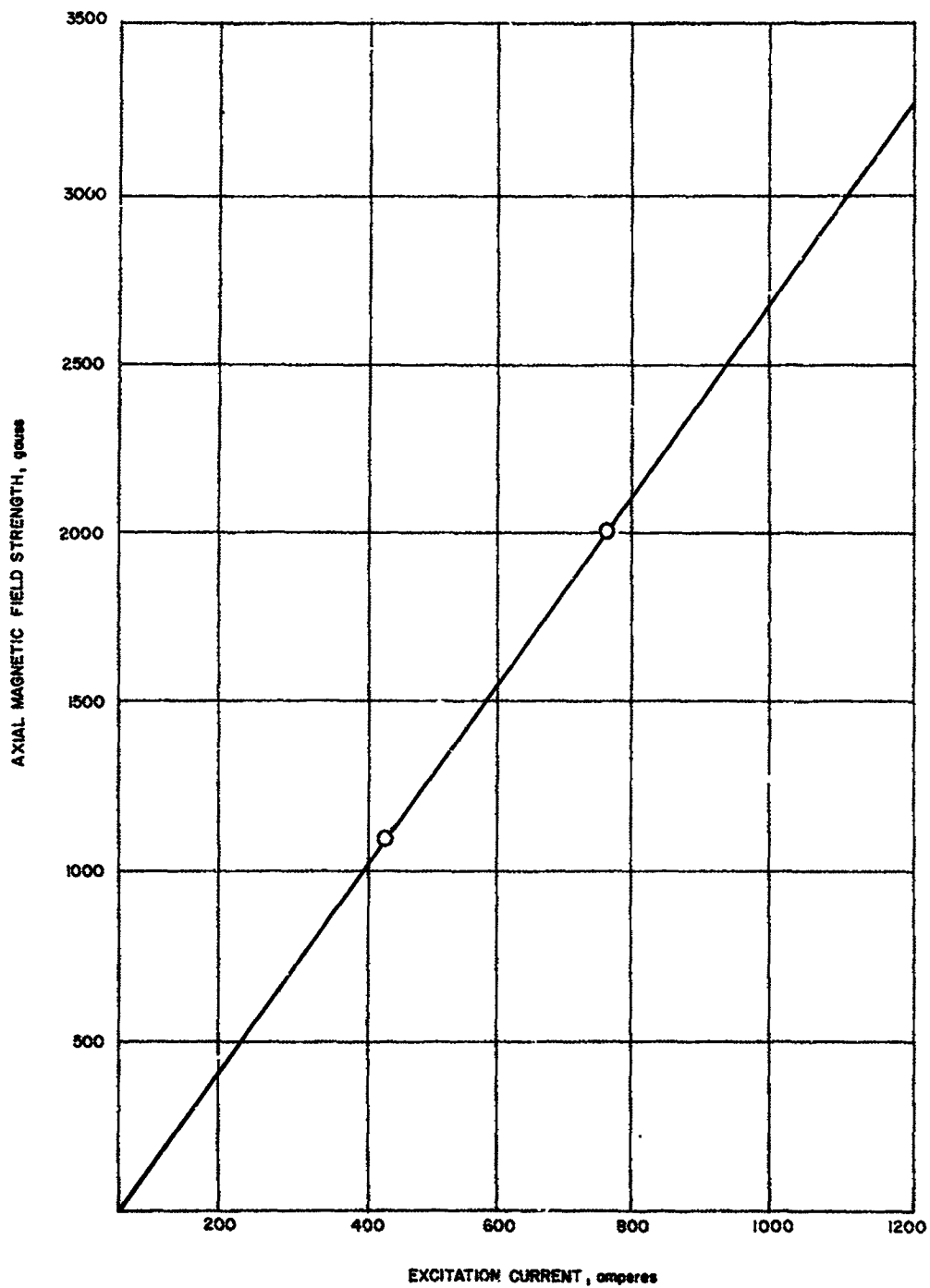


Figure 47 MAP OF MAGNETIC FIELD USED WITH CESIUM MPD ARCJET



65-10589

Figure 48 FIELD STRENGTH VERSUS CURRENT FOR MPD ARCJET MAGNET

2. Feed System

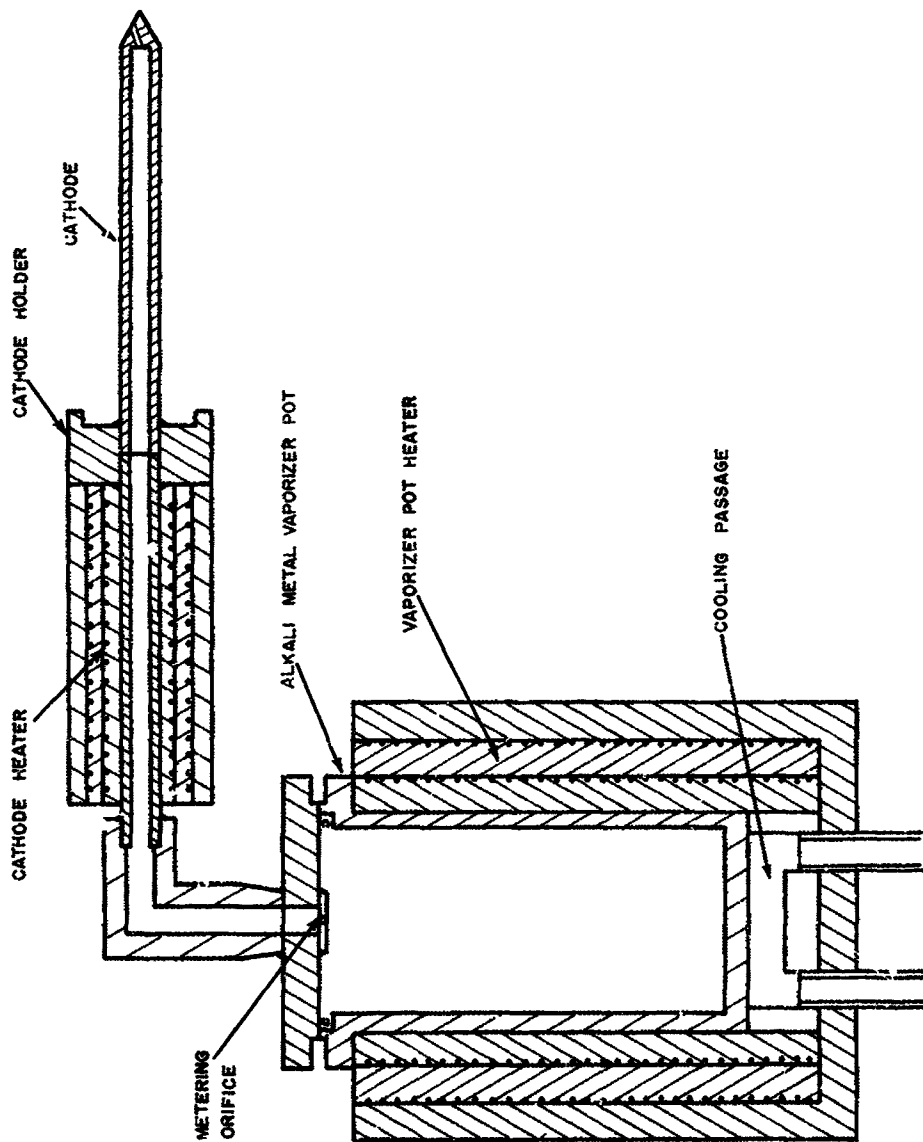
The feed system which has been used consists of a hot liquid metal reservoir (vaporizer), a metering orifice, and a heated tube for connection to the engine cathode.

The liquid metal reservoir consists of a stainless steel closed pot which has a 1-1/4 inch inside diameter and is 2-7/8 inches deep (figure 49). It is surrounded by a series of boron nitride mandrels which are wrapped with 30-mil diameter thoriated tungsten heater wire. Its base contains a region into which cool air or water may be run in order to rapidly cool the liquid metal to drop the vapor pressure. This serves to effectively reduce the mass flow rate to zero at the end of a test in a time which is very short compared with the running time, and thus allows calibration of the mass flow rate during engine operation.

The liquid metal in the vaporizer is maintained at an elevated temperature; for cesium, the temperature is in the range from 400 to 500 °C, while for lithium it is in the range from 900 to 1200 °C. The liquid metal temperature determines the vapor pressure in the vaporizer. The vaporizer cap includes a metering orifice of about 0.030-inch diameter and is welded to a 1/4-inch o.d. stainless steel tube which connects to the cathode. The stainless steel connecting tube is also surrounded by a series of boron nitride mandrels which are wrapped with 30-mil thoriated tungsten heater wire. The tube and the metering orifice are maintained at a temperature somewhat above that of the liquid metal by the use of separate heater supplies for the vaporizer and feed tube. This allows a given temperature (and thus pressure) to be maintained in the vaporizer, while the propellant is prevented from condensing in the feed tube by the still higher temperatures maintained there.

The propellant is loaded into the stainless steel reservoir in a glove box in which an argon atmosphere is maintained. The metering orifice is initially sealed with a drop of solder which melts at a temperature about 25°C below the desired operating temperature so that the propellant is not introduced until essentially the operating temperature (and thus the desired mass flow rate) is achieved. The vaporizer pot temperature and the feed tube temperature are measured with Chromel-Alumel thermocouples, an additional Iron-Constantan thermocouple imbedded in a stainless steel sheath is immersed in the liquid metal as an auxiliary measuring device.

The vapor pressure-temperature relation for cesium is shown in figure 50. The estimated mass flow rate is shown in figure 51 as a function of orifice diameter for an assumed discharge coefficient of 0.5. Measured values of the mass flow rate yield an experimental value for the discharge coefficient in the vicinity of 0.4.



65-10590

Figure 49 CESIUM VAPOR FEED SYSTEM

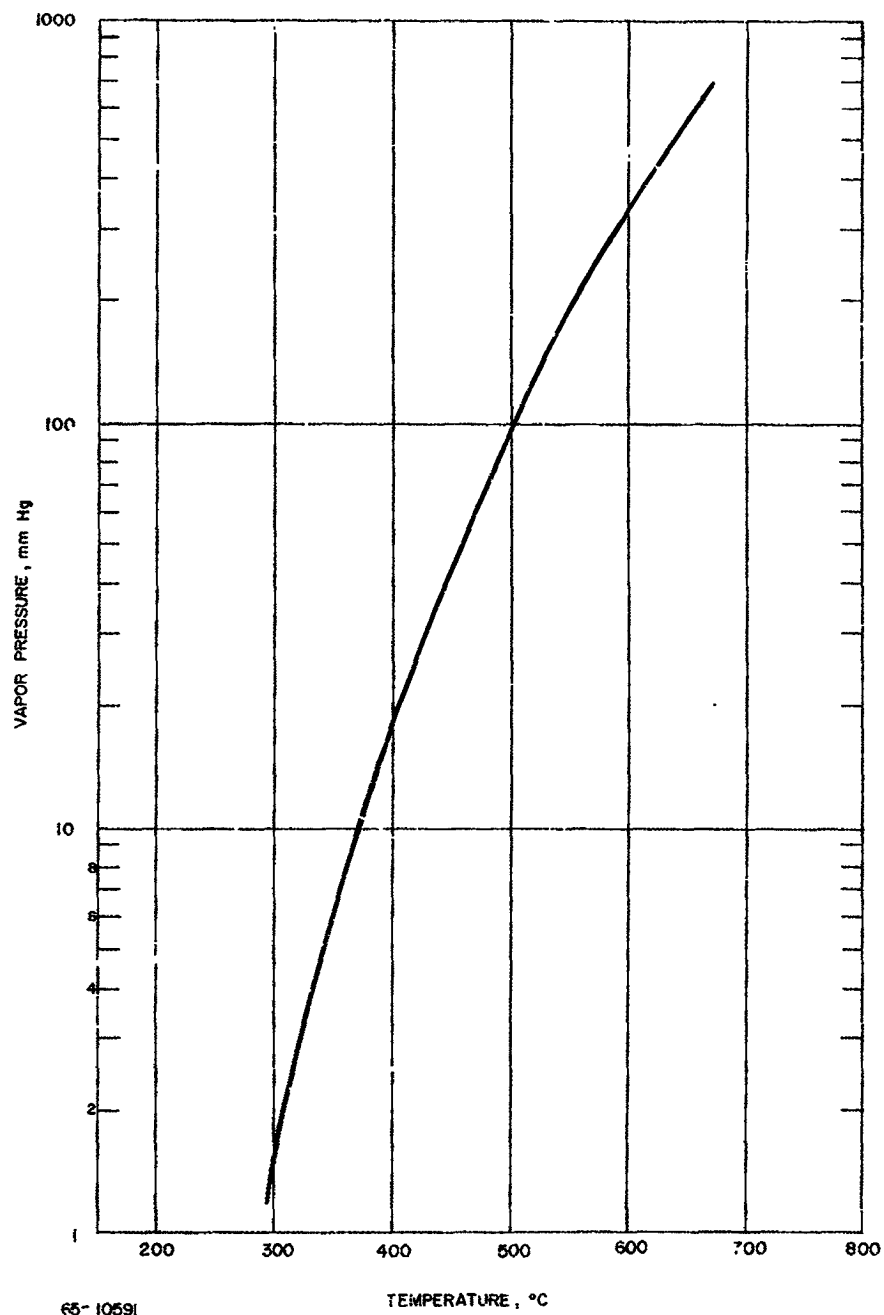
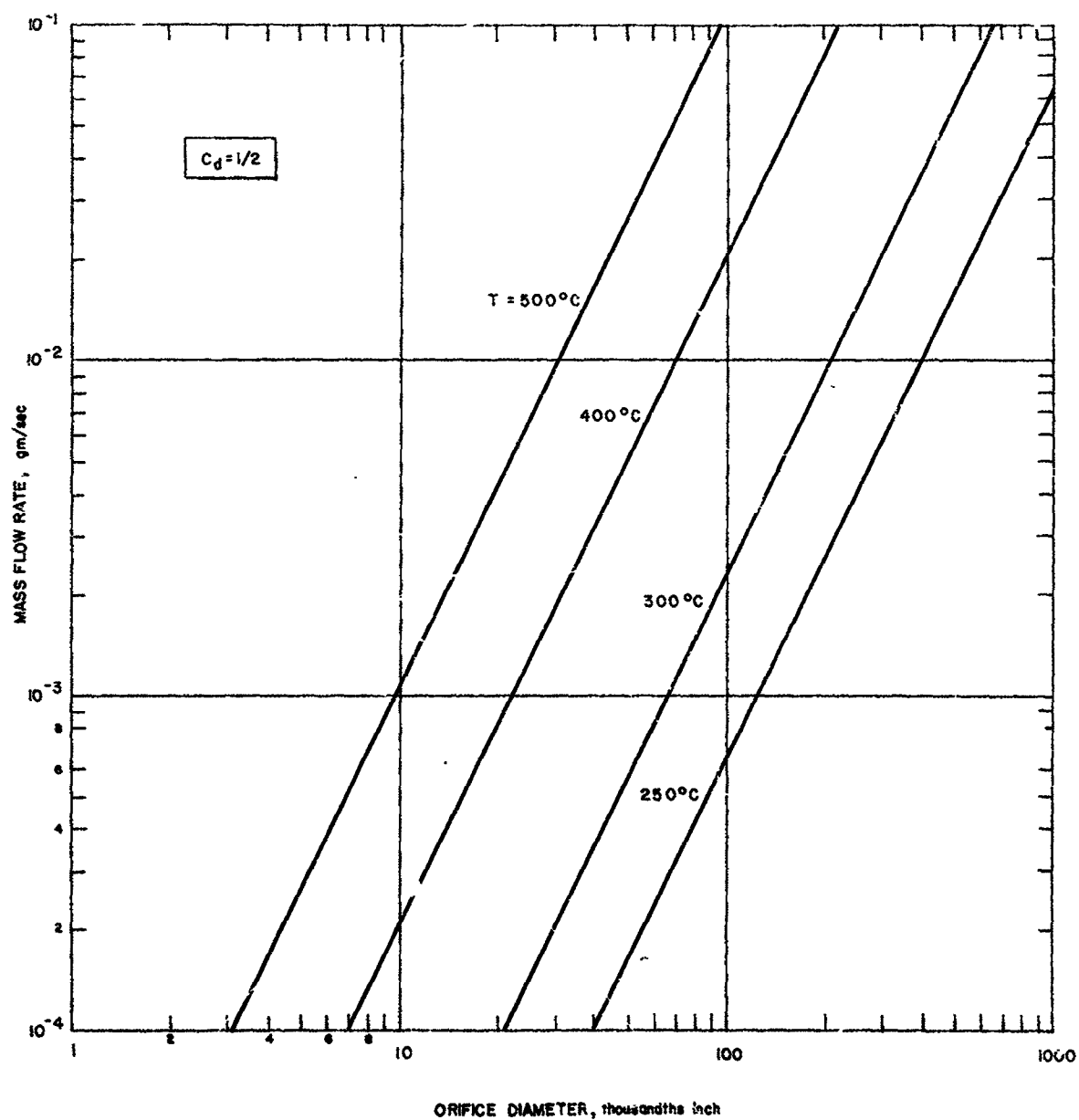


Figure 50 CESIUM VAPOR PRESSURE AS A FUNCTION OF TEMPERATURE



65-10592

Figure 51 ESTIMATED CESIUM MASS FLOW RATE AS A FUNCTION OF TEMPERATURE AND ORIFICE DIAMETER

9-1

The initial weight of propellant in the vaporizer pot is determined by weighing on a balance scale. The time at which cesium vapor begins to flow (solder plug melts) is recorded. By weighing the system again, the total cesium mass expended during the run is determined. The ratio of total mass expended to total time elapsed is taken as the average mass flow rate, at the average operating temperature. This average mass flow rate is then corrected for any temperature variations during the run by use of figure 51. As mentioned above, this method yields a value for the discharge coefficient of the order of 0.4.

3. Engine Operation

Operation of the engine with cesium is as follows. When the feed system has been brought up to a temperature of about 375°C, and the heater insulators have been allowed to outgas for some time, the line leading directly to the mechanical pump is opened and it pumps in parallel with the diffusion pump. The discharge is struck using hydrogen as propellant injected through the normal tangential ports, and the ambient pressure rises to about 200 to 300 microns. The arc current in the cathode combined with the system heaters raise the vaporizer pot temperature to about 385°C, at which point the solder plug melts and is blown out by the high internal argon pressure. (The argon pressure in the vaporizer is raised from the initial one atmosphere loading pressure to about 35 psi at the solder melting temperature.) Cesium begins to flow and the hydrogen flow is shut off. The direct line to the mechanical pump is closed and only the diffusion pump is effective. The ambient tank pressure rapidly (seconds) falls* to about 0.1 micron as the hydrogen is exhausted, and the liquid nitrogen baffle plate condenses the exhaust cesium vapor.

At the end of a run, the vaporizer pot heaters are turned off and cool air followed by water is used to lower the vaporizer temperature very rapidly to room temperature. This effectively reduces the cesium mass flow rate to zero.

4. Voltage Measurements

A series of measurements was made to determine whether the environmental test tank and/or the baffle plate were interacting with the engine. Specifically, tests were made to determine whether the tank was carrying a significant fraction of the total arc current -- a situation which would lead to erroneous engine performance measurements.

The voltages were measured using a Tektronix type D plug-in unit in conjunction with a Tektronix oscilloscope. During cesium operation, the

* As measured by an ionization gauge. The effect of cesium on the accuracy of this gauge is uncertain.

cathode-to-tank voltage was of the order of 10 to 20 volts; the remaining 50 to 80 volts between anode and cathode was present between the anode and tank. Various resistors were then connected between the cathode and tank to determine the "resistance" of this path and thus the current flow through the electrical path consisting of anode-plasma-tank-plasma-cathode. This "resistance" was measured to be of the order of 500 ohms. This corresponds to a current flow of about 25 milliamps (for a 12.5-volt drop between cathode and tank). The total arc current was about 100 amps. The tank circuit thus carried less than 1/10 of 1 percent of the total arc current.

During the performance of the above tests, several observations were made which are, as yet, not fully understood. When the engine was running on hydrogen as propellant, the tank potential was about halfway between the anode and cathode. As the engine warmed up, the tank potential came closer to that of the cathode, the cathode-tank potential difference falling from about 50 volts to about 25 volts. As the cesium began to flow, the cathode-tank potential difference dropped even further to about 15 volts.

Another, and possibly more interesting observation was also made on the difference between a hydrogen and cesium operation. When the engine was operated with hydrogen, the oscilloscope trace of both cathode-tank and anode-tank voltage differences was essentially flat, that is, any ripple present was several orders of magnitude smaller than the voltage differences themselves. On the other hand, two distinctly different voltage patterns were seen with cesium. In neither case was the ripple small. In one case, which corresponded to a large cathode-anode voltage difference (~ 100 volts), the anode-tank voltage difference showed no ripple whereas the cathode-tank voltage was on the order of 10 to 20 volts with a ripple of about ± 100 percent at a "frequency" of about a megacycle per second. In the other case, corresponding to an anode-cathode voltage difference of about 60 volts, the cathode-tank voltage difference was constant; the anode-tank voltage difference was, however, about 50 to 60 ± 10 percent volts, also at a frequency of the order of a megacycle.

5. Propulsion Performance

The liquid-cooled MPD arcjet engine described above has been operated with cesium as the propellant. A typical test lasts between 30 minutes and 60 minutes. Electrode erosion is insignificant. A table listing measured performance results is given in appendix D. With reference to this table and to the discussion which follows, it should be pointed out that the input power to the device is calculated as the product of arc current and arc voltage; power supplied to the magnet and power used to vaporize the cesium in the boiler pot are not included. The major reasons for this are that (1) it is not yet clear what sort of magnetic field is optimal,

and it is possible that the optimal magnetic field may be such that it can be supplied by a permanent magnet; (ii) no attempt has been made to optimize the boiler pot configuration; and (iii) at this stage of engine development it may obscure important trends in arc efficiency to lump all input power together.

The engine operation with cesium vapor has been fairly straightforward. With the exception that the metering of mass flow rate must be handled differently, the operation in cesium has been essentially like that with ordinary gases. Figure 52 is a photograph taken from outside the test tank during operation with cesium. The magnet coil is seen on the left side of the picture, as well as the engine exit plane. There is a central core of intense illumination issuing from the center of the exit plane and extending downstream approximately two feet. A coaxial zone of less intense illumination surrounds the central core. The outer boundary of this less intense zone is shaped essentially like a magnetic field line. These major features of the exhaust appearance are always present, although the absolute intensity of each zone, the length of the central core, etc., are functions of the operating conditions. For the photograph, the arc current was 135 amp, the voltage 70 volts, the magnetic field strength 2.15 kgauss, the cesium mass flow rate 6 mg/sec, and the ambient pressure 0.1 microns.

The voltage of the cesium MPD arcjet appears to be magnetic field dependent, as was the case with the ordinary gases tested earlier. Figure 53 shows the measured arc voltage for currents ranging from 70 to 140 amp and for cesium flow rates ranging from 3.5 to 6 mg/sec, as a function of magnetic field strength from 660 to 3300 gauss. There is a considerable scatter of the data points, with the voltage varying from about 60 volts to 120 volts at one magnetic field strength, 2200 gauss. Still, there is a trend to the data of increasing voltage with increasing magnetic field. A straight line has been drawn on figure 53, but the data scatter is such as to make a quantitative estimate of the slope rather uncertain. It does appear that if the voltage behavior of this engine with cesium is to be explained on the basis of the critical-velocity hypothesis of Patrick and Schneiderman,²³ the characteristic length which must be associated with the field-plasma interaction is extremely large -- on the order of one meter. If instead the characteristic length is of the order of one centimeter, as was the case for the ordinary gases used earlier, then the velocity arising from the slope of figure 53 is about two orders of magnitude higher than the critical velocity. Alternatively, the critical velocity can be redefined to include energy for multiple ionization; this would tend to bring the measured voltage-magnetic field slope closer into line with the critical velocity, but attempts to do this are postponed until better evidence is available to determine the slope and the degree of ionization.

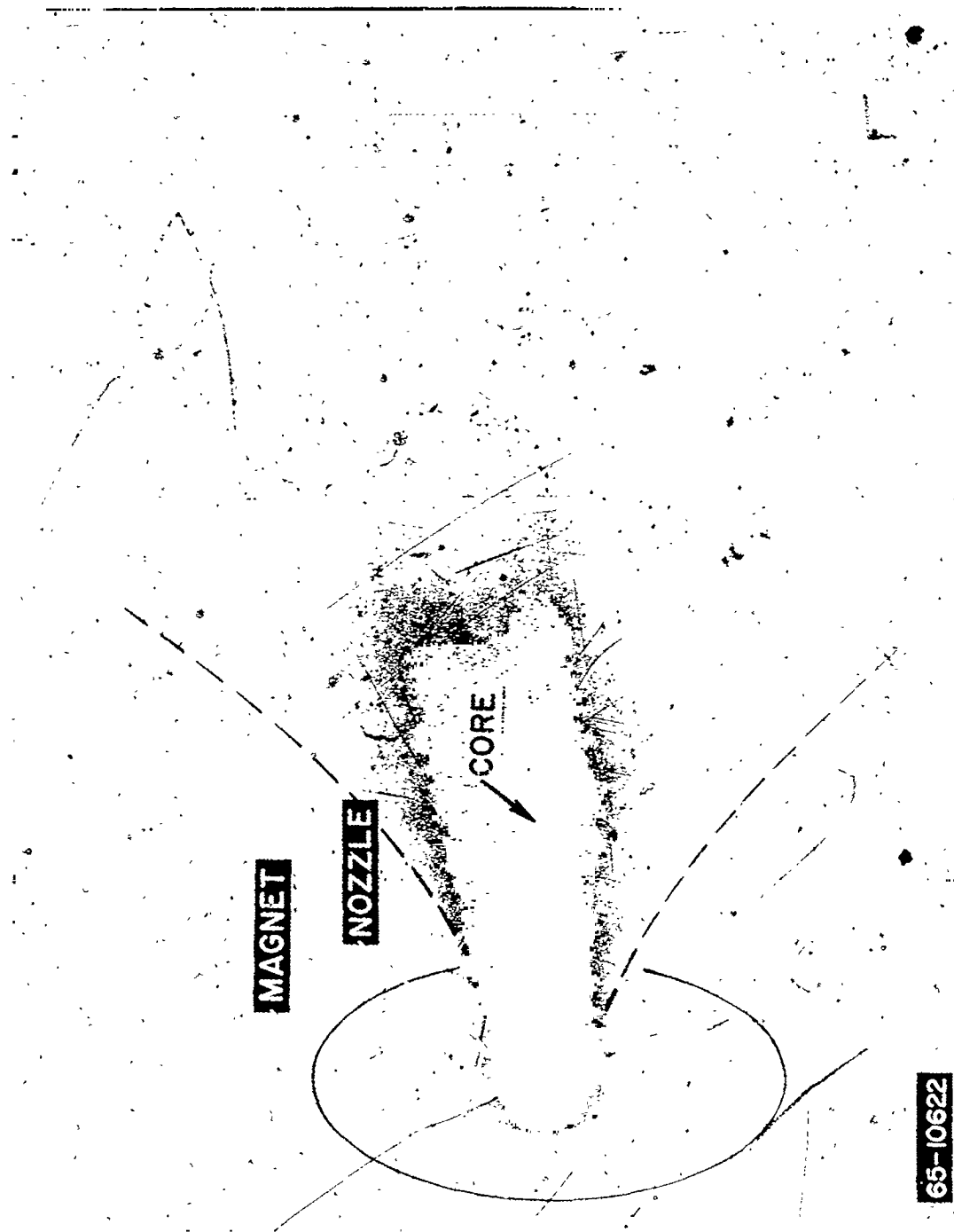
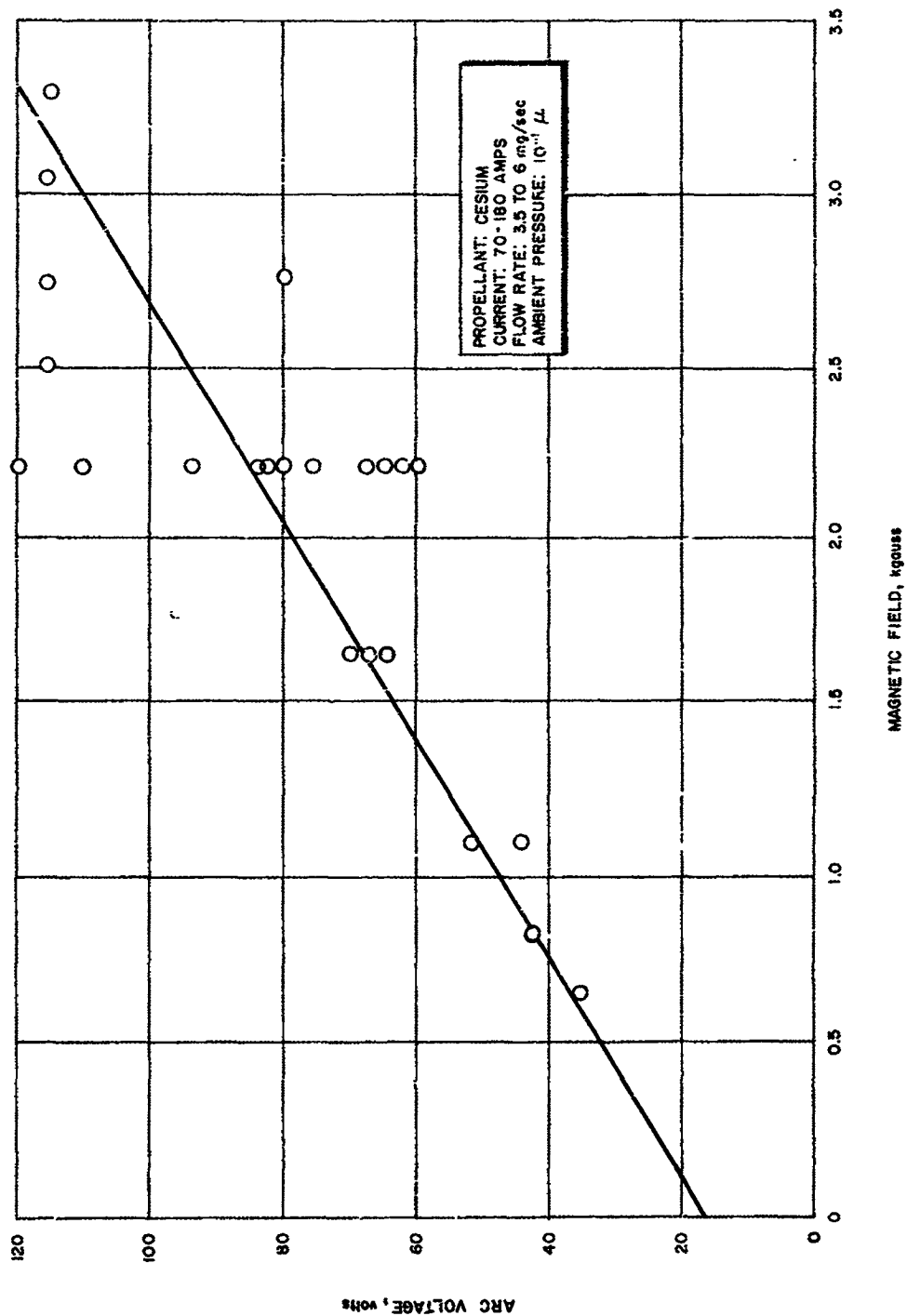


Figure 52 PHOTOGRAPH OF MPD ARCJET OPERATING WITH CESIUM

65-10622



65-10594

Figure 53 ARC VOLTAGE VERSUS MAGNETIC FIELD STRENGTH FOR CESIUM OPERATION

The power lost to cooling water during operation with cesium is plotted as a function of current in figure 54. Previous results with the ordinary gases had indicated that the power lost to cooling water in MPD engine operation correlated well with current; it appeared that the losses could be accounted for by a constant voltage drop of approximately 25 volts associated with the electrode fall regions. This is not the case for the data of figure 54. The power lost to cooling (in this case, exclusively the anode since the cathode is not cooled) is a relatively weak function of current, rising from about 5.5 kw at currents of the order of 75 amps to about 7 kw at currents of the order of 175 amps*. Since the input power levels for these data were always in the near neighborhood of 10 kw, the arc efficiency, defined as the ratio (power to the gas)/(power input to the arc) is rather low, being typically about 30 to 40 percent.

Figure 55 is a plot of overall engine efficiency as a function of specific impulse for the data obtained with cesium. All the data points are plotted to the same scale, so that there are represented a magnetic field range of 0.5 to 3.3 k gauss, a current range of 70 to 180 amp, a voltage range of 35 to 120 volts, and an input power range of 5 to 10 kw. The ambient pressure in the vacuum tank was in all cases between 0.05 and 0.2 micron, and the arc efficiency varies between approximately 22 and 38 percent.

According to figure 55, the efficiency is a linear function of the specific impulse, passing through the origin of coordinates and rising approximately 4.5 percent for each 1000 seconds of specific impulse. Sufficient data have been accumulated in the range of specific impulse from 1000 to 3000 seconds to make this correlation fairly firm.

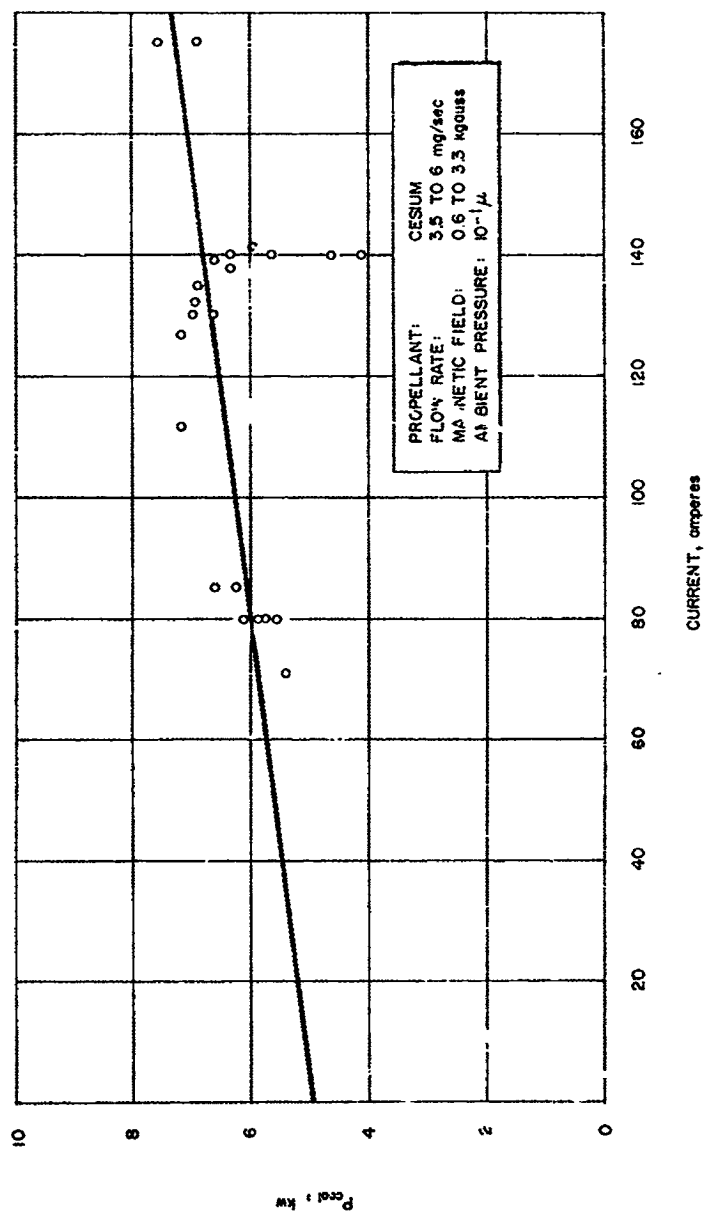
An interesting correlation is observed in figure 56. Here the ratio of overall efficiency to arc efficiency is plotted as a function of magnetic field strength. An acceleration efficiency can be defined by.

$$\epsilon_{acc} = \frac{\text{Thrust Power}}{\text{Power to Gas}}$$

such that the overall efficiency is given by

$$\epsilon_o = \epsilon_{acc} \epsilon_{arc}$$

* The cooling power can also be correlated with IB, the product of arc current and magnetic field strength. It is not yet clear what significance this has.



65-10595

Figure 54 ANODE HEATING POWER VERSUS CURRENT

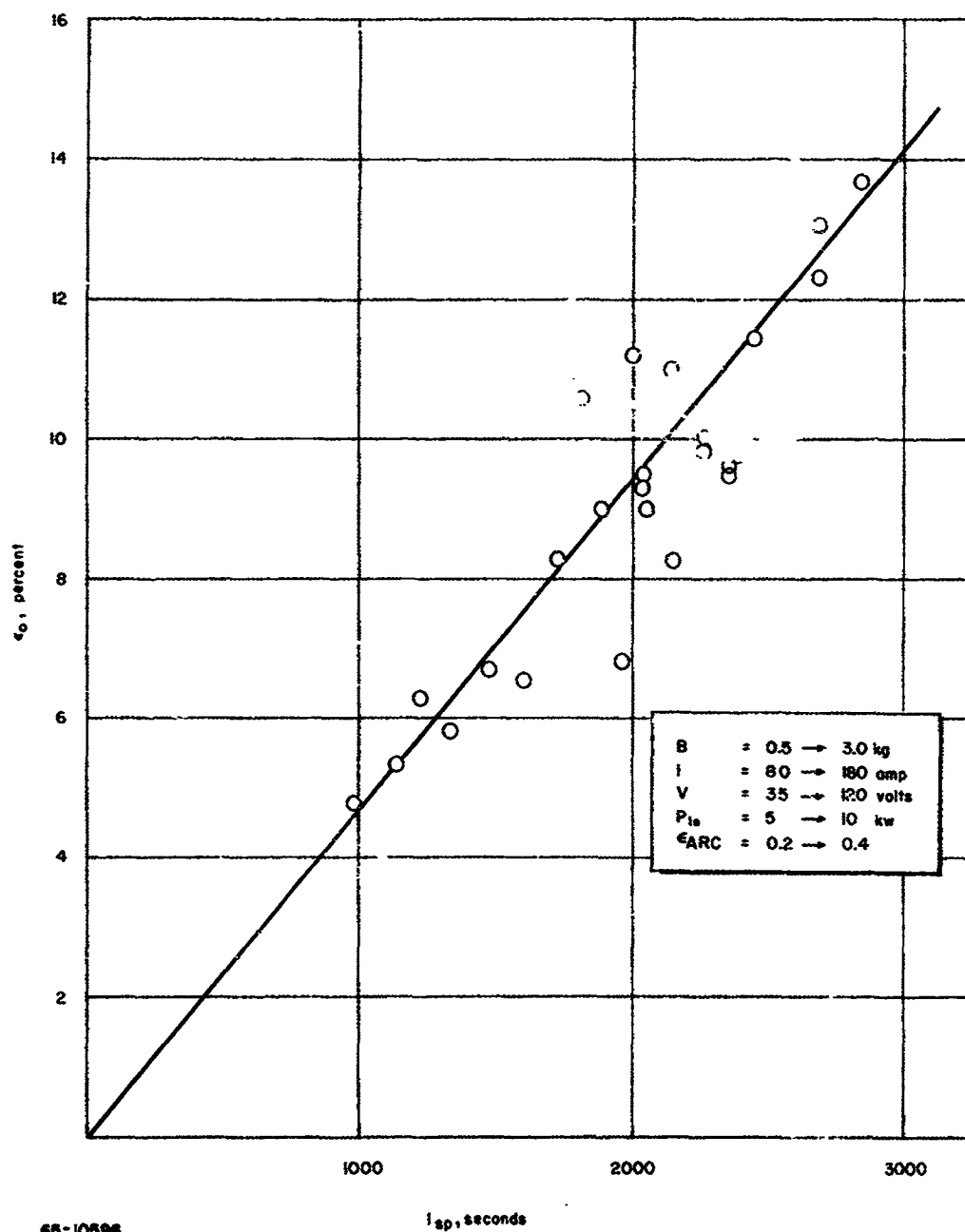


Figure 55 EFFICIENCY VERSUS SPECIFIC IMPULSE FOR CESIUM

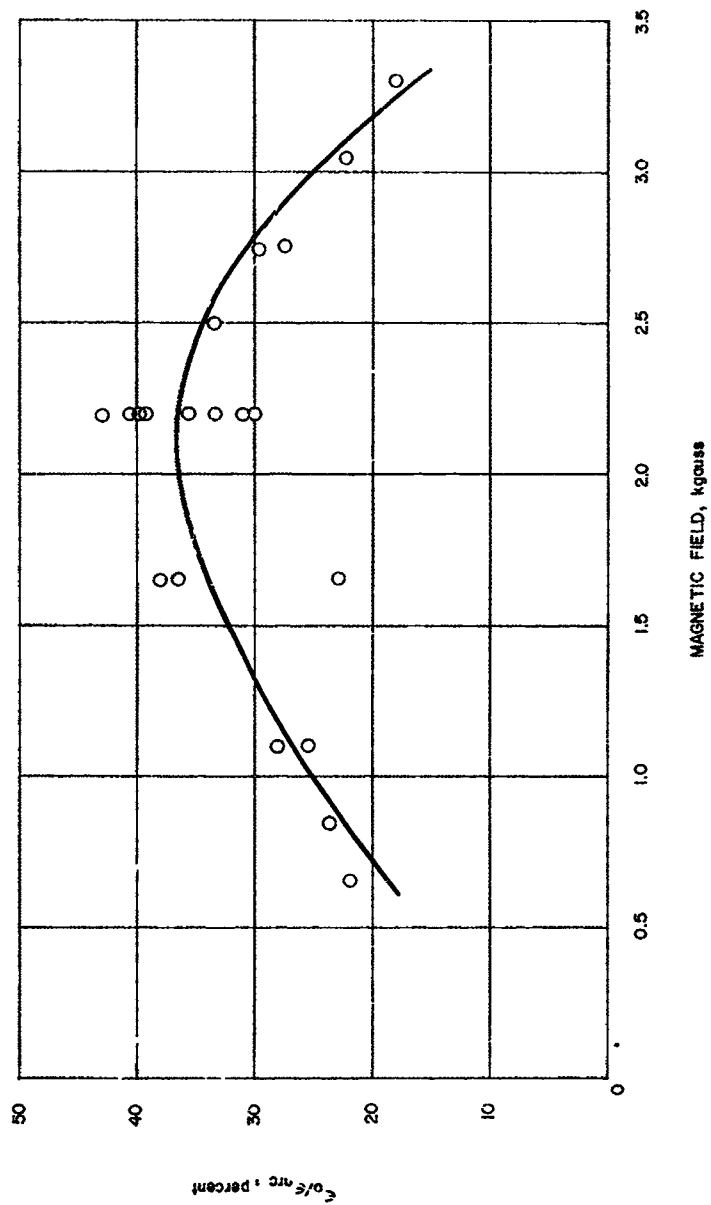


Figure 56 RATIO OF OVERALL EFFICIENCY TO ARC EFFICIENCY AS A FUNCTION OF MAGNETIC FIELD STRENGTH

65-10597

Hence,

$$\epsilon_{acc} = \epsilon_o / \epsilon_{arc}$$

and the ratio of overall efficiency to arc efficiency is the acceleration efficiency. According to figure 56, this acceleration efficiency shows a variation with magnetic strength, achieving a maximum at a field strength of approximately 2 kgauss for the engine and magnet configuration employed here. Under the best conditions the acceleration efficiency is 40 percent while at the worst it is less than 20 percent. Some caution should be observed at this time with regard to this optimum; the data points at magnetic field strengths greater than 2.2 kgauss were all taken with one value of cesium flow rate and arc current, and there may be some characteristic of operation with this flow rate and current which produces a falloff in acceleration efficiency with magnetic field strength. More data are necessary to resolve this uncertainty.

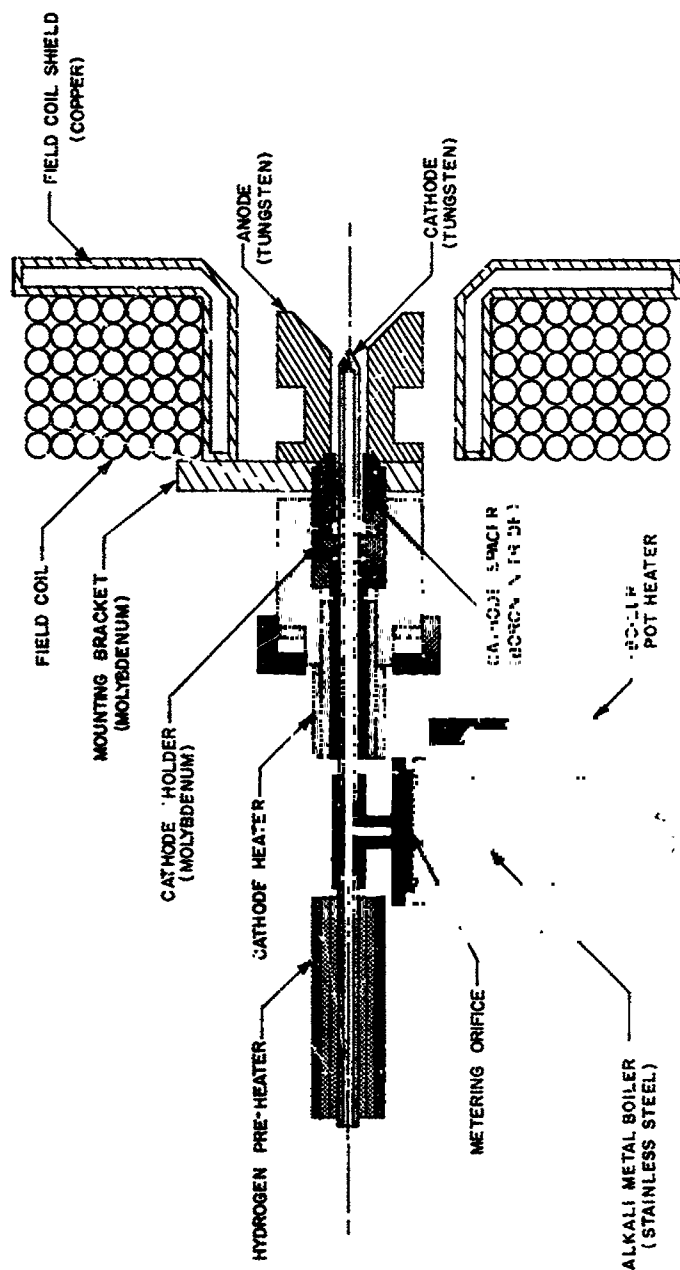
F. ALKALI METAL OPERATION--RADIATION-COOLED

1. Engine Configuration

The successful operation of water-cooled MPD arcjet engines with alkali metal propellants has led directly to testing of radiation-cooled engines of similar geometric configuration. With increased anode operating temperatures and the possible increase in thermal efficiencies, the overall or propulsion efficiencies at given specific impulse should increase as well.

The initial radiation-cooled engine to be operated at this laboratory using cesium as propellant, with essentially the same cathode injection and feed system as were used with the water-cooled engines, is shown in figure 57. The anode is fabricated from a thoriated tungsten cylinder. The starting gas (hydrogen) is injected through the cathode and is preheated by a four-inch heater. The heater consists of several mandrels of boron nitride surrounding the 1/4 inch o. d. hydrogen feed line and wrapped with about 12 feet of 30-mil thoriated tungsten heater wire. The hydrogen is preheated so that the jointure with the cesium feed line (see figure 57) is not cooled to a temperature below that of the vaporizer pot. This prevents the condensation of the cesium vapor in the feed line which would cause sporadic operation of the engine and "spitting" of droplets of liquid cesium.

For radiation-cooled operation, the magnetic field coil is shielded from the exhaust jet by a water-cooled copper jacket. There is no physical contact between the anode surface and the coil jacket, so that the anode is not cooled by thermal conduction to the jacket. The magnetic field coil has an inner diameter of 4-1/4 inches, an outer diameter of 9 inches, is 2 inches



MPD ARC JET - RADIATION COOLED

65-10396

Figure 57 SKETCH OF RADIATION-COOLED MPD ARCJET USED WITH CESIUM

long, and made up of 41 turns of 5/16 inch o.d. copper tubing. The power removed from the field coil jacket coolant is measured with a chromel-alumel differential thermopile.

Because the mass flow in the initial feed system depended upon the pressure of the vapor in the vaporizer pot, it was necessary that the vaporizer temperature be controlled within rather narrow limits in order to obtain a constant, accurately determined, mass flow. The initial system was replaced by the system shown in figure 57a. The vaporizer pot is used merely to maintain the propellant in a liquid state. The argon pressure above the liquid may be varied at will, and the mass flow is directly proportional to this pressure. A large argon reservoir is connected in parallel with the vaporizer pot to maintain a constant pressure once the pressure value has been selected. The fine tungsten wire (~5 to 10 mils) is inserted in the feed tube (~25 mils i.d.) to prevent the propellant from entering the cathode cavity in a series of drops. The propellant is allowed to "run down" the wire, in liquid form touch the hot cathode, and vaporize. It then enters the engine anode region as a vapor.

2. Propulsion Performance

Both cesium and lithium have been used as propellants in the radiation-cooled MPD arcjet, and some data have been obtained for each propellant. The engine operation with lithium has been far smoother than with cesium; with the latter propellant, perhaps because of inadequate mass flows to produce sufficient particle densities in the acceleration region, engine operation was characterized by sporadic erosion of the cathode and the cathode insulator. As a result, it was not possible to produce a set of systematic propulsion data of accuracy comparable to the data obtained with the liquid-cooled engine. However, it has been possible to compare certain operating points obtained with the radiation-cooled engine; although the comparison is subject to the scatter and inaccuracies of the data obtained in the radiation-cooled engine, it appears that the two sets of data are consistent. At power levels up to 5 kw kilowatts (approximately 40 volts at 120 amperes) peak I_{sp} values of almost 3000 seconds were reached with overall efficiencies of 15 percent. It is stressed that these data are badly scattered, and they are not tabulated here because of the uncertainties attached to them. The situation is much improved with lithium operation.

Performance data obtained with the radiation-cooled alkali metal MPD arcjet using lithium as propellant are listed in the table of appendix F. Figure 58 shows a plotting of overall efficiency versus specific impulse for this lithium fueled engine. Although the scatter in the measured values is appreciable, the data may be fit by the straight line drawn on the figure.

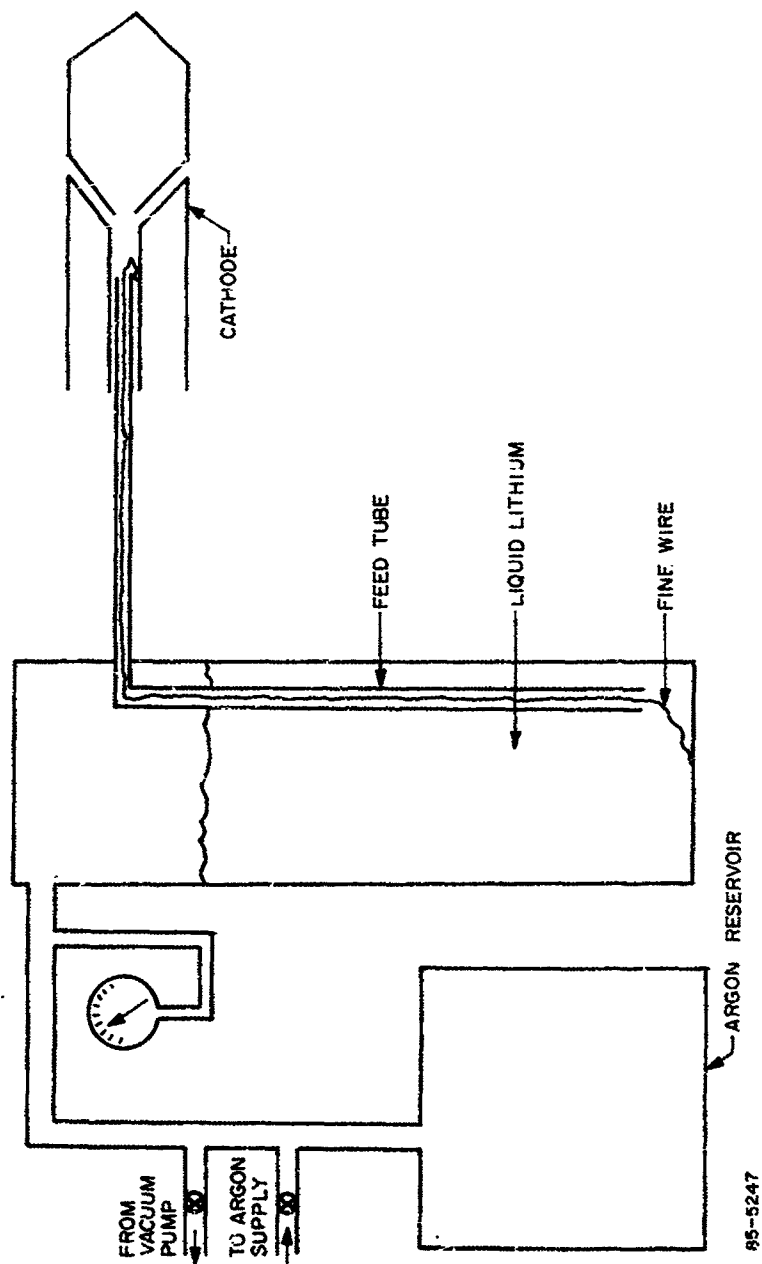


Figure 57a ALKALI FEED SYSTEM

95-5247

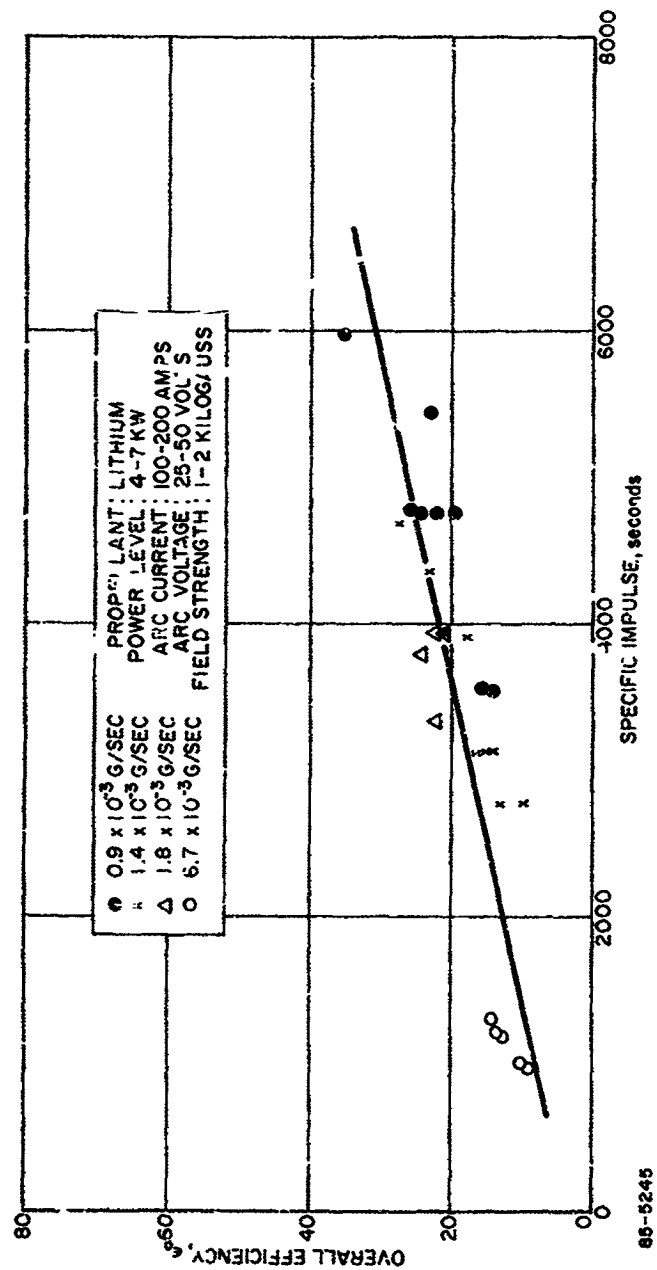


Figure 58 OVERALL EFFICIENCY VERSUS SPECIFIC IMPULSE RADIATION-COOLED MPD ARCJET

In this respect, and with respect to the efficiencies achieved in the 4000- to 6000-second specific impulse range, the lithium performance data are not greatly different from those previously obtained with, say, hydrogen, notwithstanding the extremely different ambient tank pressure conditions under which the data were taken. The hydrogen data were obtained with ambient backpressures of the order of 100 microns; those for the lithium propellant were taken with tank pressures of the order of a fraction of a micron. In comparison with the large number of hydrogen data points, however, the amount of lithium data is relatively scant and the direct comparison is not totally valid at this time. More lithium data are required for a firm comparison, and these are being compiled.

III. MAGNET SUBSYSTEM

A. ELECTROMAGNET DESIGN

Studies have been initiated to determine the weight penalty associated with the magnet subsystem required for MPD arcjet operation. Because the magnitude and shape of the magnetic field required for optimum MPD arcjet operation are not yet clearly defined, the following remarks must be considered preliminary. For the purpose of discussion, it has been assumed that the required magnetic field distribution can be obtained with a solenoid; further, for reference purposes, the field strength at the core center has been taken as the basic design parameter. Briefly, as will be described below, a semiquantitative comparison has been made of the weight of a radiation-cooled magnet system and the weight of a liquid-cooled magnet system; the weight comparison is based on the ground rule that both systems produce the same field strength at the center of the solenoid.

1. Fabry Formula

The axial field strength at the center of a solenoid is given by the Fabry relation, which has the form:²⁴

$$B_z = G \left(\frac{P \lambda}{\rho r_i} \right)^{1/2} \quad (30)$$

where, B_z (kgauss) is the magnetic field strength, G is a geometric factor which depends on the coil geometry (i.e., ratio of outside to inside radii $r_o/r_i = \alpha$, and length-to-diameter ratio, $l/2r_i = \beta$), P (megawatts) is the power input, λ is the fraction of the coil occupied by the conductor, ρ (ohm-cm) is the resistivity of the coil, and r_i (cm) is the inside radius of the coil.

The geometric factor, G , is a relatively weak function of the radii ratio, α , and the coil length to diameter ratio, β . The maximum value of G is about 0.20 which corresponds to values of both β and α in the range 2 to 3. For the purpose of the following semiquantitative discussion, G will be assumed a constant equal to the maximum value of 0.20 and both β and α will be assumed to be of the order of 2 to 3. By preselecting values of G , α , and β , the problem of estimating magnet system weights in considerably simplified; further, from the viewpoint of an order of magnitude analysis, these quantities only have a second-order effect on the calculated results.

Substituting $G = 0.20$ into equation (30) the Fabry relation can be written:

$$P = 2.5 \times 10^{-2} \rho r_i B_z^2 / \lambda \quad (31)$$

Dimensions are: the input power, P (kw), the resistivity, ρ (10^{-6} ohm-cm), the inner radius, r_i (cm), the axial field, B_z (kgauss), and the fraction of coil occupied by the conductor, λ (dimensionless). Equation (31) with the dimensional units as indicated, is used below.

From the Fabry relation (equation 31), the solenoid input power is proportional to the square of the axial magnetic field strength, and directly proportional to the solenoid material resistivity and inner radius. Figure 59 presents normalized magnet input power as a function of axial magnetic field strength at the center of the solenoid. The solenoid is at room temperature. For a 1-cm inner solenoid radius and a magnetic field strength of 2.5 kgauss the required input power is about 260 watts; if the inner radius were increased to 5 cm, the required input power would be 1300 watts.

Figure 60 shows the resistivity of copper as a function of temperature; as the temperature is increased from 50 to 500°C, the resistivity increases from about 2×10^{-6} ohm-cm to 5×10^{-6} ohm-cm. Thus, for fixed field strength and inner solenoid radius, the required input power increases with increase in solenoid temperature (equation 31). Figure 61 presents the normalized magnet power input, i. e., normalized with respect to an axial field strength of 1 kgauss and an inner radius of 1 cm, as a function of temperature. The required input power increases from 50 to 150 watts as the coil temperature is increased from 50 to 500°C.

2. Radiation-Cooled Magnet Subsystem

The major purpose of this discussion is to estimate the potential weight penalty associated with the MPD arcjet magnet subsystem. In the present section, estimates of the weight of a radiation-cooled magnet subsystem are presented; the following section includes estimates of the weight of a liquid-cooled magnet subsystem.

The weight of a magnet is given by

$$W_{\text{mag}} = 2\pi r_i^3 w (a^2 - 1) \beta \lambda \quad (32)$$

where r_i is the inner solenoid radius, w is the density of the magnet material, a is the solenoid radius ratio, β is the length to diameter ratio, and λ is the fraction of conducting material in the coil. For the radiation-cooled magnet, λ is assumed to be equal to 1. For the assumed values of

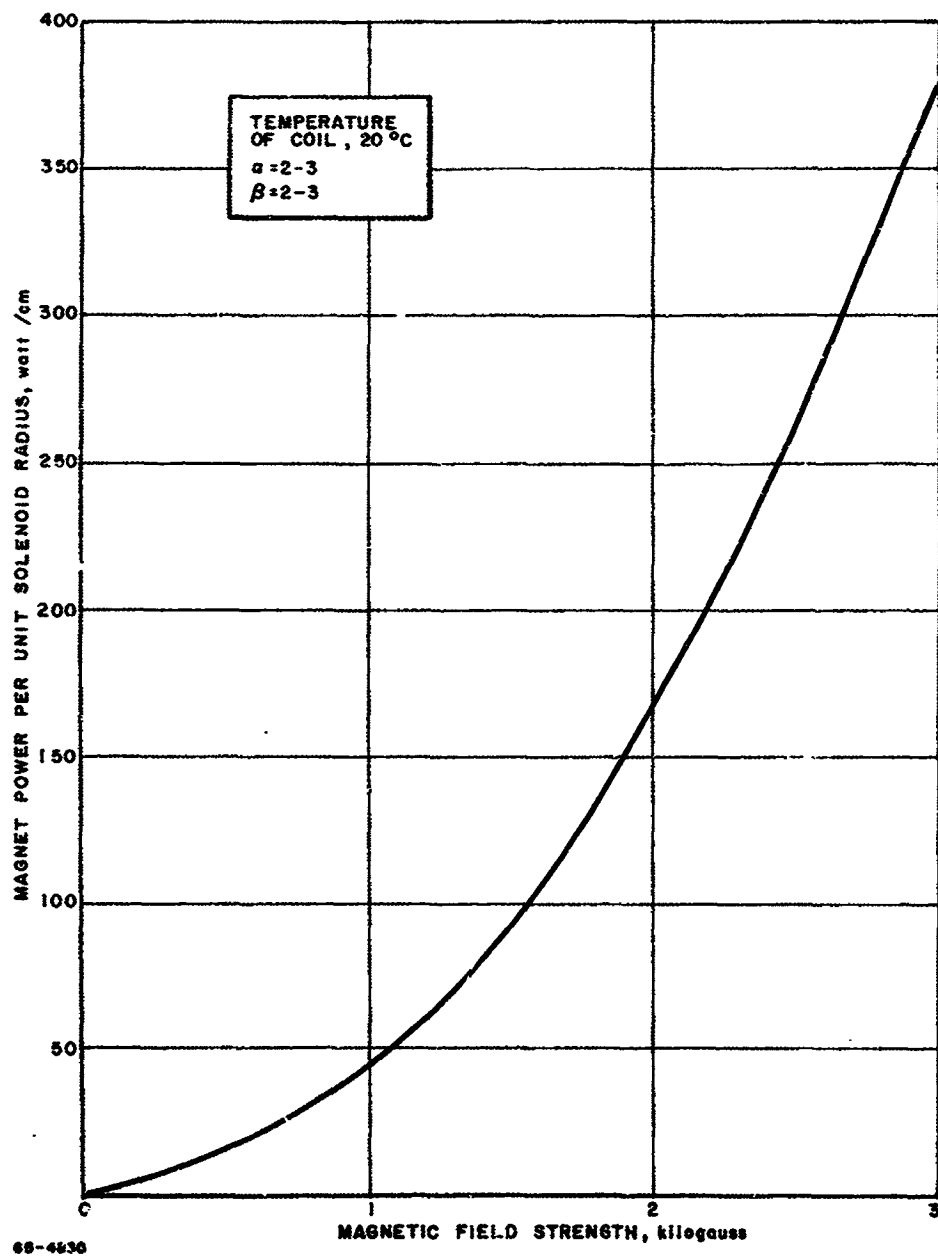


Figure 59 NORMALIZED MAGNET POWER INPUT VERSUS AXIAL MAGNETIC FIELD STRENGTH

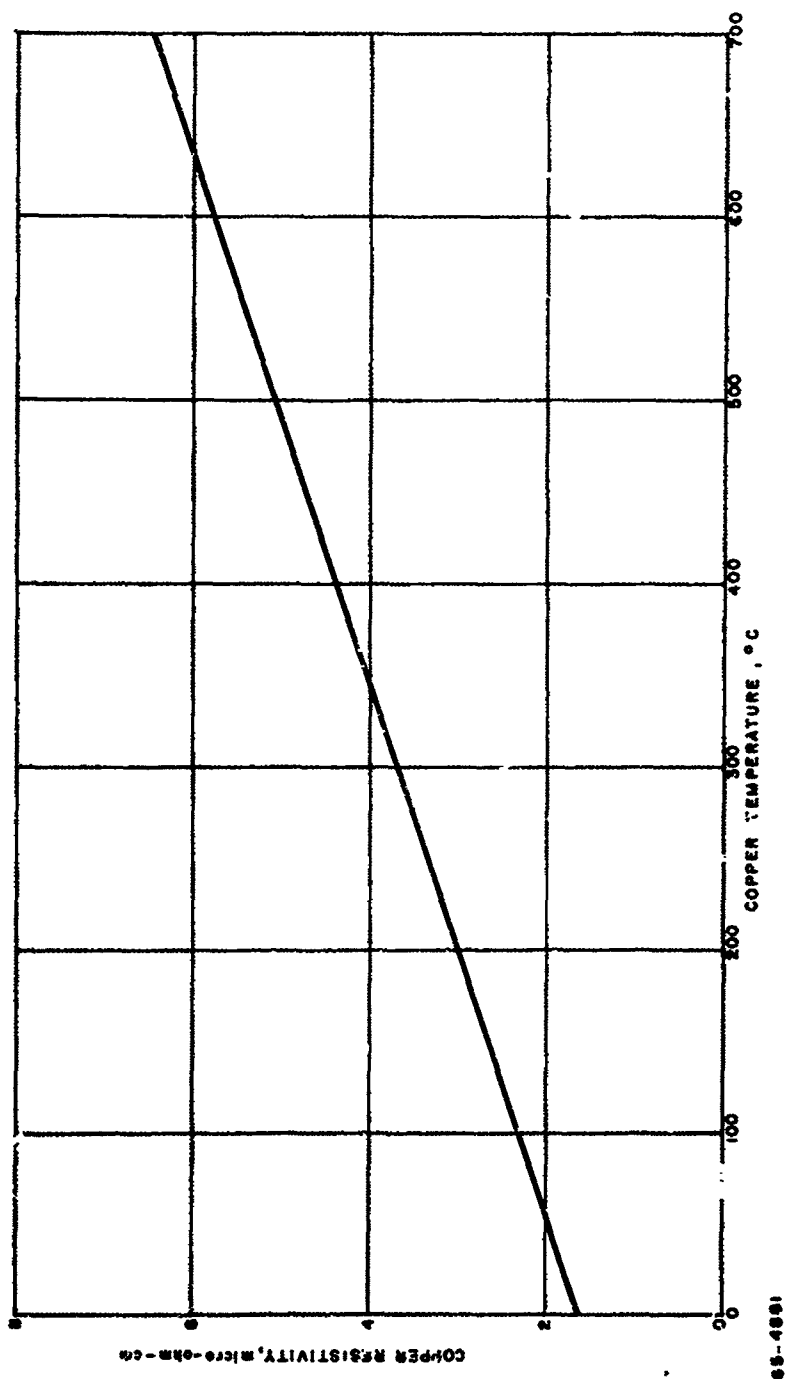
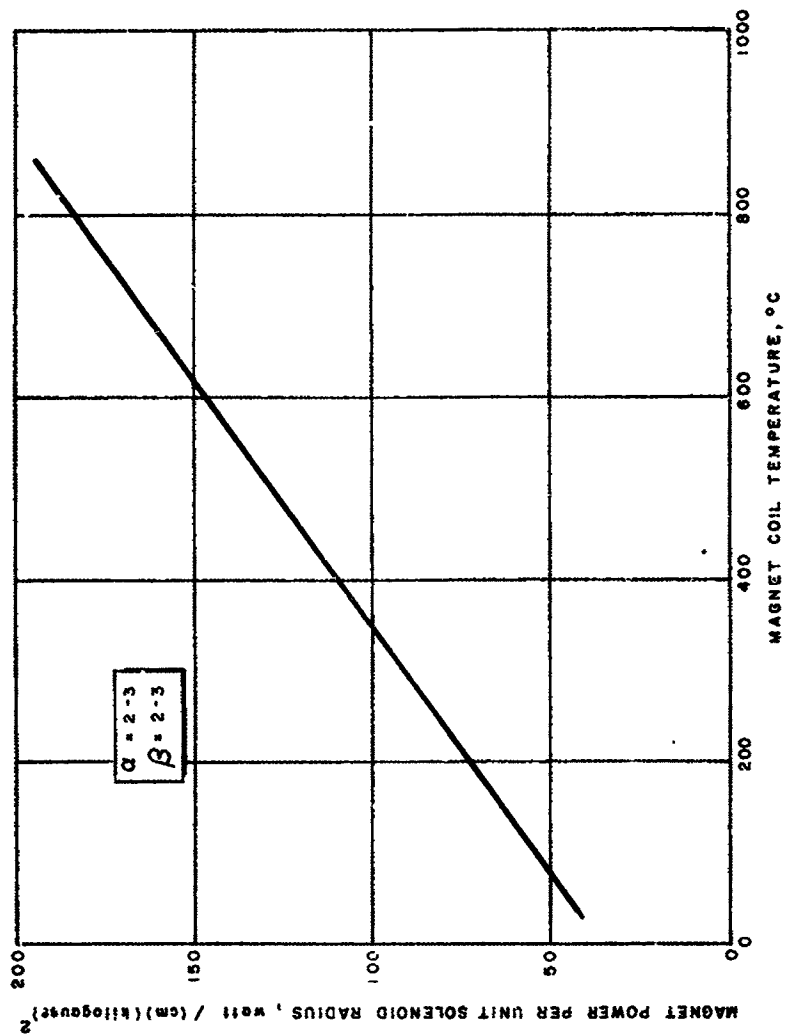


Figure 60 COPPER RESISTIVITY VERSUS TEMPERATURE



65-4882

Figure 61 NORMALIZED MAGNET POWER VERSUS COIL TEMPERATURE

a and β the coil weight, to a first approximation, is given by

$$W_{\text{mag}} \approx 75 r_1^3 w \lambda \quad (33)$$

For copper, $w = 562 \text{ lb/ft}^3$ and $\lambda = 1$, the weight of the magnet is given by

$$W_{\text{mag}} = 1.55 r_1^3 \text{ lb} \quad (34)$$

The weight of the magnet is, of course, proportional to the third power of the inner coil radius.

The radiation area of the coil is given by

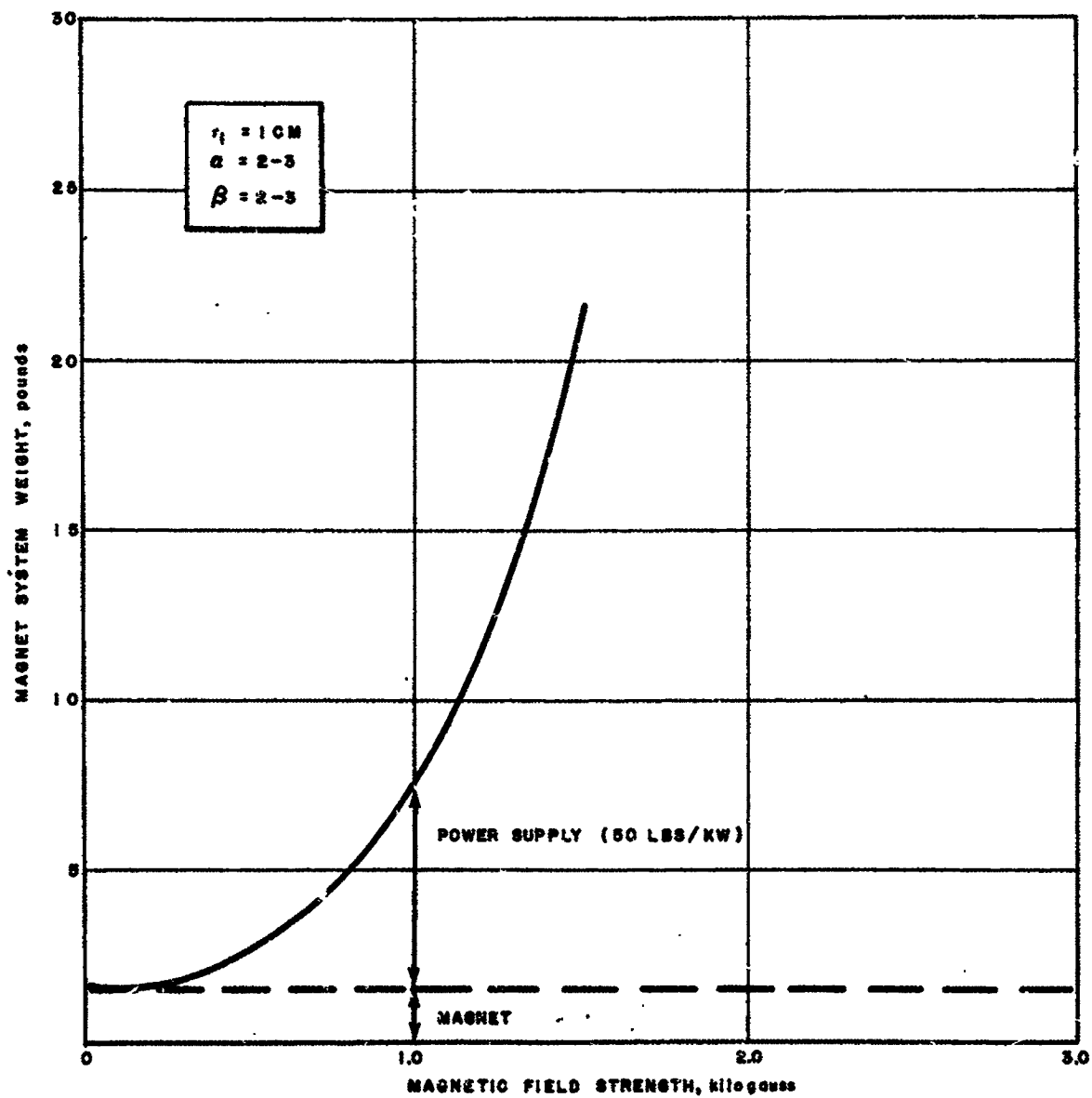
$$A = 2\pi r_1^2 (2a\beta + a^2 - 1) \quad (35)$$

For the assumed values of a and β , the radiating area becomes

$$A \approx 100 r_1^2 \text{ cm}^2 \quad (36)$$

In the case of the radiation-cooled magnet all the input power must be radiated from the magnet exterior surface. The calculational procedure then is as follows: a) select an inner coil radius, r_1 ; this establishes the radiating surface of the magnet (equation (36)) and the weight of the magnet (equation (34)); b) choose an operating temperature and estimate a surface emissivity, (e. g., in the present calculations $\epsilon = 0.60$); this determines the maximum power input from $P = \epsilon \sigma AT^4$; c) from the estimated power input, the assumed temperature which fixes the resistivity, and the assumed inner radius, the axial magnetic field on the solenoid axis can be estimated from the Fabry relation (equation 31); d) the weight of the required magnet power supply is estimated from an assumed power supply specific weight of 50 lb/kw.

The weight of a radiation-cooled magnet system is shown as a function of axial magnetic field strength for inner solenoid radii of respectively 1, 2.5, and 5 cm in figures 62, 63, and 64. The radiation-cooled magnet system weight includes the weight of the power supply and the weight of the magnet. The weight of the coil is, of course, independent of the field strength. The weight of the magnet system increases with magnetic field strength because



65-4883

Figure 62 WEIGHT OF RADIATION-COOLED MAGNET SYSTEM VERSUS AXIAL MAGNETIC FIELD STRENGTH:
INNER RADIUS = 1 CM

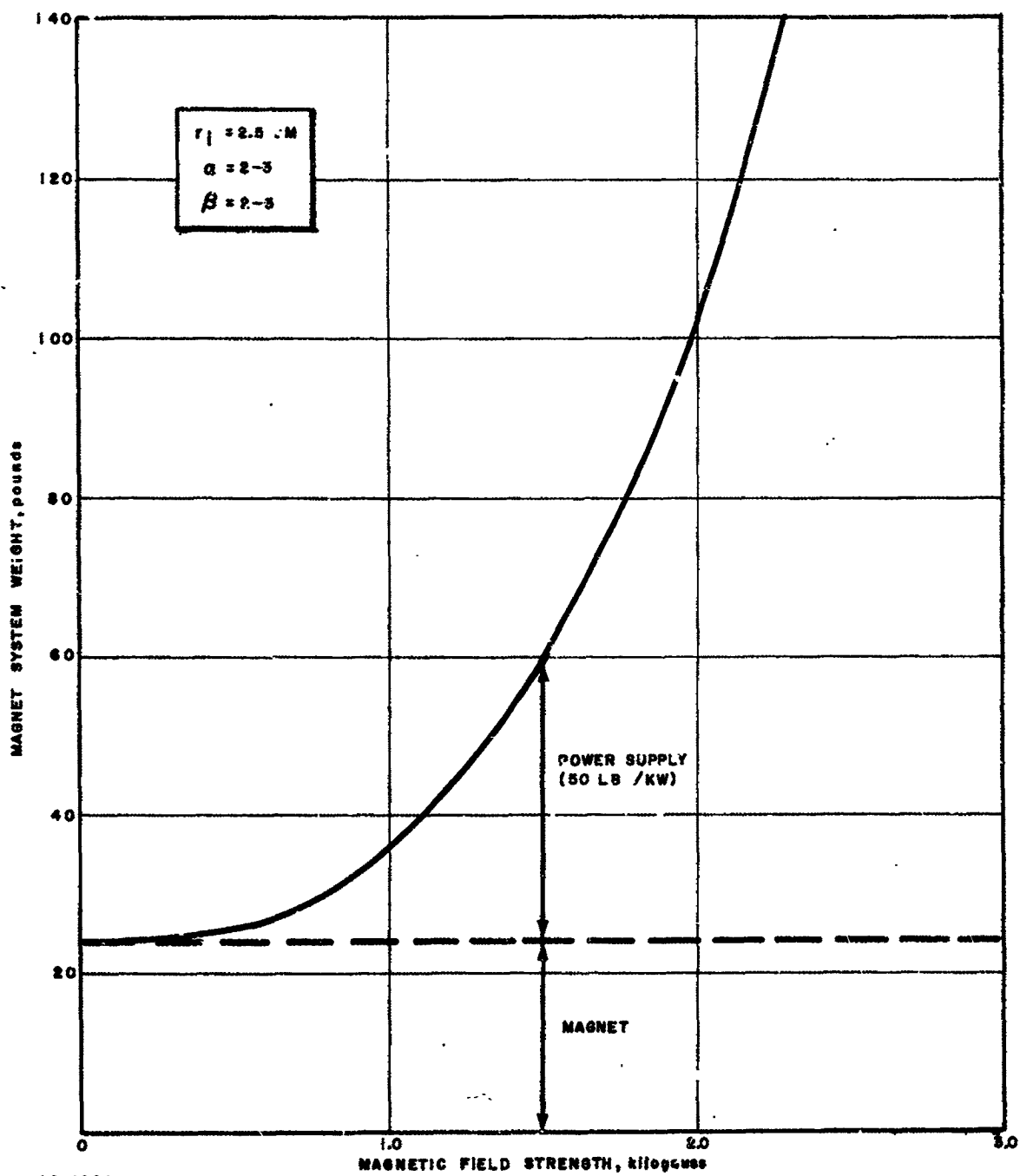
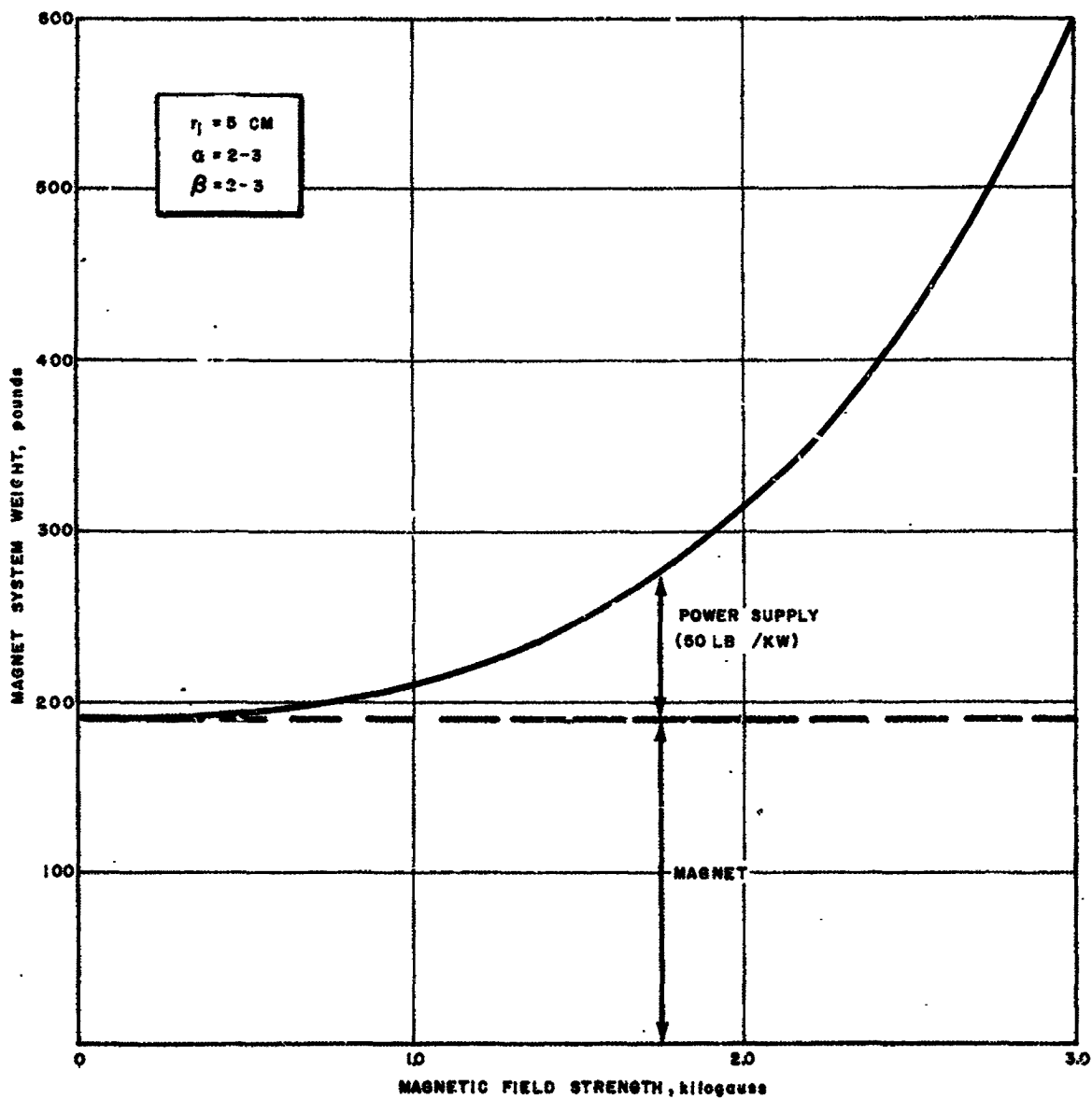


Figure 63 WEIGHT OF RADIATION-COOLED MAGNET SYSTEM VERSUS AXIAL MAGNETIC FIELD STRENGTH:
INNER RADIUS = 2.5 CM



65-4985

Figure 64 WEIGHT OF RADIATION-COOLED MAGNET SYSTEM VERSUS AXIAL MAGNETIC FIELD STRENGTH:
INNER RADIUS = 5 CM

of the increased power requirement. At a fixed strength of 1 kgauss the weight of the magnet subsystem increases from 7.5 to nearly 210 pounds as the inner radius is increased from 1 to 5 cm.

3. Liquid-Cooled Magnet Subsystem

In the case of the liquid-cooled magnet the input power is removed by a closed-loop cooling system with external radiator. The weight of the liquid-cooled magnet subsystem assembly must therefore include the weight of the radiator as well as the weight of the magnet and power supply.

The calculational procedure for determining the weight of the liquid-cooled magnet subsystem is as follows: a) select the required solenoid inner radius, r_i ; the required axial magnet field strength, B_z ; and the radiator operating temperature, T_{rad} ; b) the operating temperature establishes the coil resistivity; and the resistivity, ρ , combined with the required magnetic field, B_z , the solenoid radius, r_i , and the packing factor $\lambda = 0.70$ makes it possible to estimate the required magnet power from the Fabry relation (equation 31), c) the weight of the magnet coil can be determined from equation (34), again assuming a packing factor, $\lambda = 0.70$; d) the radiator weight is estimated using an assumed specific radiator weight of 7×10^{-4} lb/cm² (or 3.2 kg/m²).

Figures 65, 66, and 67 present plots of system weight versus magnetic field strength for inner solenoid radii of 1, 2.5, and 5 cm, respectively. The actual magnet coil becomes a larger fraction of the total system weight as the inner radius is increased; this, of course, might be anticipated since $W_{mag} \sim r_i^3$ and $W_{power\ supply} \sim r_i$. For inner solenoid radii up to 5 cm, and axial magnetic field strengths up to 3 kgauss, the weight of the external radiator is a relatively small fraction of the total system weight. It is important to recognize, however, that the presence of an external cooling system will introduce reliability problems, and further, in the above semi-quantitative calculations, no weight allowance has been made for the cooling pump or coolant.

To illustrate the probable size of the radiator, assuming an operating temperature of 100°C and an emissivity of 0.60, the emitted radiation is 6×10^{-2} w/cm²; therefore, the required radiating area for 100 watts is 0.17 m², for 500 watts, 0.85 m², and for 5000 watts, 8.5 m². At power levels of the order of 1-kw, the required radiator areas appear reasonable in terms of possible spacecraft designs.

4. Weight Comparison of Liquid- and Radiation-Cooled Magnet Subsystems

Figures 68, 69, and 70 present comparisons of total magnet system weights as a function of axial magnet field strength for inner solenoid radii of 1, 2.5, and 5 cm respectively. The basic conclusion from this comparison is that (within the limits of the analysis) the weight of a radiation-cooled

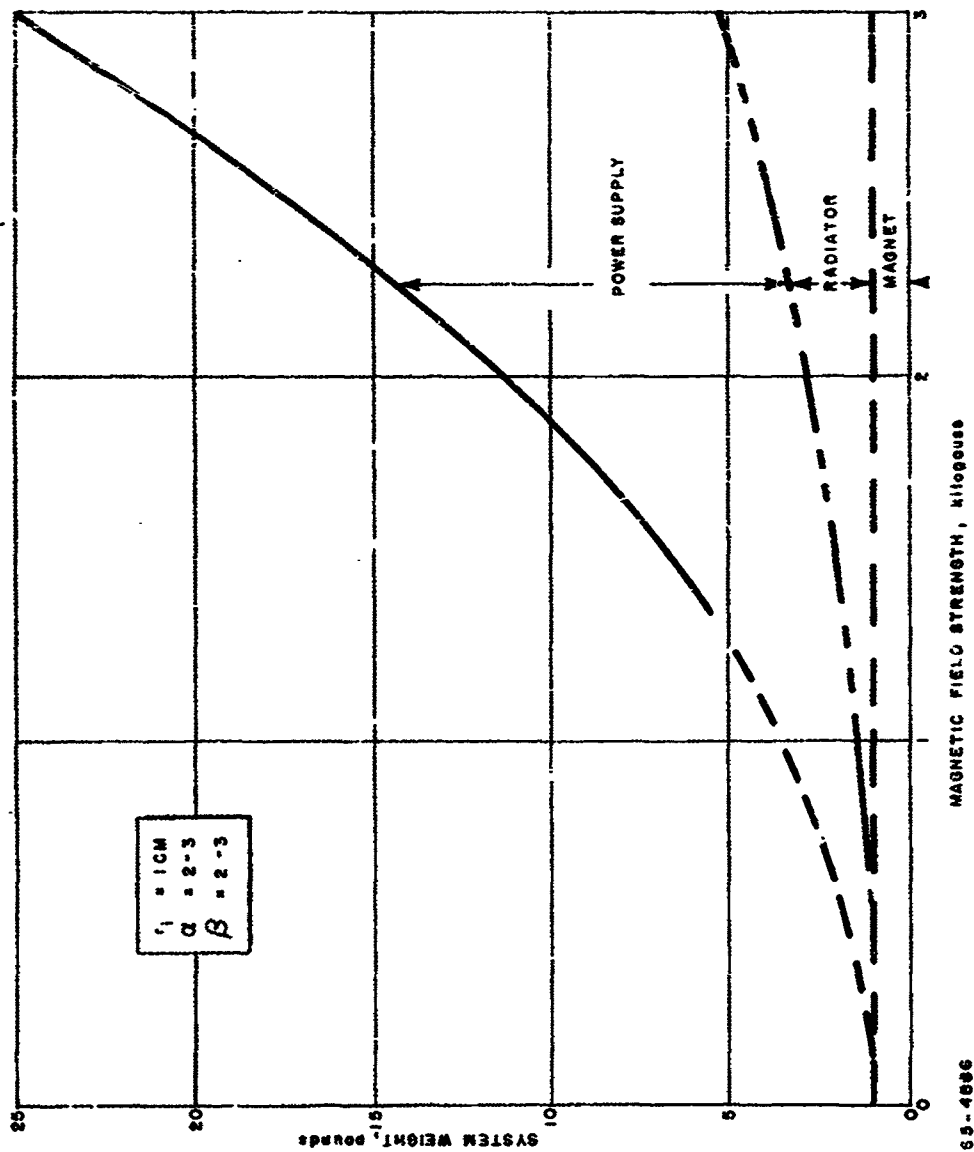


Figure 65 WEIGHT OF LIQUID-COOLED MAGNET SYSTEM VERSUS AXIAL MAGNETIC FIELD STRENGTH:
INNER RADIUS = 1 CM

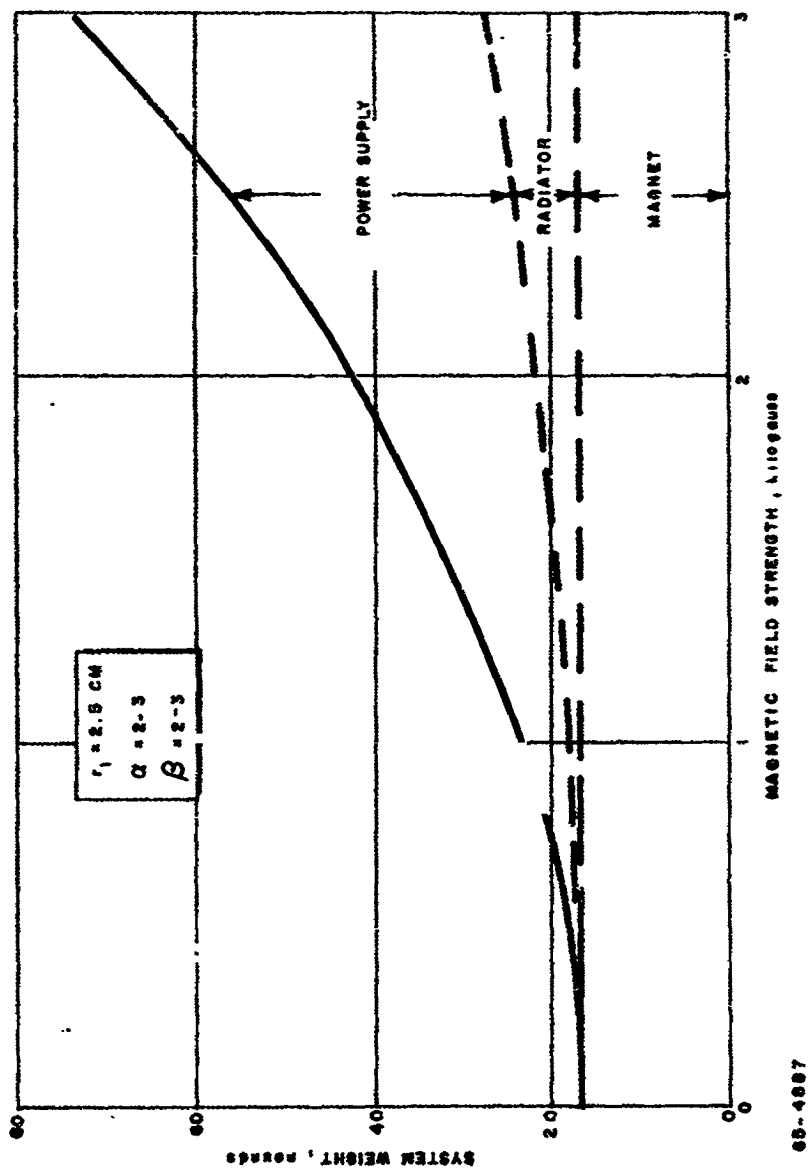
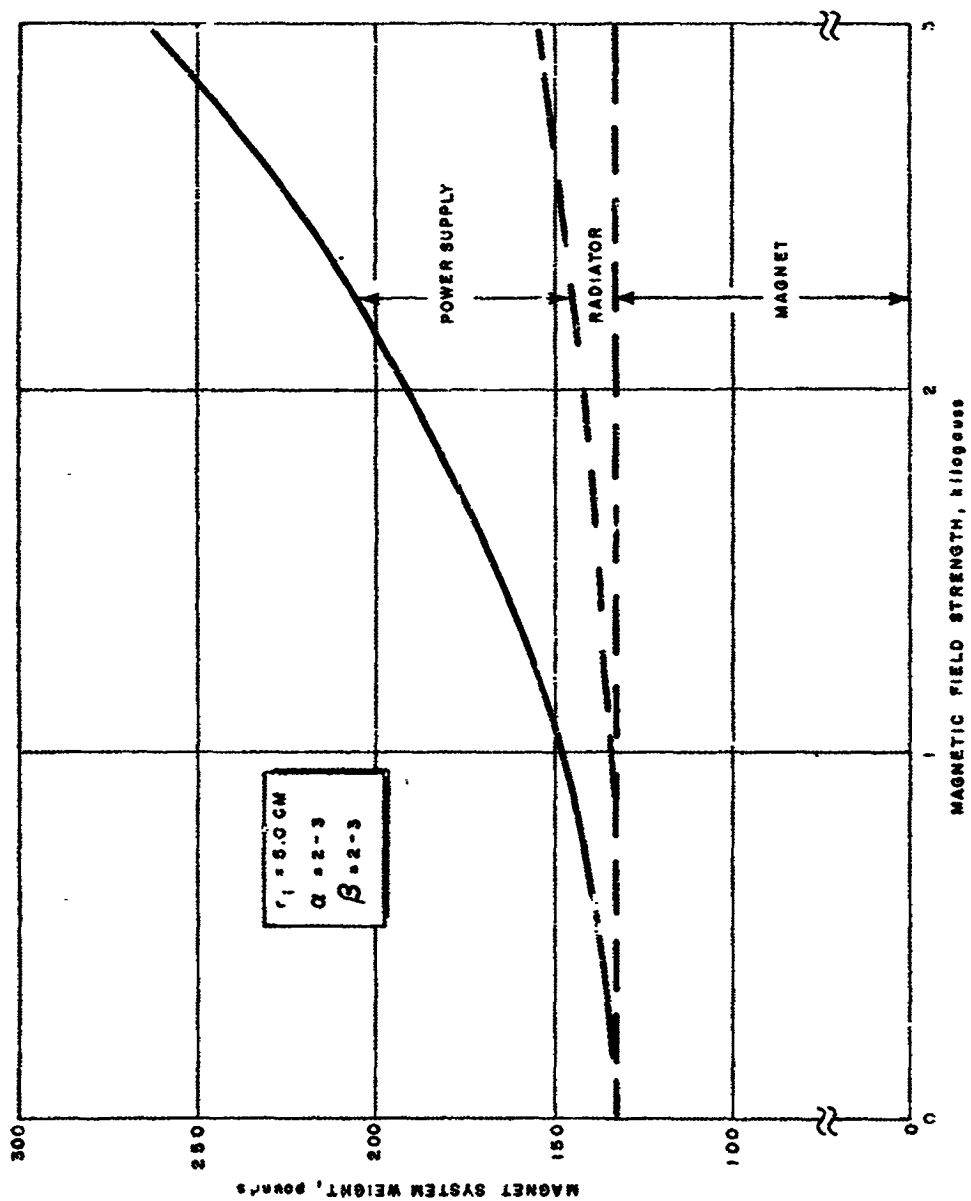


Figure 66 WEIGHT OF LIQUID-COOLED MAGNET SYSTEM VERSUS AXIAL MAGNETIC FIELD STRENGTH:
INNER RADIUS = 2.5 CM



65-4869

Figure 67 WEIGHT OF LIQUID-COOLED MAGNET SYSTEM VERSUS AXIAL MAGNETIC FIELD STRENGTH;
INNER RADIUS = 5 CM

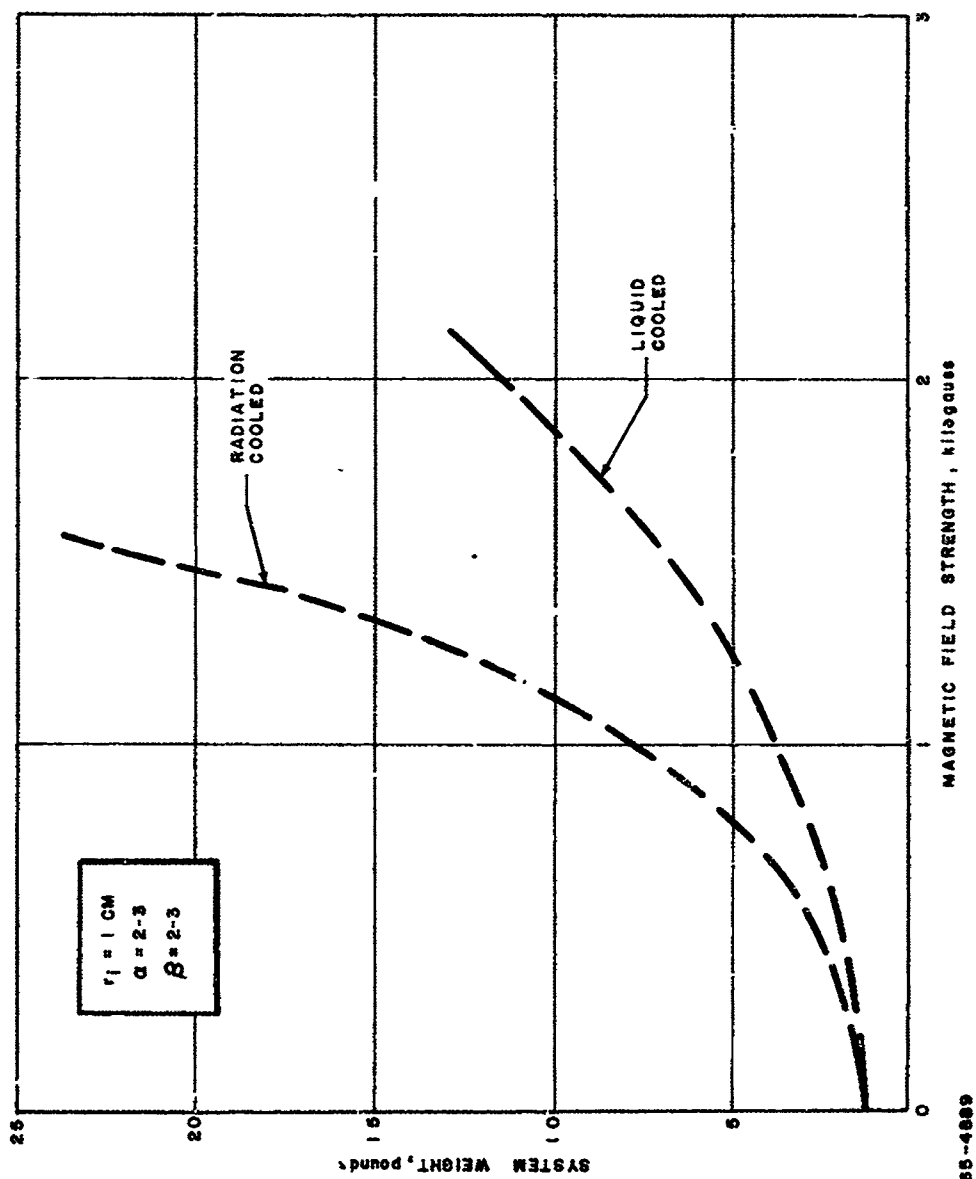
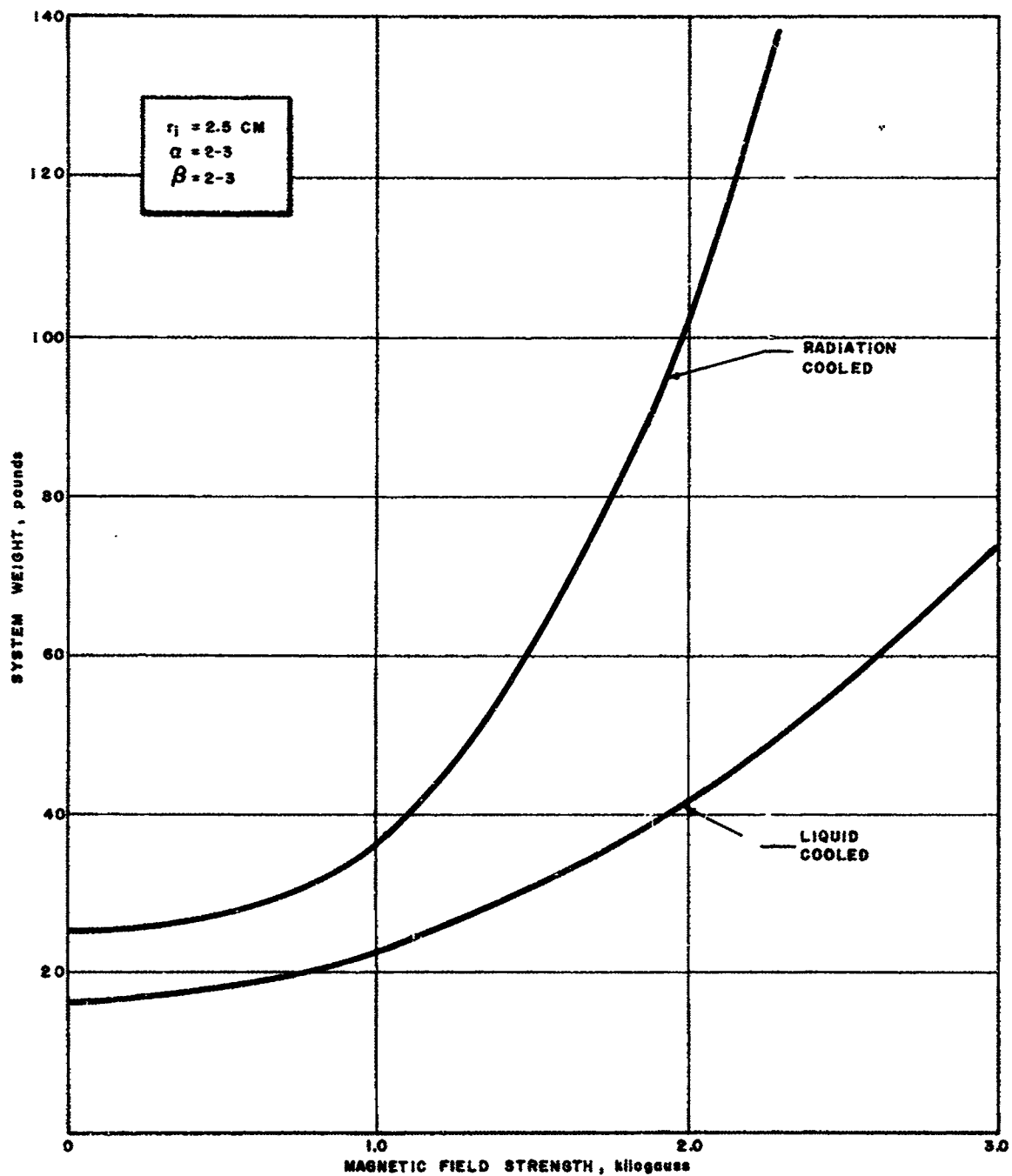


Figure 68 WEIGHT COMPARISON OF RADIATION AND LIQUID-COOLED MAGNET SYSTEM VERSUS AXIAL MAGNETIC FIELD STRENGTH: INNER RADIUS = 1 CM



65-4890

Figure 69 WEIGHT COMPARISON OF RADIATION AND LIQUID - COOLED MAGNET SYSTEM VERSUS AXIAL MAGNETIC FIELD STRENGTH: INNER RADIUS = 2.5 CM

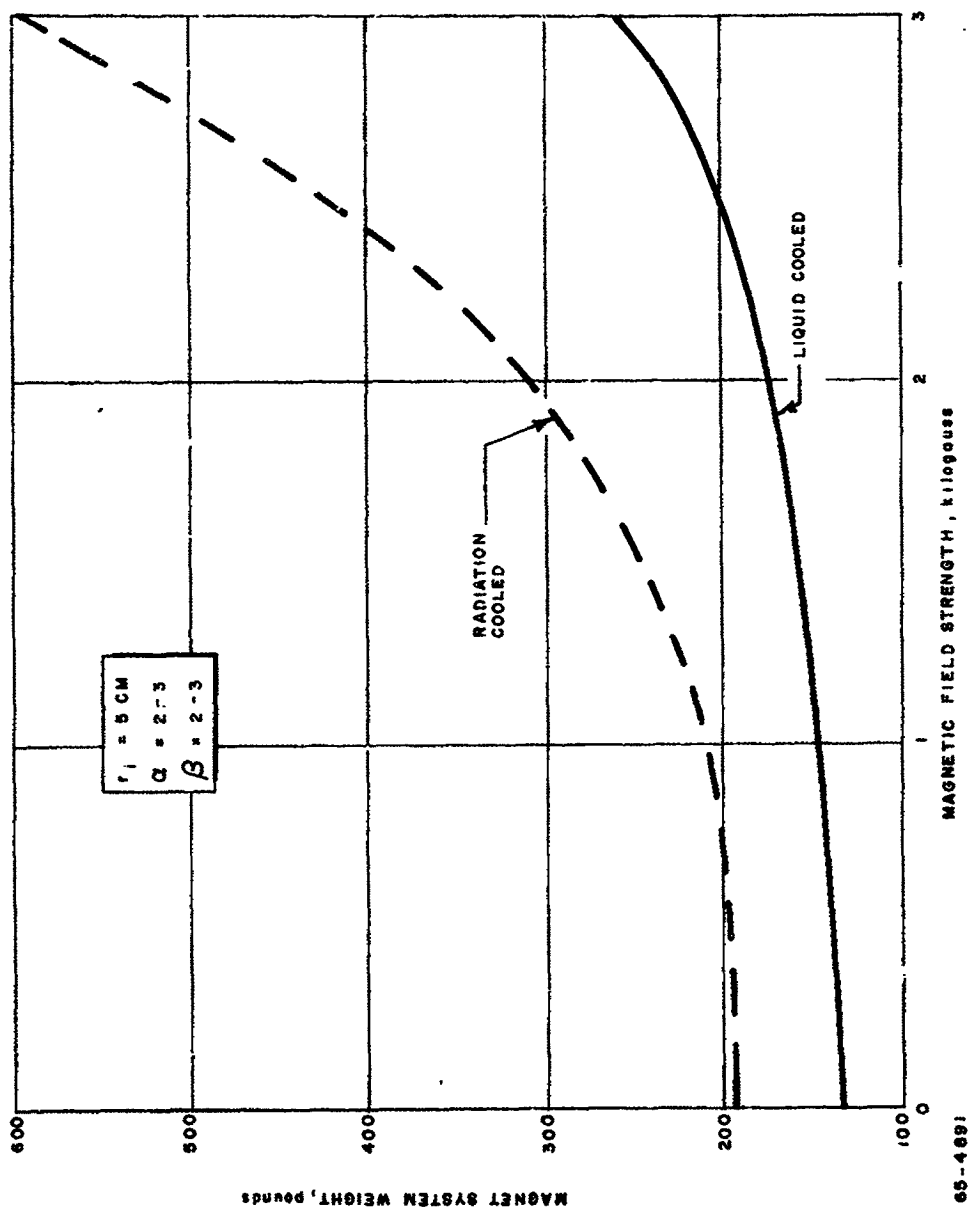


Figure 70 WEIGHT COMPARISON OF RADIATION AND LIQUID-COOLED MAGNET SYSTEM VERSUS AXIAL MAGNETIC FIELD STRENGTH: INNER RADIUS = 5 CM

magnet system is about three times the weight of a liquid-cooled magnet system to produce the same axial magnetic field strength. At values of inner solenoid radii of the order of 1 cm, and field strengths up to 1 kgauss, the absolute weight penalty accruing to the use of a radiation-cooled magnet is only of the order of a few pounds, and can perhaps be tolerated from the viewpoint of gaining reliability. At inner solenoid radii greater than 1 cm, and magnetic fields greater than 1 kgauss the weight penalty associated with the radiation-cooled system is substantial and probably cannot be tolerated.

To conclude, table IV presents estimates of magnet subsystem specific weights for the MPD arcjet. The magnet subsystem specific weight is defined as the ratio of engine power to subsystem weight. Two power levels appear attractive for solar-powered MPD arcjet operation, i.e., 1 to 10 kw and 20 to 40 kw; at the 1- to 10-kw power level the required inner solenoid is assumed to be of the order of 1 cm, while at 20 to 40 kw the required inner radius is assumed to be of the order of 2 cm. Similarly, the required solenoid axial field strengths are assumed to be in the range from 1 to 3 kgauss. It is stressed that the assumptions regarding inner solenoid radii and required field strength are working hypotheses. The results in table IV are thus only as valid as the assumptions. With due qualifications, the results in table IV do suggest, however, that, except at the very low engine input power levels, i.e., order of 1 kw the specific magnet system weights appear quite tolerable and well within the current solar-powered electric propulsion subsystem design goal of 25 lb/kw.

B. PERMANENT MAGNETS

The magnet geometry considered was a cylinder of inner and outer radii r and R , respectively, and length $2L$. The two cases are: (1) axially magnetized and (2) radially magnetized cylinders. The magnetic field strengths in the region exterior to the magnet material may be determined by the method of magnetic bound current.²⁵ The field distributions in the regions exterior to the magnet are found to be identical to those of solenoidal current distributions.

For the axially magnetized material, the field strength distribution is the same as that of two concentric solenoids of radii r and R , each carrying a current per unit length, M , but in opposite directions. M is the magnetization of the magnet material. It is seen that this configuration has certain obvious disadvantages.

First, and of major consequence, is the large cancellation of field strength due to the two "solenoids". The field strengths achieved are an order of magnitude lower than those achieved with an electromagnet. Secondly, the field distribution is not at all similar to that of a single solenoid.

The radially magnetized configuration appears much more promising at this time. The field distribution is the same as that of two very thin solenoids located at the end faces of the cylinder, although carrying currents in opposite directions. If the cylinder is of sufficient length, the field strength and its spatial distribution at one face and outside the magnet is essentially that of a single, thin solenoid situated at the end face. The other "solenoid" is far enough removed to have little or no effect upon the field in this region.

The present indications are that field strengths of the order of 1 kgauss can be achieved with such a magnet with a weight penalty on the order of 50 to 100 pounds. This is comparable to electromagnet systems.

TABLE IV

MAGNET SUBSYSTEM SPECIFIC WEIGHT

Engine Power Level (kw)	Inner Solenoid Radius (cm)	Required Field Strength (kilogauss)	System Weight (pounds)	Specific Weight (lb/kw)
1	1.0	1.0	4	4
		2.0	11	11
		3.0	25	25
10	1.0	1.0	4	0.4
		2.0	11	1.1
		3.0	25	2.5
20	2.5	1.0	24	1.2
		2.0	42	2.1
		3.0	75	3.8
40	2.5	1.0	24	0.6
		2.0	42	1.1
		3.0	75	1.9

IV. APPLIED RESEARCH

A. INTRODUCTION

At this time, MPD accelerator research is being pursued at several laboratories including this one. The research programs differ in the propellants being used, the ambient pressure levels, the magnetic field strength applied, and in other details. Various hypotheses have been put forth in an attempt to explain, or at the least to correlate, the apparent accelerator operation with the controllable parameters. In addition, varied diagnostic studies have been pursued in the different laboratories. The purpose of this section of this report is to integrate the information which is now available from all sources, and to present the results of experiments and analyses carried out at Avco RAD, with a view toward summarizing the current state of the art in our understanding of MPD arcjet operation. A tentative model of MPD arcjet operation, which is principally electrothermal in nature with a magnetic nozzle, is then proposed.

B. CONDITIONS IN THE MPD ARCJET EXHAUST

1. Appearance of the Exhaust

At a low ambient pressure (order of 100 microns or less, down to the order to 10^{-2} micron) the exhaust jet of the MPD arcjet shows several qualitative features which are common to operation over a fairly wide range of current levels and magnetic field strengths. A central core is visible which emits intense radiation, and which grows in diameter slowly in the downstream direction. The annular space immediately around this core is relatively dark. Just outside of this annular region is a second luminous region, the cross sectional area of which changes sharply with distance downstream. The inner boundary of this second annular region appears to be circular in cross section, and the diameter of this bounding circle grows in the downstream direction more rapidly than the diameter of the core. The outer boundary of this second annular region is also circular in cross section, and the diameter of this bounding circle grows extremely rapidly, such that the projected view one obtains from the side is of an exponential or horn shape. Qualitatively, each of these shapes can be explained on the basis that they represent magnetic field lines. Near the axis of the device the field lines tend to be fairly parallel, opening slightly in the downstream direction. As one proceeds away from the centerline, the spread of field lines becomes more rapid.

2. Estimates of Density and Mean Free Path

An approximate relation for the number density of particles as a function of pressure and temperature is given by

$$n = 3 \times 10^{19} \frac{P \text{ (mm)}}{760} \frac{273}{T} \text{ cm}^{-3}$$

In the ambient gas in the test tank, the temperature varies from essentially room temperature near the tank walls to a higher value near the outer boundary of the jet. If this higher temperature value is taken as approximately 1000°K, then for the data reported here with cesium flow rates of 3 to 6 mg/sec, the density of particles in the ambient gas is in the range 10^{12} to 3×10^{12} particles/cm³, where a pressure of 0.1 micron is assumed. The mean free path for collisions is related to this number density and to the cross section by

$$\lambda = \frac{1}{n\sigma}$$

so that for a collision cross section of 10^{-14} cm² (for neutral cesium)³⁸ the mean free path is of the order of 0.3 to 1 meter. This is comparable to the test tank dimensions, so that collisions of ambient gas particles with the tank walls are as frequent as particle-particle collisions.

Within the jet structure the temperature can be very much higher, but the pressure is also likely to be much higher owing to magnetic pinching. Further, the collision cross section for charged particles may be of the order of 10^{-13} cm², rather than 10^{-14} cm². The effect of these changes is to reduce the mean free path by more than two orders of magnitude, to the order of a millimeter.

3. Electrical Characteristics

Voltage probes have been used by Hess and co-workers at NASA-Langley^{26, 27} and at this laboratory.* The results of these investigations, in general, are comparable. It appears that the major voltage drops occur along lines normal to the applied magnetic field, while the voltage drops parallel to the field lines are smaller. Thus, from the cathode tip to a point well downstream (order of 12 inches) the voltage drop may be of the order of 30 percent of the arc voltage, since this is along the magnetic field.

*Voltage probe measurements at higher ambient pressures are reported by Power and Patrick.²⁸

Cann and co-workers at EOS²⁹ have used cooled Hall effect probes to measure the tangential magnetic field distribution, yielding the axial current density in the exhaust. Their results indicate that the main axial current flows in the central core of the discharge, leaks off steadily with distance downstream to join the "anode jet," and returns in the "anode jet," which is identified with the outer bright region in the exhaust.

Estimates made at Avco RAD indicate that, in the case of cesium, this current must be carried by electrons almost everywhere. The atomic weight of cesium is so large that a flow of 1 mg/sec of singly ionized cesium atoms represents a current of only 0.75 ampere. For the mass flows employed during the tests reported above, 3 to 6 mg/sec, the ions can carry only of the order of 5 amperes while arc currents of as much as 180 amperes have been run. To account for this disparity by multiple ionization would require levels of ionization of the order of 30, which appears to be quite out of the question from theoretical considerations. More complicated explanations involving neutralization, recirculation, and reionization of the cesium atoms can be proposed, but this too seems unlikely on theoretical grounds. Therefore, it is concluded that the great bulk of the current is carried by electrons which are emitted from the cathode, flow down the central core of the discharge, diffuse into the anode jet over a sizable axial distance, and return to the anode.

4. Velocity

Velocities in the MPD arcjet exhaust have been measured in three ways, two of which depend also on a mass flow measurement, and one of which is independent of the mass flow measurement. Agreement is fairly good over much of the specific impulse range investigated.

The indirect measurements have been made using thrust plates and thrust balances. Thrust balances were used at Avco RAD²¹ and at EOS³ and Giannini Scientific³⁰ and thrust plates at Avco Everett³¹, EOS³², and NASA-Langley.³³ Those groups which worked with argon or a heavier gas^{*} obtained evidence of higher velocities in the exhaust jet than could be accounted for by equating the kinetic energy per ion to the potential drop in the discharge multiplied by the electronic charge. Multiple ionization required is quite large (order 5 to 10 times ionized for some of the data) and is thought unlikely.

Since the quantity measured in these cases is associated with the jet momentum, the velocity which is calculated depends also upon the mass flow rate measurement. Entrainment of ambient gas could disturb this picture and lead to erroneous values of the deduced velocity. Even though measurements have been reported at pressures thought to be low enough to preclude significant entrainment,^{33, 34} a more direct velocity measurement is desirable.

^{*}EOS recently reported anomalous I_{sp} values for lithium, which has an atomic weight of only 7. See reference 34.

Such a measurement has been made recently at Avco RAD. A $\underline{u} \times \underline{B}$ velocity probe developed under another program has been employed in the exhaust of an MPD arcjet to make direct velocity measurement. The $\underline{u} \times \underline{B}$ probe is, in concept, an open circuited MPD generator. The emf induced in such a generator when a plasma flow passes through it with a velocity \underline{u} normal to the applied magnetic field \underline{B} is proportional to the magnitudes of \underline{u} and \underline{B} , and to a dimension between the sensing electrodes. In the particular probe employed at this laboratory the applied field \underline{B} is an alternating field, excited by ordinary 60-cycle power. Thus the output signal of the generator is also 60-cycles. Since the output signal magnitude is now independent of floating dc potentials, the signal-to-noise ratio is very large at quite modest applied magnetic field intensities. Usable signals are obtained with applied magnetic field strengths as low as 1 gauss. This value of applied field is thought to be so low that the effect of the applied field on the plasma flow is negligible. A more complete discussion of measurements made with the $\underline{u} \times \underline{B}$ probe and their interpretation and validity to direct velocity determination is given in appendix G.

The velocities measured with this probe in argon accelerated by an MPD arc correspond to a specific impulse as high as 3900 seconds. For an argon ion the kinetic energy at this velocity is approximately 200 electron volts. Since the applied arc voltage in this test was of the order of 30 volts, there is little question that the energy per ion is larger than could be obtained from dropping through the applied potential. It is thought unlikely that the argon ions would be seven times ionized.

5. Conclusions

The observations listed so far seem to indicate that the electrons are the principal current carriers, at least in cesium operation; that the anomalous I_{sp} values are obtained at a number of laboratories over a considerable ambient pressure range; and that there is so far no indication of sufficient voltage drops in the plasma to account for the acceleration of ions by electric fields. A model is tentatively proposed to account for these facts in the next section.

C. ACCELERATION MECHANISM

1. Description

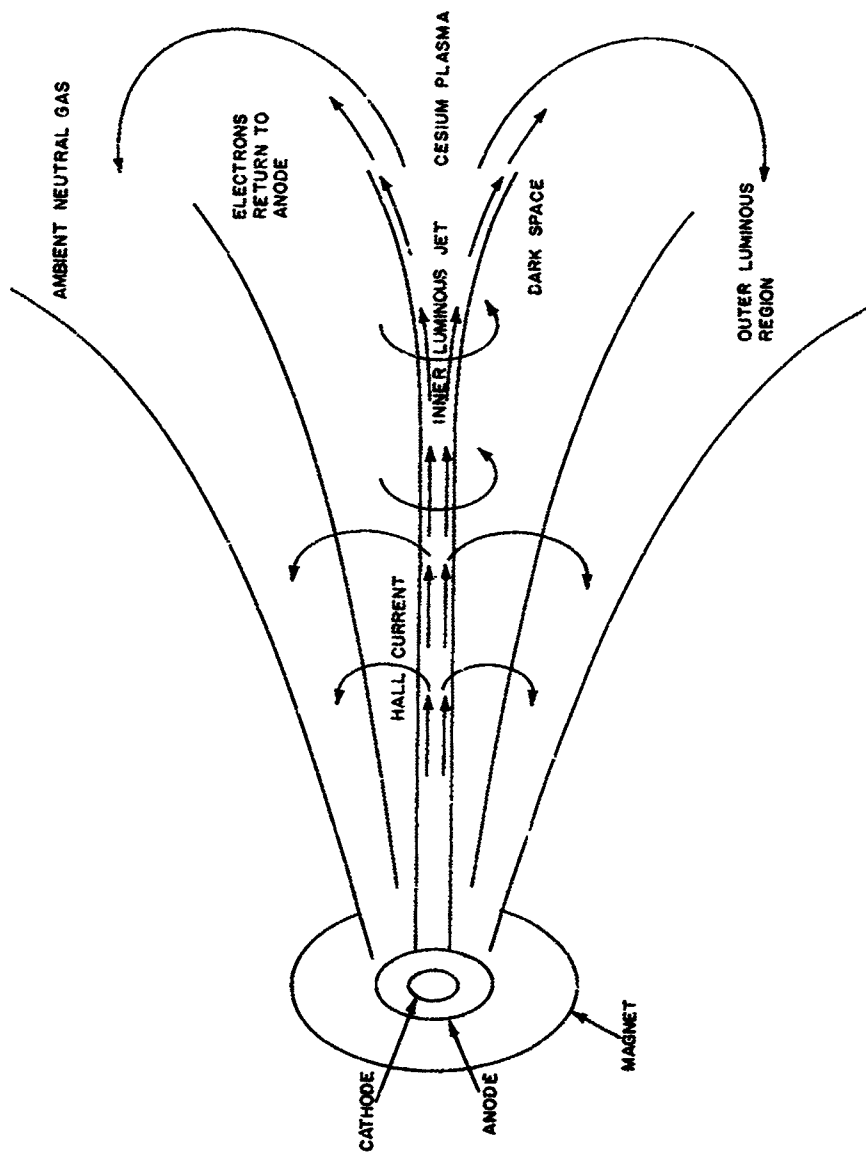
With this as a background, considerable thought has been given to the mechanism of acceleration in the MPD arcjet. A mechanism is proposed below and given in more detail in appendix E which appears to explain the observed phenomena, and which allows comparison with the experimental results. The proposed mechanism is still tentative, depending upon the outcome of further measurements.

Basically, it is tentatively suggested that the energy is added to the propellant in the form of heat through ohmic dissipation, and the high specific impulse values are obtained by expansion in a nozzle. The contribution of the applied magnetic field is to form the nozzle which is magnetic. The action of Hall currents is to modify the contour of this magnetic nozzle. This suggestion has been made previously by others, including Hess, Patrick, and Cann, in general discussions of MPD acceleration processes. We are suggesting that the performance we have so far measured in cesium can be best explained on this basis.* It is stressed that the suggestion is a tentative one. The motivation for this concept comes from the observed fact that velocities are obtained in the exhaust which appear to be too large to account for by acceleration in the applied electric field, and that voltage probe measurements in the exhaust give no indication of anomalies owing to space-charge effects. Since particles can be accelerated only by collisions or by fields, and since there is so far no indication that the required fields are present, we have attempted to investigate collisional mechanisms.

Figure 71 is a sketch of the exhaust jet issuing from the MPD arcjet operating with cesium. It is based on the photograph of figure 52. A qualitative picture of the engine operation can be stated as follows:

- a. The cesium leaves the engine structure from the vicinity of the cathode tip as a vapor. It is ionized almost immediately, since the first ionization potential is so low (3.8 volts), and the collision mean free path is short.
- b. The ionized cesium enters a vacuum chamber where the ambient pressure is kept low (approximately 0.1 micron). The static pressure within the cesium vapor is much higher, and the vapor tries to expand. However, it is a highly ionized plasma in a magnetic field. Near the cathode tip the field is nearly pure axial, and expansion in the radial direction would force the plasma to cross field lines. This would set up Hall currents to increase the magnetic pressure. As a result, the plasma expands very little in the radial direction.
- c. The arc current, carried by electrons, flows through the plasma in an essentially axial direction through this magnetic channel. There is a leakage of electrons in the radial direction, which increases in the downstream direction as the magnetic field weakens and becomes less axial. The electrons find a magnetic field line which terminates on the anode and return to the anode along it. Electrons carry the current everywhere, with only a small portion carried by ions.

*Entrainment would also explain this performance. If the pressure measurements are valid within a factor of 3, entrainment can be ruled out, but we are not sure of the behavior of ionization gauges in cesium vapor.



65-10599

Figure 71 MAGNETIC NOZZLE MODEL OF MPD ARCJET OPERATION

d. Over the return path to the anode the electrons collide with ambient cesium ions, exciting and ionizing them, and causing the outer luminous zone to appear. This outer luminous zone is not directly involved in the acceleration.

e. In the inner luminous zone, confined by the magnetic nozzle, is the entire input mass flow of cesium through which the arc current passes. This cesium is heated to extremely high temperatures, and accelerates as it expands in the magnetic nozzle. The pressure levels within the magnetic nozzle are considerable (order of 1 mm) so that the mean free paths for electron-ion collisions are quite short.

2. Evidence for the Electrothermal Model of MPD Operation

The evidence for this explanation of MPD arcjet operation is as follows:

a. Since the current is carried almost entirely by electrons, the current flow and the input propellant flow are uncoupled; it is not necessary that there be a specific number of ions created per second to account for a given current flow. We have observed that the current can exceed the flow rate of propellant atoms by such a large factor as to make alternative explanations (entrainment, erosion of electrode material, multiple ionization) unlikely. Further, the measurements of Lenn at EOS indicate that the current even in the outer luminous zone (in argon) tends to follow the magnetic field lines; if this current were being carried by ions, because they can cross field lines while electrons cannot, there would be no need for the current to be tied to field lines. This observation suggests that the electrons are the current carriers.

b. Since the number of charge carriers is large compared to the number of accelerated particles, each accelerated particle can obtain energy from a number of charge carriers. Thus, an accelerated particle can benefit from a number of particles which have fallen through the applied potential. There is, then, no limit attached to the I_{sp} as compared to the accelerator terminal voltage.

c. The magnetic effects make the pressure sizable in the acceleration region, so that there are numerous collisions to transfer energy to the ions.

d. The observed voltage patterns in the exhaust region are consistent with this picture of MPD arcjet operation. The potentially useful energy input is given by the product of the current and the voltage drop from the cathode to the end of the magnetic nozzle. The rest of the voltage drop between the nozzle surface and the anode is waste, winding up in anode heating. In our cesium data, it has generally been the case that the thrust power is a relatively small portion of the input power

(corresponding to the fact that the voltage drop along the bright core region is a small part of the total voltage drop), while the anode heating power has been a large portion of the input power (corresponding to the fact that electrons drop through a large potential in going from the bright core to the anode, and then give up this energy to the anode as they enter it).

e. In general, MPD arcjet thrust has been relatively insensitive to the magnetic field strength, while the voltage has been much more sensitive to the magnetic field strength. This is consistent with the picture which has been given above; the primary function of the magnetic field is to establish the nozzle. Variations in the field strength or configuration are analogous to variations in area ratio or divergence angle of a nozzle. These have some effect on the thrust, but, in general, the thrust is not greatly sensitive to these quantities within a wide range of variations. On the other hand, the voltage is involved principally with the return of the electrons to the anode across the magnetic field, and this is expected to be sensitive to the magnetic field strength.

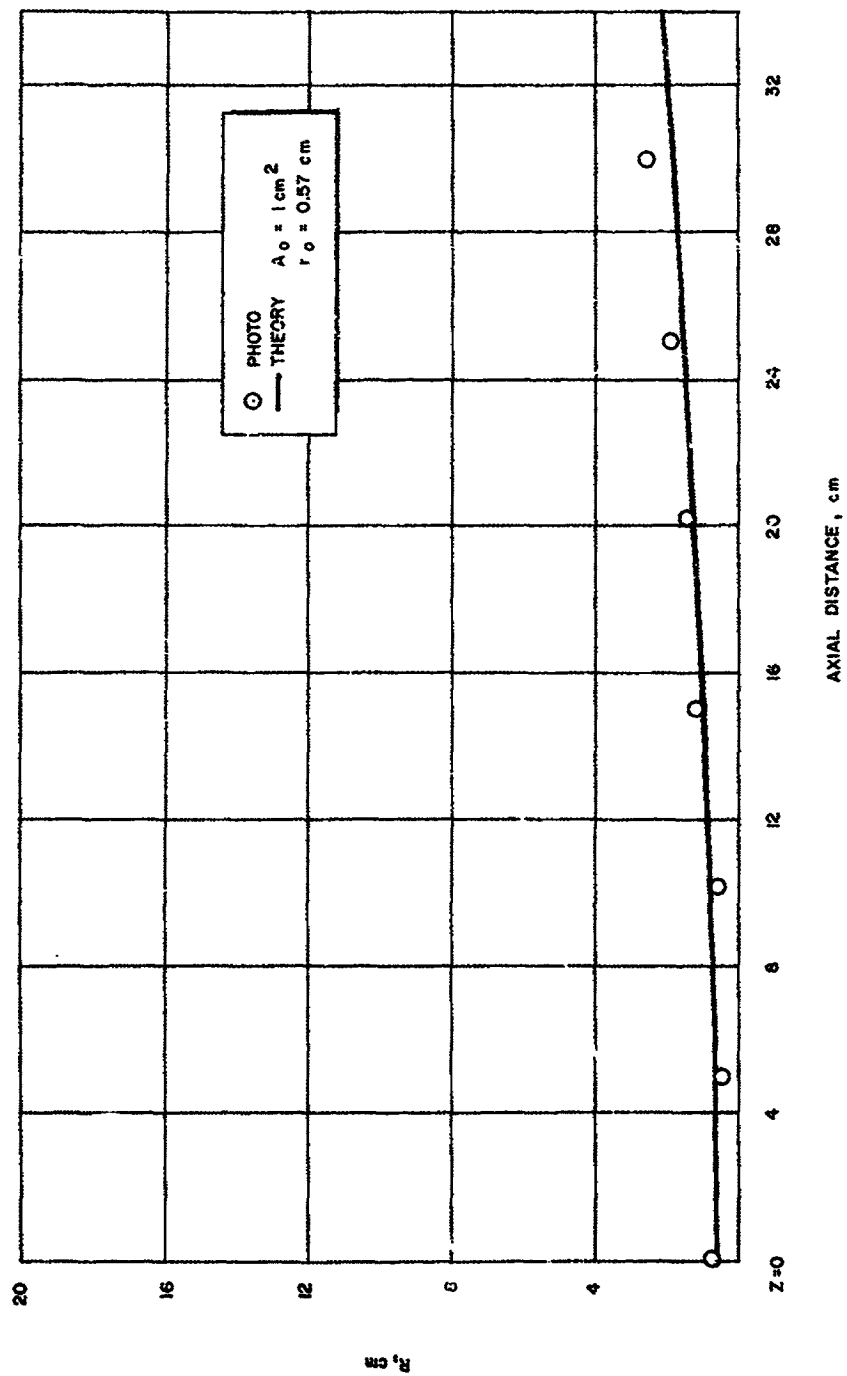
f. In general, the voltage has been quite insensitive to the specific impulse level. If the acceleration were predominantly through addition of directed kinetic energy to the plasma, one would expect the voltage to climb with specific impulse (analogous to the back emf in a motor).

3. Performance Calculations

Based on this simple picture of the acceleration process, order of magnitude calculations have been made of thruster performance. To date, a relation has been obtained for the thrust as a function of the engine operating parameters, subject to a number of simplifying assumptions. The analysis is proceeding in a direction such as to reduce the number of assumptions, and to derive also a relation for the overall efficiency.

The nozzle shape obtained in the first order analysis of appendix E is compared to measurements made from the photograph of figure 52 in figure 72 below. The theoretical nozzle shape was obtained simply by considering the magnet to be a single turn of 15 cm radius, and by stipulating that no plasma cross any magnetic field line. Starting with a circular cross section of area A_0 at the cathode tip, the nozzle channel remains circular in cross section with a cross sectional area which grows as

$$A = A_0 (1 + z^2/R^2)^{3/2}$$



65-10600

Figure 72 SHAPE OF THE MAGNETIC NOZZLE

where z is distance downstream. A_0 is unknown and was chosen as 1 cm^2 for convenience and to accord approximately with observations in the inner luminous jet.

The measured points in figure 72 are taken from the photograph of figure 52. The nozzle diameter at any z was taken to be the apparent width of the luminous inner jet. This measurement is, admittedly, subjective and crude; however, it is thought that within uncertainties of the order of 20 percent it is satisfactory. The agreement between the approximately calculated magnetic duct shape and the measurements of the luminosity diameter of the inner jet should not be evaluated too heavily; still, in the spirit of a first-order analysis it is encouraging.

It is next interesting to make first-order estimates of the plasma parameters in the nozzle. Again, these estimates will be made, not in an attempt to fix the plasma state precisely, but rather to indicate the orders of magnitude of temperature, density, etc., which are to be expected. For these purposes, it is convenient to choose a typical running condition. We select the case with:

$$\begin{aligned} V &= \text{arc voltage} = 80 \text{ volts} \\ I &= \text{arc current} = 100 \text{ amperes} \\ \dot{m} &= 5 \text{ mg/sec} \\ A_0 &= 1 \text{ cm}^2 \\ T &= \text{thrust} = 10 \text{ grams.} \end{aligned}$$

For this case, the thrust power is:

$$P_{th} = 4.8 \times 10^{-5} T I_{sp} = 0.96 \text{ kw}$$

and the kinetic enthalpy of the gas is

$$\frac{1}{2} u^2 = 2 \times 10^{12} \text{ ergs/gram.}$$

The stagnation enthalpy is larger by a factor probably between one and two, owing to frozen flow and incomplete expansion losses. We choose 1.25, so that

$$h_s = 2.5 \times 10^{12} \text{ ergs/gram}$$

and the total energy content of the discharge plasma is

$$E_{tot} = \dot{m} h_s = 1.25 \text{ kw.}$$

We now assume that the major portion of the heating occurs upstream of the sonic point, with perhaps 25 percent of the input power delivered in the supersonic region. Then, the total enthalpy at the throat is

$$h_{s,t} = 0.75 \times 2.5 \times 10^{12} = 1.8 \times 10^{12} \text{ ergs/gram}$$

and the total energy content of the discharge plasma is

$$E_{\text{tot}} = \dot{m} h_s = 1.25 \text{ kw} \cdot 25 \text{ kw}$$

We expect most of this to be in the form of static enthalpy, with a small fraction already in directed form. A rough estimate of the enthalpy of cesium as a function of temperature is given in figure 73. This has been calculated simply as

$$h = N_0 \left(\frac{1}{\bar{m}} \right) \left[\frac{5}{2} kT + E_{\text{ion}} \frac{\bar{m}}{133} \right]$$

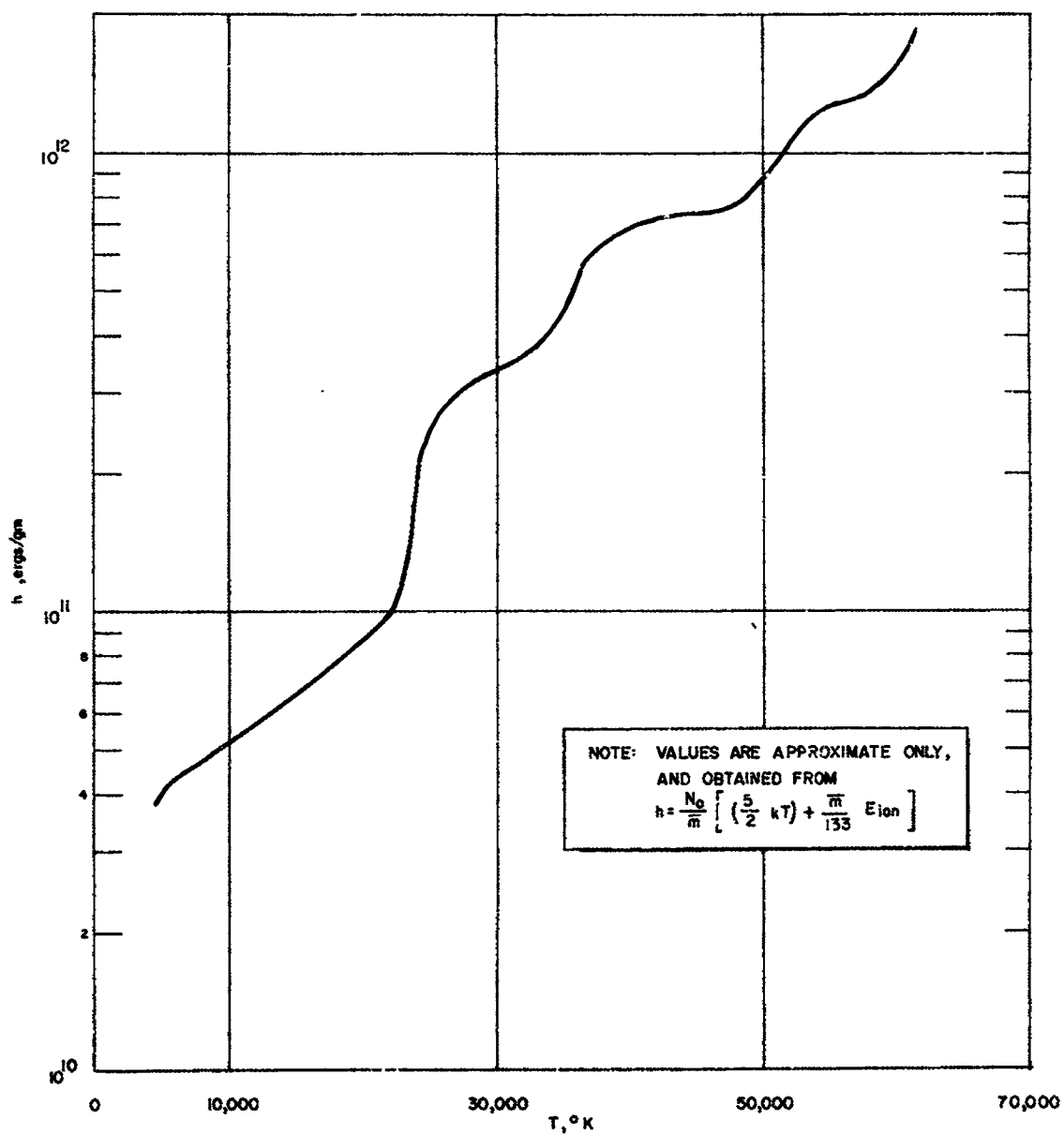
where N_0 is 6×10^{23} , \bar{m} is the mean molecular weight of the mixture of cesium, ions, and electrons, and E_{ion} is the energy per ion invested in ionization (including multiple ionization). Each stage of ionization was assumed to occur at a temperature such that

$$kT = \frac{E_I}{10}$$

where E_I is the ionization energy of the level in question. This is a fairly good assumption at low pressures, if there are sufficient collisions.

According to figure 73, an enthalpy of 1.8×10^{12} ergs/gram in cesium corresponds to a temperature of approximately 60,000°K, with essentially complete fourth ionization and partial fifth ionization. In this case, \bar{m} is about 25. We can now compute the sound speed from

$$a = \sqrt{\gamma \frac{R}{\bar{m}} T}$$



65-10601

Figure 73 ENTHALPY VERSUS TEMPERATURE FOR CESIUM

and we find with $\gamma = 1.4$

$$a = 5.3 \times 10^5 \text{ cm/sec.}$$

In this case, the directed kinetic enthalpy at the sonic point is given by

$$h_{K.E.,t} = 1/2 a^2 = 1.4 \times 10^{11} \text{ ergs/gm,}$$

or about 8 percent of the total enthalpy at the throat.

We next ask what are the electrical characteristics of the subsonic portion of the flow. At the throat temperature we find the electrical conductivity as given by Spitzer:³⁵

$$\sigma = \frac{2.6 \times 10^{-4} \gamma_e T^{3/2}}{Z \ln \lambda}$$

where γ_e is a fraction near unity for multiple ionization, $\ln \lambda$ is of the order of 10 for the conditions thought to exist in the MPD arcjet, and we take 4.5 for Z . Then

$$\sigma \sim 60 \text{ mho/cm.}$$

This conductivity actually is not a sensitive function of temperature down to the order of 10,000°K, for, as T decreases, Z also decreases. On the assumption that the entire subsonic region can be represented by a conductivity (along magnetic field lines) of 50 mho/cm, we find the electrical input power to be

$$P = I^2 R = I^2 \frac{l}{\sigma A} = 10^4 \times \frac{5}{50 \times 1} = 1 \text{ kw.}$$

For a 5 mg/sec flow rate $h_{s,t} = 2 \times 10^{12}$ ergs/gram, in fair agreement with the assumptions.

In summary, these first order estimates indicate the following approximate conditions in a typical cesium test:

Current	= 100 amperes
Voltage drop Cathode to sonic point	= 10 volts
Distance, Cathode to sonic point	= 5 cm
Enthalpy, sonic point	= 1.8 to 2 x 10 ¹² ergs/gram
Temperature, sonic point	= 60,000°K
Level of ionization	4 to 5
Sound speed, sonic point	5.3 x 10 ⁵ cm/sec
Density, sonic point $\left(\frac{\dot{m}}{a_c A}\right)$	10 ⁻⁸ gm/cm ³
Pressure, sonic point (nkT)	1.5 x 10 ⁻³ = 1 mm.

More careful analyses are planned, and they may change these estimates substantially, but in a qualitative sense they serve to indicate conditions which are present in the proposed magnetic nozzle.

It is finally of interest to examine the magnetic interaction parameter, $\sigma B^2 l / \rho v$. If there is an effective nozzle, this must greatly exceed unity. Using sonic point conditions, and MKS units,

$$\frac{\sigma B^2 l}{\rho v} \sim \frac{5 \times 10^3 \times 10^{-2} \times 10^{-1}}{10^{-5} \times 5 \times 10^2} \sim 100.$$

V. CURRENT DEVELOPMENT STATUS OF THE MPD ARCJET

The MPD arcjet and similar devices (e.g., the Hall current accelerator, the Hare jet, the magnetic annular arc, etc.) continue to hold promise as electric propulsion devices because of a relatively high thrust per unit cross sectional area compared to the ion engine, an "apparent" high electric to thrust power energy conversion efficiency, e.g., > 50 percent at 5000 seconds, lightweight power conditioning requirements, and simplicity. The enthusiasm for the device is, however, tempered by the observation that in operation with gaseous propellants, e.g., hydrogen and ammonia, at power levels of the order of tens of kilowatts and mass flow rates less than 0.01 gm/sec there is clear evidence of an interaction between the test environment and the acceleration process, which would not be present in the hard vacuum of space. This interaction is illustrated by the observation that the engine continues to run, without electrode erosion, at a no-mass-flow condition; this is clearly indicative of either mass flow ingestion into the engine or mass flow entrainment into the exhaust region. The possibility of entrainment and/or ingestion unfortunately puts into question some of the propulsion performance results on which the early enthusiasm for the MPD arcjet was based. Recent propulsion performance data obtained using the condensable alkali metal vapors, e.g., lithium, at low back pressures (order of 10^{-9} to 10^{-6} mm Hg), although promising, are still not conclusive evidence that the MPD arcjet will give the same performance in both a laboratory and space environment.

Apart from the question of the effect of test environment on MPD arcjet performance, other fundamental questions pertaining to the nature of the MPD arcjet acceleration and energy loss mechanisms remain unanswered.

1. At current flows of the order of thousands of amperes and with a negligible external magnetic field the measured engine thrust can be predicted analytically and is clearly identified with self-induced magnetic pumping, $j_z B_\theta$, and magnetic blowing, $j_r B_\theta$, effects. Predictions of overall electric-to-thrust-power efficiency can be made for this mode of operation based on complete ionization, frozen flow, and assumed anode and cathode fall voltages; however, neither the significance nor validity of these predictions is clear. Further, particularly in the case of the gaseous propellants and their attendant high test tank pressure, due to uncertainties in the "actual" mass flow rate, the significance of the "measured" electric-to-thrust-power efficiency is not certain.
2. At current flows of the order of tens and hundreds of amperes and with an externally applied magnetic field of the order of a kgauss the nature of the acceleration mechanism is not clear. Speculation on the nature of the acceleration process includes: (i) interaction of an induced azimuthal

current, i_θ , with the applied field, B_r ; (ii) electrothermal acceleration of the gas resulting from local joule heating; (iii) conversion of rotational kinetic energy (resulting from the interaction of the applied field, B_z , with the applied current, i_r), into directed kinetic energy in a magnetic nozzle; and, finally, (iv) a combination of all three. Again, as in the case of operation with self-induced fields, both analytical predictions and clear measurements on the electric-to-thrust-power efficiency are lacking.

3. In the case of water-cooled engines operated with gaseous propellants the apparent anode fall voltage, defined as the ratio of anode power to current flow, was relatively insensitive to propellant and magnetic field and was of the order of 25 volts. In the case of cesium, the apparent anode fall voltage was not independent of the current. The reason for the apparent discrepancy in anode behavior between the gaseous propellants and alkali metal vapor is not clear.

4. A critical factor in the evaluation of the possible significance or lack of significance of entrainment in terms of engine performance is the determination of the extent of the zone of thermal and/or kinetic energy addition. Although the existence of current paths downstream of the engine has been identified, the extent of the actual acceleration zone is unknown. It is important to recognize that gas entrainment outside of the gas acceleration zone will not affect engine propulsion performance.

5. Critical to an examination of the MPD arcjet acceleration process is experimental information with regard to the degree of ionization, and the electron and ion temperatures in the MPD arcjet exhaust. Estimates of the degree of ionization by different investigators using different techniques range from slightly to fully ionized. In the case of a fully ionized plasma, the steady-state Hall currents would, of course, be negligible.

VI. DIRECTION FOR FUTURE RESEARCH

1. Systematic thrust stand data are needed on the performance of a series of alkali metal vapor MPD arcjet engines as a function of configuration, current, magnetic field strength, mass flow rate, and tank pressure.
2. The thrust and specific impulse data obtained as part of item (1) must be complemented with simultaneous direct velocity measurements in the MPD arcjet exhaust. The exhaust velocity measurements should be carried out by means of a number of different techniques including Faraday-type probes, double Langmuir probes, and particle time-of-flight measurements using photomultipliers. The velocity measurements, when compared to the specific impulse measurements, will give an estimate of the significance of gas entrainment as a function of operating conditions.
3. Knowledge of the nature and extent of the acceleration region can be enhanced by a series of local B-field and E-field measurements which, in turn, can be used to establish local current, local conductivity, and local joule heating. The local magnetic field components, i.e., B_z , B_θ , B_r , can be measured by means of local, solid-state Hall probes; and the local field, i.e., E_z , E_θ , and E_r , by floating probes. The local axial velocity measurements, U_z , obtained under item (2) should be complemented by local azimuthal velocity measurements, U_θ , to investigate the possibility of the conversion of swirl velocity (resulting from the interaction of the axial magnetic field, B_z , and the radial current component, j_r) to directed kinetic energy.
4. A significant energy loss mechanism in the MPD arcjet is the power transferred to the engine electrodes, in particular, to the anode. Systematic data are required to establish the effect on anode heating, if any, of propellant, electrode configuration, and magnetic field strength. Of particular interest is the apparent difference in behavior between the anode performance of the gaseous and alkali metal vapor propellants.
5. Experimental information is required on the degree of ionization in the MPD arcjet exhaust both for the purpose of fixing electric-to-thrust-power efficiency limits, and to establish the nature of the acceleration process.

VII. REFERENCES

1. Ducati, A. C., G. M. Gianni, and E. Muehlberger, Experimental Results in High-Specific-Impulse Thermo-Ionic Acceleration, AIAA J. 2, 1452 (1964).
2. Schoeck, P. A., The Magnetohydrodynamic Arc Thrustor, ARO Internal Report (August 1964).
3. Cann, G. L., Annular Magnetic Hall Current Accelerator, AIAA Paper 64-670 (1964).
4. Avco RAD, Arcjet Technology Research and Development, First Quarterly Progress Report, RAD-SR-64-239, on Contract No. NAS 3-5900 (October 1964).
5. Maecker, H., Plasmatornungen in Lichtbogen infolge ergen magnetischer Kompression, Z. Phys., 141, 198 (1955).
6. Hess, R. V., Experiments and Theory for Continuous Steady Acceleration of Low Density Plasmas, Proceedings of the XI International Astronautical Congress, Stockholm, Volume I, pp. 404-411 (1960).
7. Hess, R. V., Fundamentals of Plasma Interaction with Electric and Magnetic Fields, Proceedings of the NASA -- University Conference on the Science and Technology of Space Exploration, Paper No. 59, Volume 2 (November 1963).
8. Ellis, M. C., Jr., Survey of Plasma Accelerator Research, Proc. NASA --University Conference, Paper No. 62 (November 1963).
9. Powers, W. E., and R. M. Patrick, A Magnetic Annular Arc, Avco Everett Research Laboratory Report RR-129 (May 1962).
10. Seikel, G. R., and E. Reshotoko, Hall Current Ion Accelerator, Bul. Am. Phys. Soc., 7, No. 6 (1962).
11. Cann, G. L., J. M. Teem, R. D. Buhler, and C. K. Branson, Magnetogas-dynamic Accelerator Techniques, AEDC-TDR-62-145 (July 1963).
12. Cann, G. L., and G. L. Marlotte, Hall Current Plasma Accelerator, AIAA J., 2, 1234 (1964).
13. Patrick, R. M. and W. E. Powers, Plasma Flow in a Magnetic Arc Nozzle, Third Symposium on Advanced Propulsion Concepts, Cincinnati, Ohio (October 1964).

REFERENCES (Cont'd)

14. Brandmaier, A. E., J. L. Durand, M. C. Gourdine, and A. Rubel, An Investigation of Hall Propulsor Characteristics, AIAA J., 2, 674 (1964).
15. Patrick, R. M., Study of Magnetic Annular Plasma Accelerator, Second Quarterly Progress Report on Contract No. NAS 3-5748 (September 1964).
16. Cann, G. L., P. D. Lenn and R. L. Harder, Hall Current Accelerator, EOS Report 5470-QL-1, First Quarterly Progress Report on Contract No. NAS 3-5909 (October 1964).
17. Ducati, A. C., E. Muelberger, and J. P. Todd, Design and Development of a Thermo-Ionic Electric Thrustor, Giannini Scientific Corp. Interim Report on Contract No. NAF w-968 (September 1964).
18. Grossman, W., R. V. Hess and H. A. Hassan, Experiments with a Coaxial Hall Current Plasma Accelerator, AIAA Paper No. 64-700 (1964).
19. Ducati, A. C., G. M. Giannini, and E. Muehlberger, Recent Progress in High Specific Impulse Thermionic Acceleration, AIAA Second Aerospace Sciences Meeting, Preprint 65-96 (January 1965).
20. Hess, R. V. (personal communication, March 1965).
21. Arc Jet Technology Research and Development, Second Quarterly Progress Report, Avco RAD-SR-65-5, Contract NAS 3-5900 (December 1964).
22. High Specific Impulse Thermal Arc Jet Thrustor Technology, ASD-TR-64, EOS Interim Report 5090-1, Contract AF33 (615)-1570.
23. Patrick, R. M., and A. Schneidermann, Performance Characteristics of a Magnetic Annular Arc, Avco-Everett Research Report No. 209 (March 1965).
24. Fabry, Eclairage Electrique 17, 133 (1898).
25. G. Sutton et al, Communications and Electronics, 687 (1962).
26. Hess, R. V., et al, Theory and Experiments for the Role of Space-Charge in Plasma Acceleration in Proceedings of the Symposium on Electromagnetics and Fluid Dynamics of Gaseous Plasma, Polytechnic Press, New York (1961).
27. Brockman, P., R. Hess, F. Bowen, and O. Jarrett, Diagnostic Studies in a Hall Accelerator at Low Exhaust Pressure, AIAA Second Annual Meeting, Preprint 65-297, (July 1965).

REFERENCES (Concl'd)

28. Patrick, R. M., and W. E. Powers, Plasma Flow in a Magnetic Arc Nozzle, 3rd Symposium on Advanced Propulsion Concepts (October 1962).
29. Cann, G. L., P. D. Lenn, and R. L. Harder, Hall Current Accelerator, Third Quarterly Progress Report, Contract NAS 3-5909 (20 March 1965).
30. Ducati, A. C., G. M. Giannini, and E. Huehlberger, Recent Progress in High Specific Impulse Thermoionic Acceleration, AIAA Second Aerospace Sciences Meeting, Preprint 65-96 (January 1965).
31. Patrick, R. M., and A. Schneiderman, Study of Magnetic Annular Plasma Accelerator, Fourth Quarterly Progress Report on Contract NAS 3-5748 (April 1965).
32. Cann, G. L., and R. L. Harder, Follow-On Investigation of a Steady State Hall Current Accelerator, Final Report, Contract NAS 3-3568 (30 October 1964).
33. Grossman, W., R. V. Hess, and H. A. Hassan, Experiments with a Coaxial Hall Current Plasma Accelerator, AIAA Journal 3, pp 1034-1039 (June 1965).
34. Moore, R. A., G. L. Cann, and L. R. Gallagher, High Specific Impulse Thermal Arc Jet Thrustor Technology, AFAPL-TR-65-48, Part I (June 1965).
35. Spitzer, L., Physics of Fully Ionized Gases, Interscience Tracts on Physics and Astronomy, Number 3, 2nd Ed., Interscience Publishers, division of John Wiley and Sons, New York, London (1962).
36. EOS, Hall Current Accelerator, Fourth Quarterly Progress Report, NAS-3-5909 (June 20, 1965).
37. John, R. R., S. Bennett, and J. F. Connors, Experimental Performance of a High Specific Impulse Arc Jet Engine, AIAA Paper No. 64-669 (1964).
38. Davies, Mason, and Munn, Phys. Fluids 8, 444 (1965).

BLANK PAGE

APPENDIX A

HIGH SPECIFIC IMPULSE ENGINE PERFORMANCE DATA

1. Performance Data for X-2C High Specific Impulse Engine

Tables A-1, A-2, and A-3 list performance values which have been obtained with the X-2C engine in hydrogen, ammonia, and argon, respectively.

2. Pressure-Tap Cathode Results

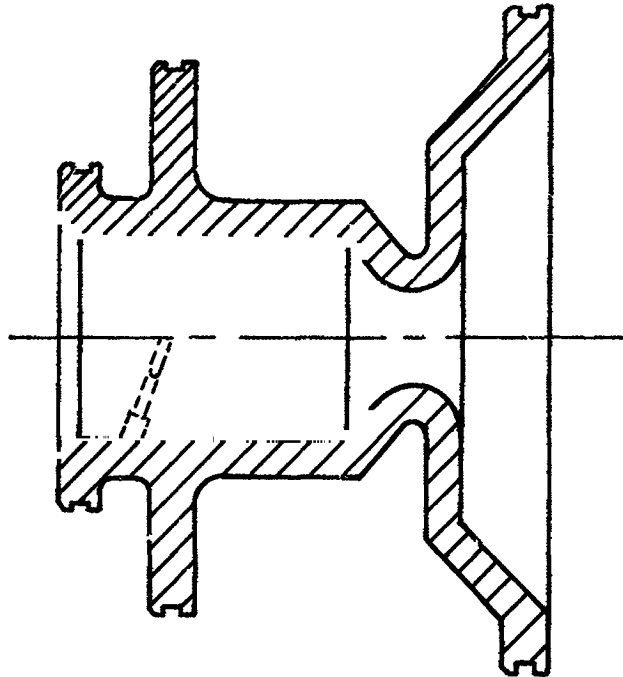
Table A-4 lists measurements which have been made with an X-2C engine in which the cathode contained a 2.3 mm diameter pressure tap at the tip.

3. Performance Data for X-2A High Specific Impulse Engine

The X-2A engine differs from the X-2C in two respects. The X-2C nozzle is replaced by the nozzle shown in figure A-1, and the separately excited magnetic field is replaced by a self excited magnetic field mounted on the thruster. Data on X-2A engine performance are listed in table A-5.

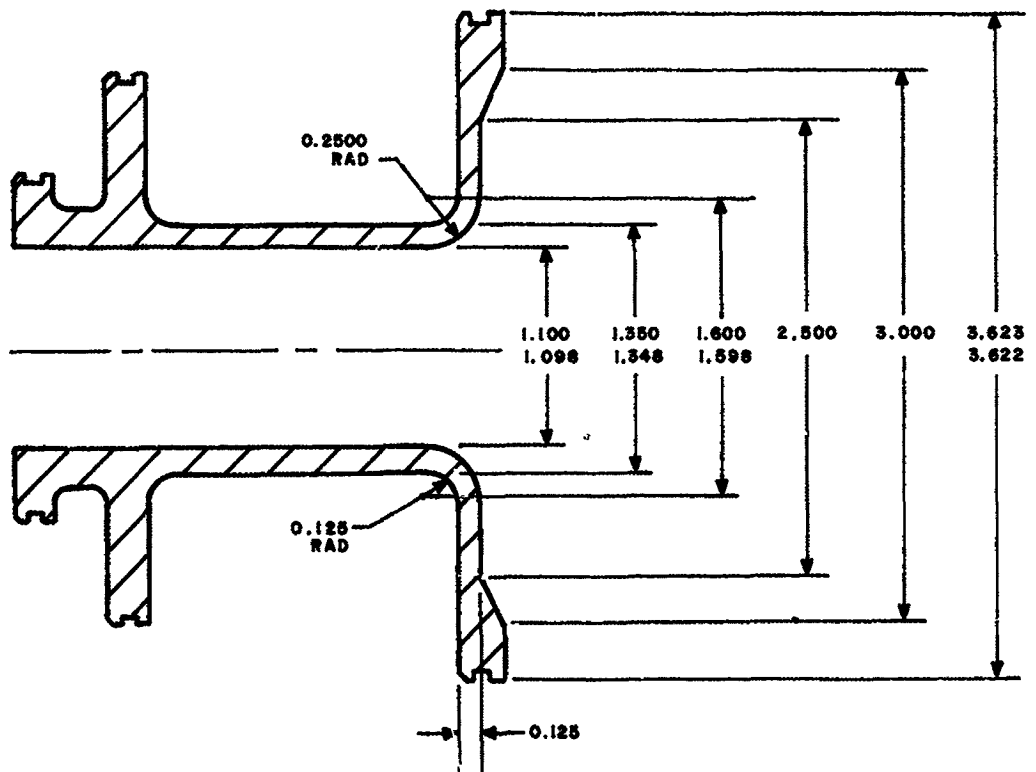
4. Performance Data for X-2B High Specific Impulse Engine

The X-2B engine differs from the X-2C in that the nozzle of the X-2C is replaced by the configuration shown in figure A-2, while the cathode is replaced by a hemisphere tipped rod. Data obtained with the X-2B engine configuration are listed in table A-6.



64-10347

Figure A-1 CONFIGURATION X2-A



64-10348

Figure A-2 CONFIGURATION X2-B

TABLE A-1
PERFORMANCE DATA ON A HIGH SPECIFIC IMPULSE ARCJET ENGINE (X-2C)
OPERATED WITH HYDROGEN

Run No.	Gas Flow \dot{m} gm/sec	Arc Current I amps	Arc Voltage V volts	Arc Power P _{arc} kw	Thrust T _{total} gm	Specific Impulse I _{sp} seconds	Thrust Power P _{thrust} kw	Overall Eff. % percent	Chamber Pressure P mm of Hg	Aero. Thrust T _{aero} gm	MPD Thrust T _{MPD} gm
1	0.05	1100	64	71	84	1680	6.9	8.2	22	37	47
2	0.04		65	72	80	2000	7.7	10.8	20	34	46
3	0.03		64	71	77	2560	9.6	13.5	15	25	52
4	0.02		64	71	70	3500	11.8	16.9	11	18	52
5	0.013	1150	65	75	66	4960	20.4	27.2	7	12	54
6	0.05	1500	71	107	123	2460	14.7	13.7	22	37	86
7	0.04		70	105	114	2850	15.7	15.0	21	35	79
8	0.03		67	100	104	3470	17.4	17.4	17	28	76
9	0.02		68	102	100	5000	24.1	23.6	11	18	82
10	0.013		70	105	96	7220	33.2	31.7	7	12	84
11	0.05	2000	74	148	173	3460	29.0	19.6	26	44	129
12	0.04		68	136	154	3850	28.6	21.0	23	39	115
13	0.03		67	134	140	4670	31.6	23.6	17.5	29	111
14	0.02		70	140	131	6550	41.5	29.6	12	20	111
15	0.013		76	152	135	10150	65.7	43.3	7.5	13	122
16*	0.010	1900	75	143	154	15400	114	79	--	--	--
17	0.05	2500	78	195	226	4520	49.6	25.4	29	49	177

*Arc Operation Unstable

TABLE A-2
PERFORMANCE DATA ON A HIGH SPECIFIC IMPULSE ARCJET ENGINE (X-2C)
OPERATED WITH AMMONIA

Run No.	Gas Flow \dot{m} gm/sec	Arc Current I amps	Arc Voltage V volts	Arc Power P_{arc} kw	Thrust T_{total} gm	Specific Impulse I_{sp} seconds	Thrust Power P_{thrust} kw	Overall Eff. ϵ_o percent	Chamber Pressure P mm of Hg	Aero. Thrust T_{aero} gm	MPD Thrust T_{MPD} gm
1	0.03	1100	34	37.4	68	2260	7.4	19.8	120	20.6	47.4
2	0.06	1500	36	54	92	1540	6.8	12.6	--	--	--
3	0.03		36	54	90	3000	13.0	24.0	11.5	19.8	70.2
4	0.06	2000	37	74	140	2330	15.6	21.1	--	--	--
5	0.05		36	72	135	2700	17.5	24.3	15.0	25.8	109.2
6	0.04		39	78	123	3080	18.2	23.4	13.0	22.4	100.6
7	0.03		39	78	115	3840	21.1	27.0	10.0	17.2	97.8
8	0.03		46	92	135	4500	29.1	31.6	10.0	17.2	117.8
9	0.02		37	74	97	4850	22.6	30.6	8.0	13.8	83.2
10	0.015		37	74	92	6140	27.1	36.6	6.0	10.3	81.7
11	0.015	2500	35	87.5	97	6500	30.1	34.4	5.0	8.6	88.4

TABLE A-3
PERFORMANCE DATA ON A HIGH SPECIFIC IMPULSE ARCJET ENGINE (X-2C)
OPERATED WITH ARGON

Run No.	Gas Flow \dot{m} gm/sec	Arc Current I amps	Arc Voltage V volts	Arc Power P_{arc} kw	Thrust T_{total} gm	Specific Impulse I_{sp} seconds	Thrust Power P_{thrust} kw	Overl. Eff. ϵ_o percent	Chamber Pressure P mm of Hg	Aero. Thrust T_{aero} gm	MPD Thrust T_{MPD} gm
1	0.049	1500	24	36	50	1020	2.5	6.8	13.5	23.2	26.8
2	0.032		25	37.5	55	1720	4.5	12.1	8.8	15.1	39.9
3	0.11	2000	25	50	92	840	3.7	7.4	21.5	37.0	55.0
4	0.049		25	50	58	1180	3.3	6.6	12.5	21.5	36.5
5	0.032	2100	30	62	69	2160	7.1	11.5	7.0	12.0	57.0

TABLE A-4
PERFORMANCE DATA ON A HIGH SPECIFIC IMPULSE ARCJET ENGINE OPERATED WITH
HYDROGEN AND WITH A PRESSURE TAP

m gm/sec	I amps	V volts	T grams	P cath. mmHg	P cham. mmHg	T _{aero} grams	T _{mpd} grams	T pinch grams	T blower grams
0.050	1100	54.5	85	77	35	61	24	6	18
	1500	57	100	98	35	61	39	11	28
0.040	1100	48	67	62	26	45.5	21.5	6	15.5
	1500	54	94.5	90	29.5	51	43.5	11	32.5
	2000	57.5	131	121	31	54	77	20	57
0.030	1100	46	59	50	23	40	19	6	13
	1500	50.5	85.5	80	23	40	45.5	11	34.5
	2000	53	114	107	23	40	74	20	54
0.020	1100	42	58	44	16	28	30	6	24
	1500	48	76	67	15	26	50	11	39
	2000	53	108	85	14	24	84	20	64
0.0133	1100	36.5	45	45	9.5	16.5	28.5	6	22.5
	1500	44	66	57.5	8.5	15	51	11	40
	2000	48	99	71	8.2	14	85	20	65

TABLE A-5
PERFORMANCE DATA ON A HIGH SPECIFIC IMPULSE ARCJET ENGINE (X-2A)
OPERATED WITH HYDROGEN

Run No.	Gas Flow \dot{m} gm/sec	Arc Current I amps	Arc Voltage V volts	Arc Power P_{arc} kw	Thrust T_{total} gm	Specific Impulse I_{sp} seconds	Thrust Power P_{thrust} kw	Overall Eff. ϵ_o percent	Chamber Pressure P mm of Hg	Aero. Thrust T_{aero} gm	MPD Thru T_{MPD} gm
1	0.050	1140	63	72	100	2000	9.6	13.3	46	77	23
2		1450	68	98	132	2640	16.8	17.1	49	82	50
3		1560	69	108	136	2720	17.8	16.5	50	84	52
4		1700	70	119	156	3120	23.4	19.7	50	84	72
5		1870	72	134	172	3440	28.4	21.1	50	84	88
6		2000	74	148	197	3940	37.2	25.1	50	84	113
7		2200	76	167	221	4420	46.8	27.1	50	84	137
8	0.040	2120	72	153	197	4980	47.2	30.8	40	67	130
9	0.026	2360	82	196	192	7400	68.2	35.3	14	23	169

TABLE A-6
PERFORMANCE DATA ON A HIGH SPECIFIC IMPULSE ARCJET ENGINE (X-2B)
OPERATED WITH HYDROGEN

1	0.049	2000	60	120	55	1130	3.0	2.5	--	--	--
2	0.049	1600	80	128	62	1260	3.8	3.0	5	21	41
3	0.039	2100	60	126	58	1470	4.2	3.3	--	--	--
4	0.049	2000	70	140	77	1560	5.8	4.2	7	--	--

BLANK PAGE

APPENDIX B

CALCULATION OF CONTRIBUTIONS TO T

We assume the following current distribution, referring to figure B-1:

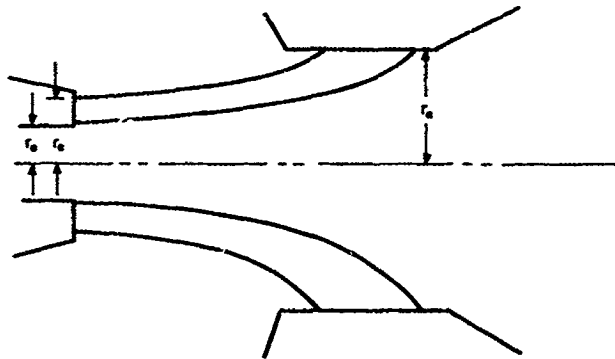


Figure B-1

At the cathode

$$j = 0 \text{ for } r < r_0$$

$$j = \text{constant for } r_0 < r < r_c$$

$$j = 0 \text{ for } r > r_c$$

At the anode

$$j = 0 \text{ except at } r = r_a.$$

With this assumption of current density distribution at the electrode surfaces, we first compute r_c from the cathode tip overpressure, then T_{pump} , and finally, T_{blow} .

1. Cathode Tip Overpressure

For $r_0 < r < r_c$ the current density at the cathode surface is

$$j_z = \frac{1}{\pi(r_c^2 - r_0^2)} \quad (\text{B-1})$$

and the resulting azimuthal magnetic field is given by Maxwell's equation for curl B as

$$B_\theta = \frac{2I}{r} \left(\frac{r^2 - r_0^2}{r_c^2 - r_0^2} \right) \quad (\text{B-2})$$

We equate the radial $j \times B$ force resulting from the interaction of this axial current density with the azimuthal magnetic field to the radial pressure gradient:

$$j_z B_\theta = \frac{2I^2}{\pi(r_c^2 - r_0^2)^2} \left(\frac{r^2 - r_0^2}{r} \right) = -dP/dr, \quad (B-3)$$

Hence,

$$P = P_0 + \frac{2I^2}{\pi(r_c^2 - r_0^2)^2} \int_r^{r_c} \frac{r^2 - r_0^2}{r} dr \quad (B-4)$$

$$P - P_0 = \frac{2I^2}{\pi(r_c^2 - r_0^2)^2} \left[\frac{r_c^2 - r^2}{2} - r_0^2 \ln \frac{r_c}{r} \right] \quad (B-5)$$

where $P - P_0$ is the cathode tip over pressure. The quantity measured is $P(r_0)$ which is obtained from equation (B-5) by letting $r = r_0$.

$$P(r_0) - P_0 = \frac{I^2}{\pi(r_c^2 - r_0^2)} \left[1 - \frac{r_c^2}{r_c^2 - r_0^2} \ln \left(\frac{r_c}{r_0} \right)^2 \right] \quad (B-6)$$

For mathematical convenience we define $r_c/r_0 = \beta$ so that

$$P(r_0) - P_0 = \frac{I^2}{\pi r_0^2} \left[\frac{\beta^2 - 1 - \ln \beta^2}{(\beta^2 - 1)^2} \right] \quad (B-7)$$

The measured pressure values as a function of current now determine β and hence r_c as a function of current. Numerical values are computed later in this appendix.

T_{pump}

By definition,

$$T_{\text{pump}} = \int_0^R [P(r) - P_0] 2\pi r dr \quad (B-8)$$

where R is the outer radial extent of the cathode. From equation (B-5), $P - P_0$ is non-zero only for $r < r_c$, so that the upper limit of integration in equation (B-8), R , can be replaced by r_c . Making this change, and substituting for $P(r) - P_0$ from equation (B-5) for $r_0 < r < r_c$, and the value of equation (B-5) for $r = r_0$ when $0 < r < r_0$, we find:

$$T_{\text{pump}} = \frac{2I^2}{\pi(r_c^2 - r_0^2)} \left[\int_0^{r_0} \left(\frac{r_c^2 - r_0^2}{2} - r_0^2 \ln \frac{r_c}{r_0} \right) 2\pi r dr + \int_{r_0}^{r_c} \left(\frac{r_c^2 - r^2}{2} - r_0^2 \ln \frac{r_c}{r} \right) 2\pi r dr \right]. \quad (\text{B-9})$$

Carrying out the indicated integration gives:

$$T_{\text{pump}} = I^2/2 \quad (\text{B-10})$$

which is the same relation used for the cylindrical sheet discharge.*

T_{blow}

The blowing term is now evaluated from a relation given in reference 37 and reproduced here:

$$F_Z = T_{\text{blow}} = \int_0^\infty \frac{I_c^2(r) - I_a^2(r)}{r} dr \quad (\text{B-11})$$

where

$$I_c(r) = \int_0^r 2\pi r j_c(r) dr$$

and

$$I_a(r) = \int_0^r 2\pi r j_a(r) dr$$

*It can be proven, although it is not demonstrated here, that T_{pump} always is given by $\frac{1}{2}I^2$, independent of the current density distribution.

For the current density distribution used in this appendix,

$$\begin{aligned}
 I_c(r) &= 0 & r < r_o \\
 \left(\frac{r^2 - r_o^2}{r_c^2 - r_o^2} \right) I, & r_o < r < r_c \\
 I, & r > r_c \\
 I_a(r) &= 0 & r < r_a \\
 I, & r \geq r_a
 \end{aligned}$$

the integral of equation (B-11) becomes

$$\begin{aligned}
 T_{\text{blow}} &= I^2 \left[\int_{r_o}^{r_c} \frac{(r^2 - r_o^2)^2}{(r_c^2 - r_o^2)^2} \frac{dr}{r} + \int_{r_c}^{r_a} \frac{dr}{r} \right] \\
 &= I^2 \left[\frac{\frac{r_c^4}{4} - r_c^2 r_o^2 + r_o^4 \ln r_c - \frac{r_o^4}{4} + r_o^4 - r_o^4 \ln r_o}{r_c^4 - 2 r_o^2 r_c^2 + r_o^4} + \ln \frac{r_a}{r_c} \right].
 \end{aligned} \tag{B-12}$$

Again using $\beta = r_c/r_o$, and neglecting terms of order $r_o^4 \ln$,

$$T_{\text{blow}} = I^2 \left[\ln \frac{r_a}{r_c} + \frac{1}{4} \left(\frac{\beta^2 - 3}{\beta^2 - 1} \right) \right]. \tag{B-13}$$

This differs from the result obtained for a cylindrical sheet current by the addition of the term $1/4 (\beta^2 - 3/\beta^2 - 1)$. Since typically, β is of the order of 2 or 3, the additional term is of the order $0.1I^2$ to $0.2I^2$.

2. Numerical Results

For the current distribution used in this appendix we evaluate T_{self} as a function of current and compare the values so obtained with those calculated for a cylindrical sheet current distribution.

a. $T_{\text{pump}} = 1/2 I^2$

b. β is evaluated from equation (B-7) using the measured $p(r_o) - p_o$. This is best done graphically.

c. $r_c = \beta r_o$

d. T_{blow} is evaluated from equation (B-13), using β obtained in step b, r_c in step c, and $r_a = r_{\text{throat}}$

e. $T_{\text{self}} = T_{\text{pump}} + T_{\text{blow}}$

The results are given in table B-I below:

TABLE B-I

FOR UNIFORM CATHODE CURRENT DENSITY WITH PRESSURE TAP

I amp	T_{pump} gram	β	r_c cm	T_{blow} gram	T_{self} gram	T_{self}^* gram
1000	5.1	2	0.230	11.5	16.6	17.5
1500	11.5	2.45	0.282	22.5	34.0	37.2
2000	20.4	2.75	0.316	36.2	56.6	59
2500	31.8	3.05	0.351	50.1	81.9	86.4

* T_{self} for cylindrical sheet current distribution

$r_o = 0.114$

$r_a = 0.635$

It is clear from table B-I that the effect of this variation in current distribution is small on T_{self} .

BLANK PAGE

APPENDIX C

MPD ARCJET ENGINE PERFORMANCE DATA

Tables C-I, C-II, and C-III list performance values which have been obtained with the X-2C MPD engine in hydrogen at mass flows of 0.05, 0.03, and 0.02 gm/sec, respectively. Tables C-IV and C-V list the performance values obtained in ammonia at mass flows of 0.058 and 0.029 gm/sec, respectively.

TABLE C-I

PERFORMANCE OF THE MPD ARC X-2C WITH HYDROGEN MASS FLOW OF 0.05 GM/SEC

Arc Current (amperes)	Field Coil Current (amperes)	Arc Voltage (volts)	Thrust (grams)	Specific Impulse (seconds)	Input Power (kw)	Thrust Efficiency (percent)	Power to Anode and Cathode (kw)	Thermal Efficiency (percent)
600	700	72	62	1240	43.3	8.5	18.7	57
1000		70.5	104	2080	70.5	14.8	26.8	62
1300		70.5	146	2920	91.7	22.3	32.0	65
1600		81	204	4080	129.5	30.9	38.3	70
600	800	76	66	1320	45.6	9.2	20.3	55
1000		76	116	2320	76.0	17.0	28.2	63
1300		80	158	3160	104.0	23.1	33.8	68
1600		86	216	4320	137.5	32.6	39.3	71
600	900	80	70	1400	48.0	9.8	20.7	57
1000		80.5	120	2400	80.5	17.1	29.1	64
1300		85	174	3840	110.5	26.3	34.7	69
1600		90	222	4440	144.0	32.8	40.2	72
600	1000	85	74	1480	51.0	10.3	21.7	57
1000		85	129	2580	85.0	17.8	30.0	65
1300		90	183	3660	117.0	27.5	36.5	69
1600		95	241	4820	152.0	36.7	41.2	73
600	1100	88.5	83	1660	53.1	12.5	22.6	57
1000		90	145	2900	90.0	22.4	31.0	66
1300		95	200	4000	123.5	31.1	37.4	70
1600		100	258	5160	160.0	40.0	41.6	74
600	1200	92	87	1740	55.2	13.2	22.6	59
1000		94	149	2980	94.0	22.6	31.9	66
1300		99	208	4160	129.0	32.2	37.9	71
1600		103.5	270	5400	166.0	42.2	42.6	74

TABLE C-II

PERFORMANCE OF THE MPD ARC X-2C WITH HYDROGEN MASS FLOW OF 0.03 GM/SEC

Arc Current (amperes)	Field Coil Current (amperes)	Arc Voltage (volts)	Thrust (grams)	Specific Impulse (seconds)	Input Power (kw)	Thrust Efficiency (percent)	Power to Anode and Cathode (kw)	Thermal Efficiency (percent)
600	600	65.5	58	1930	39.3	13.7	17.2	56
1000		67	104	3460	67.0	25.8	25	63
1300		65.5	129	4300	85.0	31.3	29.7	65
1600		89	234	7810	143	61.2	36.7	74
600	700	70	62	2070	42.0	14.7	16.4	61
1000		75	121	4030	75.0	31.2	25.4	66
1300		83	175	5830	107.7	45.5	31.5	71
1600		91	250	8320	146	68.5	37.1	75
600	800	75	66	2200	45.0	15.5	18.5	59
1000		80	129	4300	80	33.3	26.9	66
1300		85.5	188	6260	111	51.0	33.0	70
1600		70	195	6500	112	54.4	37.0	67
600	900	79	70	2330	47.4	16.5	18.9	60
1000		80	133	4420	80	35.4	28.8	64
1300		83.5	179	5960	108.5	39.4	34.6	68
1600		87.5	241	8020	140	66.5	39.3	72
600	1000	82.5	74	2460	49.5	17.7	19.8	60
1000		82.5	133	4430	82.5	34.2	29.9	64
1300		86.5	181	6030	112	46.8	36.0	68
1600		90.0	245	8160	144	66.6	40.4	72
600	1100	85	78	2600	51	19.1	20.4	60
1000		85.5	141	4700	85.5	37.2	31.3	63
1300	1200	87.5	197	6560	104	59.7	35.6	66
1000		83	139	4620	83	37.2	30.0	64
600		87.5	80	2660	52.5	19.5	20.4	61

TABLE C-III

PERFORMANCE OF THE MPD ARC X-2C WITH HYDROGEN MASS FLOW OF 0.02 GM/SEC

Arc Current (amperes)	Field Coil Current (amperes)	Arc Voltage (volts)	Thrust (grams)	Specific Impulse (seconds)	Input Power (kw)	Thrust Efficiency (percent)	Power to Anode and Cathode (kw)	Thermal Efficiency (percent)
300	400	59	26	1300	17.7	9.7	7.9	55
400		56	34	1700	22.4	12.5	10.4	54
500		56	42	2100	28.0	15.0	11.8	58
300	600	62.5	28	1400	18.8	10.1	7.9	58
400		62	36	1800	24.8	12.5	13.0	48
500		61.5	52	2600	30.8	21.1	12.3	60
600		62.5	54	2700	37.5	18.7	16.2	57
1000		67	104	5200	67.0	38.7	24.2	64
1300		70	138	6900	91.0	50.2	29.5	68
1600	700	65	159	7950	104	58.3	35.6	66
600		68	65	3250	40.0	27.2	17.1	58
1000		70	112	5600	70.0	43.0	25.0	64
1300	800	70	150	7500	91.0	59.3	30.7	66
300		70	34	1700	21.0	13.3	8.8	58
400		71.5	50	2500	28.6	21.0	11.5	60
500	1000	71	65	3250	35.5	28.3	13.6	62
300		80	41	2050	24.0	16.7	9.2	62
400		80	60	3000	32.0	26.9	12.0	63
500	1200	79.5	74	3700	39.8	33.0	14.6	63
300		86	47	2350	25.8	19.8	9.7	62
400		86	58	3400	34.4	32.0	12.5	64
500		85	89	4450	42.5	44.5	15.1	66

TABLE C-IV

PERFORMANCE OF THE MPD ARC X-2C WITH AMMONIA MASS FLOW OF 0.058 GM/SEC

Arc Current (amperes)	Field Coil Current (amperes)	Arc Voltage (volts)	Thrust (grams)	Specific Impulse (seconds)	Input Power (kw)	Thrust Efficiency (percent)	Power to Anode and Cathode (kw)	Thermal Efficiency (percent)
600	350	38	48	830	22.8	8.3	15.1	34
	400	40.5	51	880	24.3	9.1	15.1	38
	600	44.5	61	1050	26.7	11.6	15.6	42
	800	47	66	1140	28.2	12.8	16.5	41
	1000	50	65	1120	30.0	11.7	17	43
	1200	54	74	1275	32.4	13.9	17.9	45
800	340	38	57	980	30.4	8.9	20	34
	400	40	64	1100	32	10.6	20	37
	600	43	74	1275	34.4	13.1	20	42
	800	45	83	1430	36.0	15.8	20.9	42
	1000	47	89	1535	37.6	17.3	21.9	42
	1200	51	95	1640	40.8	18.1	22.8	44
1000	300	39	52	895	39	5.6	23.8	39
	400	40.5	59	1020	40.5	7.2	23.8	41
	600	44	74	1275	44	10.2	23.8	46
	800	46	84	1450	46	12.6	24.2	47
	1000	48.5	90	1550	48.5	13.8	25.2	48
	1200	50	100	1725	50	16.6	26.1	48
1200	300	39	74	1280	46.8	9.6	27.1	42
	400	40	85	1465	48	12.5	27.1	44
	600	43	100	1725	51.7	16.0	27.6	47
	800	45	110	1900	54	17.0	28.1	48
	1000	49	120	2070	59	20.4	29	51
	1200	50	130	2240	60	23.4	30.4	49
1400	300	39	124	2140	54.6	23.2	31.5	42
	400	40	129	2220	55	24.4	31.1	44
	600	43	152	2620	60.2	31.8	31.3	48
	800	45	166	2860	63	36.2	34.3	46
	1000	48	176	3030	67.2	38.0	32.7	51
	1200	50	186	3200	70	41.0	35.6	49

TABLE C-V

PERFORMANCE OF THE MPD ARC X-2C WITH AMMONIA MASS FLOW OF 0.029 GM/SEC

Arc Current (amperes)	Field Coil Current (amperes)	Arc Voltage (volts)	Thrust (grams)	Specific Impulse (seconds)	Input Power (kw)	Thrust Efficiency (percent)	Power to Anode and Cathode (kw)	Thermal Efficiency (percent)
600	400	37.5	38	1310	22.5	10.7	16.2	28
	600	40.5	44	1520	24.3	13.1	16.7	31
	800	43	53	1830	25.8	17.8	17.2	33
	1000	45	56	1930	27.0	19.3	18.6	31
800	1200	49	61	2100	29.4	20.8	19.1	35
	400	35	52	1790	28	16.1	19.1	32
	600	40	58	2000	32	17.5	21	34
	800	42	67	2310	33.6	22	21.5	36
1000	1000	44	73	2520	34.2	25	22.9	35
	1200	46	75	2590	36.8	25.3	23.9	35
	400	35	55	1900	35	14.3	25	29
	600	39	66	2280	39	18.5	25.5	35
1200	800	41	75	2580	41	22.6	26.9	34
	1000	43	81	2790	43	25.2	27.8	35
	1200	45	87	3000	45	27.8	28.7	36
	400	35	59	2040	42	13.8	28.7	32
1400	600	38.5	74	2550	46.2	19.7§	28.7	38
	800	41.5	88	3040	49.8	25.7	29.8	40
	1000	44	94	3240	52.9	27.7	31.6	40
	1200	45	100	3450	54.0	30.6	32.6	40
1400	400	35	68	2345	49	15.6	30.7	37
	600	37.5	89	3070	52.5	24.9	31.6	40
	800	40	100	3450	56	29.4	32.6	42
	1000	43.5	111	3830	60.9	33.6	35.4	42
	1200	45	112	3860	63	32.8	36.4	42

BLANK PAGE

APPENDIX D

PROPULSION PERFORMANCE OF A LIQUID COOLED MPD THRUSTOR WITH CESIUM PROPELLANT

Point	Cesium Flow (gm/sec)	Arc Voltage (volts)	Arc Current (amps)	Arc Power (kw)	B (kilogauss)	Thrust (grams)
1	3.5×10^{-3}	110	85	9.35	2.2	9.4
2		115	80	9.2	2.5	8.7
3		115	80	9.2	2.75	8.1
4		115	80	9.2	3.05	7.4
5		114	80	9.12	3.3	6.7
6		110	85	9.35	2.2	8.1
7	3.8×10^{-3}	120	71	7.5	2.2	8.1
8		93	112	10.4	2.2	10.1
9		83	127	10.5	2.2	10.7
10	4.2×10^{-3}	80	130	10.4	2.2	9.4
11		79	130	10.3	2.75	9.4
12		75	131	9.8	2.2	8.7
13		70	132	9.2	1.65	8.7
14		69	135	9.3	1.65	8.7
15		64	135	8.6	1.65	8.7
16	5.1×10^{-3}	52	140	7.3	1.1	6.7
17		67	139	9.3	2.2	9.4
18		42.5	140	5.95	0.83	6.0
19	5.5×10^{-3}	37.5	140	5.25	0.66	5.4
20		64	138	8.8	2.2	10.7
21		44	140	6.15	1.1	6.7
22	6.0×10^{-3}	52	175	9.1	1.1	8.7
23		67	175	10.7	1.65	9.4
24		62	140	8.7	2.2	10.7
25		59	141	8.3	2.2	10.7

Point	I _{sp} (seconds)	Thrust Power (kw)	Overall Efficiency (percent)	Power to Cooling (kw)	Arc Efficiency (percent)	$\epsilon_o / \epsilon_{arc}$ (percent)
1	2690	1.21	13	6.25	33	39.5
2	2480	1.04	11.3	6.1	34	33.4
3	2320	0.9	9.8	5.9	36	27.2
4	2120	0.75	8.2	5.75	37	22.2
5	1920	0.62	6.8	5.6	38	17.9
6	2320	0.9	9.6	6.6	29	33.1
7	2120	0.83	11	5.4	28	39.3
8	2660	1.28	12.3	7.2	31	39.8
9	2810	1.44	13.7	7.2	32	42.9
10	2240	1.01	9.7	7.1	32	30.3
11	2240	1.01	9.8	6.9	33	29.7
12	2070	0.87	8.9	6.9	30	29.7
13	2070	0.87	9.5	6.9	25	38.0
14	2070	0.87	9.4	6.9	26	36.2
15	1700	0.71	8.3	6.6	23	36.1
16	1310	0.42	5.8	5.6	23	25.2
17	1840	0.83	8.9	6.6	29	30.7
18	1090	0.32	5.4	4.6	23	23.5
19	980	0.25	4.8	4.1	22	21.8
20	1945	1.0	11.4	6.3	28	40.6
21	1220	0.39	6.3	4.6	25	25.2
22	1450	0.61	6.7	6.9	24	28.0
23	1570	0.71	6.6	7.6	29	22.8
24	1780	0.92	10.6	6.3	27	39.3
25	1780	0.92	11.0	5.9	29	36.0

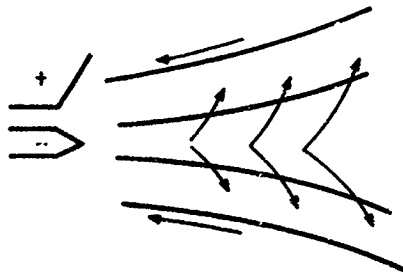
APPENDIX E

A THEORETICAL MODEL FOR THE MPD ARCJET IN A STRONG MAGNETIC FIELD

A. PRELIMINARY DESCRIPTION OF THE MODEL

In the model for the MPD arcjet proposed here, it is assumed that the externally applied magnetic field is sufficiently strong that it can effectively prevent the flow of gas across the magnetic field lines, so that gas and current flow are essentially constrained to follow the lines of the applied magnetic field. The applied field thus acts basically as a "magnetic nozzle" which confines the gas and allows it to be heated to rather high temperature by the arc current at relatively high pressures. Because of the high pressures, the electron energy can be transferred efficiently to thermal energy of the ions by collisions, and this energy is then converted into directed motion by expansion through the nozzle just as in the case of an ordinary material nozzle. The gas momentum is transferred back to the engine partially by direct gas pressure in the cathode region, but primarily indirectly through the magnetic field by gas pressure on the "magnetic nozzle." This latter interaction between the gas and the "magnetic nozzle" is, of course, just another way of describing the $\mathbf{j} \times \mathbf{B}$ forces on the gas.

In the "magnetic nozzle" model of the MPD arcjet proposed here, the region outside of the central gas flow should have a very low density and hence a very large value of $\omega\tau$ for electrons. Hence, in this region, current flow will be easy along the magnetic field lines, but very difficult across them. The arc current will thus tend to flow out from the



cathode along the central gas core for a considerable distance, but at the same time will gradually leak off through the surrounding low-density region across the magnetic field lines and return to the anode along the magnetic field lines, as indicated in the figure. Although the resistivity for current flow across the low-density sheath region is very high, the cross-sectional area is large and the current density at any point is low, so that the total arc current can get through this region without requiring an excessively high potential drop.

B. CONFINEMENT MECHANISM

For the arcjet model proposed above to be applicable, the applied magnetic field must, of course, be sufficiently strong to provide the assumed confinement of the gas jet. One necessary condition for this is evidently that the magnetic pressure of the applied field must be greater than the gas pressure, i.e.,

$$P < \frac{B^2}{8\pi} \quad (1)$$

For an applied magnetic field $B \approx 1000$ gauss, the magnetic pressure $B^2/8\pi \approx 0.1$ atm.,

so that condition (1) should be very well satisfied for the conditions existing in the MPD arcjet.

Equation (1) gives the maximum gas pressure which can be contained by the applied magnetic field if the gas does not leak across the magnetic field lines, but it does not indicate how long this pressure can be maintained under actual arc conditions. In order to investigate this confinement time, it is necessary to determine how fast the gas can diffuse across the magnetic field lines.

There are apparently a number of mechanisms by which this diffusion process can occur, and many of these are not well understood at the present time, so that it is not possible to give a definitive answer to this question here. However, it is possible to consider a few of the more likely diffusion mechanisms. One of the simplest of these is the diffusion produced by the finite resistivity of the gas. For this mechanism the diffusion velocity of the gas across the magnetic field lines is given by (Spitzer, 2nd edition, equation 2-39)

$$v_D = - \frac{1}{\sigma B^2} \nabla p = - \frac{1.78 \times 10^{-3} Z \ln \lambda}{B^2 T^{1/2}} \nabla n \quad (2)$$

Assuming a fully ionized gas with $T = 10,000^\circ\text{K}$, $p = 1$ mm Hg, and applied magnetic field $B = 1000$ gauss, and a jet diameter of about 1 cm, equation (2) gives a diffusion velocity $v_D \sim 10^5$ cm/sec. For a jet velocity $v \sim 10^6$ cm/sec (corresponding to a specific impulse $I_{sp} \sim 1000$), this gives $(v_D/v) \sim 0.1$ so that the gas flow is approximately along the magnetic field lines under these conditions. For higher temperatures or lower pressures, the diffusion velocity calculated from equation (2) would be smaller and the confinement of the gas to the magnetic field lines correspondingly better.

Another possible mechanism for the diffusion of gas across the magnetic field lines is provided by turbulence in the field. For this mechanism, Bohm has suggested a formula for the diffusion velocity of the form (Spitzer, equation 2-45)

$$\vec{v}_D = - \frac{540 \text{ T}}{nB} \vec{V}_n \quad (3)$$

For the jet conditions considered previously, this formula gives $v_D \sim 10^4$ cm/sec and $v_D/v \sim 10^{-2}$ so that again the gas is constrained to follow the field lines rather closely.

Although it is not possible to draw definite conclusions without a better understanding of the phenomena involved, it appears from the above discussion that for many conditions of interest in MPD arcjet operation it should be a good approximation to assume that the gas flow follows the magnetic field lines rather closely, so that the "magnetic nozzle" treatment of the flow will be applicable. This should be especially true for conditions of low mass flow or high specific impulse. The force which prevents the flow of gas across the magnetic field lines as discussed in the preceding paragraphs is of course just the usual magnetic induction force which arises when a conductor moves in a magnetic field. Thus, when the gas tries to move across the magnetic field lines, it induces an azimuthal current j_θ which interacts with the applied field B in such a way as to oppose the motion which produced it, and thus to keep the gas moving along the magnetic lines. Within the applicability of the magnetic nozzle approximation discussed above, we see that the induced current j_θ automatically adjusts to provide just the force which is required to keep the gas from moving across the field lines. Since this force is proportional to $j \times B$, it follows that, for the same gas conditions, the azimuthal current j_θ will be inversely proportional to the applied field B ,

$$j_\theta \propto \frac{1}{B}$$

while the gas flow and the net thrust produced will be independent of B , for sufficiently large applied fields B .

C. FLOW CONDITIONS IN THE "MAGNETIC NOZZLE"

For a first approximation, we may treat the flow of gas through the "magnetic nozzle" by means of conventional one-dimensional nozzle theory. The equations of motion then become:

$$\begin{aligned} \frac{d}{dz} (\rho v A) &= 0 \\ A \frac{dp}{dz} + \rho v A \frac{dv}{dz} &= 0 \\ \rho v A \frac{d}{dz} \left(h + \frac{1}{2} v^2 \right) &= S \end{aligned} \quad (5)$$

where A is the cross-sectional area of the nozzle, S is the power added to the flow per unit length, and all quantities are assumed to be functions only of the axial co-ordinate z . The cross-sectional area A is determined in this approximation by the condition that the total flux $\int B \cdot dA$ through the nozzle is constant, so that

$$A \propto \frac{1}{B} \quad (6)$$

where B is the applied field.

In order to get a qualitative idea of the nature of the solutions of equation (5), we now introduce the further approximations that the gas is ideal so that

$$h = \frac{\gamma}{\gamma - 1} \frac{p}{\rho} \quad (7a)$$

and that the energy deposition in the gas is entirely due to Joule heating

$$S = \frac{I^2}{A\sigma} \quad (7b)$$

where the arc current I and the electrical conductivity σ are assumed to be constants. One notes that among other things, equation (7) assumes that the gas is in equilibrium and that energy transport is negligible, two assumptions which are likely to be quantitatively rather poor. Further, we assume that the magnetic field is that produced by a single coil of radius R , so that along the axis

$$B = \frac{2\pi i_B R^2}{(z^2 + R^2)^{3/2}}.$$

The corresponding area from equation (6) is then

$$A = A_0 (1 + z^2/R^2)^{3/2} \quad (8)$$

where A_0 is the cross-sectional area of the flow at $z = 0$.

Using equations (7) and (8), the mass energy conservation equations (5a) and (5c) may now be integrated to give

$$\rho v A = \dot{m}$$

$$h + \frac{1}{2} v^2 = W \sqrt{\frac{\xi}{1+\xi}} \quad (9)$$

with

$$W = \frac{I^2 R}{\sigma \dot{m} A_0} ; \quad \xi = \left(\frac{z}{R} \right)^2 . \quad (10a)$$

Using this result and introducing the new variable

$$\eta = v^2 (\gamma p / \rho) = M^2 \quad (10b)$$

where M is the Mach number, the momentum conservation equation (5b) can be written in the nondimensional form:

$$\frac{d\eta}{d\xi} = \frac{\eta \left(1 + \frac{\gamma-1}{2} \eta \right) (1 - 6\xi + \gamma \eta)}{\xi (1 + \xi) (1 - \eta)} . \quad (11)$$

An analysis of equation (11) shows that the solutions will be thermally choked at the point

$$\eta = 1 , \quad \xi = \frac{1}{5} (\gamma + 1) \quad (12)$$

and this furnishes the required boundary condition for the solution of equation (11). This solution has not yet been obtained; however, some general information about the nature of the solution can nevertheless be obtained from a knowledge of conditions at the sonic point (12). The formulas for the various gas properties at the sonic point are readily obtained from equations (7), (8), (10), and (12) above, as follows:

$$h_s = \frac{2 W}{\sqrt{(\gamma + 1) (\gamma + 7)}} \quad (13a)$$

$$v_s = \sqrt{\frac{2(\gamma - 1)}{\sqrt{(\gamma + 1) (\gamma + 7)}}} \sqrt{W} \quad (13b)$$

$$\rho_s = \left(\frac{6}{\gamma + 7} \right)^{3/2} \sqrt{\frac{\sqrt{(\gamma + 1) (\gamma + 7)}}{2(\gamma - 1)}} \frac{\dot{m}}{A_0 \sqrt{W}} \quad (13c)$$

$$p_s = \frac{1}{\gamma} \left(\frac{6}{\gamma + 7} \right)^{3/2} \sqrt{\frac{2(\gamma - 1)}{\sqrt{(\gamma + 1) (\gamma + 7)}}} \frac{\dot{m} \sqrt{W}}{A_0} \quad (13d)$$

$$T_s = \frac{\gamma - 1}{\gamma} \frac{M}{k(1 + Z)} \quad h = \frac{2(\gamma - 1)}{\gamma \sqrt{(\gamma + 1) (\gamma + 7)}} \frac{M}{k(Z + 1)} W \quad (13e)$$

where M is the atomic mass, Z is the average charge on the ions, k is Boltzmann's constant and W is, of course, the quantity defined in equations (10a) above. In addition, we find from the energy balance (equation (9)) that the total voltage drop between the cathode and the sonic point is

$$V_s = \sqrt{\frac{\gamma+1}{\gamma+7}} \frac{\dot{m} W}{I} \quad (13f)$$

while the total drop along the arc axis is simply

$$V_\infty = \frac{\dot{m} W}{I} \quad (13g)$$

If it is assumed that all this energy is converted into directed motion, one obtains a final expansion velocity for the gas of

$$v_\infty = \sqrt{2W} \quad (13h)$$

D. CONCLUSIONS

The main conclusions to be drawn from the results presented above are apparently the following: 1) the jet temperature is rather high, 2) the jet pressure is also relatively high compared to the ambient for a considerable distance downstream from the exit, and 3) the gas acceleration is primarily thermal in nature. The $j \times B$ forces play an important, but somewhat indirect role in the acceleration mechanism by confining the jet gas within a "magnetic nozzle" configuration so that it can be heated to the temperatures and pressures required for the thermal acceleration.

Because of the large number of rather gross approximations which were made in the present calculations, they should be taken only as indicating qualitatively the sort of conditions which are to be expected in the MPD arcjet. To obtain a more quantitative prediction of the arc behavior, the "magnetic nozzle" calculation reported here should be extended to include, among other things, non-equilibrium effects, in particular the possibility of different electronic and ionic temperatures and the effects of current and energy losses or gains in the "nozzle" due to radial flow of current and energy through the sides. Work is now underway to try to incorporate these effects into the model.

APPENDIX F

PROPULSION PERFORMANCE OF A RADIATION-COOLED MPD THRUSTOR WITH LITHIUM PROPELLANT

Lithium Flow Rate (mg/sec)	Arc Current (amps)	Arc Voltage (volts)	Arc Power (kw)	Field Excitation Current (amps)	Thrust (gm)	Specific Impulse (sec)	Overall Efficiency (percent)
0.9	110	48	5.3	600	4.4	4780	19.2
	150	37	5.6	600	5.0	5440	23.4
	150	25	3.8	440	3.3	3580	15.2
	150	27	4.1	440	3.3	3580	14.0
	150	27	4.1	600	4.4	4780	25.0
	150	28	4.2	800	4.4	4780	24.0
	150	30	4.5	800	4.4	4780	22.4
	150	30	4.5	1000	5.5	5980	35.2
	150	40	6.0	800	5.5	3940	17.4
	160	35	5.6	680	6.1	4350	22.8
1.4	140	40	5.6	800	6.1	4360	22.8
	168	33	5.6	800	6.6	4720	27.0
	140	30	4.2	800	4.4	3160	16.0
	130	35	4.6	800	4.4	3160	14.8
	140	30	4.2	800	3.9	2800	12.6
	110	45	5.0	800	4.4	3160	13.6
	100	50	5.0	800	5.5	3940	20.8
	165	35	5.8	800	3.9	2800	9.2
	150	31	4.7	600	6.1	3350	21.2
	150	31	4.7	440	6.1	3350	21.2
6.7	120	45	5.4	800	6.9	3800	23.4
	160	40	6.4	800	7.2	3950	21.4
	165	40	6.6	600	7.2	3750	20.8
	158	26	4.1	600	7.2	1080	9.0
	163	25	4.1	440	6.7	1000	8.0
	150	29	4.4	800	8.3	1240	11.4
	140	31	4.3	1000	8.9	1330	13.2
	158	26	4.1	600	7.2	1080	9.0
	200	35	7.0	600	8.3	1240	12.4

BLANK PAGE

APPENDIX G

EXHAUST VELOCITY MEASUREMENTS USING A $\underline{u} \times \underline{B}$ PROBE

The use of a $\underline{u} \times \underline{B}$ probe for directly measuring the velocity in the exhaust of the MPD arcjet was initiated because the velocity values obtained at this laboratory using the probe in the exhaust of a 30-kw constricted arc arcjet were found to agree well with the values of velocity determined for such an engine by the conventional method of determining engine specific impulse by taking the ratio of engine thrust to mass flow rate.

Four different gases were used with the 30-kw engine, namely hydrogen, helium, nitrogen, and argon. The power levels were in the vicinity of 5 to 20 kw and the specific impulses ranged from 180 seconds (velocity of 1.8×10^5 cm/sec) for argon to 1000 seconds (1.0×10^6 cm/sec velocity) for hydrogen. The experimental measurements are summarized in table G-1 which lists the engine operating conditions, the average velocity as determined by the $\underline{u} \times \underline{B}$ probe, $\langle u \rangle$, the average velocity from the specific impulse values, $i_{sp} g$, and finally, the relative difference, $\frac{\langle u \rangle - i_{sp} g}{\langle u \rangle}$. By general inspection of the table, it is seen that on the average, the relative disagreements are not very great and several measurements were therefore performed using the $\underline{u} \times \underline{B}$ probe in the exhaust of an MPD arcjet (Model X-2C).

Figure G-1 shows a plot of $g i_{sp}$ versus the average velocity $\langle u \rangle$ determined by the $\underline{u} \times \underline{B}$ probe method with ammonia propellant. Ideally, the points would lie on the straight line drawn on the figure. The points shown do not represent individual measurements, but are rather the averages obtained over a large number of measurements. The scatter in the measured values was quite large, as high as 50 percent at the 1.0×10^6 cm/sec velocity point.

It is at present not completely clear exactly what the validity of the $\underline{u} \times \underline{B}$ measurement is in the exhaust of the MPD arcjet. This is due to the fact that, unlike the exhaust of the constricted arc engines, the extent of current flowing in the MPD exhaust is not known with any great accuracy and these currents, if and where they do exist, can introduce parasitic electric fields (such as the Hall field) between the probe sensors and lead to erroneous interpretation of the velocity measurements.

A second interpretative consideration arises from the somewhat different quantities measured by the two methods. The specific impulse is determined by

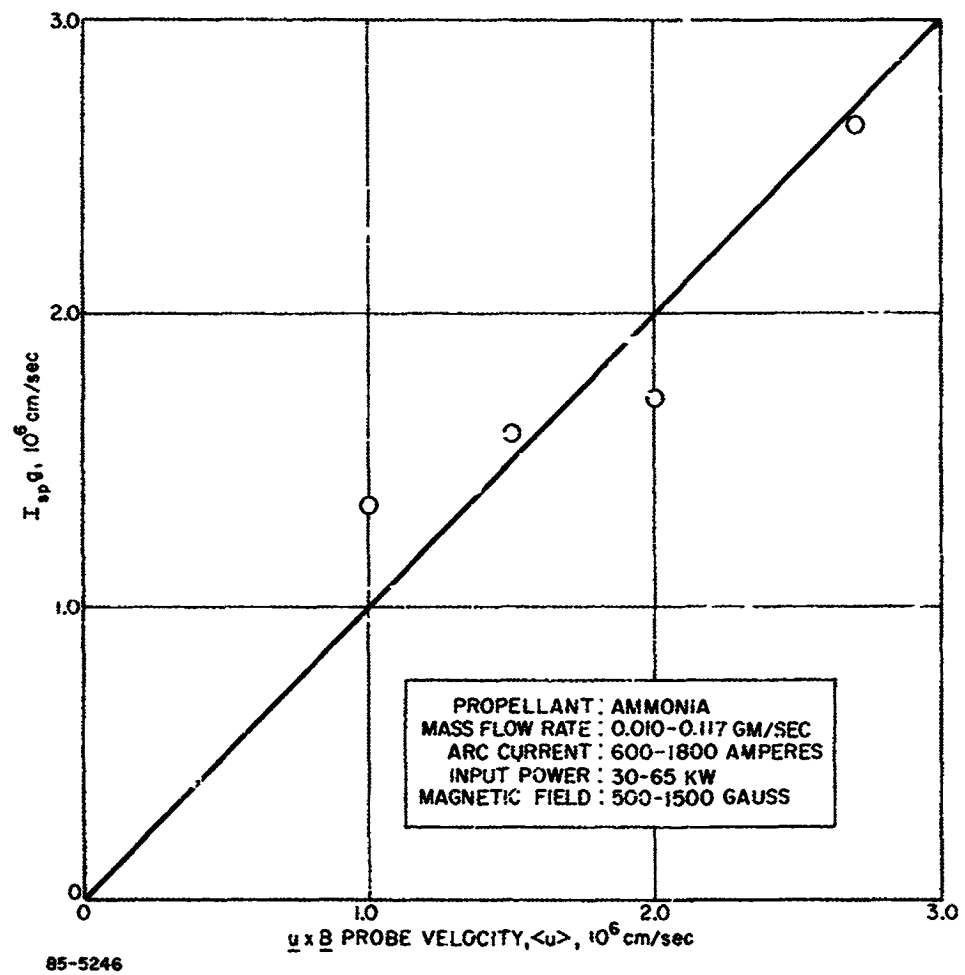


Figure G-1 COMPARISON OF VELOCITIES AS MEASURED BY T/A AND $u \times B$ PROBE

$$I_{sp} g = \frac{T}{m} = \frac{\int_0^R \rho u^2 r dr}{\int_0^R \rho u r dr}$$

whereas the $\underline{u} \times \underline{B}$ probe measures

$$\langle u \rangle = \frac{\int_0^R u r dr}{\int_0^R r dr}$$

It can, however, be shown that unless the exhaust momentum and mass flow distributions are very unusually extreme, as for example, if all the momentum is restricted to the exhaust axis, while the mass flow is restricted to the wings of the exhaust, that this difference does not exceed approximately 10 to 20 percent. Even for the extreme example just cited, the difference would be only of the order of 35 to 40 percent.

Work with the $\underline{u} \times \underline{B}$ probe is presently continuing under another program and the considerations just outlined, as well as several others considered to be of much less importance, are being studied to determine their importance in the interpretation of the data obtained.

The program under which the $\underline{u} \times \underline{B}$ probe was developed originates from the Aeronautical Systems Division, Wright-Patterson Air Force Base, and is entitled Gas Acceleration through Interaction of Electrical Discharges with Pre-Ionized Gases and Magnetic Fields, and is conducted at Avco RAD under Contract No. AF33(657)-11310. The data of table G-I were taken from Monthly Letter Report No. 9 of this program.

TABLE G-I

gas	h	I _{arc}	V _{arc}	(IV) _{st.}	P _{oh}	T	B ₀	uB ₀	<u>	I _{sp}	<u>-I _{sp}
	gm/sec	amperes	Volts	mw	mm Hg	gm	gauss	mV	10 ⁵ cm/sec10 ⁵ sec	cm/sec	%
1a											
H ₂	.10	150	90	13.5	290	80	13	240	8.2	8.0	+ 2
b											
H ₂	.10	150	90	13.5	290	80	26	420	7.2	8.0	-11
2a											
H ₂	.15	150	115	17.2	387	112	13	280	9.6	7.5	+21
b											
H ₂	.15	150	115	17.2	387	112	26	460	7.9	7.5	+ 5
3a											
H ₂	.20	100	115	11.5	440	120	13	150	5.2	6.0	-15
b											
H ₂	.20	100	115	11.5	440	120	26	300	5.4	6.0	-15
4a											
H ₂	.20	200	115	23.0	505	150	13	200	6.9	7.5	- 9
b											
H ₂	.20	200	115	23.0	505	150	26	400	6.9	7.5	- 9
5a											
H ₂	.13	200	30	6.0	320	70	6.5	100	.8	5.4	+20
b											
H ₂	.13	200	30	6.0	320	70	13.0	200	6.8	5.4	+20
6a											
H ₂	.15	135	40	5.4	330	80	13	110	3.0	5.3	-60
b											
H ₂	.15	135	40	5.4	330	80	26	210	3.6	5.3	-47
7a											
H ₂	.18	130	40	5.2	385	95	13	130	4.5	5.3	-17
b											
H ₂	.18	130	40	5.2	385	95	6.5	65	4.5	5.3	-17
8a											
H ₂	.20	130	40	5.2	400	95	13	120	4.2	4.7	-12
b											
H ₂	.20	130	40	5.2	400	95	26	230	4.0	4.7	-17
9a											
H ₂	.20	200	38	7.6	440	105	13	140	4.8	5.2	- 8
b											
H ₂	.20	200	38	7.6	440	105	26	270	4.6	5.2	-13

TABLE G-1 (Cont'd)

gas	λ	I_{arc}	V_{arc}	$(IV)_{arc}$	P_{ch}	T	B_0	u_{B_0}	$\langle u \rangle$	$f_{sp, B}$	$\frac{\langle u \rangle - f_{sp, B}}{\langle u \rangle}$
	gm/sec	amperes	Volts	kw	mm Hg	gm	gauss	mV	10^5 cm/sec 10^5 cm/sec	%	%
10	H_2	200	50	10.0	365	120	13	95	3.2	3.5	-9
11	H_2	100	60	6.0	340	110	13	75	2.6	2.8	-7
12a	H_2	100	60	6.0	345	113	5.6	35	2.8	2.8	0
b	H_2	100	60	6.0	345	113	16.8	105	2.8	2.8	0
13a	H_2	200	57	11.4	445	146	5.6	45	3.6	3.6	0
b	H_2	200	57	11.4	445	146	16.8	135	3.6	3.6	0
14	H_2	200	60	12.0	470	154	13	95	3.2	3.9	-22
15	H_2	200	60	12.0	395	130	13	95	3.2	3.3	-3
16	H_2	200	60	12.0	425	140	13	100	3.4	3.5	-3
17	H_2	300	60	18.0	510	167	13	130	4.4	4.4	+4
18	H_2	200	60	12.0	420	137	13	95	3.2	2.6	+19
19a	H_2	200	60	12.0	530	175	5.6	45	3.6	3.3	+9
b	H_2	200	60	12.0	530	175	11.2	90	3.6	3.3	+9
c	H_2	200	60	12.0	530	175	16.8	115	3.6	3.3	+9
20	H_2	200	60	12.0	630	208	13.0	90	3.0	2.6	+13
21a	H_2	200	65	13.0	720	237	5.6	45	3.6	3.0	+16
b	H_2	200	65	13.0	720	237	16.8	135	3.6	3.0	+16

TABLE G-1 (Concl'd)

	gas	m gm/sec	I _{arc} amperes	V _{arc} Volts	(IV) _{arc} kw	Pch mm Hg	T gm	R ₀ gauss	uB ₀ /l mV	<u> 10 ⁵ cm/sec	I _{eps} 10 ⁵ cm/sec	<u> - I _{eps} <u> %	
22a	A	.47	200	17	3.4	335	90	13	60	1.9	1.9	0	0
b	A	.47	200	17	3.4	335	90	26	120	1.9	1.9	0	0
23a	A	.47	300	16	4.8	385	110	13	75	2.6	2.3	+12	+12
b	A	.47	300	16	4.8	385	110	26	145	2.5	2.3	+8	+8
24a	A	.47	300	18	5.4	372	98	16	90	2.5	2.1	+16	+16
b	A	.47	300	18	5.4	372	98	27	150	2.5	2.1	+16	+16
25a	A	.63	150	20	3.0	400	110	13	60	2.0	1.8	+10	+10
b	A	.63	150	20	3.0	400	110	26	115	1.9	1.8	+5	+5
26a	A	.63	150	20	3.0	425	115	13	65	2.2	1.8	+18	+18
b	A	.63	150	20	3.0	425	115	26	130	2.2	1.8	+18	+18
27	A	.63	180	19	3.4	425	110	39	180	2.0	1.8	+10	+10
28a	A	.63	200	20	4.0	465	125	13	70	2.4	2.0	+16	+16
b	A	.63	200	20	4.0	465	125	26	140	2.4	2.0	+16	+16
29a	A	.63	300	17	5.1	480	126	13	65	2.2	2.0	+8	+8
b	A	.63	300	17	5.1	480	126	26	130	2.2	2.0	+8	+8
30	A	.63	300	18	5.4	475	123	27	150	2.5	2.0	+20	+20
31	A	.63	300	18	5.4	475	125	27	150	2.5	2.0	+20	+20
32a	A	.63	300	20	6.0	482	135	13	65	2.2	2.2	0	0
b	A	.63	300	20	6.0	482	135	26	130	2.2	2.2	0	0
33a	A	.79	200	21	4.2	560	145	13	70	2.4	1.8	+24	+24
b	A	.79	200	21	4.2	560	145	26	140	2.4	1.8	+24	+24